Simulations of Recrystallization in Metals

Godiksen, Rasmus Brauner

Publication date:
2007

Document Version
Publisher's PDF, also known as Version of record

RISØ

Risø-PhD-thesis

Simulations of Recrystallization in Metals

Rasmus Brauner Nyberg Godiksen

Risø-PhD-36(EN)

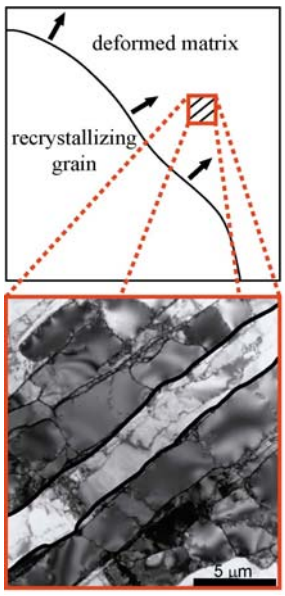

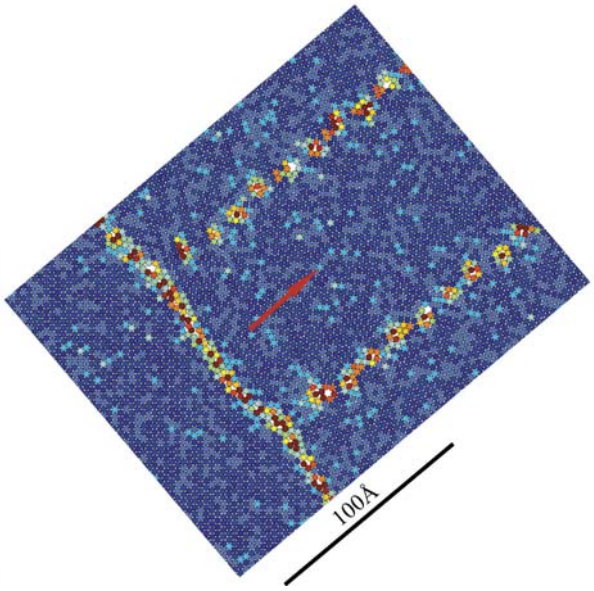

Risø National Laboratory
Technical University of Denmark
Roskilde, Denmark
October 2007

DTU

Author: Rasmus Brauner Nyberg Godiksen
Title: Simulations of Recrystallization in Metals
Department: Materials Research Department

This thesis is submitted in partial fulfillment of the requirements for obtaining the PhD degree in physics from Roskilde University (RUC) in collaboration with Risø National Laboratory, part of the Technical University of Denmark (DTU).

Short Abstract: The growth of new near-perfect grains during recrystallization of deformed metals is governed by the migration of the grain boundaries surrounding the new grains. The grain boundaries migrate through the deformed metal driven by the excess energy of the dislocation structures created during deformation. Recently, it has been found that recrystallization is far more inhomogeneous than previously thought. The purpose of this PhD-project is to study recrystallization by computer simulations with special focus on inhomogeneous growth. Two types of simulations have been employed: geometric- and molecular dynamics simulations (MD).

The geometric simulation method developed and used in this study is a generalization of an existing method. The geometric simulations have been used to investigate simplistic situations where one type of growth-inhomogeneity exists in an otherwise very basic model. Simulations of grains possessing distributions of growth rates and simulations of anisotropic growing grains, where grains have individual preferred growth-directions, have been performed. The MD simulations have been used to study grain boundary motion driven by dislocation structures at the atomic level. This is the first time that dislocation structures have been used to drive grain boundary migration in MD simulations. Different types of dislocation structures and grain boundaries have been simulated using different inter-atomic potentials.

The geometric simulations show that the introduction of growth-inhomogeneities into a simple recrystallization-model can affect the recrystallization kinetics and microstructure significantly, which makes it very important to understand the origin of such inhomogeneities. The MD simulations show that grain boundary migration during recrystallization is strongly affected by the dislocation structures in the deformed metal due to local effects: Inhomogeneous boundary morphologies and dislocation-structure-dependent migration rates are observed. The effects that the dislocation structures have must be taken into account in order to create realistic recrystallization models, and through that improve the processing and properties of metals.

Kort Resumé: Når metaller rekrystalliseres, vokser nye perfekte korn ved at kornenes grænser migrerer gennem det deformerede metal. Korngrænserne er drevet af den ekstra energi, der findes i de dislokationsstrukturer, som er skabt ved deformering af metallet. Det har vist sig, at rekrystallisation er en meget mere inhomogen proces end tidligere antaget. Formålet med dette PhD-projekt er at studere rekrystallisation ved hjælp af computersimuleringer med særligt fokus på inhomogen vækst. To typer simuleringer er blevet anvendt: Geometriske- og 'molecular dynamics' (MD) simuleringer.

Den geometriske simuleringsmetode, som er blevet udviklet og benyttet i dette projekt, er en generalisering af en eksisterende metode. De geometriske simuleringer er blevet brugt til at undersøge simple situationer, hvor en og kun en slags vækst-inhomogenitet er til stede i en ellers meget simpel model. Simuleringer hvor korn har vækshastigheds-fordelinger samt simuleringer af anisotropt voksende korn, hvor kornene har individuelle foretrukne vækstretninger, er blevet udført. MD simuleringerne er blevet brugt til at studere korngrænsemigration drevet af dislokationsstrukturer på det atomare niveau. Dette er første gang, at dislokations-strukturer er blevet brugt til at drive korngrænser i MD simuleringer. Forskellige typer af dislokationsstrukturer og korngrænser er blevet simuleret med forskellige interatomare potentialer.

De geometriske simuleringer viser, at introduktionen af vækst-inhomogeniteter i en simpel rekrystallisationsmodel kan påvirke kinetikken og mikrostrukturen af rekrystallisation voldsomt, hvilket igen viser, at det er særdeles vigtigt at forstå hvorfor inhomogeniteterne opstår. MD simuleringerne viser, at korngrænsemigration under rekrystallisation er stærkt afhængig af dislokationsstrukturerne på grund af lokale effekter: Inhomogene korngrænse-morfologier og korngrænser med hastigheder som er stærkt afhængige af dislokationsstrukturerne er blevet set. Dislokationsstrukturers effekter på korngrænsemigration skal derfor inkluderes for at kunne opbygge realistiske rekrystallisationsmodeller, som kan forbedre bearbejdningsmetoder og egenskaber af metaller.

Risø-PhD-36(EN)
October 2007

ISBN 978-87-550-3639-0

Supervised by:
Dorte Juul Jensen (Risø)
Søren Schmidt (Risø)
Jeppe Dyre (RUC)

Sponsorship: The Danish National Research Foundation has supported this work.

Cover: The basic idea behind the molecular dynamics simulations of recrystallization. Top left image: Illustration of a grain boundary of a recrystallizing grain migrating through the deformed matrix. Bottom left image: TEM image showing a typical microstructure of a deformed metal. Long elongated dislocation boundaries dominate the deformation microstructure. Right image: Snapshot from a molecular dynamics simulation. Atoms are colored according to their potential energy; blue indicate low and red indicate high energy. A continuous grain boundary and two dislocation boundaries with individual dislocations are seen as high energy areas. The simulation captures the essential feature of recrystallization: A migrating grain boundary driven by the presence of dislocations.

Pages: 122 / 244
Tables: 5
Figures: 48
References: 10 + 98

Information Service Department
Risø National Laboratory
Technical University of Denmark
P.O.Box 49
DK-4000 Roskilde
Denmark
Telephone +45 46774004
bibl@risoe.dk
Fax +45 46774013
www.risoe.dk

Abstract

The growth of new near-perfect grains during recrystallization of deformed metals is governed by the migration of the grain boundaries surrounding the new grains. The grain boundaries migrate through the deformed metal driven by the excess energy of the dislocation structures created during deformation. Recently, it has been found that recrystallization is far more inhomogeneous than previously thought. The purpose of this PhD-project is to study recrystallization by computer simulations with special focus on inhomogeneous growth. Two types of simulations have been employed: geometric- and molecular dynamics simulations (MD).

An existing geometric simulation method has been refined during this PhD-project and used to study the overall recrystallization kinetics and microstructure as a result of inhomogeneous growth parameters. The geometric simulations are used to investigate simplistic situations where only one type of inhomogeneity exists in an otherwise very basic model. Special focus has been put on simulations of distributions of growth rates and of anisotropically growing grains. The simulations show that distributions in growth rates and growth directions typically have a significant impact on the recrystallization microstructure. The overall recrystallization kinetics are greatly affected by certain growth-rate distributions. Anisotropic growing grains on the other hand have a surprisingly small effect on the kinetics, which can be predicted by relatively simple models.

The MD simulations have been used to study grain boundary motion driven by dislocation structures at the atomic level. This is the first time that dislocation structures have been used to drive grain boundary migration in MD simulations. Different types of dislocation structures and grain boundaries have been simulated using different inter-atomic potentials. Very significant changes in the grain boundary migration rate and apparent mobility can be obtained by varying the dislocation structures. For some structures, the correlation between the boundary migration rate v and the driving pressure P is $v \propto P$ as expected; for other structures $v \propto P^2$. It is proposed that the P^2-dependence stem from dislocation structures that are providing a locally varying driving pressure, something that is not taken into account in existing recrystallization models. The interactions between the grain boundaries and the dislocation structures are studied in detail: grain boundaries may interact with some types of dislocation boundaries in ways which perturb the grain boundary morphology. The grain boundary dynamics and morphology are qualitatively not very dependent on the character of the grain boundary or on the interatomic potentials used, but quantitative measures such as the mobility and the activation energy are affected by the choice of potential.

The geometric simulations show that the introduction of growth-inhomogeneities into a simple recrystallization-model can affect the recrystallization kinetics and microstructure significantly, which makes it very important to understand the origin of inhomogeneities. The MD simulations show that grain boundary migration during recrystallization is strongly affected by the dislocation structures in the deformed metal due to complex local interactions between the grain boundaries and the dislocation structures due to local effects: Inhomogeneous boundary morphologies and dislocation-structure-dependent migration rates are observed. The effects that the dislocation structures have must be taken into account in order to create realistic recrystallization models, and through that improve the processing and properties of metals.

Resumé

Når metaller rekrystalliseres, vokser nye perfekte korn ved at kornenes grænser migrerer gennem det deformerede metal. Korngrænserne er drevet af den ekstra energi, der findes i de dislokationsstrukturer, som er skabt ved deformering af metallet. Det har vist sig, at rekrystallisation er en meget mere inhomogen proces end tidligere antaget. Formålet med dette PhD-projekt er at studere rekrystallisation ved hjælp af computersimuleringer med særligt fokus på inhomogen vækst. To typer simuleringer er blevet anvendt: Geometriske- og 'molecular dynamics' (MD) simuleringer.

En eksisterende metode til at udføre geometriske simuleringer er blevet forbedret i løbet af dette projekt og er blevet brugt til at simulere udviklingen i mikrostruktur og kinetik under rekrystallisation resulterende fra inhomogene vækstparametre. De geometriske simuleringer er blevet brugt til at undersøge simple situationer, hvor kun en type inhomogenitet er til stede i en ellers meget simpel model. I projektet er der især blevet fokuseret på fordelinger af vækstrater og anisotrop vækst. Simuleringerne viser, at både fordelinger af vækstrater og fordelinger af vækstretninger har en stor effekt på mikrostrukturen af det rekrystalliserede metal. Den overordnede kinetik under rekrystallisation er stærkt påvirket af visse fordelinger af vækstrater. Anisotropt voksende korn derimod har en overraskende lille effekt på kinetikken, og standard-modeller kan bruges til at beskrive denne kinetik.

MD simuleringerne er blevet brugt til at studere korngrænsemigration drevet af dislokationsstrukturer på det atomare niveau. Dette er første gang at dislokationsstrukturer er blevet brugt til at drive korngrænser i MD simuleringer. Forskellige typer af dislokationsstrukturer og korngrænser er blevet simuleret med forskellige inter-atomare potentialer. Meget store ændringer i korngrænsernes migrationsrater og tilsyneladende mobiliteter opnås ved at ændre på dislokationsstrukturerne. For nogle strukturer er sammenhængen mellem grænsemigrationsraten v og det drivende tryk P givet ved $v \propto P$ som forventet, men for andre dislokationsstrukturer er $v \propto P^2$. P^2-afhængigheden kan skyldes dislokationsstrukturer der giver en lokalt varierende drivende kraft, en effekt som ikke er medtaget i eksisterende rekrystallisationsmodeller. Interaktionerne mellem korngrænser og dislokationsstrukturer er blevet studeret i stor detalje i dette projekt: Korngrænserne kan interagere med visse typer af strukturer på en måde som perturberer korngrænsemorfologien. Kvalitativt afhænger korngrænsedynamikken og -morfologien kun svagt af korngrænsetypen og det benyttede inter-atomare potentiale, men kvantitative mål så som mobiliteten og aktiveringsenergien er stærkt afhængige af valget af potentiale.

De geometriske simuleringer viser, at introduktionen af vækst-inhomogeniteter i en simpel rekrystallisationsmodel kan påvirke kinetikken og mikrostrukturen af rekrystallisation voldsomt, hvilket igen viser, at det er særdeles vigtigt at forstå hvorfor inhomogeniteterne opstår. MD simuleringerne viser, at korngrænsemigration under rekrystallisation er stærkt afhængig af dislokationsstrukturerne på grund af lokale effekter: Inhomogene korngrænse-morfologier og korngrænser med hastigheder som er stærkt afhængige af dislokationsstrukturerne er blevet observeret. Dislokationsstrukturers effekter på korngrænsemigration skal derfor inkluderes for at kunne opbygge realistiske rekrystallisationsmodeller, som kan forbedre bearbejdningsmetoder og egenskaber af metaller.

Preface

This thesis is submitted in partial fulfillment of the requirements for obtaining the PhD degree in physics from Roskilde University (RUC) in collaboration with Risø National Laboratory, part of the Technical University of Denmark (DTU).

The PhD project was carried out within the Center For Fundamental Research: Metal Structures in Four Dimensions (M4D), at Risø. I would gratefully acknowledge the Danish National Research Foundation for supporting M4D. The study was conducted during the three-year period November 2004 to October 2007.

I visited two research-institutions other than RUC and Risø during the PhD project in order to get familiar with the molecular dynamics computer programs used for the study. From May 20 to June 20 2005, I visited the group for Simulation and Theory of Atomic-scale Material Phenomena (STAMP) at Colorado School of Mines. I was supervised by Moneesh Upmanyu and aided greatly by PhD student Zachary T. Trautt. I am very grateful to both for much support during my stay and also during the rest of the PhD-project. During the spring of 2006, I worked for a total of approximately one month at the Center for Atomic-scale Materials Design (CAMd) at DTU in Lyngby supervised by Jakob Schiøtz. I would like to thank Jakob for teaching me much about molecular dynamics simulations and for a lot of help working out some of the articles that has come out of this study.

The part of the study using the geometric simulations has been guided a lot by discussions with Paulo R. Rios (Federal Fluminense University, Brazil) and Roy Vandermeer (US Naval Lab.). I would like to acknowledge both for educating me in the area of geometric analytical models.

I would also like to thank Brian Ralph (Brunel University, UK) for many good discussions regarding my work during his frequent visits to Risø as well as for helping me improve my written English in articles and in this thesis.

During my engagement with the M4D, I have had the opportunity to work with many very skilled professionals. I would like to thank everybody within the center for a very open working environment where the answers to most metallurgical questions can be found just down the corridor. Wolfgang Pantleon deserves to be mentioned in particular, at times he acted almost as a Co-supervisor. I would especially like to thank the young people at the center for making the time at M4D very enjoyable. Also, Bo Jakobsen has read and commented on this thesis before it was handed in, which indeed has been a great help.

I would like to thank my supervisors, Jeppe Dyre (RUC), Søren Schmidt (M4D) and Dorte Juul Jensen (M4D) for much support during the entire project. Although it has been busy times for all of you, I have always received the help and guidance that I needed, when I needed it.

Finally I would like to thank my wife Mia Titine Nyberg Godiksen for supporting and encouraging me throughout the duration of the PhD; both at times where it was tough and at times where it was not so tough.

Rasmus Brauner Nyberg Godiksen
Risø, October 26, 2007

List of Articles

During the course of the PhD-project, a number articles have been written; most of them are published while other are in the reviewing/publishing process. The articles are listed below.

Article A Analytical expression for the evolution of interfacial area density between transformed grains during nucleation and growth transformations. P.R. Rios, R.B. Godiksen, S. Schmidt, D. Juul Jensen, R.A. Vandermeer, *Scripta Materialia* **54**, 1509–1513 (2006).[1]

Article B Effects of distributions of growth rates on recrystallization kinetics and microstructure. R.B. Godiksen, S. Schmidt, D. Juul Jensen, *Scripta Materialia* **57**, 345–348 (2007).[2]

Article C Three-Dimensional Geometric Simulations of Anisotropic Growth during Transformation Phenomena. R.B. Godiksen, P.R.Rios, R.A.Vandermeer S. Schmidt, D. Juul Jensen, Accepted for publication in *Scripta Materialia*, doi:10.1016/j.scriptamat.2007.10.003 (2007).[3]

Article D Towards atomic level simulations of recrystallization - setting up suitable geometry. R.B. Godiksen, Z.T. Trautt, M. Upmanyu, S. Schmidt, D. Juul Jensen, *Materials Science and Technology* **21**, 1373–1375 (2005).[4]

Article E Simulations of Boundary Migration during Recrystallization using Molecular Dynamics. R.B. Godiksen, Z.T. Trautt, M. Upmanyu, J. Schiøtz, D. Juul Jensen, S. Schmidt, *Acta Materialia* **55**, 6383–6391 (2007).[5]

Article F Atomistisk Simulering af Rekrystallisation. R.B. Godiksen, S. Schmidt, D. Juul Jensen, *Proceedings of Dansk Metallurgisk Selskabs Vintermøde*, 27–37 (2007).[6]

Article G Simulation of Recrystallization using Molecular Dynamics; Effects of the Interatomic Potential. R.B. Godiksen, Z.T. Trautt, M. Upmanyu, S. Schmidt, D. Juul Jensen, *Materials Science Forum* **558–559**, 1081–1086 (2007).[7]

Article H Molecular dynamics simulations of grain boundary migration during recrystallization employing different types of dislocation structures to produce the driving pressure. R. B. N. Godiksen, S. Schmidt, D. Juul Jensen, submitted to *Modelling and Simulation of Materials Science and Engineering.*[8]

Article I Measurement of the components of plastic displacement gradients in three dimensions. S. F. Nielsen, G. Beckmann, R. B. Godiksen, K. Haldrup, H. F. Poulsen and J. A. Wert, Developments in X-Ray Tomography IV. Edited by Ulrich Bonse, *Proceedings of SPIE*, **5535**, 485–492, (2004).[9]

Article J Bulk investigations of grain boundary migration during recrystallization utilizing the 3DXRD microscope. S. Schmidt, R. B. Godiksen and D. Juul Jensen, *Proceedings of Solid-Solid Phase Transformations in Inorganic Materials '05*, edited by J. M. Howe, D. E. Laughlin, J. K. Lee, D. J. Srolovitz and U. Dahmen, 583, (2005).[10]

List of Commonly Used Symbols and Abbreviations

T	Temperature.
t	Time.
k_B	Boltzmann's constant.
E_a	Activation energy.
θ	Misorientation.
θ_b	Misorientation across grain boundary.
θ_d	Misorientation across dislocation boundary.
v	Grain boundary velocity.
M	Grain boundary mobility.
M_∞	Infinite temperature mobility.
P	Driving pressure.
N	Number of atoms.
l_x,l_y,l_z	Size of simulation.
V	Total volume.
V_V	Recrystallized volume fraction.
V_X	Extended volume fraction.
S_V	Free surface fraction of recrystallizing grains.
R_V	Impinged surface fraction of recrystallizing grains.
S_X	Extended surface fraction.
Crr	Contiguity $Crr = 2R_V/(2R_V + S_V)$.
$< d >$	Mean intercept length.
p	JMAK-parameter.
α,A	Growth parameters for grain radius $r = At^{1-\alpha}$.
g, h	Growth parameters for grain velocity $v = g(t - t_0)^h$
MD	Molecular Dynamics.
MC	Monte Carlo.
JMAK	Johnson-Mehl-Avrami-Kolmogorov.
MP	Microstructural Path.
RS	Read-Shockley.
EAM	Embedded Atom Method.
EMT	Effective Medium Theory.
LJ	Lennard-Jones.
CAMd	Center for Atomic-scale Materials Design.
CSM	Colorado School of Mines.

Note: Some symbols may be used differently than the above tabulated in certain parts of the thesis. This will be pointed out in the text where appropriate.

Contents

1 Introduction and Background

This chapter introduces the field of study and the project documented the present thesis. First the project is presented briefly and thereafter the necessary theoretical and experimental background for understanding the project is described. Throughout this chapter the choices of the investigations performed and the methods used in this study are given. A precise description of the project is presented at the end of the chapter.

1.1 Short Introduction to the Project

Recrystallization is a transformation-process that plastically deformed metals may undergo when annealed. When a metal is deformed plastically, some of the applied work is stored in the metal in the form of defects that are generated due to the straining of the crystal-lattice. During recrystallization most (or all) of the energy that is stored in the metal is released by a mechanism that is governed by the nucleation and growth of new grains (crystallites). The boundaries surrounding new grains migrate through the deformed material (the deformed matrix) and the new recrystallizing grains will eventually consume all of the deformed matrix. Fig.1.1 show a sequence of images illustrating growth of grains during recrystallization. The scale in this sequence is arbitrary but grains in a fully recrystallized metal have sizes from a few to several hundred μ.

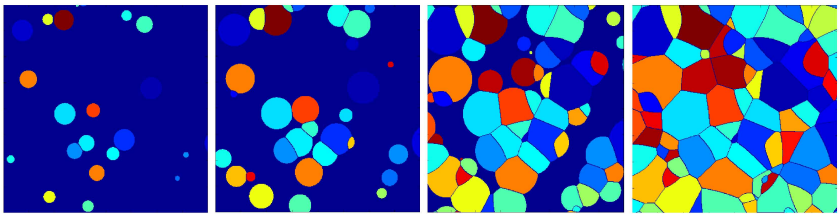

Figure 1.1 Time sequence illustrating growing grains during recrystallization. The matrix is shown in dark blue and the growing grains in other colors. The grains appear and grow, eventually transforming the entire matrix into a polycrystalline grain structure. The sequence originates from a simulation using simplistic assumptions; normally recrystallizing grains will for example not grow as spheres.

Recrystallization is typically associated with changes in the local crystallographic orientations because the orientation of a part of the deformed matrix rearrange into the orientation of the grain that consumes it. Recrystallization is a very radical process that alters *every* part of the metal; according to R.W.Cahn: *In* recrystallization*, the crystal orientation of any region in the deformed matrix is altered.* [23]p.1596.

The microstructure after recrystallization is essential to the properties of the metal. The overall orientation of the crystal lattices (texture) is for example very important for the forming properties and the grain size distribution affects the strength of materials[40]. Since recrystallization is involved in the processing of nearly every piece of metal produced, understanding recrystallization is of enormous importance to understanding and controlling metal-properties.

Experiments involving recrystallization in metals are complicated to carry out, analyze and interpret for many reasons; limited temporal and spatial resolution, competing processes taking place at the same time, data reconstructions necessary to access the studied properties etc. Modelling can be used to create simplified scenarios, where the researcher has *full access* to the processes studied. Recrystallization models, such as the famous JMAK model [14, 15, 16, 43, 47], typically assume very idealized nucleation and growth behavior, although it is known that recrystallizing grains may typically exhibit very inhomogeneous growth patterns. It is a main goal of recrystallization modelling to understand what causes the observed inhomogeneous growth and what influence inhomogeneities have on recrystallization. In this study two modelling approaches have been used to study recrystallization in metals: geometric simulations and molecular dynamics simulations (MD).

The geometric simulations deal with recrystallization on a mesoscopic level by simulating collections of recrystallizing grains with predefined properties. The methodology is well suited to study the average behavior of many recrystallizing grains. During this study an existing geometric simulation methodology was extended significantly and new algorithms were developed and implemented. These were applied to problems that were not well understood, such as the influence of boundary migration rate distributions and grain shape on the overall recrystallization kinetics.

The MD technique can be used to study physical processes on different length-scales, but is most often used to study phenomena on the atomic level, or phenomena involving many atoms, where atomic resolution is desired. In this study MD has for the first time been used to simulate migrating grain boundaries driven by the stored energy of deformation, i.e. recrystallization. In order to do this, a new way of setting up 'simulation-geometries' to represent recrystallization have been developed as part of this study. MD is widely used to study materials and many computer-programs for MD are available and existing MD-programs have been used to simulate the geometries developed. The main issue addressed in this MD-study is the influence of the microstructures introduced during deformation on the boundary migration.

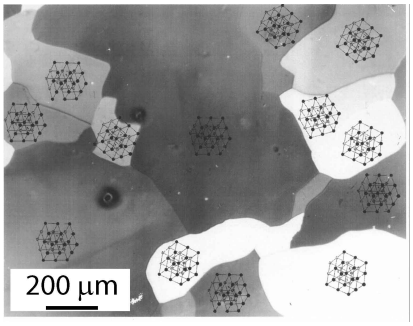

Figure 1.2 Undeformed polycrystalline microstructure. Each grain has a crystal orientation represented by the symbolic lattices. The differences in gray tone represent the orientations of the grains depicted. The even intensities throughout the separate grains indicate that the misorientations within the grains are very small.

1.2 Phenomenology

The thermo-mechanical process-cycle, of which recrystallization is a part of, can be divided into:

deformation > recovery > recrystallization > grain growth

A metal that has not undergone any deformation is typically a polycrystal consisting of grains with near-perfect crystal-lattices (fig.1.2). The grain boundaries separating the grains are associated with a lattice misorientation defined as the rotation that would transform the lattice on the one side of the grain boundary into the lattice on the other side.

A very important concept in metallurgy is the dislocation: a dislocation is a line defect within a crystal lattice, illustrated in fig.1.3. Imagine drawing a line from atom to atom around the dislocation and counting the number of times that you have moved one atom up, down, left and right until you end up at the starting atom. This is called a Burger's circuit; a Burger's circuit for the dislocation in fig.1.3 is shown in blue. A dislocation will always be associated with a closing failure, meaning that you would not have moved as many times up as down or as many times right as left. The closing failure is a vector called the Burger's vector (the red vector in fig.1.3). Two special types of dislocations exist: edge- and screw dislocations. An edge dislocation is defined as a dislocation that has its Burger's vector perpendicular to the direction of the dislocation (as for the one in fig.1.3) and a screw dislocation is defined as dislocation that has its Burger's vector parallel to its direction. Any other type of dislocation is called a mixed dislocation.

By shifting the location of a dislocation the atoms surrounding it can move relative to each other. When a metal is deformed plastically, the distortion of the crystal lattice is mitigated by the creation and movement of huge numbers of dislocations; dislocation densities can be of the order of kilometers per cubic centimeter [103]. Also huge numbers of point defects are produced. The dislocations, point defects and the elastic straining of the crystal increase the free energy of the metal considerably and the metal is therefore, in principle, out of equilibrium. High-energy barriers, however, hinder the movement of dislocations and the return to an undeformed lattice-structure. If a deformed metal is subsequently

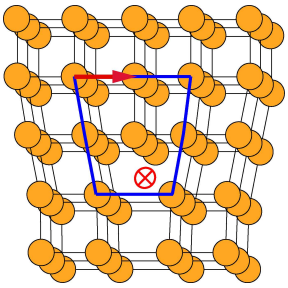

Figure 1.3 Dislocation within a crystal lattice indicated by the red crossed out circle. The direction of the dislocation is perpendicular to the figure plane traversing through the atom planes shown. A Burger's circuit is drawn around the dislocation showing the closing failure as a red vector, i.e. the Burger's vector.

annealed the energy barriers can be overcome, and a perfect crystal lattice can re-emerge through recovery, recrystallization and grain growth.

During recovery most of the point defects are removed and the dislocation density is lowered by dislocation movements and annihilations. The dislocations that do not annihilate may arrange into configurations containing lower energy[23].

During recrystallization new essentially defect- and strain-free grains nucleate and grow by migration of the surrounding grain boundaries [40]. These boundaries are driven by the excess free energy stored in the surrounding dislocation structures: when the grain boundaries sweep through the yet un-recrystallized material the dislocation structures in the deformed matrix are replaced by the defect free material of the recrystallizing grain. The boundaries will in most cases continue to migrate until all the deformed matrix has been transformed. After total recrystallization all of the deformed microstructure will be removed and the metal will have a polycrystalline structure that is made up of near-perfect grains. This is essentially the same structure as before the deformation, although the grain size typically is different. Recrystallization can be regarded as a special case of the more general framework of inhomogeneous phase transformations, where one phase nucleates and grows within another.

If annealing is continued the grain boundaries separating the recrystallized grains may move in a way that minimizes the grain boundary area and thus reduces the grain boundary free energy. This is called grain growth. During grain growth the large grains will increase in size while the smaller ones will disappear because small grains are associated with a larger surface area per volume compared to large grains.

Recrystallization and grain growth typically happen at different temperatures due to the large differences in the magnitude of the energy reductions produced by the migrating boundaries. Grain growth, governed by the reduction of grain boundary energy, gives energy reductions of 10^3–$10^6 \mathrm{J/m}^3$, whereas recrystallization, driven by the removal of deformation structures, gives reductions of 10^5–$5 \cdot 10^7 \mathrm{J/m}^3$ [12]. A typical thermo-mechanical process-cycle is illustrated in fig.1.4.

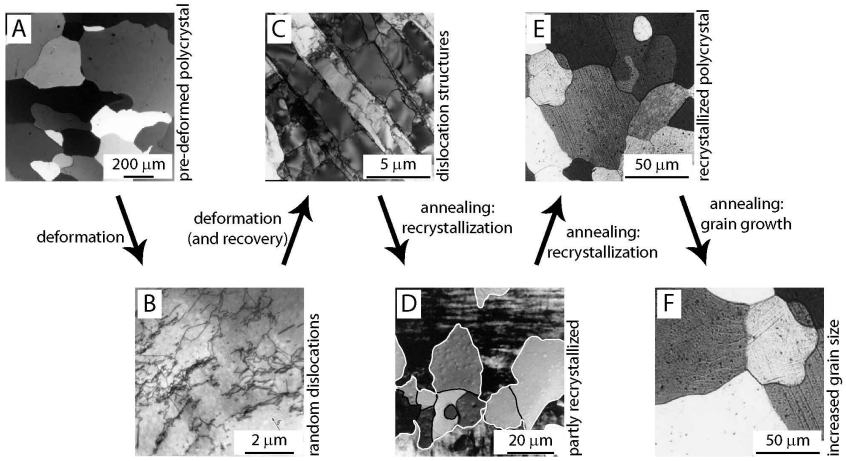

Figure 1.4 Typical process-cycle. A: Initial undeformed polycrystal. B: After some deformation dislocations have formed throughout the sample. C: After further deformation the dislocations have formed dislocation structures. D: At higher annealing temperatures recrystallization sets in, D shows a partly recrystallized microstructure. Free boundaries are highlighted in white, impinged boundaries in black (see section 1.4.3). E: After total recrystallization the topology of the grain structure resembles the initial polycrystal. F: If annealed further grain growth may set in leading to an increase of the grain size.

1.3 Microstructures at the Onset of Recrystallization: Deformation Structures

The structures present in the metal before the onset of recrystallization are primarily made up of dislocation structures. These are created during deformation and/or recovery. Structures will form during deformation, but may change (recover) during recovery depending on the type of metal. Cu for example, have a clear recovery stage before the onset of recrystallization while this is not the case for Al. Recovery may take place during recrystallization, which is the case for Al. This will lead to a reduction in the stored energy in the deformed matrix during recrystallization. In this thesis the term *deformation structure* will be used as a synonym for the structure present at the onset of recrystallization.

The microstructure depends both on the type of metal and kind of deformation, but some common features do exist. The dislocations are typically not distributed randomly, but accumulated in dislocation boundaries, which separate regions with relatively low dislocation density [34]. The for formation of structures happens because dislocation structures have low energy compared to randomly distributed dislocations. Two types of dislocation boundary morphologies are typically seen: 1) extended nearly planar boundaries and 2) almost randomly ori-

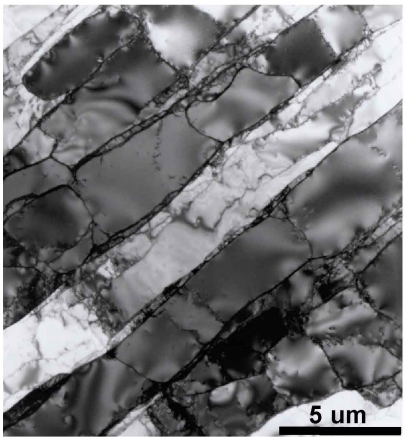

Figure 1.5 Typical rolled microstructure observed by TEM. The micrograph shows a 40% cold rolled Al single crystal. The structure is subdivided by elongated, almost planar dislocation boundaries inclined 30° to 35° to the rolling direction. A second set of dislocation boundaries (cell boundaries) is seen on top of the first, dividing the microstructure into small elongated cells. Figure by the curtesy of D. Juul Jensen.

entated cell boundaries [34]. Fig.1.5 show an example of a microstructure that contains both types, which is typical for cold rolled materials. The planar dislocation boundaries have relatively high misorientations across them; for metals cold rolled to large strains these can be up to 60 deg.[34]. Neighboring extended boundaries often have alternating misorientations: if the misorientation of a particular boundary corresponds to a positive rotation around a given axis the misorientations of the neighboring boundaries corresponds to negative rotations around the same axis. Another set of dislocation boundaries (the cell boundaries), which have much lower misorientations across them, is seen intersecting the planner boundaries. The two sets of dislocation boundaries together produce a deformed matrix consisting of cells. Inside the cells the dislocation density is typically much lower than in the dislocation boundaries.

The misorientation across a crystal interface can always be associated with a rotation of the crystal around some axis $\boldsymbol{\theta}$. Moreover, the misorientation across a dislocation boundary can be related to the dislocations within the boundary. The average of the Burger's vectors of all dislocations in the boundary is some finite vector $\boldsymbol{B}$, which obeys the relation: $\boldsymbol{B} \perp \boldsymbol{\theta}$.

A dislocation boundary is called a *tilt boundary* if it consists only of edge dislocations and a *twist boundary* if it consists only of screw dislocations. The normal vector of the dislocation boundary is termed $\boldsymbol{N}$. For tilt boundaries $\boldsymbol{N} \perp \boldsymbol{\theta}$ and for twist boundaries $\boldsymbol{N} || \boldsymbol{\theta}$.

B can be related to the misorientation θ in simple cases. If for example the dislocation boundary consists of an array of parallel equally spaced edge dislocations with Burger's vectors b [103]:

$$D = \frac{b}{2\sin\left(\frac{1}{2}\theta\right)} \Leftrightarrow \theta \approx \frac{b}{D} \tag{1.3.1}$$

where D is the distance between the dislocations. We see that if θ increases and b remains constant, D will decrease. At some point D will

become so small that it does not make sense to talk abound individual dislocations and the dislocation boundary will similtude a grain boundary.

As mentioned above a huge amount of dislocations are generated during deformation. Typical dislocation densities in well annealed samples are $\rho = 10^{10}$–$10^{11}\mathrm{m}^{-2}$ (length per volume) but deformed metals have values as high as [12, 103]:

$$\rho = 10^{16}\mathrm{m}^{-2} \tag{1.3.2}$$

Although it is the dislocation structures in the deformed matrix that drives recrystallization not much is known about how different types of dislocation structures influence the recrystallization process. Typically the deformed structure is assumed to be continuous and modelled by average parameters as done for example in [66].

1.3.1 Energy of Dislocation Structures

The dislocations in the deformed matrix create an excess free energy density P in the deformed matrix, the driving force:

$$P = \frac{F_{\mathrm{matrix}}}{V_{\mathrm{matrix}}} - \frac{F_{\mathrm{grain}}}{V_{\mathrm{grain}}} \tag{1.3.3}$$

where F is the free energy and V is the volume. Since the P has the same dimensions as a pressure, P is often termed the driving pressure. Throughout this thesis the two terms driving pressure and driving force will be used interchangeably. The energy of dislocation boundaries are often determined using the Read-Shockley formula [74]:

$$\gamma = \gamma_0\theta[A - \ln(\theta)] \tag{1.3.4}$$

where γ is the energy per unit area of the dislocation boundary, θ is the misorientation across the boundary, γ_0 is a constant that depends only on the orientation of the boundary and the macroscopic elastic constants, and A is a constant that depends on the orientation of the boundary and the atoms near the dislocation itself.

Eq.1.3.4 is derived on the basis of elasticity but it can readily be used to determine the free energy difference $\Delta F = \Delta U - T\Delta S$ between the matrix and the recrystallizing grain. ΔF is essentially equal to the potential energy difference ΔU (derivable from eq.1.3.4) because the excess entropy in the deformed matrix ΔS due to the presence of dislocations is very small [103]. Although the Read-Shockley formula is only valid for low-angle symmetric tilt dislocation boundaries ($\theta < 10$ deg.) it often fits data for other boundary-types up to much higher misorientations quite well [30, 67, 74].

The RS-formula can be used to model the energy in the deformed matrix. This can for example be done by assuming an average misorientation across dislocation boundaries and an average cell size as done

in [66]. This approach does not, however, take into account the local inhomogeneities such as the two separate sets of boundaries with different misorientations seen in fig.1.5 and the deformed matrix may therefore not be well represented. Many recrystallization experiments have focused on the relation between the degree of deformation/the driving force and rate of recrystallization e.g. [73], but correlations to the actual detailed deformation structure are rarely seen, although the influence of variations in the stored energy on recrystallization kinetics has been considered [27].

1.4 Recrystallization – Basic Concepts

The recrystallization process has, due to its industrial importance, been studied by a vast variety of techniques, both experimental and theoretical: optical- and electron microscopy, x-ray diffraction techniques, analytical-, stochastic models and simulations and much more.

Many things have been learned about recrystallization. Some of the important points, believed to be true, have been formulated in what Humphreys and Hatherley call 'the laws of recrystallization'[40]:

1. A minimum deformation is needed to initiate recrystallization.
2. The temperature at which recrystallization occurs decreases as the time of anneal increases.
3. The temperature at which recrystallization occurs decreases as the strain increases.
4. The recrystallized grain size depends primarily on the amount of deformation, being smaller for large amounts of deformation.
5. For a given amount of deformation the recrystallization temperature will be increased by:
   - A larger starting grain size.
   - A higher deformation temperature.

These phenomenological 'laws' give a practical handle on recrystallization. These should, however, not be confused with natural laws and in order to improve our understanding of recrystallization, the underlying mechanisms that control the 'laws' must be known.

1.4.1 Nucleation of Recrystallization

It is widely recognized that nucleation does not happen randomly throughout the recrystallizing metal [22, 85, 40, 97]. Volumes with high stored energy are required for nucleation to set in, which makes nucleation on the grain boundaries and triple-junctions (intersections between three grains) of the pre-deformed grains easier. The situation where nucleation happens on grain boundaries is similar to the situation where grains nucleate along planes in the sample and the situation where grains nucleate along triple junctions is similar to nucleation along lines. Grain corners (intersections of four grains) are also good nucleation sites, but since these only take up a very small portion of the sample they may not contribute significantly to the nucleation sites.

The effective nucleation rate per unit volume $\dot{N}$ can be defined as:

$$\dot{N}(t) = \frac{1}{V_{\text{unrecrystallized}}} \frac{\mathrm{d}N(t)}{\mathrm{d}t} \tag{1.4.1}$$

where N is the number of nucleated grains. Two simplified situations are often considered:

- **Constant nucleation rate:** In this situation, also termed 'steady state', the amount of new grains per unit volume of untransformed material is constant. Mathematically:

$$\dot{N}(t) = \text{const.} \tag{1.4.2}$$

- **Site-saturation:** If all possible nucleation sites have produced nuclei, the condition is said to be site saturated[22]. Often, the term 'site saturated' is used for a situations where all grain nucleate instantaneously. This corresponds to an infinite nucleation rate at $t = 0$ and a nucleation rate of zero thereafter. Mathematically the nucleation rate is given by the Dirac delta function:

$$\dot{N}(t) = \frac{N_0}{V}\delta(t) \tag{1.4.3}$$

  where N_0 is the total number of nuclei and V is the total volume.

Both situations are seen experimentally depending on the material at hand and experimental conditions. Nucleation is a very complex problem due to the many mechanisms which may give rise to the formation of nuclei and it has also received much attention [39]. My work has primarily focused on the growth aspects of recrystallization.

1.4.2 Kinetics of Recrystallization – Volume Fraction

The overall kinetics of recrystallization are most often measured by the so-called volume fraction V_V defined as:

$$V_V = \frac{V_{\text{recrystallized}}}{V} \tag{1.4.4}$$

When measuring V_V as a function of time a characteristic S-shaped curve is typically seen (see 1.6 for an illustration).

1.4.3 Impingement

The shape of the V_V vs. t curve can be explained by the term impingement. As explained in section 1.2 grain boundaries will continue to migrate as long as there is still untransformed material present in the sample. This does not mean, however, that all grain boundaries move until the end of the transformation. Only those boundaries that are next to untransformed material are free to move. A grain boundary of a recrystallizing grain that has migrated in such a way that it has come into

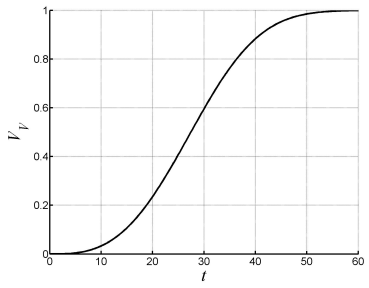

Figure 1.6 S-curve for recrystallization, V_V as a function of time. The characteristic shape is due to grains impinging as explained in section 1.4.3.

contact with a grain boundary from another recrystallizing grain will not move any further during recrystallization and is said to be impinged. In fig.1.4,D the free-to-move boundaries are highlighted in white and the impinged boundaries are highlighted in black.

The S-curve arises because all grain boundaries are free to move in the initial stages of recrystallization and very few boundaries are free to move towards the end. If the boundary migration rate is assumed to be constant for all grains in all directions, and the grains nucleate by site-saturation, the transformed volume will initially have a time dependence proportional to t^3. As impingement sets in the rate of recrystallization $\mathrm{d}V_V/\mathrm{d}t$ goes down and is approaching zero towards the end of the process. The problem of how to deal with impingement is one of the major challenges of modelling recrystallization. How this can be done is explained in section 1.5.

1.4.4 Microstructural Descriptors

The volume fraction V_V is not the only parameter used to describe the kinetics of the overall recrystallization process. Other descriptors are the free to move surface fraction S_V, often just called the surface fraction [99]:

$$S_V = A_{\mathrm{free}}/V \tag{1.4.5}$$

where A_{free} is the area of the free to move boundaries, the impinged surface fraction R_V [58]:

$$R_V = A_{\mathrm{impinged}}/V \tag{1.4.6}$$

where A_{impinged} is the area of the impinged boundaries, the contiguity Crr [94]:

$$Crr = 2R_V/(2R_V + S_V) \tag{1.4.7}$$

The contiguity is the fraction of total boundary area that is impinged. R_V enters into the formula by a factor of two because two free surfaces become one impinged surface. This measure is often used to characterize the clustering of nuclei or grains [94]. As a measure of grain size the descriptor most often used is the mean intercept length. An intercept

length of a grain is the length of the part of a straight line (drawn randomly through a sample and intersecting the grain) that lies inside the grain. The mean intercept length is defined as [77]:

$$< d >= \frac{1}{M} \sum_{m=1}^{M} d_m \tag{1.4.8}$$

where M is the number of grain intercepts by random straight lines drawn through the sample and d_m is the m'th grain intercept length.

1.4.5 Measuring Microstructural Descriptors

A common method to measure microstructural properties/descriptors is stereology [77], which is a way to get information on a larger dimensionality than measured: for example getting 3D information from 2D sections of a experimental sample.

One-dimensional stereology using lines (line-scans) can be used to measure V_V, S_V, R_V and d in the following simple way: create random straight lines through the sample and measure the total length of the lines that pass through recrystallized (transformed) material L_t, the total number of intersections with free boundaries N_f, the total number of intersections with impinged boundaries N_i and the total length of all lines L. Then it can be shown that [77]:

$$V_V = \frac{L_t}{L} \tag{1.4.9}$$

$$S_V = \frac{2N_f}{L} \tag{1.4.10}$$

$$R_V = \frac{2N_i}{L} \tag{1.4.11}$$

$$< d > = \frac{4V_V}{S_V} \tag{1.4.12}$$

1.4.6 Boundary Migration Rates

Since recrystallization proceeds because the grain boundaries surrounding the recrystallizing grains move through the deformed matrix much attention has been directed towards understanding the mechanisms behind boundary migration. The basic formula used for boundary migration is:

$$v = M \cdot P \tag{1.4.13}$$

where v is the boundary velocity, P is the driving pressure and M is the so-called mobility. Although this formula is generally accepted, at least as a first-order approximation, there is no a priori reason why M should not depend on P in some way or why P should be to the power of one, and many discussions about the shape of this formula have been made [33, 73, 95].

It has been established that the mobility depends on the misorientation between the recrystallizing grain and the surrounding matrix. Low-angle boundaries exhibit low mobilities whereas high angle boundaries have high mobilities [32, 37]. Especially boundaries with $\approx$ 40deg. misorientation around crystallographic <111>-axis in face centered cubic (fcc) metals have high mobilities [13, 19, 37]. There has been much debate about so-called 'special' boundaries, i.e. boundaries where the crystal lattices on both sides of the boundary share lattice points. Especially the $\Sigma 7$ boundary in fcc metals, created by a 38.2 deg. rotation around an <111> axis, have exhibited high mobilities in both simulations and experiments [90]. It should be noted, however, that in recrystallization special boundaries are not well-defined due to the misorientation spread present in the deformed microstructure.

The grain boundary mobility as a function of misorientation θ is sometimes modelled by a sigmoidal shaped function such as:

$$M = M_0 \left(1 - \exp\left(-a\left(\frac{\theta}{\theta_0}\right)^b\right)\right) \tag{1.4.14}$$

where a and b are constants and M_0 and θ_0 are phenomenological parameters. Often θ_0 is defined as the values where the boundary goes from being low to being high angle [86].

The impurity-content of a metal has an enormous influence on the boundary migration and even small contents of impurities have been shown to decrease the migration rate significantly [13, 52]. As an example Aust and Rutter showed that changing the tin concentration from 0.0004 to 0.006 wt pct. in dilute lead-tin alloys could make the migration rate decrease by a factor of about 1000 [13]. Second-phase particles in alloys have also been shown to have severe retarding effects on grain boundary migration [12, 38].

The mobility is expected to have an Arrhenius temperature dependence:

$$M = M_\infty \exp\left(\frac{-E_a}{k_b T}\right) \tag{1.4.15}$$

M_∞ is the mobility when extrapolated to infinite temperature, E_a is the activation energy, k_b is the Boltzmann constant and T is the temperature.

1.4.7 Irregular Growth

During recent years it has been established that recrystallization is a very inhomogeneous or irregular process. The irregularities exist on many length scales; from the level of collections of recrystallizing grains down to the details of the individual migrating grain boundaries.

By following the volume of individual recrystallizing grains Lauridsen et al. found that the grains showed very different growth behaviors [46, 51]. Every grain had an individual recrystallization rate, that also varied over time in a non-trivial way. Fig.1.7 shows a selection of the measured

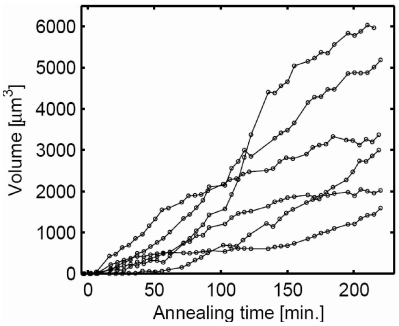

Figure 1.7 The growth of individual grains measured by the grain volume as a function of time. Different growth kinetics are observed for the grains. The figure is from Lauridsen et al. [51].

growth curves exhibiting large variations in the growth kinetics of the individual grains. What causes the grains to exhibit different growth behaviors and what effect this has on the recrystallization kinetics and microstructure is to a large degree unknown.

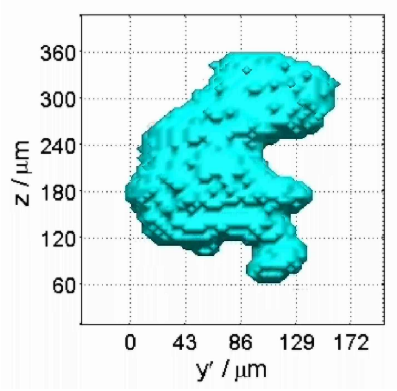

Figure 1.8 Recrystallizing grain exhibiting irregular growth morphology possibly due to interactions with the surrounding deformation structures [80].

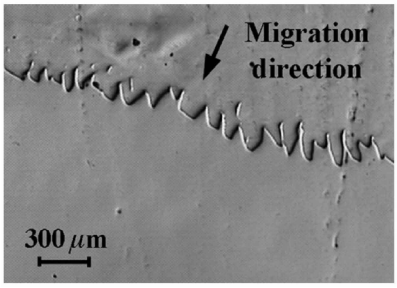

Figure 1.9 Protrusions on a migrating boundary. The figure is from Martorano et al. [57].

The experiments by Lauridsen et al. [51] were performed using the so-called 3-Dimensional X-Ray Diffraction (3DXRD) microscope developed at the Materials Research Department at Risø National Lab., Denmark and situated at the European Synchrotron Radiation Facility (ESRF), France. Another 3DXRD experiment, performed by Schmidt et al. [80], followed the growth morphology of single grains deeply embedded in a

sample during recrystallization [80]. It was clear from the experiment that the boundaries surrounding the recrystallizing grain had a very irregular shape and that the growth was not a smooth process; often one part of the grain would grow very quickly for a while and then wait for the rest of the boundary to catch up. A snapshot of a grain followed in this experiment is shown in fig.1.8. The reasons for these irregular growth patterns are unknown, but it is expected to be due to the inhomogeneous deformation structures surrounding the recrystallizing grains [80].

At a very detailed level protrusions (local bulges) have been observed on grain boundaries in experiments [19, 57]. An example is seen in fig.1.9. The existence of such protrusions is rather surprising if grain boundaries are believed to follow the growth predicted by eq.1.4.13 because a flat segment of a grain boundary according to this equation should move at the same rate. Simple models suggest that these protrusions may be due to a varying driving force in the deformed matrix [56], but the phenomenon is still largely unexplored.

1.5 Simulations of Recrystallization

This section contains a brief review of some of the approaches for modelling growth during recrystallization and explains the motivations behind the choice of geometric and molecular dynamics simulations for this study. There exist a host of different models for recrystallization and it is not possible to cover all, so only the most important models are included. But first a notice on modelling in general.

1.5.1 Modelling

What is meant by the terms *modelling* and *simulation* depend on the scientific field in which they are used. The following is the terminology that will be used in this thesis.

Theories are constructed by hypotheses, and are the building blocks of scientific knowledge. Often theories can not be applied directly to real-life systems due to the complexity of these systems and assumptions need to be made. Theory and assumptions constitute a model. Simulation is a way where the number of assumptions is reduced at the cost of more elaborate computational procedures. One should remember though, that although simulations may in some cases be able to incorporate very complex situations, this may not be an advantage: *There is no inherent virtue in an excessively complex model if there is no way of establishing that all its features are essential for the desired results*[72]. In this thesis the words model and simulation will be used interchangeably because of the conceptual similarity of the two. The way that theoretical predictions are made can be viewed as the following sequence:

- Theory > Assumptions > Model/Simulation > Predictions

Experimental results can be produced by the sequence:

- Experiment > Interpretation > Results

Often interpretations based on assumptions or models are needed to obtain results from an experiment. In X-ray diffraction experiments for example, reconstructions are needed to obtain information on the scattering object under investigation from the scattered x-rays.

Models/simulations may be constructed to imitate experiments. This is often done in materials science, where it is necessary for engineers to have computational models to predict material properties before going into production. In this study models are used quite differently: not to produce predictions of material properties, but to gain insight into the underlying mechanisms of recrystallization:

Predictions from models/simulations can be compared with experimental results to *test assumptions* of a given model/simulation. In this way the main controlling underlying phenomena may be identified. Also some models may have better temporal or spatial resolution than is accessible via experiments, which means that models may be used as a *magnifying glass*, enhancing experimental results (this approach of course only works if the model reproduces the experimental results where model and experiment can be compared). Another way of using models/simulations is to 'play around' with the assumptions. This could be called the *what if* approach, where the modeler can test what would happen if certain assumptions applied. In this way it is possible to identify which assumptions have the greatest impact on the predictions of the model.

1.5.2 JMAK - The Basic Model

The most important model, without comparison, for the growth kinetics of recrystallization is the JMAK model named after its inventors Johnson, Mehl, Avrami and Kolmogorov [14, 15, 16, 43, 47]. The JMAK model is based on a number of simple assumptions and is mathematically exact under these assumptions. Therefore any other recrystallization model has to produce the same results as the JMAK in the case where the JMAK-assumptions are fulfilled. The assumptions are:

1. Nucleation of new recrystallizing grains happens randomly in space at some time dependent nucleation rate. Often the simple cases of constant nucleation rate or site-saturation are assumed.
2. The typical stated JMAK-assumption is that all recrystallizing grains grow at the same rate in all directions. This is equal to stating that the recrystallizing grains grow as spheres as long as no impingement has set in. This assumption can be relaxed to requiring that all grains have the same arbitrary shape similarly oriented in space and grow at the same rate, which may be time-dependent as Kolmogorov showed[47].

These assumptions are clearly oversimplified, but they makes it possible to derive the kinetics for the transformed volume $V_V(t)$. The key mathematical construction for deriving the kinetics is the *extended volume fraction* V_X. This it the sum of the volume fractions that all grains would have if no impingement took place and the grains were allowed

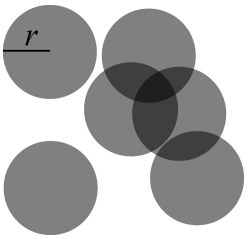

Figure 1.10 Concept of extended volume. The gray circles represent recrystallizing grains in the JMAK model. The extended volume is the sum of the volumes of all six grains calculated individually: $6 \cdot 4\pi r^3/3$. The extended volume therefore over-counts the dark gray areas in the figure, maybe more than once, compared to the real volume.

to grow through each other. In this way V_X may be larger than one. The concept of the extended volume is illustrated in fig.1.10. Imagine now that the grains grow by a small amount dV_V. If no grains overlap (impinge) during this small growth step $dV_V = dV_X$, but if overlapping exists some of the growth of the extended volume will 'disappear' into the already recrystallized volume. The assumption of random nucleation is crucial here: if the nucleation is random one may argue that the growth also takes place at random locations and the amount of growth that goes into already recrystallized material is proportional to the amount of material recrystallized, meaning that*:

$$dV_V = (1 - V_V)dV_X \tag{1.5.1}$$

Solving this leads to:

$$V_V = 1 - \exp(-V_X) \tag{1.5.2}$$

The virtue of this formulation is that it is very easy to calculate the extended volume if the grain shape is known. If for example we have site-saturated nucleation conditions where N grains nucleate in a volume V and grow as spheres with the growth rate g, $V_X = N/V\, 4/3\, \pi r^3 = N/V\, 4/3\, \pi (gt)^3$ and V_V is given by:

$$V_V(t) = 1 - \exp\left(-\frac{N}{V}\frac{4}{3}\pi(gt)^3\right) \tag{1.5.3}$$

Experimental data is often presented in the so-called JMAK-plot, where $\log(-\ln(1 - V_V(t)))$ is plotted versus $\log(t)$. For data following the JMAK model this plot gives a straight line. The JMAK-plot for V_V from fig.1.6 can be seen in fig.1.11.

The JMAK-parameter p defined as the slope of the JMAK-plot:

$$p(t) = \frac{\mathrm{d}\log(-\ln(1 - V_V(t)))}{\mathrm{d}\log(t)} \tag{1.5.4}$$

is often used to characterize the kinetics of recrystallization. For three-dimensional growth with site-saturated nucleation this gives a constant

* This line of argument can be made more rigourously as done by Kolmogorov. By 'inverting' the problem asking for the probability that any grains could reach a certain point in space at a certain time he very beautifully reached eq.1.5.2 as well.

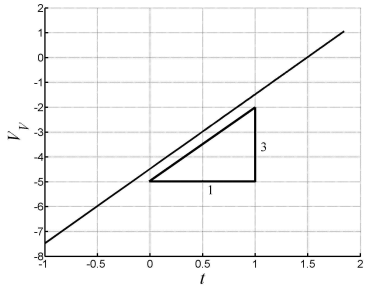

Figure 1.11 JMAK-plot of V_V from fig.1.6. The S-curve is transformed into a straight line with a slope of three.

value of three and for constant nucleation a constant value of four. Generally if the grains grow with a radius given by:

$$r = At^{1-\alpha} \tag{1.5.5}$$

where A and $\alpha \in [0; 1[$ are constants, p would be given by:

$$p = (1 - \alpha)d + c \tag{1.5.6}$$

where d is the dimensionality of the growth, which could be 1,2 or 3 and c takes the value 0 or 1 dependent on whether site saturation ($c = 0$) or constant nucleation ($c = 1$) applies. This can be shown by using eq.1.5.5 to calculate V_X and inserting the result in eq:1.5.2 and eq:1.5.4.

p can of course be extracted from data that do not obey the JMAK model. Variations in p extracted from experimental data can arise from many factors but can often be associated with the break-down of the assumptions of the JMAK model. Examples of this can be seen in articles B and C.

1.5.3 Analytical JMAK approaches / Microstructural Path Modelling

Much work has been done in extending the analytical JMAK framework and in this section some of the results are presented.

S_V and R_V can be calculated analytically under the same assumptions as the JMAK model. S_V can be predicted by the model of DeHoff [26] and Vandermeer et al. and DeHoff [98]:

$$S_V = S_X(1 - V_V) \tag{1.5.7}$$

where S_X is the extended surface fraction defined in a similar way as V_X. By using eq.1.5.2, eq.1.5.7 can be rewritten to:

$$S_V = S_X \exp(-V_X) \tag{1.5.8}$$

A parameter for S_V, similar to the JMAK-parameter defined above, can be defined:

$$p_S = \log\left(\frac{S_V}{1 - V_V}\right) \tag{1.5.9}$$

If eq.1.5.7 is true p_S correspond to $\log(S_X)$, which is easily calculated. For example, site-saturated nucleation yields $p_S = 2$.

R_V can be predicted by a model proposed by Gokhale [31] and Rios et al. (Article A):

$$R_V = R_{VF} \frac{\int_0^{V_X} S_X \exp(-V_X) dV_X}{\int_0^{\infty} S_X \exp(-V_X) dV_X} \tag{1.5.10}$$

where R_{VF} is the value for R_V in the fully-transformed sample. R_{VF} for spherical grains can be predicted theoretically by $R_{VF} = 2.91(N/V_{\text{total}})^{1/3}$ as shown by Meijering [58].

The models eq.1.5.2 and eq.1.5.7–1.5.10 can be considered as extensions to the JMAK model that are able to predict other parameters such as S_V and R_V under the same conditions as the JMAK model can predict V_V, i.e. the models apply to conditions of random nucleation and equal shape-preserved growth. As mentioned above, these assumptions are very simplified and may be very wrong in many cases. Furthermore every deviation from the assumptions may have the potential of making the model break down. Since the JMAK model and the JMAK parameter is used extensively as a fitting tool in recrystallization, understanding what produces deviations from the model are essential.

One of the most successful analytical approaches to extend the JMAK framework is the microstructural path modelling (MPM) approach [98]. In this the microstructural transformation that takes place during recrystallization is considered as a path in the phase space spanned by microstructural descriptors, such as V_V, S_V, R_V and Crr. Using this approach Vandermeer and Masumura managed to describe transformations where nucleation did not happen randomly in space but along lines or planes in the sample [97], a problem also considered in the article by Cahn [22]. Clustering along lines or on planes can be perceived as a 'loss of dimensionality'. When for example grains cluster along lines, they will impinge very quickly with neighboring grains on the line. After impingement of all grains on the line, the grains can only grow outward from the line, thus one dimension of growth has been blocked. Likewise, nucleation along planes will cause grains on the plane to impinge quickly, blocking two dimensions of the growth.

Recently Rios et al. introduced the impingement function as a way to deal with deviations from the JMAK model, exemplified by clustering of nuclei [75]. This methodology is still very new but shows great promise in detecting clustering from kinetic data.

1.5.4 Computer JMAK Methods / Geometric Simulation

When situations become to complicated to analyze analytically computer simulations are able to take over. Geometric simulations, where certain nucleation and growth behaviors are assumed, constitute a very flexible way of extending the analytic JMAK modelling scheme to more general situations that can then be solved numerically. Different methods exist, but basically grains with certain predefined shapes are set to nucleate and grow according to certain rules in a discretized simulation volume. All of

the computer JMAK methods are deterministic since everything about the nucleation and growth is known before the simulation is started.

One of the first studies using computer JMAK methods was performed by Mahin et al., who compared simulations using site-saturated and constant nucleation [54]. Other geometric simulations have studied the effect of changed nucleation rates or decreasing growth rates [78]. Non-random distributions of nuclei in clusters, along lines and on planes, have been simulated by Juul Jensen [45].

As shown in section 1.4.7 recrystallizing grains may exhibit distributions of growth rates. Simulations applying a distribution of decreasing growth rates have been performed by Marthinsen et al. [55]. It was found that the distribution changed the JMAK parameter p, but could otherwise be fitted using the JMAK model [55]. However, only one type of distribution was used. Juul Jensen performed simulations using two distinct decreasing growth rates and found that the microstructure changed dramatically but did not find any strong deviations from the JMAK model in the kinetics either [45]. Due to the limitations of the distributions simulated uncertainties still remain whether or not growth rate distributions can affect the kinetics.

The effects of anisotropic (non-spherical) growing grains are an issue which may be of importance in recrystallization because grains do not grow homogeneously as seen in section 1.4.7. Although the JMAK model covers situations where anisotropic growing grains have equal growth directions, it is not clear how the kinetics of transformations involving anisotropic growing grains with random growth directions looks like. Random anisotropic growth is of interest in related fields because many processes involve grains that do not grow spherically, such as martensitic transformations [102] or γ-α transformations [53] and have been studied primarily in two dimensions [20, 48, 69]. Also three-dimensional simulations have been carried out [49, 83], but in these, growing grains were either completely two-dimensional (flat) [49] or not allowed to grow around each other [83], which grains are observed to do experimentally during recrystallization. Therefore it is not clear what the effect on the kinetics and microstructure randomly oriented anisotropic growing grains will have.

Geometric computer JMAK models constitute the perfect *what if* type model for recrystallization. With a minimum of assumptions about the underlying process a variety situations can be simulated.

1.5.5 More Detailed Simulations

The analytical and geometric JMAK type models and simulations all make assumptions about the nucleation and growth of the recrystallizing grains. In reality it is the deformed structures that are driving the recrystallization, so the explanations for the nucleation and growth behavior is to be found in the interactions between the grains and the deformed matrix. One could say that the JMAK-type models simply assume that the deformation structure is homogeneous, something that we know is not correct (section 1.3).

Many simulations that treat the deformation structure on a more detailed level have been proposed. The most dominant of these, *Phase Field Simulations*, *Monte Carlo Simulations* and *Cellular Automata Simulations*, are described in the following.

1.5.6 Phase Field Simulations

A Phase Field (PF) simulation is as the name indicates concerned with a 'phase field' ϕ of certain properties. This could for example be an orientation field or a deformation field. An orientation field would have a certain value within a grain of the given orientation and be zero outside whereas a deformation field would have some value within the deformed matrix while being zero within the recrystallized grains [17]. On the basis of the phase fields involved a energy function $g(\phi)$ is defined. g can be defined in such an way that deformed matrix as well as boundaries are associated with certain excess energies. The fundamental equation in the PF simulations are then:

$$\frac{\partial \phi}{\partial t} = M \frac{\partial g(\phi)}{\partial \phi} \tag{1.5.11}$$

where M is the mobility for the interface separating the phase and the non-phase for the given phase field. The mobility as well as g can be made to depend on various parameters such as boundary-misorientation. Recently a PF simulation modelling the entire deformed structure as a collection of cells divided by dislocation boundaries has been presented [86]. In this simulation no phase for the deformed matrix was needed, only the properties of the cell boundaries and the boundaries of the recrystallizing grain. Boundary energies and mobilities were then modelled using eq.1.3.4 and eq.1.4.14.

1.5.7 Monte Carlo (Potts) Simulations

The Monte Carlo (MC) technique was developed in the forties[61, 88] and has gotten it's name after the famous 'Monte Carlo' casinos due to the methods extensive use of random numbers. The term 'Monte Carlo simulation' is used for a variety of simulation techniques. Here what could be called 'microstructural Monte Carlo simulations' are described. In MC simulations the microstructure is discretized in a lattice consisting of 'calculation cells'. Each cell can have certain properties, such as orientation and stored energy. The key ingredient of the simulation procedure is the total energy of the system, which typically consists of contributions from the grain and cell boundaries as well as a contribution from the stored energy. An energy function could be of the form [76]:

$$E = \sum_{i=1}^{N} H_i + \frac{1}{2} \sum_{j=1}^{Z} \sum_{i=1}^{N} \gamma_{ij} \tag{1.5.12}$$

where H_i is the stored energy of cell i, γ_{ij} is the boundary energy between cells i and j ($\gamma_{ij} = 0$ if $i = j$, $\gamma_{ij} > 0$ if $i \neq j$), N is the number of cells and Z is the number of nearest neighbor cells.

The simulation proceeds in iterations: in each iteration a state-change of one cell is tested. Such a state-change could be from deformed to recrystallized (with a certain orientation). The change of the system energy ΔE is calculated and the state-change accepted by the probabilities:

$$p = \begin{cases} 1 & \Delta E \leq 0, \\ \exp(-\Delta E/k_b T) & \Delta E > 0. \end{cases} \tag{1.5.13}$$

It is this use of probabilities that is the origin of the name Monte Carlo. More advanced procedures also exist for ensuring for example boundary-misorientation dependent boundary migration rates [24].

One of the advantages of MC simulations is that it is possible to simulate simultaneous recovery, recrystallization and grain growth because stored energy as well as grain boundary and cell boundary energies and mobilities can be treated within the same framework [24, 76]. Recrystallization is sometimes simulated by making cell boundaries provide the driving pressure for migrating grain boundaries and thereby avoiding including a specific term for the stored energy [71].

1.5.8 Cellular Automata Simulations

Cellular Automata (CA) can be viewed as a deterministic version of the MC technique for simulating microstructures. CA uses a discretized lattice of cells with certain properties in the same manner that MC does. One important difference is, however, that while in MC one cell may change its state in an iteration by a certain probability, every cell in a CA simulation may change its state in one iteration according to some predefined rules. In its basic form a deformed cell changes to a recrystallized cell if one of its neighbors is recrystallized and the orientation of the transformed cell is assigned to the value of the cell that recrystallized it [35]. However there exist a huge number of transformation rules that can be applied [70] and complex schemes to simulate situations where the boundary migration depends on, for example, stored energy and boundary orientation can be made [64].

1.5.9 Molecular Dynamics Simulations

All of the models described in sections 1.5.6 to 1.5.8 make assumptions about the interactions between grain boundaries and the deformed matrix. Mobilities may for example be assumed to have a sigmoidal shape, as in eq.1.4.14, and the driving pressure may be assumed to be homogeneous throughout volume. The cell boundaries themselves have an internal structure consisting of dislocations that have agglomerated during deformation and recovery. This structure can not be simulated by the methods described in sections 1.5.6 to 1.5.8 but may have an impact on the migration of the recrystallizing grains other than simply providing a driving pressure.

Atomistic simulation schemes, such as molecular dynamics simulations, have existed for many years and are presently, due to the increased computational power available, able to simulate systems with many millions of atoms [21, 79] during short times or smaller systems for very long times[68]. Using atomistic simulations, dislocation and grain boundaries can be investigated on a detailed level, which may provide an insight into the interactions between dislocation boundaries and grain boundaries that goes on during recrystallization.

Atomistic simulation techniques probe the behavior of individual atoms within a simulated specimen, and have found widespread use within many scientific areas [11, 72] in the study of metals and alloys [79, 87], supercooled liquids [82], phase transformations [29], polymers [50] and much much more.

Two main types of atomistic simulation techniques dominate: atomistic Monte Carlo and molecular dynamics (MD). Atomistic MC works in iterations in the same way as the microstructural MC described in section 1.5.7 but instead of making a state-change of microstructural cells in an iteration atomistic MC displaces an atom. The energy change from this displacement is calculated like the the energy change of the microstructural state-change was calculated in the microstructural MC and the probability of accepting the displacement is given by eq.1.5.13 as well. Atomistic methods were originally used for generating trajectories in phase space with efficient sampling from certain statistical ensembles, but in our case it will be used to minimize out-of-equilibrium atomic configurations. When out-of-equilibrium structures that consist of many atoms, such as grain boundaries or dislocations, are simulated, atomistic MC techniques are typically not very efficient and MD is by far the dominant atomistic simulation technique for this.

The idea behind MD is very simple: set up the atoms and solve the equation of motion for all of them collectively, using Newton's equations of motion iteratively [11]. In practice this becomes more complicated. It is for example important that the interatomic potential, which defines the forces between the atoms, represents what is simulated (metals, polymers etc.) and much effort has been devoted to developing realistic interatomic potentials for describing, for example, metallic systems[18, 41, 100]. The choice of potential is very important for the properties of the system simulated such as bulk- and shear-moduli, melting point, vacancy creation energy etc. Different ways of performing the actual simulations exist: the boundary conditions, the way iterations for solving the equations of motion are performed, temperature- and pressure-controls etc. may be varied and also many tricks for speeding up computational time exist [11, 72]. Computer-programs for performing MD simulations are available and can be used as simulation toolboxes for researchers.

MD makes assumptions on the atomic level as to how the atoms interact — the collective behavior of the atoms are not controlled and structures such as grain boundaries and dislocations do not exist in the simulations as entities but are built by atomic configurations. There-

fore, atomistic simulations often take the form of *computer experiments* because the behavior of the collective structures is to a large extend unknown. The complexity of typical MD simulations also means that, although the governing equations are deterministic, even small differences in the initial conditions of a simulation may lead to large deviations as the simulation progresses.

Atomistic simulation techniques can handle time scales some order of magnitude larger than the typical vibrational times of atoms in solids. Recrystallization is a very slow phenomenon compared to this and often recrystallization is observed over minutes or hours during experiments. The size of a nucleated grain is typically more than 1μ in diameter and contains more than 10^{10} atoms, not including the atoms in the surroundings. Atomistic simulations can handle up to $4 \cdot 10^8$ atoms in extreme cases [21] at this point in time, but only during short-time simulations. Also, no experimental data on recrystallization, with a sufficient quality and resolution to be compared directly to MD simulations, are available. These limitations may be a good reason why recrystallization has not been studied using atomistic techniques to any significant extent before, although a proof of concept simulation in two dimensions has been performed by Upmanyu and co-workers [92]. The idea behind the simulations in [92], which is also adopted in this project, is to study only a part of a migrating grain boundary to reduce the simulation size.

Grain boundary migration of other processes has been investigated using MD, but prior simulations have been performed using different driving pressures, and therefore represent processes other than recrystallization. Examples of such are simulations of curvature-driven boundary migration[90], triple-junction migration[91], stress-driven boundary migration[81, 105] or boundary migration driven by synthetic pressures obtained by altering the interatomic potentials[42]. Zero-driving pressure simulations, where the mobility is extracted from the random walk of the grain boundary, have also been performed [87]. Curvature driven and triple junction simulations are related to grain growth, where the driving pressure is the reduction of grain boundary energy. Stress-driven and synthetically driven boundary migration simulations make use of volumetric driving pressures, where the excess energy driving the boundaries is distributed homogeneously over volumes of the sample. MD simulations of dislocations interacting with grain boundaries[63] or voids[62] have been performed, but these have been carried out under loading of the simulation-cell.

1.6 Project Description

As stated initially, two types of recrystallization simulations have been carried out in this study: geometric and and molecular dynamics simulations. The aim of the study is to try to understand recrystallization better, in particular to try to understand some of the irregularities observed, see section 1.4.7.

Due to the extensive use of the JMAK model to interpret experimental data, it is of great interest to know the limitations of the model and how well it performs in different situations. The geometric simulations will be used to test how the kinetics and microstructure change if certain assumptions underlying the JMAK model do not apply. Due to the experimental observation that every recrystallizing grain grow differently from the rest, this study will investigate the changes due to two 'anisotropies' in the growth behavior: 1) *collections of grains having distributions of growth rates* and 2) *randomly oriented non-spherically growing grains*. The effects that these changes have on the kinetics and microstructure have not been investigated to any significant extend (see section 1.5.4) and the aim of this study is to improve the understanding of the effects that growth anisotropies have. The geometric simulations are performed with a method that has been developed during this project, described in chapter 2. The results obtained from these simulations are presented and discussed in chapter 3.

The origin of growth irregularities during recrystallization, such as grain boundary protrusions[57] or irregular growth morphologies[80] is not known, although they are expected to originate from the interplay between recrystallizing grain boundaries and the structures in the deformed matrix (see section 1.4.7). MD simulations have the necessary temporal and spacial resolution to resolve the interactions between grain boundaries of recrystallizing grains and the dislocations within the deformed matrix, but MD simulations of recrystallization have never been carried out before. A new MD simulation procedure has been developed as part of this study in order to use MD to study boundary migration during recrystallization. The simulations have been performed using two existing computer-programs – one developed at the Center for Simulation and Theory of Atomic-Scale Material Phenomena (STAMP) at Colorado School of Mines, the other developed at the Center for Atom-Scale Materials Design (CAMd) at The Technical University of Denmark. In chapter 4 the simulation procedure and the computational details are explained. Many simulations have been carried out in this study investigating different dislocation- and boundary structures, but focus has been on investigating how different dislocation structures influence the migrating grain boundaries. Simulations using different interatomic potentials have been used to test the generality of the simulation procedure. The potentials applied represent basic crystalline systems (Lennard-Jones potential), an Aluminium system (Embedded Atom Method) and a Copper system (Effective Medium Theory). The advantages and disadvantages of the potentials used are described in chapter 4. The results obtained by the MD simulations are presented and discussed in chapter 5.

2 Algorithm for Geometric Simulations of Recrystallization

In this chapter the geometric algorithm developed in the present study is described. The description is of course presented in terms of recrystallization, but the algorithm is useable for any kind of inhomogeneous transformation-like process, where a nucleation and growth mechanism governs the change of material from one state to another. In the simulations, recrystallizing grains nucleate and grow in the deformed matrix. The grain boundaries migrate through the deformed matrix transforming it from a deformed state to a recrystallized state. The migration of a grain boundary will continue until the boundary impinges upon a grain boundary from another recrystallizing grain.

The approach behind the simulation technique developed is very versatile and grains with a host of nucleation- and growth-properties can in principle be simulated. The properties that have been implemented in the algorithm so far are:

- Nucleation placement:
  - Randomly in space.
  - Randomly on lines placed randomly in space.
  - Randomly on planes placed randomly in space.
- Nucleation rate
  - All grains nucleate at $t = 0$.
  - Grains nucleate at a constant nucleation rate.
- Growth rate:
  - General decreasing rate: $v = gt^h, h =]-1; 0]$ (constant rate is included in this for $h = 0$).

    This correspond to $v = A(1-\alpha)t^{-\alpha}$ when using the notation from eq.1.5.5 page 17.
  - Distribution of g and h.
- Grain shape:
  - General ellipsoidal shape (including spheres as a special case).
- Orientation:
  - Randomly oriented.
  - Aligned along the same direction.

After a simulation has been carried out the simulation-cell can be investigated by standard methods; either volume-, plane- or line-analysis can be carried out. Volume analysis can be used to create three-dimensional figures of individual grains. Plane-analysis can be used to make imitations of polishes, which can be used to get a visual impression of the microstructure of the simulation-cell, either during or after total recrystallization. Finally, line scans combined with stereology can be used to obtain microstructural descriptors such as V_V, S_V, R_V and Crr (see section 1.4.5 page 11).

2.1 Fundamental Assumptions and Simulation Strategy

The simulated transformation is purely geometric, meaning that no *physical* mechanism controls the growth. The algorithm is a numerical solution of the following analytical problem: *Given grains that nucleate in certain locations at certain times with certain growth parameters, how will the microstructure evolve over time?* The algorithm solves the problem in a discretized volume; the discretization used is a division of the volume into cubic voxels. The method is entirely deterministic and parameters for all grains should be known beforehand. The parameters can be grouped into 1) nucleation parameters and 2) growth parameters. The nucleation parameters include nucleation location and nucleation time. Growth parameters include growth rate in every direction at all times. The parameters define how the grain would grow if no impingement were present. Since every grain is given individual properties, distributions of various properties can easily be simulated.

The overall strategy of the approach adopted here is to make an initial solution where no impingement between growing grains occurs and subsequently refine the initial solution to handle problematic voxels; what makes voxels problematic is explained later. During a simulation run the algorithm stores information about what grain the recrystallized voxels belongs to (the grain number) as well as the time the voxels are recrystallized (the recrystallization time).

In the initial solution the growth of every grain occurs as if no other grains were present, the voxels are simply recrystallized by the nucleus that can reach (transform) it quickest by direct growth. The initial solution have the obvious drawback that grains can not screen each others growth and may therefore grow trough each other if they have different growth rates. The initial solution is identical to the method developed by Dorte Juul Jensen [44, 45].

A refinement of the method has been added during this project to be able to handle collections of grains with complex growth properties, which was a problem in the original method. The refinement proceeds in a time sequence, where in each time step a number of problematic voxels are analyzed in a way similar to the initial solution, but in the refinement all already recrystallized voxels can act as new growth centers. The program treats the recrystallized voxels on the same footing as nuclei

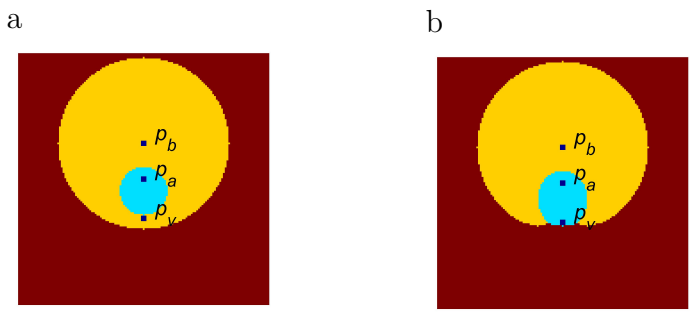

Figure 2.1 Microstructural effects of the refinement procedure on problematic voxels. (a) Initial solution before refinement and (b) final solution after refinement, both at time $t = 1.2$. Light blue indicates grain a, yellow grain b and red untransformed material. The growth rates of the grains are $g_a = 10$ and $g_b = 20$. $P_a = (0, 0, 0)$, $P_b = (0, 10, 0)$ and $P_v = (0, -11, 0)$ indicate the grains centers and the position of the problematic voxel discussed in the text.

but with nucleation times equal to their recrystallization times. For each problematic voxel, the neighborhood is investigated for nuclei or already recrystallized voxels that may reach the problematic voxel.

The refinement procedure is very time consuming compared to the initial solution but it is necessary in order to handle certain growth scenarios. Consider the following example also illustrated in fig.2.1 . Two spherical grains a and b nucleate at $t = 0$ in locations $p_a = (0, 0, 0)$ and $p_b = (0, 10, 0)$ and grow with rates $g_a = 10$ and $g_b = 20$. Now consider a voxel in position $p_v = (0, -11, 0)$. The initial solution would conclude that the voxel will be recrystallized by grain b since the recrystallization time by direct growth from b is $t_b = 21/20 = 1.05$ (fig.2.1(a)) and the recrystallization time by direct growth from grain a is $t_a = 11/10 = 1.1$. But this is not correct since grain a is located in grain b's direct growth path and grain b would have to grow around grain a to reach the voxel. This would make the actual path of growth for grain b longer and it would have no chance of reaching the voxel before grain a. Therefore the correct solution will be that the voxel is recrystallized first by grain a and not b. The voxel just discussed is an example of a problematic voxel.

2.2 Algorithm

This section describes the geometric algorithm for recrystallization developed. First, the algorithm is explained step by step. Following this, in the sections 2.2.1–2.2.3, the calculations carried out within the algorithm are explained in detail in order to give a full presentation of the method. The algorithm is structured like this:

1. Generate the initial configuration. Assign nucleation- and growth properties to all grains.
2. Make an initial solution by direct growth.
3. Identify problematic voxels
4. Make a refined solution.
    a) Assign problematic voxels to time bins according to the initial solution
    b) Go through the time bins.
        i. Select a problematic voxel in the actual time bin.
        ii. Investigate if the problematic voxel can be reached in the given time bin by a direct line of growth by an already recrystallized voxel in the neighborhood:
            - Yes: Assign the recrystallization time and grain number to the problematic voxel.
            - No: Shift the problematic voxel to the time bin of the earliest possible recrystallization time according to the current situation.
5. Analyze the final microstructure using line scans.

1. The first step in the algorithm is the generation of the growth parameters for all grains. The parameters used are explained in section 2.2.1.

2. In the second step the initial solution is made. The recrystallization times produced in this represent the earliest possible recrystallization times for the voxels since the solution is made by direct growth of all nuclei in the simulation-cell. As explained in section 2.1 this is identical to the method of Dorte Juul Jensen.

3. The third step is the identification of problematic voxels, which can be found from the initial solution alone. This is because the initial solution consists of the earliest possible recrystallization times for all voxels. If a voxel is recrystallized in the initial solution by some grain and there exists a direct path in the initial solution from the nucleus of the grain to the voxel, where all voxels along the path also belong to the grain, then the voxel must also belong to that grain. This is because the entire path from the nucleus to the voxel consists of voxels that are recrystallized in the earliest possible times by the same grain: No other grain can interrupt this. The problematic voxels are those that have been recrystallized in the initial solution by a grain where it is not possible to make a direct uninterrupted path from the nucleus to the voxel.

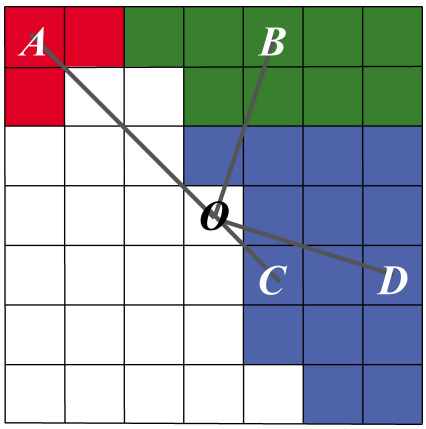

Figure 2.2 7×7 voxel Neighborhood around voxel O under consideration. The colors indicate the state of the voxels: white is unrecrystallized, red, green and blue are recrystallized by three different grains. In the refinement method, all voxels in the neighborhood are investigated, but this figure, only the examples A, B, C and D are analyzed. Voxel A can not reach O because the path is broken by unrecrystallized voxels. Voxel B cannot reach O because the path is broken by recrystallized voxels from another grain. Voxels C and D can both reach O. The recrystallization time of C and D combined with their distance to O defies which will recrystallize O. Although D's distance from O is greater than C's, D may have recrystallized much earlier than C and may therefore be able to recrystallize O before C.

4. After the problematic voxels have been identified they are recalculated in the refinement procedure. First a series of time bins are generated. Enough time bins are generated to ensure that no grain can grow a distance of more than one voxel in any time step. The problematic voxels are assigned to these according to the time they would have been recrystallized according to the initial solution. In this way the initial solution is used as the starting point for the refinement. The voxels may not end up being recrystallized in the time bins that they are assigned but shifted to others if necessary as explained below.

For each time bin, an investigation of every problematic voxel in that bin is carried out. The voxel under investigation is termed O from this point on. The investigation of O is essentially carried out in the same way as the initial solution, but instead of calculating which nuclei from the entire simulation-cell that can reach O quickest by direct growth, it is calculated which nuclei or already recrystallized voxels in the neighborhood of O that can reach O quickest. Furthermore it is required that the already recrystallized voxels or nuclei that reach O can do so by a path where all voxels along the path belong to the same grain. The principle is illustrated figure 2.2.

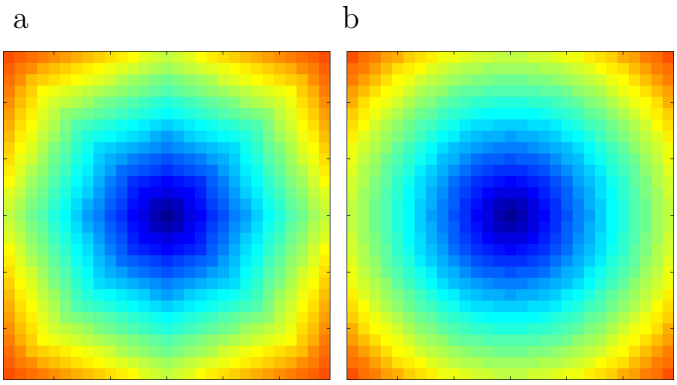

Figure 2.3 Voxelation-errors. Two images showing the growth of a spherical grain with a neighborhood consisting of (a) the nearest neighbors (26 neighbors) and (b) an infinite neighborhood. The colors of the voxels indicate the time at which the pixels were recrystallized. It is seen that the spherical growth is destroyed when only the nearest neighbors are used. Normally a spherically growing grain would be treated correctly by the initial solution. This figure is generated by performing a special simulation where every voxel is calculated using the refinement method for the sake of exemplification.

The refinement method treats O according to the properties of the neighborhood in the following way: If there are no recrystallized voxels in the neighborhood that can reach O by a direct path, O is shifted to the subsequent time-bin. If there exist already recrystallized voxels in the neighborhood that can reach O by an unbroken path, but none of these are able to reach it within the present time bin, O is shifted to the time-bin, where it would be recrystallized quickest by the already recrystallized voxels that can reach it. If there exist already recrystallized voxels in the neighborhood that can reach O by an unbroken path in the present time bin it is investigated which of these that can reach O quickest. O is assigned to the same grain as the voxel that reached it quickest and the recrystallization time is given as the time it was reached.

It is not necessarily the closest recrystallized voxel that reaches O first. This is because the closest voxel may be recrystallized at a later time than some of the recrystallized voxels further away. When recrystallized voxels far away, and not only the nearest neighbors, are taken into consideration in the investigation voxelation-errors are reduced significantly. This can be seen from figure 2.3. Note: Normally, a neighborhood up to the third nearest neighbor in every direction is used giving ($7^3-1 = 342$ neighbors). Each of these neighbors needs to be checked in the investigation, which is very computationally demanding. Significant speed-ups can be obtained by reducing the size of the neighborhood.

5. Finally after all voxels in all time-bins has been investigated the results are analyzed using a line-scan technique. Many lines can be an-

alyzed in a short amount of time, making line scans very efficient. V_V, S_V, R_V, Crr and $< d >$ can all easily be calculated from line scans by the formulae given in section 1.4.5 page 11. The lines used for the line scans are along the x-, y-, and z-directions and therefore not random as normally required by stereology. This should not produce any errors since the locations and orientations of the grains simulated in this study generally are random. Time resolution is obtained by combining information on the recrystallization times and the grain numbers.

The following sections describe in detail how the calculations for determining the recrystallization times are carried out.

2.2.1 Grain Parameters

The A recrystallizing grain is defined as an ellipsoid of the basic form:

$$\left(\frac{x-x_0}{a(t)}\right)^2+\left(\frac{y-y_0}{b(t)}\right)^2+\left(\frac{z-z_0}{c(t)}\right)^2=1 \tag{2.2.1}$$

where x_0, y_0 and z_0 is the position of the nucleus and a, b and c are the axes, which (as a starting point) are along the x-, y- and z-directions. If the grain is rotated so that the axes are no longer along the x-, y- and z-directions eq.2.2.1 becomes more complex, but as will be shown in section 2.2.2 there is an easy way around this. The *natural* coordinate system of the ellipsoid is defined as the one in which eq.2.2.1 holds. If $a=b=c=1$, eq.2.2.1 would describe a sphere with a radius of 1. In the algorithm the shape of the ellipsoid is preserved during growth, meaning that a, b and c change over time but the aspect ratios:

$$\frac{a}{b},\quad \frac{b}{c},\quad \frac{c}{a} \tag{2.2.2}$$

do not. If the growth rate is constant, a, b, and c are given by:

$$\frac{a}{a_0}=vt,\quad \frac{b}{b_0}=vt,\quad \frac{c}{c_0}=vt \tag{2.2.3}$$

where a_0, b_0 and c_0 are size parameters and v is the normalized growth rate, which is the same for all directions due to the preserved shape of the ellipsoid. If the growth rate varies with time the general normalized growth rate can be defined as:

$$v(t)=\frac{1}{a_0}\frac{\mathrm{d}a(t)}{\mathrm{d}t},\quad v(t)=\frac{1}{b_0}\frac{\mathrm{d}b(t)}{\mathrm{d}t},\quad v(t)=\frac{1}{c_0}\frac{\mathrm{d}c(t)}{\mathrm{d}t} \tag{2.2.4}$$

Again $v(t)$ is the same in all direction due to the preservation of shape. In the algorithm, the velocity function $v(t)$ is defined as:

$$v(t)=g(t-t_0)^h \tag{2.2.5}$$

where $-1<h\leq 0$ is used to define a declining growth rate if $h<0$. Comparing eq.2.2.5 to eq.1.5.5 page 17:

$$g = A(1-\alpha) \tag{2.2.6}$$

$$h = -\alpha \tag{2.2.7}$$

2.2.2 Transformation to the natural coordinate system

Because the ellipsoids can be rotated away from their natural coordinate system, coordinate transformations are needed to simplify the time calculations.

Assume that the investigated voxel is placed at position (x_v, y_v, z_v). Nearby grain i is at position (x_i, y_i, z_i), has dimensions a_i, b_i and c_i. The orientation of the grain is obtained by rotating the grain θ_i around the x-axis, ρ_i around the y-axis, and σ_i around the z-axis from a starting position where the x-, y-, and z-axes are the natural coordinate system for the ellipsoid. The growth rate is a constant g_i and the nucleation time is t_{0_i}.

In order to calculate the time it takes grain i to reach the voxel, the coordinates of the voxel and the grain are initially shifted so that the voxel is at the origin:

$$x'_v = 0, \quad y'_v = 0, \quad z'_v = 0 \tag{2.2.8}$$

and the grain is in the position:

$$x'_i = x_i - x_v, \quad y'_i = y_i - y_v, \quad z'_i = z_i - z_v \tag{2.2.9}$$

Thereafter the grain is rotated around the origin so that the x-, y-, and z-axes becomes the natural coordinate system of the ellipsoid. The new coordinates for x'_i, y'_i, z'_i becomes:

$$\begin{pmatrix} x''_i \\ y''_i \\ z''_i \end{pmatrix} = \boldsymbol{R} \begin{pmatrix} x'_i \\ y'_i \\ z'_i \end{pmatrix} \tag{2.2.10}$$

where $\boldsymbol{R}$ is the rotation matrix defined as:

$$\boldsymbol{R} = \boldsymbol{R}_x \boldsymbol{R}_y \boldsymbol{R}_z \tag{2.2.11}$$

$$\boldsymbol{R}_x = \begin{pmatrix} 1 & 0 & 0 \\ 0 & \cos\theta_i & -\sin\theta_i \\ 0 & \sin\theta_i & \cos\theta_i \end{pmatrix} \tag{2.2.12}$$

$$\boldsymbol{R}_y = \begin{pmatrix} \cos\rho_i & 0 & \sin\rho_i \\ 0 & 1 & 0 \\ -\sin\rho_i & 0 & \cos\rho_i \end{pmatrix} \tag{2.2.13}$$

$$\boldsymbol{R}_z = \begin{pmatrix} \cos\sigma_i & -\sin\sigma_i & 0 \\ \sin\sigma_i & \cos\sigma_i & 0 \\ 0 & 0 & 1 \end{pmatrix} \tag{2.2.14}$$

$$\tag{2.2.15}$$

2.2.3 Time calculations

To find the time taken for the grain to reach the voxel, eq.2.2.1 for t using x''_i, y''_i, z''_i is solved:

$$\left(\frac{x''_i}{a}\right)^2 + \left(\frac{y''_i}{b}\right)^2 + \left(\frac{z''_i}{c}\right)^2 = 1 \tag{2.2.16}$$

First the generalized radius k is defined:

$$k = \sqrt{\left(\left(\frac{x_i''}{a_0}\right)^2 + \left(\frac{y_i''}{b_0}\right)^2 + \left(\frac{z_i''}{c_0}\right)^2\right)} \tag{2.2.17}$$

If we set $a = ka_0$, $b = kb_0$, and $b = kb_0$ eq.2.2.16 is solved:

$$\left(\frac{x_i''}{ka_0}\right)^2 + \left(\frac{y_i''}{kb_0}\right)^2 + \left(\frac{z_i''}{kc_0}\right)^2 = \frac{\left(\frac{x_i''}{a_0}\right)^2 + \left(\frac{y_i''}{b_0}\right)^2 + \left(\frac{z_i''}{c_0}\right)^2}{k^2} = \frac{k^2}{k^2} = 1 \tag{2.2.18}$$

Finally, the time t^* where the ellipsoid has grown to the size where $a(t^*) = ka_0$, $b(t^*) = kb_0$ and $c(t^*) = kc_0$ has to be calculated. This can be done by integrating eq.2.2.4 (due to shape preservation equation for either a, b or c can be used):

$$v(t) = \frac{1}{a_0}\frac{\mathrm{d}a}{\mathrm{d}t} \Rightarrow a(t^*) = a_0 \int_{t_{0_i}}^{t^*} v(t)dt. \tag{2.2.19}$$

By inserting eq.2.2.5 and using $a(t^*) = ka_0$:

$$k = \int_{t_{0_i}}^{t^*} g_i(t - t_{0_i})^{h_i}\, dt = \int_0^{t^*-t_{0_i}} g_i t'^{h_i}\, dt' \tag{2.2.20}$$

where $t' = t - t_{0_i}$. Integrating yields:

$$k = \frac{g_i}{h_i + 1}(t^* - t_{0_i})^{h_i+1} \tag{2.2.21}$$

Solving this for t^* leads to:

$$t^* = \left(\frac{k(h_i + 1)}{g_i}\right)^{\frac{1}{h_i+1}} + t_{0_i} \tag{2.2.22}$$

This is the way the program calculates the time taken for the different nuclei to reach every voxel in the initial calculation. The time calculations in the refinement procedure is somewhat different. This is because already recrystallized voxels act as new growth centers and are treated as nuclei, but with nucleation times other than the original nucleus had. Eq.2.2.20 must be modified to:

$$k = \int_{t_v}^{t^*} g_i(t - t_{0_i})^{h_i}\, dt \tag{2.2.23}$$

where t_v is the time the recrystallized voxel acting as a nucleus was recrystallized. When integrated this gives:

$$k = \frac{g_i}{h_i + 1}\left((t^* - t_{0_i})^{h_i+1} - (t_v - t_{0_i})^{h_i+1}\right) \tag{2.2.24}$$

which when solved for t^* gives:

$$t^* = \left(\frac{k(h_i + 1)}{g_i} + (t_v - t_{0_i})^{h_i+1}\right)^{\frac{1}{h_i+1}} + t_{0_i} \tag{2.2.25}$$

2.3 General Discussions

The geometric simulation methodology, which was originally developed by Juul Jensen [44, 45], has been extended during this PhD-project. This was necessary because the original geometric simulations were not capable of correctly simulating situations where different grains have different growth rates as a function of time or as a function of growth direction. Such situations are of interest because recent experimental results show that grains may have individual growth behavior or grow with different rates in different directions, as discussed in section 1.4.7 page 12.

The extension of the method was done by using the original method as an initial solution and using a refinement procedure to correctly handle problematic voxels, i.e. voxels that can not be reached by a straight unbroken path from the nuclei (see section 2.2). The refinement basically tracks the grain boundary through the problematic voxels over time in small time intervals. This modification of the geometric simulation algorithm makes it very versatile and capable of simulating a host of complex situations, employing distributions of growth rates, grain-shapes etc., while keeping all the virtues of the original algorithm. In situations where the original algorithm performs correctly the modified algorithm produces the same result in the initial solution using the same amount of computing time.

The refinement, when necessary, comes at the cost of computational speed. The refinement procedure requires a lot of 'book-keeping', which is computationally demanding. For each problematic voxel, the neighborhood has to be investigated for already recrystallized voxels that can act as growth centers (instead of the nuclei) and recrystallize the problematic voxel. The size of the neighborhood has to be chosen carefully. If a small neighborhood is chosen, the algorithm runs quite quickly, but voxelation errors occur; if a large neighborhood is chosen, the algorithm runs slowly, but a high precision in the results is obtained.

3 Results from Geometric Simulations

The geometric simulations performed show what happens to the recrystallization kinetics when nucleation- and growth parameters are changed from normal JMAK-behavior to situations involving growth rate distributions or anisotropic growing grains. The JMAK model is used as the reference point in this study; although the JMAK model is clearly over-simplistic in it's assumptions, it is the most widely used kinetic recrystallization model. In the following, different parameters are changed one at a time to identify the effects of the particular parameter on the recrystallization kinetics. This chapter presents the results obtained by the geometric simulation method, developed during this PhD project, and contains discussions and interpretations of the results as well.

In section 3.1, results from simulations performed under JMAK-conditions are presented and section 3.2 presents the results using clustered nucleation sites along lines or on planes. Analytical solutions exist for these scenarios and the simulations serve as examples of verifications of the method. More tests have been carried out, which are not shown in full detail in this thesis. These are described briefly in section 3.3. Section 3.4 describes the results obtained when distributions of growth parameters are used. These results have also been presented in article B. Finally, section 3.5 describes the results obtained when shape parameters are changed, which have also been presented in article C.

The two main situations considered, distributions of growth rates and anisotropic growth, can be considered as situations where the recrystallizing grains have individual growth parameters: In the former case, naturally, the grains have distributions of the growth rates; in the latter case, the grains have distributions in the preferred growth direction. Since the orientation of the grains are random, this is a uniform distribution of growth directions.

3.1 JMAK

The JMAK model assumes site-saturated or constant nucleation at random locations and aligned growth as described in section 1.5.2 page 15. Under site-saturated conditions the JMAK-parameter p should be three for three-dimensional growth (eq.1.5.4). A test-simulation of 3.375×10^6 grains using JMAK-conditions and site-saturation has been performed

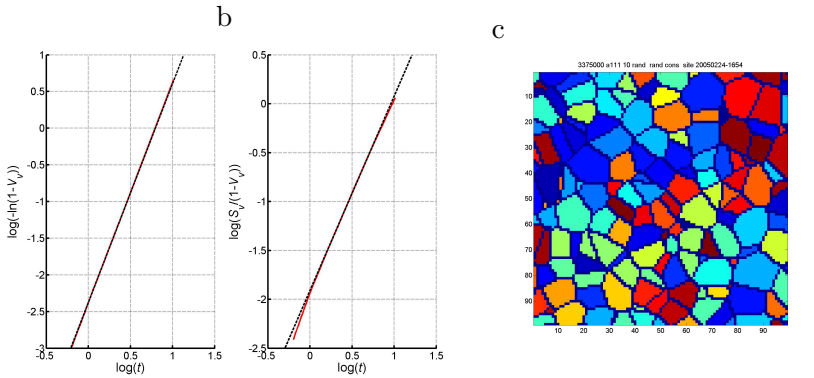

Figure 3.1 JMAK-plots for for (a) V_V and (b) S_V as well as (c) the microstructure from a geometric simulation employing JMAK assumptions with site-saturation. In (a) and (b), red full lines represent simulated data, black dotted lines the expected data from the models eq.1.5.2 and 1.5.8. (c) Microstructure after total transformation. Different colors represent different grains and the grain boundaries are highlighted by blue lines.

in a cubic simulation box of side length 1500 voxels. Fig.3.1(a) shows a JMAK-plot from this of $\log(-\ln(1-V_V))$ vs. $\log(t)$. As expected the data show a straight line with slope three. In fig.3.1(b) $\log(S_V/(1-V_V))$ is plotted vs. $\log(t)$. The data produces a straight line of slope two as expected (see eq.1.5.9). Small deviations are seen for very small values of S_V (start and finish of the transformation) due to numerical uncertainties that arises when a very small surface fraction is determined by line scans.

Besides the kinetic data, the microstructure can be investigated using the geometric simulations. Fig.3.1(c) shows an example of a layer of 100×100 voxels from the same simulation as the one behind fig.3.1(a,b) after total transformation. Equiaxed grains are seen with straight grain boundaries as expected. In summary, both the kinetic and the microstructural data obtained with the geometric simulations are almost identical to the analytical predictions for the classical JMAK.

3.2 Clustering on Lines and Planes

The recrystallization kinetics can be perceived as a loss of growth dimensionality when nuclei are clustered along lines or on planes, as explained in section 1.5.3 page 17. The exact growth kinetics for infinite lines and planes can be predicted analytically [22, 97]. The apparent extended volume-fraction $V'_X = -\ln(1-V_V)$ changes behavior when clustering is present. Under site saturated conditions in three-dimensional growth, $V'_X \propto t^3$ in the beginning of the transformation but changes to $V'_X \propto t^{3-k}$, where $k = 1$ for lines and $k = 2$ for planes, when impingement along the

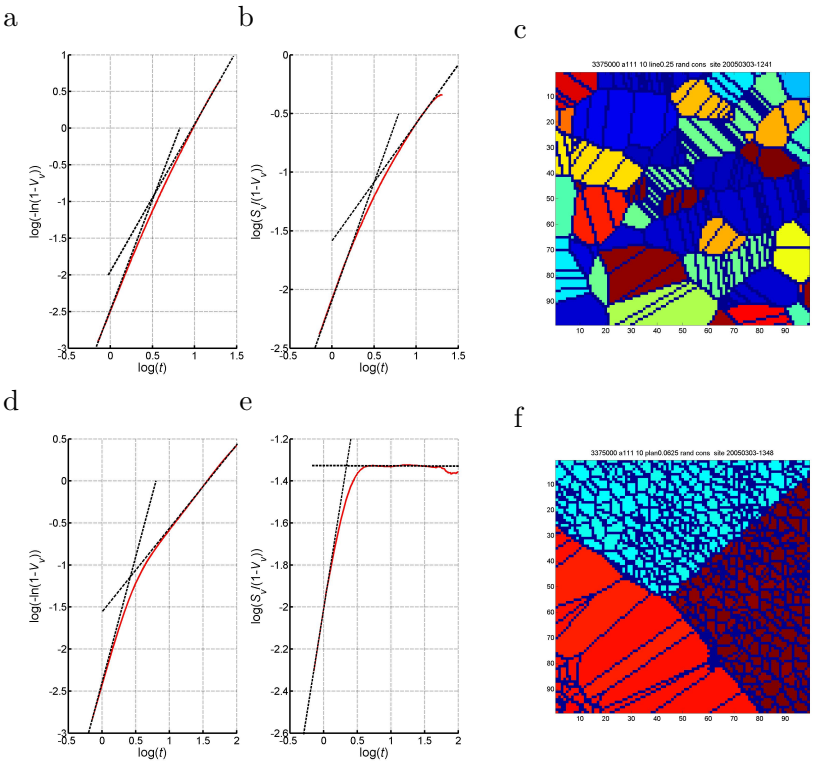

Figure 3.2 JMAK-plots for clustering along lines and planes. The kinetics data for (a) V_V and (b) S_V and (c) the microstructure from a simulation with site saturated nucleation along lines. (d) and (e) show the kinetics data and (f) the microstructure from a simulation with site saturated nucleation on planes. In (a), (b), (d) and (e) red lines are data curves while black dotted lines are theoretical predictions according to analytical models [97]. In (c) and (f), colors indicate different grains and the grain boundaries are highlighted by blue lines. Grains along the same line or on the same plane have similar colors.

lines or planes set in[97]. In the same manner, the apparent surface fraction $S'_X = S_V/(1 - V_V)$ changes: $S'_X \propto t^2$ in the beginning of the transformation but changes to $S'_X \propto t^{2-k}$ when impingement set in.

Simulations where the nuclei have been placed along lines or planes have been carried out. The same number of nuclei and the same simulation size as the JMAK-simulation described in section 3.1 was used. Fig.3.2(a) and (b) show the kinetics data for a site-saturated JMAK simulation, where the nucleation happens along straight lines. The dotted lines have slopes equal to three and two in fig.3.2(a) and two and one in fig.3.2(b), which shows that the JMAK-parameter goes down by one as a consequence of the line-impingement in agreement with the predictions [97]. Fig.3.2(d) and (e) show the equivalent plots for a site-

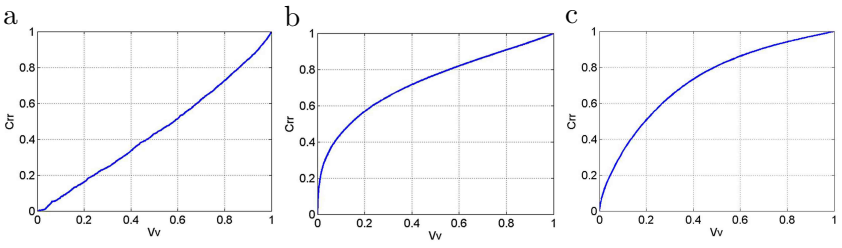

Figure 3.3 Effect of clustering on the contiguity Crr. Crr is plotted vs. V_V for (a) random nucleation, (b) nucleation along lines and (c) nucleation on planes.

saturated JMAK simulation, where the nucleation happens on planes. Here the JMAK-parameter goes down by two due to the impingement, also in agreement with the predictions. In fig.3.2(c) and (f) the corresponding microstructures are shown. The different colors represent different grains. Grains along the same line or on the same plane are colored in almost equal colors to easily distinguish different lines or planes. These microstructures are clearly different from the classical JMAK case. Elongated plate-shaped grains are seen in fig.3.2(c) due to the line-impingement. In fig.3.2(f) grains from three nucleation-planes are seen: The direction from which the grains are observed is nearly perpendicular to two of the planes and along the plane in the third case. The grains have a columnar shape giving a JMAK-like structure when seen from a direction perpendicular to the plane and an elongated microstructure when seen edge-on. The densities of nuclei along the lines or on the planes are very high, which produce even more unrealistic microstructures in fig.3.2(c) and (f) than the classical JMAK in fig.3.1(c). This is done to clearly distinguish the two kinetic regimes seen for lines in fig.3.2(a) and (b) and for planes seen in fig.3.2(d) and (e). In the simulations the size of the lines and planes are finite, in contrast to the models[97], where the lines and planes extend infinitely. The high nuclei-densities ensure, however, that the size of the lines and planes become very large compared to the recrystallized grain size.

As described in section 1.4.4 page 10 the contiguity Crr can be used as a measure of the clustering of the nuclei[94]. In fig.3.3 Crr vs. V_V are plotted for (a) random nucleation, (b) clustering along lines and (c) clustering on planes. Clear differences can be seen between random and clustered nucleation. Crr increases rapidly for clustered nucleation because a large fraction of the grain boundaries will impinge very quickly (the actual shape of Crr vs. V_V depends on the nucleation density on the planes and lines).

3.3 Verification of the Method

The geometric simulations have been tested on other cases, not presented in the above sections. These include: Constant nucleation rates for nuclei distributed randomly, on lines and on planes and decreasing growth rate $r = At^{1/2}$ (equal for all grains). In these cases the simulations also produce the expected results.

As seen in the previous sections, the geometric simulations reproduce the analytical solutions very accurately in all the cases where comparisons are made, which validates the method. Strictly speaking, the tests presented above only covers the initial solution of the method and not the refinement, because the situations tested above can be solved with the initial solution alone. It is much harder to test the refinement because this is only used in complicated growth scenarios (where analytical solutions are not known). However, the situation consisting of only two grains with different growth rates, illustrated in fig.2.1 page 27, can be solved analytically. In this case the refinement produce the expected result. Connectivity tests have also been carried out. In the initial solution, grains grow as if no other grains are present. If the grain shapes are strongly anisotropic, this may result in grains that grow through each other. The tests show that no grain ends up being separated into different parts after the refinement method is applied. In the next sections the geometric simulations will be used for situations where no analytical solutions exist.

3.4 Distributions of Growth Rates

Selected types of growth rate distributions have been simulated using geometric simulations as discussed in section 1.5.4 page 18. The goal of the simulations presented in this section is to give a picture of what happens to the recrystallization kinetics and microstructure when distributions of growth rates are simulated. The results are also presented in article B.

The growth rates of the grains in the simulations are given by $r = At^{1-\alpha}$ (see eq.1.5.5). By varying A and α various growth behaviors can be achieved. Lauridsen et al. [51] showed that growth rates just after nucleation, where no impingement is present, follow a distribution that resembles a log-normal distribution. Juul Jensen et al. [46] analyzed distributions of A of the form:

$$n(A) = C_A/A^m \tag{3.4.1}$$

and 'bell'-shaped distribution-functions of α of the form:

$$n(\alpha) = C_\alpha \alpha^p (1-\alpha)^q, \quad \alpha \in [0;1] \tag{3.4.2}$$

where n is the probability density, m, p and q are constants that determine the shape of the distributions and C_A and C_α are normalization constants ($1 = \int n$). In this study we have chosen distributions according

to eq.3.4.1 and 3.4.2 using different values for the parameters m, p and q, a log-normal distribution of A and uniform distributions of A and α to simulate a range of distributions and in this way identify the generic effects of introducing growth rate distributions on recrystallization kinetics and microstructure.

The simulated distributions are listed in table 3.1. No simulations where collections of grains posses distributions in both A and α have been performed because the results obtained from such would be difficult to interpret. The distribution eq.3.4.2 is bell-shaped approaching zero as $\alpha \to 0$ and $\alpha \to 1$. p and q determines the specific shape of the distribution. The peak will be shifted to the left if $p > q$ and to the right if $p < q$ and the distribution becomes narrower as the values for p and q increase.

All simulations of growth rate distributions have been performed in a cubic simulation volume with periodic boundary conditions and a side length of 200, giving a volume of $8 \cdot 10^6$ voxels. Each simulation contains $N = 1000$ nuclei. The simulations have been performed with spherical grains under site saturated conditions. For each type of distribution, three simulations with different seeds of nuclei positions and growth parameters have been performed to increase data quality.

Microstructural descriptors, such as V_V, S_V, R_V and Crr, can be measured in order to follow the overall kinetics during simulation. Fig.3.4(a) shows a pre-factor-normalized version of the standard JMAK-plot for all simulations. The normalization is performed by dividing the apparent extended volume fraction $-\ln(1-V_V)$ by the extended volume fraction at $t = 1$: $V_X(1) = \frac{4}{3}\pi N < A^3 > /V$, where N is the number of nuclei, V is the simulation volume and $< A^3 >$ is the average of the growth rate to the power of three. All simulations with distributions in A collapse onto a single line, indicating that *any* distribution solely in A *can only* change the pre-factor of $V_V(t)$. It has been predicted[46] that the $1/A$ distribution would not fundamentally change the growth kinetics compared to the JMAK model, only the pre-factor of $V_V(t)$. This seems to be true in general for all distributions solely in A.

A change in the distribution of α seems, however, to have a significant impact on the growth kinetics. It appears that distributions with a majority of the grains having α's near 1 deviates more strongly from the JMAK model than distributions with a majority of α's near 0. This makes sense because the JMAK can be considered as having a delta-function distribution of α centered at $\alpha = 0$.

JMAK	$A = 1,\ \alpha = 0$	
A uniform	$n(A) = 1/2$ $0 \le A < 2, \quad \alpha = 0$	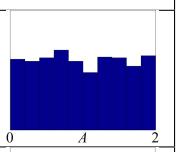
A log-normal	$n(A) = \frac{1}{A\sigma\sqrt{2\pi}} \exp \frac{-(\ln A - \mu)^2}{2\cdot\sigma^2}$ $0 < A, \quad \alpha = 0$	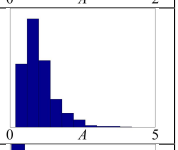
$1/A^{(1)}$	$n(A) = \frac{1}{\ln 100}\frac{1}{A}$ $.05 < A < 5, \quad \alpha = 0$	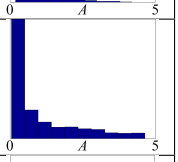
α uniform	$n(\alpha) = 1$ $0 \le \alpha < 1, \quad A = 1$	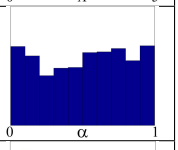
α p1q10-bell$^{(2)}$	$n(\alpha) = 132 \cdot \alpha(1-\alpha)^{10}$ $0 \le \alpha < 1, \quad A = 1$	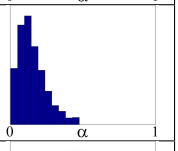
α p1q1-bell$^{(3)}$	$n(\alpha) = 6 \cdot \alpha(1-\alpha)$ $0 \le \alpha < 1, \quad A = 1$	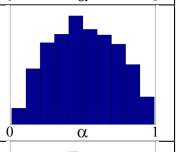
α p10q10-bell$^{(4)}$	$n(\alpha) = 3879 \cdot 10^3 \cdot \alpha^{10}(1-\alpha)^{10}$ $0 \le \alpha < 1, \quad A = 1$	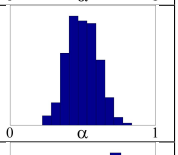
α p5q1.5-bell$^{(5)}$	$n(\alpha) = 87.98 \cdot \alpha^5(1-\alpha)^{1.5}$ $0 \le \alpha < 1, \quad A = 1$	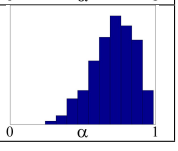

(1) $n(A) = \frac{c}{A^m}$, used with parameter $m = 1$ [46]. (2) $C\alpha^p(1-\alpha)^q$, used with parameters $p = 1$ and $q = 10$ [46]. (3) $C\alpha^p(1-\alpha)^q$, used with parameters $p = 1$ and $q = 1$ [46]. (4) $C\alpha^p(1-\alpha)^q$, used with parameters $p = 10$ and $q = 10$ [46]. (5) $C\alpha^p(1-\alpha)^q$, used with parameters $p = 5$ and $q = 1.5$ [46]. The specific parameters $p = 5$ and $q = 1.5$ are chosen because these were used as data-fitting parameters in [46].

Table 3.1 Distributions used for $r = At^{1-\alpha}$. All distributions are normalized so that $\int n(x) = 1$ and $< A >= 1$. Histograms show examples of distributions. The table is reproduced from article B.

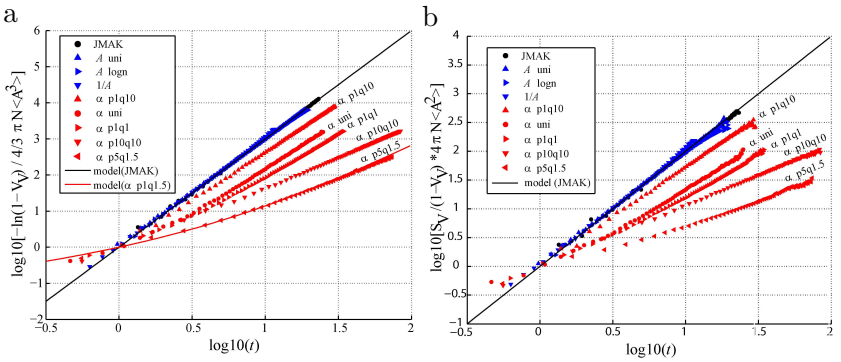

Figure 3.4 Averaged and pre-factor normalized JMAK-plots of (a) V_V and (b) S_V. (a) is reproduced from article B.

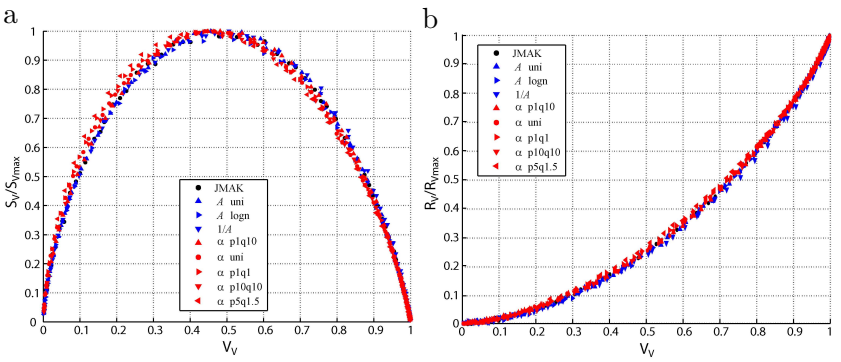

Figure 3.5 Microstructural paths of (a) $S_V/S_{V\max}$ vs. V_V and (b) R_V/R_{Vmax} vs. V_V.

The data for the various α distributions in fig.3.4(a) exhibits upwards curvatures in various degrees. In this study the upward-curving is interpreted in the context of 'the dominating grains': V_V from a collection of grains with equal growth parameters A and α would produce a straight curve with a slope of $3(1-\alpha)$ if plotted in fig.3.4(a) (see eq.1.5.4 page 16). A very small slope in fig.3.4(a) indicates that the dominating grains have high α values and a slope near three indicates that $\alpha \approx 0$. An upward curved data series indicates that the dominating grains initially have high α-values but grains with low α-values take over later on. This is plausible because the grain radius is given by $r = At^{1-\alpha}$, which means that the high-α grains grow rapidly initially but lose pace as time passes, while the low-α grains more or less keep their growth rate throughout the simulation. Using this interpretation we see that the curvature observed in fig.3.4(a) must be related to the width of the distribution. A very narrow distribution can not produce grains with significantly different α-parameters and the grains will all have almost the same growth prop-

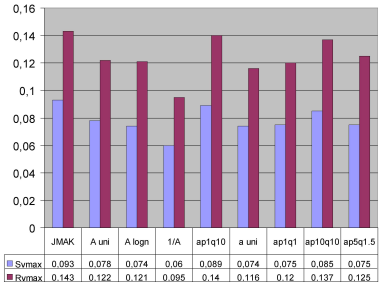

Figure 3.6 The grain boundary areas after total recrystallization $R_{V\max}$ and $S_{V\max}$ for the distributions of growth rates simulated.

erties. By comparing the data from p1q1 and p10q10 we see that they initially start out with the same slope but deviate later on. p1q1 which is the broader of the two distributions curves upward more than p10q10 which is expected from the arguments above.

Fig.3.4(b) shows a pre-factor-normalized version of a JMAK-type plot for S_V for all simulations. The normalization is done by dividing the apparent extended surface fraction $S_V/(1-V_V)$ by the total extended surface fraction at $t=1$: $S_X(1) = 4\pi N < A^2 > /V$. The plot reveals that S_V exhibit a behavior very similar to V_V: All distributions in A fall onto a single master-curve, while distributions in α exhibit deviations with a lower JMAK-parameter and upwards-curved data-series.

Because V_V and S_V are affected in similar ways by the introduction of growth rate distributions, one would expect that the microstructural path (MP) would not be affected. This is indeed the case. The MP S_V vs. V_V and R_V vs. V_V from all simulations are shown in fig.3.5. S_V and R_V are normalized by their maximum values $S_{V\max}$ and $R_{V\max}$. It is clear that the S_V- and R_V-curves are almost independent of growth rate distributions. The only noticeable difference is that $S_V/S_{V\max}$ is shifted slightly to the left for the α-distributions. This means that a MP-model for predicting the kinetics during a classical JMAK recrystallization process can be used to predict the kinetics for a process that contains any kind of growth rate distribution.

The plots in fig.3.5 are normalized by $S_{V\max}$ and $R_{V\max}$. Although the practical interpretation of $S_{V\max}$ is unclear, the meaning of $R_{V\max}$ is straight forward: $R_{V\max}$ is the total grain boundary area density after total recrystallization. Depending of the final microstructure, $R_{V\max}$ will be different. Fig.3.6 shows the values for $R_{V\max}$ and $S_{V\max}$ for the simulations performed. Some variations are seen but they are rather limited.

The similarity of the MP-kinetics and $R_{V\max}$ conceal some very large differences between the simulations however. The microstructures after total recrystallization from one layer of voxels from the various simulations are shown in fig.3.7. As seen, distributions in growth parameters may have a big impact on the recrystallized microstructure. Even though the number of grains is equal in all simulations, the recrystallized microstructures are very different. Notice that the grain boundaries in the

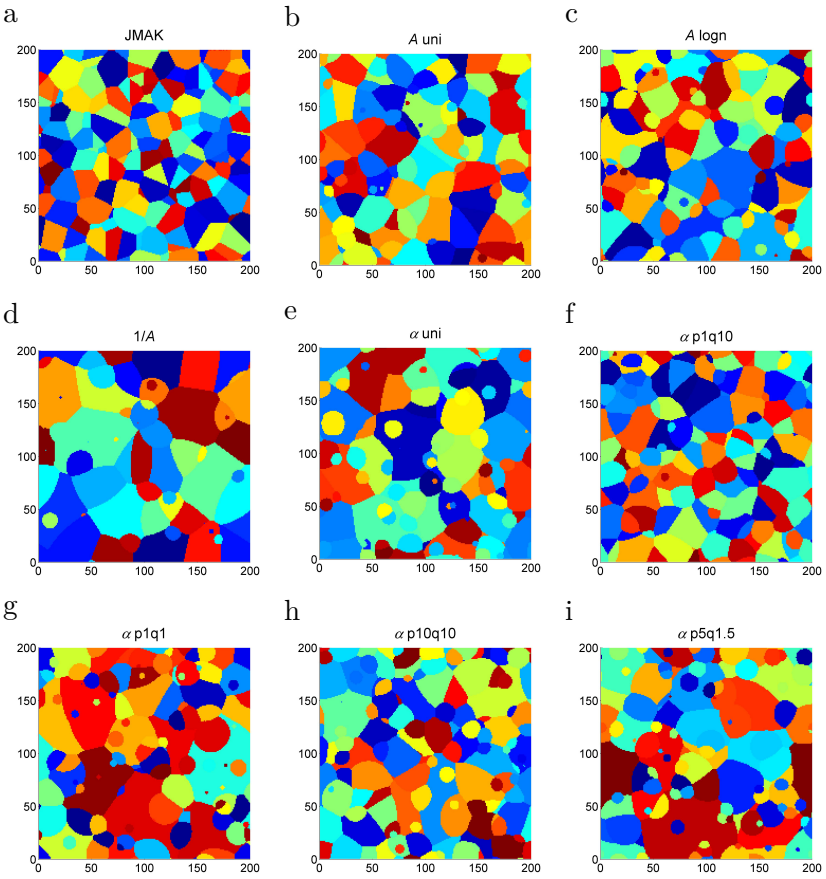

Figure 3.7 Examples of microstructures from the performed simulations: (a) JMAK, (b) uniform distribution of A, (c) log-normal distribution of A, (d) A distributed with a probability density proportional to $1/A$, (e) uniform distribution of α, (f) bell shaped distribution of α using $(p, q) = (1, 10)$, (g) bell shaped distribution of α using $(p, q) = (1, 1)$, (h) bell shaped distribution of α using $(p, q) = (10, 10)$ and (i) bell shaped distribution of α using $(p, q) = (5, 1.5)$. Different colors represent different grains.

classical JMAK simulations are straight (see fig.3.7(a)), as they should be (see section 3.1), but curved in all other cases. Very small grains are observed in many of the simulations, completely embedded in other grains. These may normally not be seen in experiments because such small grains would tend to disappear if grain growth occurs. In the present simulation, this is of course not allowed to happen.

The microstructures in fig.3.7 give a good qualitative impression of the effects that distributions of growth rates have on the microstructure. Distributions of growth rates also have large effects on quantitative measures such as the distributions of single-grain-intercept length d. d for

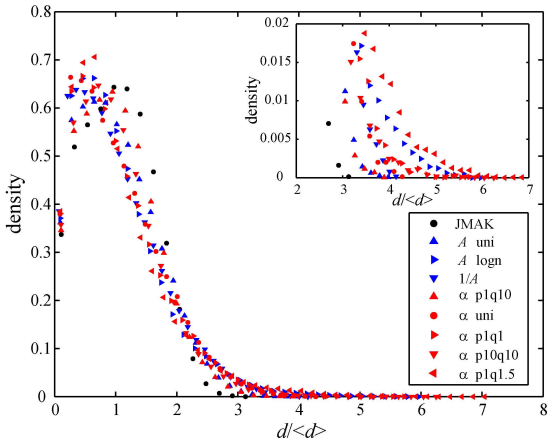

Figure 3.8 Distributions of single grain line scan intercepts d normalized to the mean intercept length $< d >$. The inset shows a close up of the intercept distribution tails. The figure is reproduced from article B.

all simulations normalized by the mean intercept length $< d >$, given by eq.1.4.8 page 11, are shown in fig.3.8. A clear difference is seen between the JMAK simulation and all distributions both in A and α: The JMAK simulation have a typical intercept length (the peak of the intercept distribution) close to the mean intercept length, whereas data from all simulations employing distributions of either A or α have typical intercept lengths that are smaller than the mean length. The simulations with growth rate distributions also exhibit extended tails in their distributions, clearly seen in the inset of fig.3.8. The inset show that for some distributions, grains intercept lengths more than six times average are seen; these grains are clearly very large. In the classical JMAK-simulation only very few grains larger than three times average are seen.

The grain size distribution in a metal is very important for it's properties and therefore of great industrial importance. When good formability is needed, for example, an even grain size distribution is often required. In other situations, a few very large grains are preferred. This is the case for turbine-lamella, where each lamella preferably contain one single grain. Another important issue is texture, i.e. the orientation distribution within the metal. If the growth rates of the recrystallizing grains are correlated with the orientations of the grains in an experiment, distributions of growth rates will lead to texturing: Recrystallization textures will arise because grains with some orientations grow to sizes much larger than average and their orientations consequently dominate the recrystallization texture. Texturing is also very important industrially. Random texture is for example needed to obtain good formability whereas a strong texture is preferred in metals that should convey strong magnetic

fields. Growth rate distributions have a strong influence on the grain size distributions, as shown above, and understanding how growth rate distributions influence the recrystallization microstructure is therefore very important from an industry point of view.

Overall, the geometric simulations of distributions of growth rates show that, although large effects are seen in the fully recrystallized microstructures, the kinetics are not affected in the case of A-distributions. This means that if all grains grow at constant, although different, rates, this would not be detected by the use of microstructural descriptors such as V_V alone. Other investigations, such as microstructural investigations, are necessary.

3.5 Random Ellipsoidal Growth

Anisotropic growth is typical during recrystallization as discussed in chapter 1 and as mentioned in section 1.5.4, many two-dimensional simulations have been carried out. Three-dimensional simulations have also been performed, but these have either involved completely flat two-dimensional grains in a three-dimensional volume[49] or grains that were not allowed to grow around each other[83]. These situations does not represent recrystallization well: Grains are not flat and complicated grain shapes observed in fully recrystallized samples indicate that the grains can grow around each other. The purpose of this part of the study is to investigate the effects of randomly oriented anisotropic growing grains and to illuminate the extent to which the geometric models, described in sections 1.5.2 and 1.5.3, can be used to describe the recrystallization kinetics.

The simulations of anisotropic growth are carried out with the geometric simulations using prolate ellipsoids with aspect rations up to 16: 1:1:16, 1:1:8, 1:1:4, 1:1:2, and 2:2:3 and oblate ellipsoids, also with aspect rations up to 16: 16:16:1, 8:8:1, 4:4:1, 2:2:1 and 3:3:2. Simulations employing all JMAK assumptions including spherical growth are also carried out for comparison with the JMAK model. Simulations in two dimensions are carried out for 2d/3d-comparisons and to be able to compare the simulations to two-dimensional simulations performed by others. The aspect ratios of the two-dimensional ellipses* simulated are again up to 16: 1:16, 1:8, 1:4, 1:2 and 2:3. Circles, i.e. classical two-dimensional JMAK, are also simulated. The grains in all the simulations performed are shape preserved, meaning that the shape of the grains are perfect ellipses/ellipsoids with the prescribed aspect ratio as long as no impingement have set in. When impingement sets in, the shape of the grains will of course depend on the impingement details. The shape-preserved growth applied in these simulations is a clear simplification compared to experiments, but it is the least severe modification of the original JMAK model that still embodies random anisotropic growth. In

* In two dimension ellipses, instead of ellipsoid, are simulated.

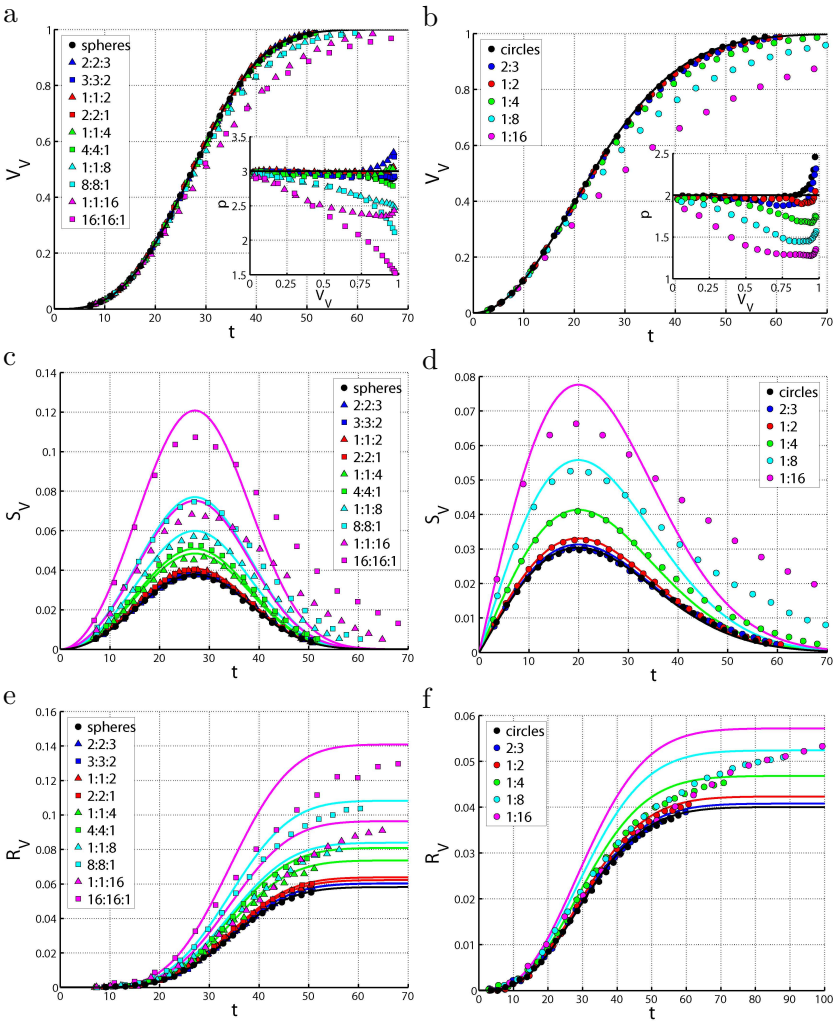

Figure 3.9 V_V, S_V and R_V as a function of t for (b,d,f) two- and (a,c,e) three-dimensional geometric simulations. The full lines show model predictions produced by the eq.1.5.2, 1.5.8 and 1.5.10. The insets in (a) and (b) show the JMAK-parameter p as a function of V_V. (a) and (b) are reproductions from article C.

the study by Kooi [49] two-dimensional grains were grown inside a three-dimensional simulation volume. Such grains can be considered as having infinite aspect-ratios, which makes these simulations an extreme case. Large deviations from JMAK behavior were also seen in by Kooi[49].

The ellipsoids are oriented randomly in space in three dimensions and the ellipses randomly in the simulated plane in two dimensions making the 2d simulations similar to the ones performed by Pusztai and Granasy[69]. Each three-dimensional simulation consists of 100 nuclei in

a cubic simulation-cell with periodic boundary conditions along x, y and z directions and a side length on 232 voxels giving a total of approximately $\approx 12.5 \cdot 10^6$ voxels. Each two-dimensional simulation consists of 100 nuclei in a square simulation-cell side length 500 pixels giving a total of $250 \cdot 10^3$ pixels. All simulations are performed under site-saturated conditions and with constant growth rate making the shape of the growing grains the only difference between these simulations and the JMAK model. The growth rates are defined so that the volume of an unimpinged grain would be the same for all grain-shapes as explained in article C. This makes direct comparisons between the simulations with differently shaped grains possible.

Every three-dimensional simulation is repeated six times with different seeds[†] (positions of nuclei and orientations of grains) and every two-dimensional simulation is repeated 12 times to improve statistics.

The kinetics of the simulations have also been investigated. Fig.3.9 shows the microstructural descriptors V_V, S_V and R_V for all two- and three-dimensional simulations as a function of time. The data in fig.3.9(a) and the model predictions fall almost exactly on top of each other for aspect rations up to four and the JMAK model eq.1.5.2 is therefore useable in three dimensions for phenomena with ellipsoidal anisotropic growth up to this aspect ratio. Since V_X is the same for all the ellipsoids simulated, as explained above, eq.1.5.2 gives the same predictions for all simulations. The inset of fig.3.9(a) shows the JMAK-parameter p as a function of V_V. For all simulations, apart from the ones with aspect ratios above four, p is close to three during the entire process.

Fig.3.9(c) shows S_V vs. t for the three-dimensional simulations. The deviations between the simulations and the model (eq.1.5.8) are very clear for aspect ratios above four. Especially towards the final stages of the transformation where long tails are seen. Deviations are also seen for R_V vs. t for three-dimensional simulations shown in fig.3.9(d). The model (eq.1.5.10) works fine up to an aspect ratio of four, but breaks down beyond this point.

In two dimensions, the equivalents to fig.3.9(a), (c) and (d) are shown in fig.3.9(b), (d) and (f). The deviations between the models (eq.1.5.2, 1.5.8 and 1.5.10 page 16) and the data are clearly larger in two dimensions than in three. Deviations are seen for V_V, p, S_V and R_V already at aspect ratios of four, where the models in three dimensions worked fine. This is in agreement with results obtained in other studies that show strong effects of two-dimensional random anisotropy [20, 48, 69].

The time averages of the JMAK-parameters $< p(t) >$ during the entire growth processes for two and three dimensions are listed in table 3.2. Up to an aspect ratio of four the deviations in $< p(t) >$ from JMAK behavior is less than three percent in three dimensions. We see that the deviations from JMAK behavior are stronger for the oblate ellip-

[†] The extreme aspect ratios 1:1:16 and 16:16:1 are only carried out three times due to the long computational times required in these cases.

Aspect ratio (a/b)	3D-prolate ellipsoids (a:b:b)	3D-oblate ellipsoids (a:a:b)	2D ellipses (a:b)
1	2.95	2.95	2.03
1.5	3.02	2.97	1.98
2	3.00	2.96	1.96
4	2.97	2.92	1.80
8	2.73	2.62	1.60
16	2.57	2.27	1.38

Table 3.2 Average JMAK-parameters $< p(t) >$ for simulations of prolate and oblate ellipsoids in three dimensions and ellipses in two dimensions. The table is reproduced from article C.

soids than for the prolate ellipsoids, which may be due to the greater blocking potential of 'plates' compared to 'needles' in three dimensions (see fig.3.12). $< p(t) >$ for the two-dimensional simulations show much stronger deviations than for three dimensions: For an aspect ratio of four $< p(t) >$ is for example reduced by 10% in two dimensions, whereas the three-dimensional simulations show very small reductions. Some numerical errors exist in the determinations of the JMAK-parameters in table 3.2. This can be seen from the first row of numbers that represent classical JMAK-simulations, which should be equal to 3.0, 3.0 and 2.0 respectively. The errors are within two percent of the expected values.

The stronger effect of anisotropic growth in two than in three dimensions is due to a more efficient blocking between grains: In two dimensions, the major axis of all ellipses will be distributed randomly in the same plane (the simulation plane). In three dimensions, the major axis of the ellipsoids will be distributed randomly in all directions of space. This will make the probability that grains impinge quickly along their fast growth directions much smaller in three dimensions than in two.

The ability for grains to grow around each other is utilized in these simulations in contrast to other three-dimensional simulations of anisotropic growth [49, 83]. This ability influences the transformation kinetics. The results reported by Shepilov and Baik [83], where no growing around was allowed, show larger deviations between random oriented ellipsoidal and spherical growth in three dimensions than what is reported in this study: For an aspect ratio of five clear reductions in p were observed by Shepilov and Baik [83], whereas no significant change up to an aspect ratio of four is seen here as explained above. This difference must be ascribed to the possibility for grains to grow around each other.

Microstructural path (MP) plots of S_V, R_V and Crr vs. V_V for two- and three-dimensional simulations are shown in fig.3.10. We see that the model-predictions work rather well for S_V in three dimensions for aspect ratios up to eight. For aspect ratios of 16 the model can not predict the simulated data. For R_V the model predictions are even better; here only

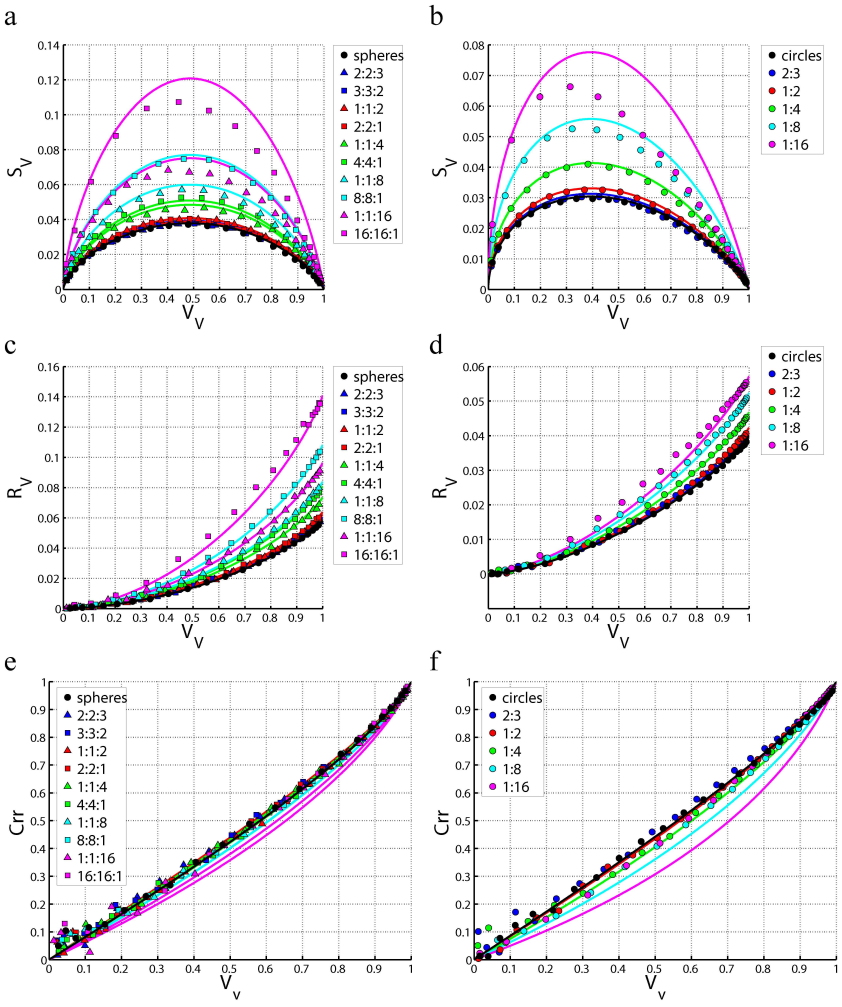

Figure 3.10 MP plots of S_V, R_V and Crr vs. V_V for (b,d,f) two- and (a,c,e) three-dimensional simulations. The full lines show model predictions produced by the eq.1.5.2, 1.5.8 and 1.5.10. (a), (c) and (e) are reproductions from article C.

the oblate grains with an aspect ratio of 16:16:1 cannot be described by the model. It is expected, however, that the model predictions for R_V are better since eq.1.5.10 uses the value for R_V after total transformation from the simulations as input and some kind of fitting therefore is present. Also in two dimensions, the models for S_V and R_V plotted as the MP (fig.3.10) works better than when plotted in the time-domain, but we still see larger deviations between simulations and models in two than in three dimensions.

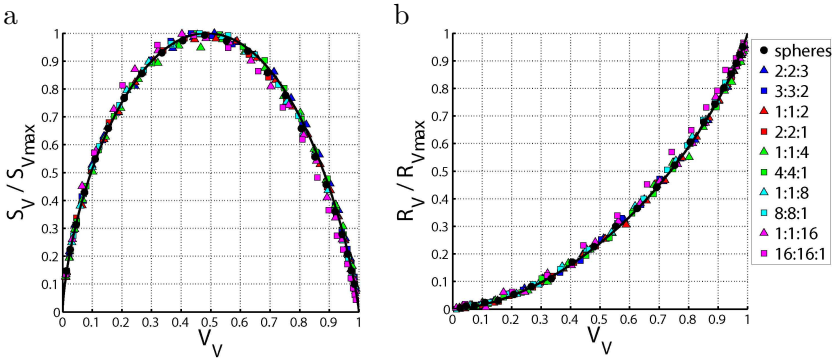

Figure 3.11 (a) $S_V/S_{V\max}$ and (b) $R_V/R_{V\max}$ for the three-dimensional simulations.

The microstructural path for Crr vs. V_V exhibit very interesting behavior in both two and three dimensions. The data from all simulations fall on top of each other, although the models predicts otherwise. Crr is typically used to characterize whether nucleation sites are located randomly or in clusters (see fig.3.3). The fact that the Crr-curves for simulations of all aspect ratios fall on top of each other show that anisotropy do not have any effect on Crr in a MP framework. Therefore, Crr can be expected to be useable for detecting clustering, also if the grains grow anisotropically.

The MPs for all aspect ratios in three dimensions have almost the same shape and can be brought to fall on top of each other by simple scaling (see fig.3.11). This shows that the MP of the ellipsoids are very similar, although the aspect ratios differs a lot.

Examples of microstructure of the simulations performed in three dimensions with various aspect ratios are shown in fig.3.12. More and more elongated grains with curved boundaries are observed as the aspect ratio is increased. The oblate grains produce more 'extreme' microstructures. The microstructure of the 16:16:1-simulation (fig.3.12(i)) has grains that apparently have been separated into different parts by other grains growing through them. This is not the case. The simulation procedure ensures that all parts of a grain are connected (see chapter 2). What is observed is grains that grow around each other and the apparent separation of the grains is because only one layer of the simulation is displayed. It becomes clear that all parts of a grain is connected when the whole grain is observed. An example of this is seen in fig.3.13. The grain has a very complicated shape, which shows that it must have grown around it's neighbors.

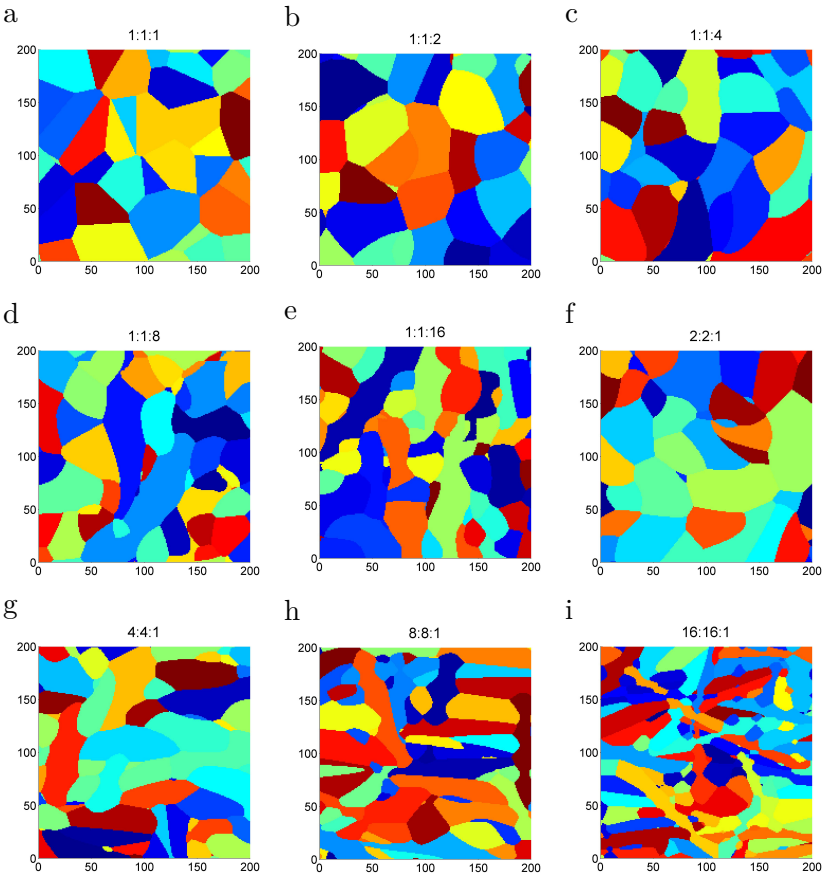

Figure 3.12 Examples of microstructures from the simulations performed with ellipsoidal shaped grains in three dimensions with aspect ratios as given above the figures. Different colors represent different grains.

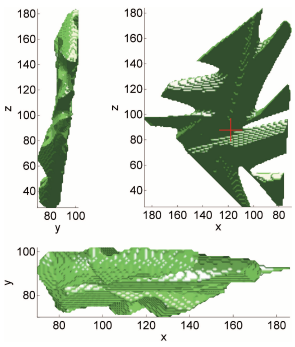

Figure 3.13 Example showing the final shape of an oblate ellipsoid with aspect ratio eight after total transformation, seen from directions along the x, y and z axes. The cross marks the position of the nucleus of the grain. The figure is reproduced from article C.

The microstructures of the two-dimensional simulations are shown in fig.3.14. Clear deviations from JMAK behavior is seen in simulations where grains have high aspect ratios, but the microstructures do not look as 'extreme' as they did in three dimensions. This may be because the grains block each other very efficiently as they can not grow around each other. In fig.3.14, examples of microstructures from simulations of aligned anisotropic growth are included for comparison. These appear as 'stretched' versions of ordinary JMAK-microstructures. Notice for example the straight grain boundaries, which is a result of all grains having the same growth rate in any particular direction.

The geometric simulations of anisotropic growth show that large deviations from JMAK-kinetics are to be expected only when grains have extreme aspect ratios. Large aspect ratios are very seldom seen in recrystallization of typical metals, which means that the models assuming spherical or aligned anisotropic growth will work nicely for the description of the recrystallization kinetics in most cases. Examples of extreme anisotropy can be found though. Fig.3.15 shows an interesting example: two polished surfaces of a meteorite composed of an unspecified iron-alloy. Large elongated grains are seen along two main directions, which are perpendicular to each other and clear signs of grain-impingement are seen. For such a situation, new models are needed to predict the kinetics during recrystallization correctly.

3.6 General Discussions

The JMAK model is used as the reference point for the kinetics of the geometric simulations because the geometric simulations basically are numerical solutions of the JMAK model. In the more complex growth-scenarios, simulated in this study, numerical solutions of JMAK-like problems are necessary because the scenarios are too complex to solve analytically.

One use of geometric simulations, like the ones presented in this thesis, is that experimental data can be interpreted on the basis of these. Certain features in the JMAK-kinetics of an experiment may be ascribed to certain aspects of the nucleation and growth parameters. A drop in the JMAK-parameter p may for example be ascribed to clustering or anisotropic growth. This works in principle, but it may be very hard to do in practise. It may for example be difficult to tell whether a drop in p is due to boundary nucleation, random anisotropic growth or a general loss of the grow rates of the grains from the kinetics alone. Other investigations must accompany the kinetic investigations.

The JMAK model often works surprisingly well in descriptions of the kinetics of experimental data. p may vary from experiment to experiment but often stays constant within the duration of a single recrystallization process. One of the reasons for this may be that signatures of deviations from standard JMAK behavior are weak or non-existing, as seen for the

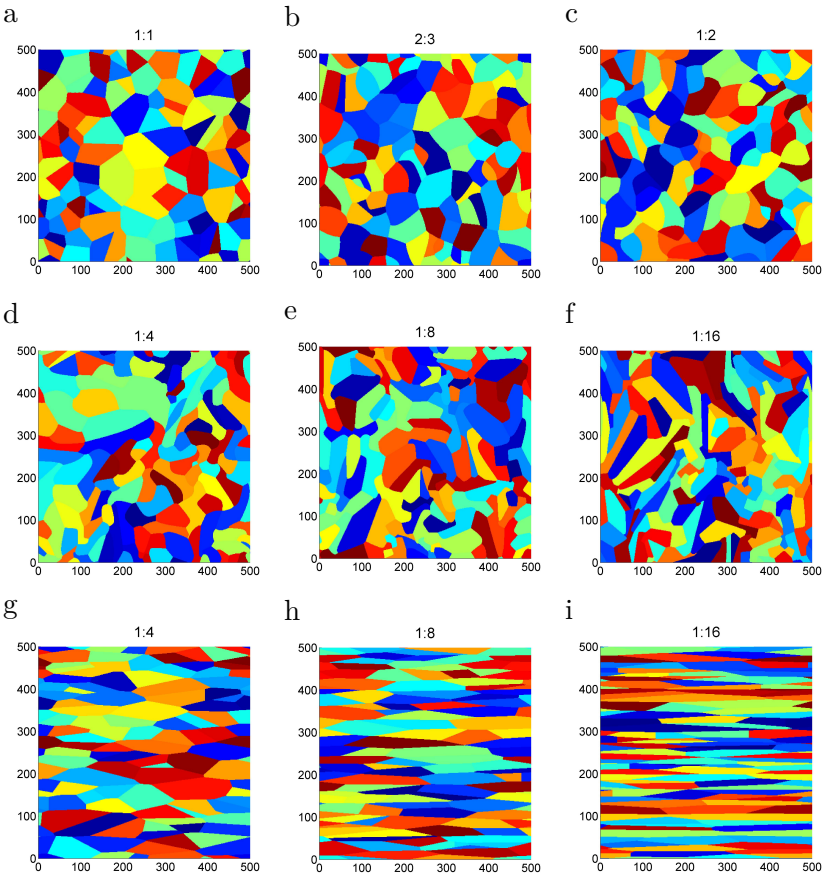

Figure 3.14 (a-f) Examples of microstructures from the simulations performed with elliptical shaped grains in two dimensions with aspect ratios as given above the figures. Different colors represent different grains. (g-i) Microstructures from simulations of aligned anisotropic growth are included for comparison.

random oriented ellipsoidal growth with low aspect ratios or distributions the A-parameter. This means that in many cases the kinetics alone may not be enough to describe recrystallization precisely; microstructures or detailed studies of single grain kinetics, which is possible with techniques such as the 3DXRD-microscope, are necessary.

Although JMAK-type investigations like the geometric simulations may be difficult to use for exact interpretations of experimental data, geometric simulations constitute the perfect 'what if' model because they test what happens if certain growth scenarios are assumed. The simulations can be used in situations where the effects of certain parameters are unknown, like the examples of growth rate distributions and random anisotropic growth presented in this thesis.

Figure 3.15 Photo of the surface of a meteoroid. Large elongated grains are seen with their main axis along two perpendicular directions. The two images are photographed with the same resolution, the tic-marks on the scale-bar on the image to the right indicate mm. By the curtesy of Dorte Juul Jensen.

The simulations performed in this study highlight a very important assumption in the JMAK model. Although time dependent nucleation- and growth-rates are allowed within the assumptions of the JMAK model, the model requires that at a given moment in time and for a given direction, all grains must grow at the same rate. This assumption basically allows for all grains to be treated collectively as one in the extended volume framework. The simulations performed in this study violate this assumption in two different ways; by employing distributions of growth rates or distributions of growth directions, which both lead to deviations from JMAK-behavior. A collective behavior of all grains is expected in recrystallization only if all grains grow in the same way in the deformed matrix. This requires that neither the crystallographic orientation of the grains relative to the deformed-matrix nor the detailed structure of the matrix play any significant role. We know that this can definitely not be true because experiments have shown that each grain has individual growth behavior and even parts of the grain boundary surrounding the same grain may grow with different rates at different times (see section 1.4.7 page 12).

4 Method for Molecular Dynamics Simulations of Recrystallization

This chapter describes the molecular dynamics (MD) simulations performed in this study. The simulation 'engines' are developed and implemented elsewhere, but the methodology for simulating recrystallization using MD is developed as a part of this PhD-project during discussions with supervisors and collaborators. This is to the best of the author's knowledge the first time that MD have been used directly in connection with recrystallization. A limited two-dimensional study was performed by [92].

As explained in section 1.6 page 23, two MD programs have been used: The one is developed at the Colorado School of Mines (termed the CSM-program in the following), the other is developed at the Center for Atomic-Scale Materials Design at the Technical University of Denmark (termed the CAMd-program in the following). Both programs were provided by collaborators and have been used as black box programs to some extent. No modifications to the actual 'MD engines' have been made in connection to this study. The two MD programs and the interatomic potentials used in connection with these are explained throughout this chapter. The differences of the programs used are summed up in section 4.5 where a comparison of the computational speed is also given.

The crucial point for the application of MD to recrystallization is how the simulations are set up: Due to the spatial and temporal scales that MD simulations are limited to, the problem has to be reduced in some way, both temporally and spatially, in order to simulate recrystallization. The simulations should only contain the most essential features. Since recrystallization is characterized by migrating grain boundaries driven by the excess energy stored in the structures of the deformed matrix, high angle boundaries as well as dislocations should be present in a MD simulations of recrystallization, and the grain boundaries should be migrating due to the presence of dislocations. The main achievement of this study is the development of a method for setting up migrating grain boundaries driven by dislocation structures.

In section 4.1 some general features of MD simulations and the two simulation-programs that have been applied are described. The interatomic potentials used are described in section 4.2. In section 4.3 the method developed for simulating boundary migration during recrystallization is described and in section 4.4 the data analysis schemes developed and used are described.

4.1 Molecular Dynamics Simulations

As mentioned in section 1.5.9 page 21, the idea behind MD is simple: solve the classical equations of motion for a system of N elements (atoms) that are interacting via a potential U[11]:

$$m_i \frac{\mathrm{d}^2 \boldsymbol{r}_i}{\mathrm{d}t^2} = -\nabla_{\boldsymbol{r}_i} U(\boldsymbol{R}) \tag{4.1.1}$$

where m_i is the mass, $\boldsymbol{r}_i$ the position, $\frac{\mathrm{d}^2 \boldsymbol{r}_i}{\mathrm{d}t^2}$ the acceleration and $-\nabla_{\boldsymbol{r}_i} U(\boldsymbol{R})$ the force on atom i calculated from U. $\boldsymbol{R} = \boldsymbol{r}_1, \ldots, \boldsymbol{r}_N$ is the collective positions of all atoms on which U depends. Each atom has an equation of motion of the form given by eq.4.1.1.

A general approach for solving equations of motion such as eq.4.1.1 is the so-called finite difference approach. The basic idea is that if positions, velocities and forces for the atoms are known at time t we can attempt to find the positions, velocities and forces at a later time $t + \delta t$. In turn positions, velocities and forces are updated iteratively. One iteration covers a time step of δt. One of the most used algorithms is the velocity Verlet algorithm. The update-scheme is as follows:

$$\boldsymbol{r}(t+\delta t) = \boldsymbol{r}(t) + \boldsymbol{v}(t)\delta t + \frac{1}{2}\boldsymbol{a}(t)(\delta t)^2 \tag{4.1.2}$$

$$\boldsymbol{v}(t+\delta t) = \boldsymbol{v}(t) + \frac{\boldsymbol{a}(t) + \boldsymbol{a}(t+\delta t)}{2}\delta t \tag{4.1.3}$$

First $\boldsymbol{r}(t+\delta t)$ is calculated on the basis of $\boldsymbol{r}(t)$, $\boldsymbol{v}(t)$ and $\boldsymbol{a}(t)$. Then $\boldsymbol{a}(t+\delta t)$ is calculated on the basis of the new positions $\boldsymbol{r}(t+\delta t)$. Finally $\boldsymbol{v}(t+\delta t)$ is calculated on the basis of $\boldsymbol{v}(t)$, $\boldsymbol{a}(t)$ and $\boldsymbol{a}(t+\delta t)$. The velocity Verlet offers some error-reduction properties and does only require the storage of $\boldsymbol{r}$, $\boldsymbol{v}$ and $\boldsymbol{a}$ (memory issues are important when running large simulations) [11]. The velocity Verlet algorithm is used in the simulations with the CSM-program. Although the program is capable of running with different algorithms, the velocity Verlet was chosen due to the low memory requirements. In the CAMd-program a different integrator is used, which is coupled to the temperature control (see eq.4.1.7 below).

During typical recrystallization experiments, a sample is heated at a certain fixed temperature at ambient pressure. In order to perform simulations at constant temperatures and pressures, control-mechanisms must be in place. The kinetic energy K of an atomic system and the temperature T are related through*:

$$K = \sum_i^N \frac{1}{2} m_i v_i^2 = N\frac{3}{2}k_B T \tag{4.1.4}$$

where k_B is Boltzmann's constant. Since the velocities of the atoms and the temperature are directly related, a simple way of adjusting the

* Eq.4.1.4 is valid if the atoms do not poses any rotational degrees of freedom.

temperature is by 'velocity rescaling'. In the Berendsen velocity rescaling algorithm used in the CSM-program the following equation replaces eq.4.1.3:

$$\boldsymbol{v}(t+\delta t) = \eta\left(\boldsymbol{v}(t) + \frac{\boldsymbol{a}(t)+\boldsymbol{a}(t+\delta t)}{2}\delta t\right) \tag{4.1.5}$$

η is the scaling parameter given by:

$$\eta = \sqrt{1+\frac{\delta t}{\tau}\left(\frac{T_{\text{ext}}}{T}-1\right)} \tag{4.1.6}$$

where T_{ext} is the target temperature and τ is a user defined time constant controlling the rate by which the system approaches the target temperature.

So-called Langevin dynamics are used in the CAMd-program. Here the equation of motion (eq.4.1.1) is changed in the following way:

$$m_i\frac{\mathrm{d}^2\boldsymbol{r}_i}{\mathrm{d}t^2} = -\nabla_{\boldsymbol{r}_i}U(\boldsymbol{R}) - \gamma_i\boldsymbol{v}_i + \boldsymbol{G}_i(t) \tag{4.1.7}$$

Two terms have been added, which model the atom's interactions with the 'electron bath' of the system. The first term is a friction term, which models the resistance experienced by the atom moving through the electron bath. γ_i is the coefficient of friction experienced by atom i, which may be different for different species of atoms. The second is a random force, which models the random collisions between the simulated atoms and the electrons. The temperature is controlled through the random force $\boldsymbol{G}$, which has the following properties:

$$<\boldsymbol{G}(t)> \;=\; 0 \tag{4.1.8}$$

$$<\boldsymbol{G}(t)\cdot\boldsymbol{G}(t')> \;=\; 2mk_BT\gamma\delta(t) \tag{4.1.9}$$

where $\delta(t)$ is the Dirac-delta function. The first equation states that the direction of $\boldsymbol{G}$ is random. The second equation states that the values of $\boldsymbol{G}$ at different times are uncorrelated and defines the size of $\boldsymbol{G}$. It can be shown that T in eq.4.1.9 is the temperature that the system will eventually reach [11]. When using Langevin dynamics eq.4.1.7 can be solved by finite difference methods similar to the velocity Verlet.

Pressure control can be applied by varying the simulation volume. In the CAMd-program this is done by adjusting the dimensions of the simulation-cell at regular intervals in the following way:

$$l_i' = l_i\left(1+\frac{\sigma_i}{3K}\right) \tag{4.1.10}$$

where l_i' is the adjusted simulation-cell length in the i'th direction ($i = x$, y or z), l_i is the pre-adjusted length, σ_i is the i'th normal stress component and K is the bulk modulus for the material. This adjustment will produce a relative volume change of $\Delta V/V \approx (\sigma_x+\sigma_y+\sigma_z)/3K$

(first order approximation). By assuming that the only overall pressure in the simulation is the hydrostatic pressure $P = (\sigma_x + \sigma_y + \sigma_z)/3$ this can be reduced to $\Delta V/V = P/K$. A relative volume change will produce a pressure change of $\Delta P = -K\Delta V/V$. By making the volume change prescribed by eq.4.1.10, the pressure change will be: $\Delta P = -K\Delta V/V = -KP/K = P$. This means that by making the adjustment in eq.4.1.10 any excess pressure will be eliminated (this is, however, only true for small excess pressures where the first order approximation used above holds). The adjustments of cell size was typically done for each 100 iterations in the CAMd-program.

In the CSM-program no pressure control was applied during the simulations, however, the simulations were initiated at zero pressure by a procedure explained in section 4.3.2.

4.2 Interatomic Potentials

Different interatomic potentials can be used in MD simulations in order to represent different materials. The potential U 'controls' the equation of motion eq.4.1.1 and therefore determines the dynamics in the system. In this study three different potentials have been used: a *Lennard-Jones* (LJ) pair-potential, an *Embedded Atom Method* (EAM) Al potential and an *Effective Medium Theory* (EMT) Cu potential. The LJ and EAM potentials were used with the CSM-program and the EMT potential was used with the CAMd-program. Initially it was important to test the applicability of the simulation methodology and less important to have realistic metal-properties in the simulations. Because of the simplicity and efficiency of the LJ potential, this was used in the first simulations. Later the EAM-potential and finally the EMT potential were used in the simulations. The EAM-Al and EMT-Cu potentials used were chosen because Al and Cu are common metals and much experimental data from them exist. Together the three potentials to some degree span a range of potentials which makes it possible to test the generality of the methodology.

4.2.1 Lennard-Jones Pair-Potential

The LJ potential is a simple atomic potential very often used for MD simulations. The potential does not model any real substance, but can be used as a synthetic 'test-material' in situations where the phenomena studied exist in many types of materials, e.g. the glass transition in supercooled liquids [82]. The LJ potential can also be used in situations where the overall or qualitative behavior of the phenomena studied are not expected to depend much on the interactions of the individual atoms. The LJ potential models the energy of interaction between atoms by [11]:

$$U_{\mathrm{LJ}} = \frac{1}{2}\sum_{j\neq i} 4\epsilon\left((\sigma/r_{ij})^{12} - (\sigma/r_{ij})^{6}\right) \tag{4.2.1}$$

r_{ij} is the mutual distance between atoms i and j, σ is the length parameter given by $\sigma = (1/2)^{1/6} r_0$, where r_0 is the equilibrium intermolecular distance (nearest neighbor distance) and ϵ is the bonding energy between two atoms. The factor $1/2$ is introduced to avoid double-counting of interactions. In the CSM-program, the potential is truncated at a cutoff distance $r_c = 2.1 r_0$ and modified by a spline fit beyond r_0, so that it goes to zero smoothly at $r = r_c$. It is important that the potential is smooth because the forces in the system are calculated by differentiations of the potential.

Scaled units are often used in connection with LJ simulations: mass is given in units of m_0, the mass of one atom, length in units of r_0, energy in units of ϵ, time in units of $\tau = (m_0 r_0^2/\epsilon)^{1/2}$, temperature in units of ϵ/k_B. By inserting appropriate values for m_0, σ and ϵ results corresponding to various metals can be obtained, although one cannot expect this simplistic potential to capture all features of real materials.

The LJ potential is quite good at representing rare gasses but it is relatively inexact when it is used to represent metallic systems[18]. The vacancy formation energy E_v and the cohesive energy E_c is equal for all pair-potentials including the LJ [100]. For Cu E_c has a magnitude that is three times as large as E_v [41]; for Al E_c is five times E_v [59]. The so-called *Cauchy pressure* given by $C_{12} - C_{44}$[†] is zero for pair-potentials but positive for most fcc metals such as Al or Cu[18]. Although the elastic shear modulus G may represent typical values for metals within a factor of approximately two the bulk modulus B is two to four times greater for LJ than for metals [18]. The melting point T_m for LJ is around .7 $\epsilon/k_B K$, which corresponds to ≈ 2300 for Al and ≈ 2400 for Cu. These numbers are obtained by inserting values for ϵ corresponding to E_c per atom divided by the number of nearest neighbors: $\epsilon_{c-\mathrm{Al}} = 3.39/12eV$, $\epsilon_{c-\mathrm{Cu}} = 3.54/12eV$. The melting point and also bulk modulus can be determined more precisely by choosing a lower value for ϵ, but then the cohesive energy will of course be wrong.

4.2.2 Embedded Atom Method Al Potential (EAM)

Pair interaction potentials often have difficulties when used to represent metallic systems. One way to address the problems is to perceive atoms as being *embedded* in the background electron gas of the system. This is done by introducing, in addition to the pair-interaction term in the potential, a term that depends on the local free volume or the local electron density around the atoms[59, 60]:

$$U_{\mathrm{EAM}} = \frac{1}{2} \sum_{j \neq i} \phi(r_{ij}) + \sum_i F(\rho_i) \tag{4.2.2}$$

Here ϕ is the pair-interaction function and F is the embedding function that depends on the local electron density ρ_i around atom i. ϕ, F and ρ can be modelled in different ways but typically some functional forms are chosen and parameters fitted to experimental data.

[†] C_{11}, C_{12} and C_{44} are the three independent elastic constants for cubic materials, $C_{11} - C_{12}$ is the *tetragonal shear modulus* and C_{44} is the *trigonal shear modulus*.

The macroscopic properties for the Mendelev-EAM used in the CSM-program is much closer to the experimental target values than the LJ. Both E_c and E_v are within five percent of the target values, all elastic constants are within one percent and T_m given by the potential is 939K compared to the experimentally measured 933K [59].

4.2.3 Effective Medium Theory Cu Potential (EMT)

The EMT approach for modelling atomic interactions is related to the EAM, although the underlying idea is somewhat different. In EMT the potential energy is calculated by first calculating the energy of an atom in a known reference system and then adding the perturbation energy of changing the reference system into the actual system. The reference system used in the CAMd-program is a perfect fcc crystal [41]. The functional form of the EMT potential is:

$$U_{\mathrm{EMT}} = \frac{1}{2}\left[\sum_{j\neq i}\phi(r_{ij}) - \sum_{j\neq i}^{ref}\phi(r_{ij})\right] + \sum_{i}E(\rho_i) \qquad (4.2.3)$$

ϕ is a pair interaction function that is used to describe the difference between the actual and the reference system and E is the cohesive function that describes the energy of the reference system with electron density ρ. By using various models for ϕ, E and ρ, eq.4.2.3 can be determined by using known values for the cohesive energy, the bulk and the shear moduli, the lattice constant and electron density parameters, obtained from quantum mechanical density functional theory calculations, without fitting [41].

As in the case of the EAM potential E_c, E_v and the elastic constants are very well represented by the EMT potential (within a few percent of the target values) [41]. The melting point has not been reported for this potential but simulations performed in this study suggests that it is near 1300K, not too far from the experimental value of 1358K.

4.3 Atomistic Simulation Methodology for Recrystallization

This section presents the methodology used to simulate recrystallization by atomistic simulations developed during this project. As discussed in the beginning of this chapter, MD simulations of recrystallization should contain the essential features of recrystallization: migrating grain boundaries driven by dislocation structures. This means that both grain boundaries and dislocation structures must be present during a simulations. Article D showed that the simulation methodology described in this section can produce both grain- and dislocation boundaries and article E showed amongst other things that it is the dislocations that are producing the driving pressure.

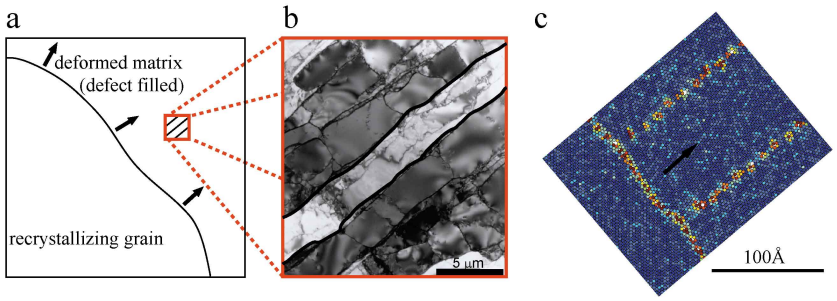

Figure 4.1 The idea behind the simulation methodology. (a) Sketch showing a recrystallizing grain growing through the deformed matrix. (b) Magnification of a part of the deformed matrix containing elongated dislocation boundaries as the main feature. (b) Snapshot from a simulations showing a grain boundary migrating through the part of the simulation-cell containing dislocation walls. Colors indicate potential energy of the atoms: blue is low energy and red is high. A grain boundary moving into an area containing individual dislocations within two dislocation boundaries can be seen (the dislocations have a direction into the viewing-plane). The arrow indicate the direction that the grain boundary is migrating. The figure is reproduced from article F.

Before the detailed treatment of the methodology is presented, an overview of the idea behind the it is presented briefly. The idea is illustrated in fig.4.1. Fig.4.1(a) show a sketch of a recrystallizing grain growing into the deformed matrix. As described in section 1.3 page 5, a typical microstructure in the deformed matrix at the onset of recrystallization may have elongated dislocation boundaries as the dominating feature as shown in fig.4.1(b). If an overlay of fig.4.1(a) and (b) is made, the grain boundary will migrate through the deformed matrix in a direction that is parallel to the dislocation boundaries. This is of course a special direction, but this is the situation that has been chosen for this study as a starting point. A snapshot from a simulation that corresponds to this situation is shown in fig.4.1(c). The colors represent the potential energy of the atoms and the grain boundary and dislocations stand out as high energy areas.

The simulation procedure is divided into three separate steps: Setup, relaxation and annealing. Setup covers how the atoms are initially arranged, relaxation covers what is done to avoid large tensions or excess energies in the as-setup simulation-cells and annealing is the actual simulations.

4.3.1 Setup

The procedure for setting up the simulation-cells is designed in the following way: First a rectangular three-dimensional simulation-cell is set up. Afterwards, lattices of atoms are created. In all simulations the cre-

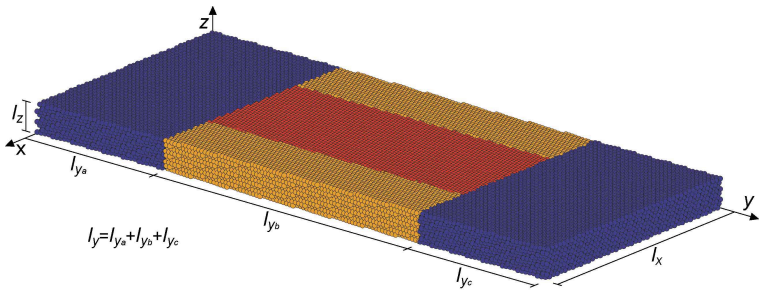

Figure 4.2 Example of a simulation-cell. Five crystal blocks are seen: two blue, two yellow and one red. The boundary conditions ensure that the two blue blocks and the two yellow blocks can be taken as one blue and one yellow block. Each color represent a certain orientation of the crystal lattice inside the block. The figure is reproduced from article E.

ated lattices are of the fcc type because Al and Cu are fcc-metals and LJ-atoms also crystallize in a fcc lattice. The lattices have certain orientations compared to the axes of the simulation-cell. Blocks of atoms are 'cut out' from these lattices and placed inside the simulation-cell. The blocks are cut out in such a way, that they fill the entire simulation-cell. An example of a simulation-cell is shown in fig.4.2. Periodic boundary conditions are applied at all boundaries of the simulation-cells to avoid surface effects.

Differences in crystal orientations across the interfaces between the blocks will eventually create grain- and dislocation boundaries. One of the main properties of this method for performing MD simulations is that the grain- and dislocation boundaries are created 'naturally'. By naturally is meant that no rearrangements of the atoms are necessary in the setup to create the grain-boundaries and the dislocation. These are formed at the interfaces between crystal blocks during the relaxation and the annealing as a result of the atomic movements. This was shown in article D.

The misorientation across an interface between two crystal blocks must be accommodated by atomic configurations at the interface region. In these simulations, the atoms arrange in the configuration with the least extra energy compared to the perfect lattice that can accommodate the misorientation. If the misorientation is small, dislocations will accommodate the misorientation and the interface will be a dislocation boundary. If the misorientation is large the dislocations necessary for producing the misorientation is so closely packed that it would be meaningless to talk about individual dislocations (as explained in section 1.3 page 5) and the interface will be an amorphous layer, i.e. a grain boundary.

In principle, the crystal lattices within the blocks can have any orientation as long as the lattices match up at the periodic boundaries. In

this study, however, it was chosen that every block should have a [111]-direction along the z-axis. The main reason for this is that fast moving boundaries are necessary for making simulations with reasonable computational resources and grain boundaries with $\approx$ 40deg. misorientation created by a rotation around a [111]-axis are observed experimentally to have high mobilities (see section 1.4.6 page 11). When the [111]-directions of the blocks are along the z-axis, rotations around this axis can easily be created, while keeping the blocks matched up at the simulation-cell boundaries perpendicular to the z-axis.

More care has to be taken to match up the blocks at the boundaries perpendicular to the x- and y-axes. A fcc lattice can be defined by the three crystallographic directions [1–10], [11–2] and [111](or any other set of perpendicular vectors with integer values). The non-rotated crystallographic orientation will be defined as the one where [1–10] is along the x-axis of the simulation-cell, [11–2] is along the y-axis and [111] is along the z-axis. Since all rotations are made around the z-axis, all crystals will have the [111]-direction along the z-axis. The rotation angle θ between a rotated crystal and the non-rotated crystal can be found by:

$$\cos\theta = \frac{[1\text{–}10]\cdot \boldsymbol{d}_x}{\sqrt{2}|\boldsymbol{d}_x|} = \frac{[11\text{–}2]\cdot \boldsymbol{d}_y}{\sqrt{6}|\boldsymbol{d}_y|} \tag{4.3.1}$$

where $\boldsymbol{d}_x$ and $\boldsymbol{d}_y$ are crystallographic orientations along the x- and y-axes that are perpendicular to each other and to [111]. By choosing the box-dimensions l_x and l_y along x and y such that:

$$l_x = i|\boldsymbol{d}_x| \tag{4.3.2}$$

$$l_y = j|\boldsymbol{d}_y| \tag{4.3.3}$$

where i and j are integers the atoms will match up at the boundary. The hard part is to find directions $\boldsymbol{d}_x$ and $\boldsymbol{d}_y$ with integer values and the right misorientations. This has been done on an trial-and-error basis in this study.

As explained in section 1.3 the average Burger's vector of dislocations in a dislocation boundary $\boldsymbol{B}$ is related to the rotation axis associated with the misorientation across the boundary $\boldsymbol{\theta}$ through $\boldsymbol{B} \perp \boldsymbol{\theta}$. Since $\boldsymbol{\theta}$ used to generate the misorientations across the interfaces is the same for all simulation-cells the type of dislocations generated depend on the normal vector to the dislocation boundary $\boldsymbol{N}$: by varying $\boldsymbol{N}$ edge ($\boldsymbol{N} \perp \boldsymbol{\theta}$), screw ($\boldsymbol{N}||\boldsymbol{\theta}$) or mixed dislocations can be generated.

The dislocations created may not be mobile. Normally a mobile dislocation will have a Burger's vector equal to the minimum lattice spacing along a [110]-direction and slip on a (111)-plane[103]. This is not guaranteed by the setup here because the dislocations have to accommodate the misorientation across the interface. The effect may be that the dislocation structures created are more or less stable than they would be normally.

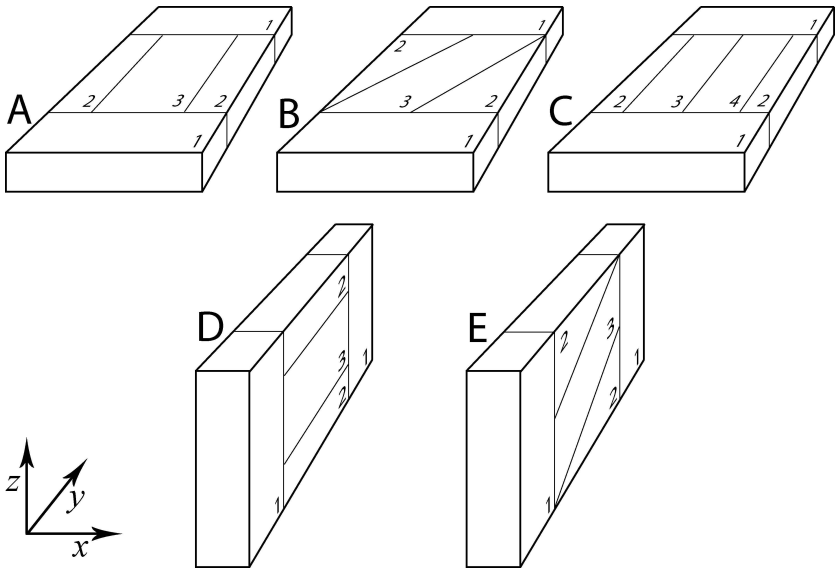

Figure 4.3 The five types of simulation geometries. A: Tilt dislocation boundaries perpendicular to the grain boundaries. B: Tilt dislocation boundaries inclined to the grain boundaries. C: Dual-type tilt dislocation boundaries, one with twice as high misorientation angle as the two others. D: Twist dislocation boundaries. E: Dislocation boundaries consisting of mixed dislocations. The numbers indicate the blocks of crystal lattice: 1 indicates the recrystallizing grain, 2–4 indicates different parts of the recovered structure.

Five overall types of simulation-cells (simulation geometries) have been created; A, B, C, D and E. Type A has edge dislocations in dislocation boundaries perpendicular to the grain boundaries, type B has edge dislocations in dislocation boundaries inclined to the grain boundaries, type C has edge dislocations in two types of dislocation boundaries (one with higher misorientation that the other), type D has screw dislocations in dislocation boundaries perpendicular to the grain boundary and type E has mixed dislocations in dislocation boundaries inclined to the grain boundaries. Fig.4.3 shows these geometries in schematic form. Variations within each type of simulation-cell can be made, such as size of the simulation-cell, magnitude of the dislocation- and grain boundary misorientations, number of dislocation boundaries and so forth. The important point when setting up a geometry to simulate recrystallization is that both grain boundaries and dislocation boundaries exist in the simulation-cell.

The mixed dislocation-geometry is of course somewhere in-between the edge- and the screw-geometry. This can be seen from fig.4.3: The inclination of the dislocation boundaries differentiates the mixed- from the screw- and edge-geometry. The dislocation boundaries in the mixed-

geometry is inclined 30 deg. compared to the dislocation boundaries in the screw-geometry (and therefore 60 deg. to the dislocation boundaries in the edge-geometry). It can therefore be expected that the dislocations in the mixed-geometry have more of a screw- than an edge-character.

Normally the simulation-cells will consist of two dislocation boundaries, but simulations with four boundaries have also been performed. The misorientations across the two dislocation boundaries are always opposite. This corresponds to the situation described in section 1.3, i.e. elongated dislocation boundaries with alternating misorientations. The opposite misorientations produce dislocation boundaries that develop dislocations with opposite Burger's vectors.

The simulation-cells are created with high dislocation densities in order to increase the simulation speed. The dislocation density can be changed by either changing the distance between the dislocation boundaries or changing the misorientation across dislocation boundaries (higher misorientation produce more dislocations according to eq.1.3.1 page 6).

4.3.2 Relaxation

At the interfaces between the crystal blocks atoms may overlap. If two atoms are closer than a certain cut-off distance, one of them is removed. This is done in order to avoid excess atoms which will create an increased energy and atom density at the boundary. The excess energy and density may be hard to handle in the simulations; excess energy may lead to local melting and excess densities to high pressures in certain areas of the simulation-cell.

Even though the overlapping atoms are removed the atomic configurations near the interfaces are energetically very unfavorable because the structure changes abruptly from one fcc crystal lattice to another when crossing the interface. A relaxation scheme is performed to improve the atomic configurations and to reduce the energy at the interfaces before running the MD simulation. If the MD simulation is started without the relaxation local melting may still occur although overlapping atoms are removed. The relaxation is performed differently in the two simulation programs. In the CSM-program a MC simulation is performed and in the CAMd-program a special MD minimization is carried out.

In the CSM-program a constant pressure and temperature MC algorithm is used; this relaxes both atom positions and cell dimensions. The MC run is carried out at the same temperature as the MD simulation for the particular simulation. Simulation-cells are relaxed using approximately 50 atom movements and .5 cell movements per atom in the simulation. These settings are chosen because experience from this study has shown that local melting is avoided when these are used. By running the MC at the same temperature as the MD, the zero pressure conditions are obtained, at least at the onset of the MD simulation run.

The MD minimization in the CAMd-program can be considered as a 'high-friction' MD, where the atoms are not allowed to gain momen-

tum/kinetic energy and therefore local melting cannot occur. Pressure control is not carried out during relaxation because continuous pressure control according to eq.4.1.10 is applied during the actual MD simulation.

Each simulation is randomized during relaxation. In the CSM-program this happens naturally due to the MC-minimization but in the CAMd-program this is done by displacing each atom a random distance (less than .1Å) in a random direction. The randomization is strictly speaking not necessary due to the random force acting in the Langevin dynamics, but is performed regardless.

4.3.3 Annealing

The final step in the simulations is the annealing. This is the 'normal' MD procedure described in section 4.1. Besides the differences between the CSM- and the CAMd-programs regarding MD engines, temperature/pressure controls and potentials, described in sections 4.1 and 4.2, the onsets of the simulations are different. The relaxed simulation-cells in the CSM-program can be considered as being at the target simulation temperature due to the MC-approach while the simulation-cells in the CAMd-program is at zero temperature after relaxation. Therefore a controlled heating from zero temperature is performed in the CAMd-program (while the MD simulations in the CSM-program is initiated directly at the target temperature). The initiation of the temperature is done by assigning velocities to the atoms that correspond to the target temperature (eq.4.1.4).

4.3.4 Size Considerations

As explained in section 1.5.9 MD simulations with millions of atoms have been performed, however only for short times [79, 21]. Recrystallization is a thermally driven process, which takes a long time to simulate atomistically because every vibration of every atom is simulated in detail. Therefore a goal has been to setup simulations as small as possible while still containing stable migrating grain boundaries and dislocations. It turned out that a practical simulation size is around 100k atoms. The relatively small number of atoms can be used because the simulations can be reduced in size due to the high degree of symmetry: the A,B and C type simulations can be reduced in the z-direction and the D and E types can be reduced in the x-direction. The size of the simulation-cells may have an effect on the dynamics of the grain boundaries and the dislocations because periodic boundary conditions are used. The periodic boundaries forces a dislocation that exits one side of the simulation-cell to enter on the opposite side (examples of this can be seen op page 78). If the simulation is very thin, structures, such as dislocation or grain boundaries, may not move very freely because they are 'tied' by the periodic boundaries. Therefore, some large simulations have been carried out, which show no noticeable size effects.

The simulations were all run on the 240 node PC-cluster 'Mary' at Risø National Laboratory. Each node is an ordinary off the shelf PC with a 3GHz processor and 2GB RAM. One simulation was run on one node. Parallelization was not used because the size of the simulation-cells of around 100k atoms would require so much cross-communication that only small gains in computational speed would be achieved by doing so. One simulation would typically last for one to two months.

4.4 Data Analysis Schemes

Different schemes for extracting data from the MD simulations have been developed for this study: visualization schemes as well as numerical boundary and dislocation tracking. Two quantities are especially important for the data analysis: 1) the potential energy and 2) the local crystallographic configuration. It is straight forward to get the potential energies of atoms from MD simulations, but local crystallographic configurations are more tricky to extract. In this study the so-called common neighbor analysis (CNA) is used.

4.4.1 Common Neighbor Analysis (CNA)

CNA analyzes the local structure around atoms and can be used to identify for example fcc, hcp and other structures [25]. As the name indicates, the CNA focuses on neighboring atoms. Neighboring atoms are said to form a *bond* if they are nearest neighbors. One pair of neighboring atoms is assigned three indices jkl. j is the number of common nearest neighbors between the atoms of the pair, i.e. atoms that both 'parent' atoms bond to. k is the number of bonds between the common neighbors. l is the number of bonds in the longest continuous chain formed by the k nearest neighbors. In fcc metals all pairs that any atoms can be a part of have $jkl = 421$. In hcp metals, half of the 12 pairs that one atom can participate in have the 421-configuration and the other half have the 422-configuration. By considering all pairs that an atom can form, fcc and hcp can be distinguished. Fcc and hcp can also be distinguished from other types of configurations. In the CAMd-program atoms are assigned the value 0 if they are in a fcc neighborhood, 1 if they are in a hcp neighborhood and 2 if none of the above. Atoms near stacking faults in fcc metals show up as hcp atoms in the CNA.

In order for CNA to work, the atom positions must be very close to their equilibrium positions (local energy minima). Therefore the equilibrium configurations must be identified. An easy way to identify these, is to average the atomic positions from several consecutive iterations in the MD integrator. Since most of the atomic movements are vibrations around the atoms' minimum energy configurations, averaging the positions from several iterations yields the minimum configurations.

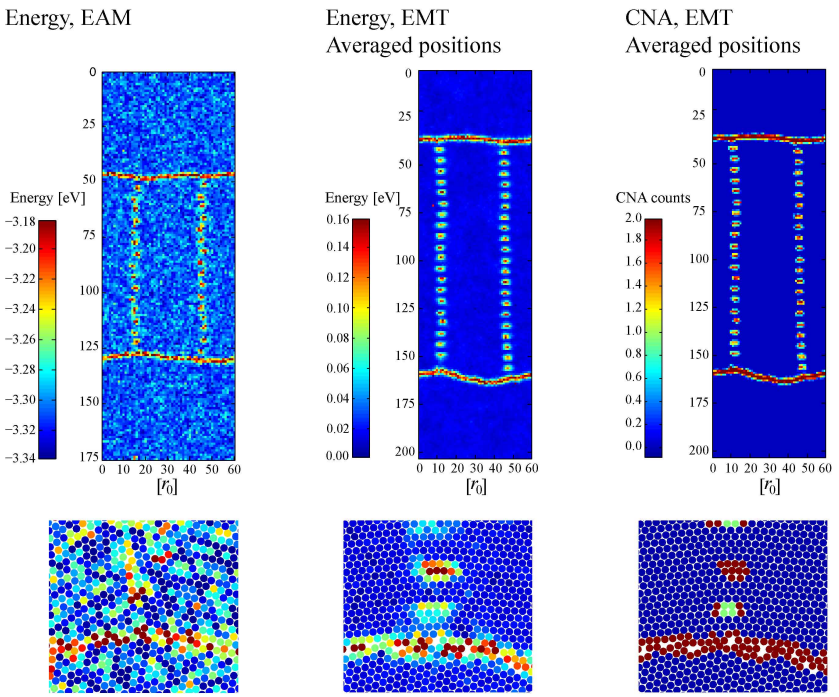

Figure 4.4 Examples of visualization schemes. The images are colored according to either the potential energy or CNA-counts. The top row of images show entire simulation-cells of the A type seen along the z-direction. The bottom row of images show single layers of atoms, also seen from the z-direction. The first simulation-cell depicted is from a simulation performed using the CSM-program and the last two from simulations using the CAMd-program. A clear difference is seen between the data from the CSM-program, where no averaging is performed, and the data from the CAMd-program, where averaging is done automatically. The effect of using CNA is clearly seen at the atomistic level. For further explanations see section 4.4.2.

CNA is an integral part of the CAMd-program and the averaged positions of the most recent iterations are updated and saved throughout the simulation process. CNA can be used in connection with in the CSM-program if the output-positions are either relaxed by some method or if the atom-positions from several outputs are averaged.

4.4.2 Visualization

Visualization based on potential energy or CNA is used to get qualitative results regarding boundary and dislocation configurations as well as atomic configurations. Fig.4.4 shows some of the visualization possibilities using potential energy and CNA. Three examples are considered: 1) energy analysis, 2) energy analysis, where the energy is calculated on the basis of averaged positions, 3) CNA-analysis. The upper row of images show entire simulation-cells of the A-type seen from the z-direction (the simulation-cells of the D and E types are better viewed from the x direction). The lower row of images show atomistic close-ups of single layer of atoms. The images of the entire cells are generated by dividing the simulation volume into small rectangular boxes of size $r_0 \times r_0 \times l_z$ where l_z is the height of the simulation-cell (for the simulation-cells of the D and E types boxes of size $l_z \times r_0 \times r_0$ are used). The analyzed property of all atoms (potential energy or CNA-value) within each box is averaged. The boxes are colored according to the averaged value. This boxing can also be perceived as a way of projecting the analyzed property onto the x-y-plane. In the atomistic images the atoms are just colored according to the analyzed property. In both overall and atomistic images, grain boundaries show up as massive high intensity areas of some width while dislocations show up as individual peaks of high intensity.

For the energy-analysis, especially the one without position-averaging, the projection procedure improves the visibility of grain boundaries and dislocations. For the CNA-images projection does not make much difference because the atomic images by themselves are very clear. It can be seen that the position-averaging greatly improves the visibility of features. The thermal fluctuations are almost completely gone.

In the projected energy-image of the averaged positions certain boxes within otherwise very low energy areas have been assigned very high energies. This is due to the fact that some atoms might change place during the iteration-span of the averaging and therefore receive positions almost on top of each other. These errors are removed by applying the CNA-analysis.

4.4.3 Boundary Tracking

In order to extract quantitative measures related to the migration of the grain boundaries a way to extract grain boundary positions and velocities was needed. The simple geometries of the simulation-cells have made it possible to develop a technique to track the positions of the migrating grain boundaries over time. This section describes the technique.

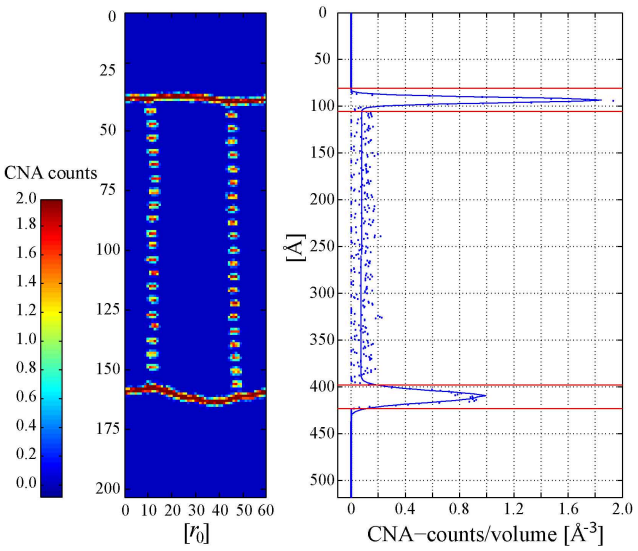

Figure 4.5 Examples of boundary tracking. Blue dots represent data points, the full blue lines the data fit obtained with eq.4.4.1 and the red lines indicate the widths of the boundaries.

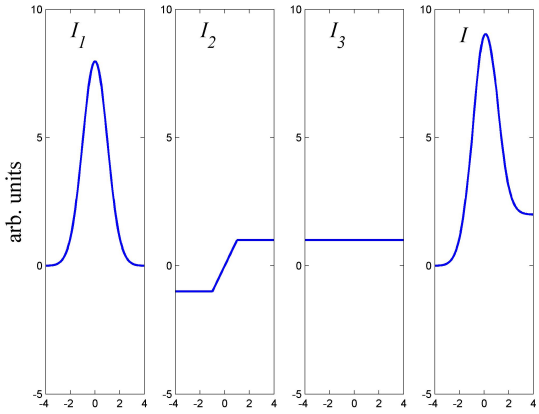

Figure 4.6 The fitting function eq.4.4.1. The different terms I_1, I_2 and I_3 as well as the combined function I are shown.

By projecting the analyzed property (energy or CNA-values) of a simulation-cell onto the y-axis, the grain boundaries clearly stand out as areas where the analyzed property has a high intensity. An example of this can be seen in fig.4.5. The intensity of the projected data is fitted by the function:

$$I(y) = \frac{A}{\sigma\sqrt{2\pi}} \exp\left(-\frac{(y-m)^2}{2\sigma^2}\right) + \frac{\Delta I}{2} \min\left(\left|\frac{y-m}{w/2}\right|, 1\right) \mathrm{sgn}(y-m) + I_0 \tag{4.4.1}$$

The first term $I_1 = \frac{A}{\sigma\sqrt{2\pi}} \exp\left(-\frac{(y-m)^2}{2\sigma^2}\right)$ is a Gaussian with mean value m, standard deviation σ and a total integrated area A. The gaussian is chosen because the intensity-peak associated with a grain boundary typically resembles this (see fig.4.5. The second term $I_2 = \frac{\Delta I}{2} \min\left(\left|\frac{y-m}{w/2}\right|, 1\right) \mathrm{sgn}(y-m)$ is a step-like function that has a constant value of $-\Delta I/2$ when $y < m - w/2$, changes linearly from $-\Delta I/2$ to $\Delta I/2$ when y goes from $m - w/2$ to $m + w/2$ and has a constant value of $\Delta I/2$ when $y > m + w/2$. This term is necessary because the overall intensity-level changes from the recrystallized part of the simulation-cell to the deformed part of the simulation-cell due to the presence of dislocations in the latter. The last term $I_3 = I_0$ is an offset level for the intensity. m is taken as the position of the boundary and w as the width. The individual terms of the fitting function as well as the combined function are shown in fig.4.6.

4.4.4 Driving pressure

In this study the driving pressure P for grain boundary migration is defined as the potential energy density difference between the recrystallizing part and the dislocation filled part of the simulation-cells. The *true* driving pressure is the free energy density difference but, as discussed in section 1.3.1 page 7, the potential energy difference and the free energy difference due to the presence of dislocations are almost identical numerically. P can be found by:

$$P = U_m/V_m - U_g/V_g \tag{4.4.2}$$

where U_m is the sum of the potential energy of all atoms in the matrix-part of the simulation, U_g is the equivalent in the grain-part and V_m and V_g are the volumes of the matrix- and grain-parts.

It is important that the grain boundaries are excluded from the driving pressure calculations. Therefore the matrix- and grain parts of the simulation are defined as:

$$\text{matrix} = \{m_1 + w_1 < y < m_2 - w_2\} \tag{4.4.3}$$

$$\text{grain} = \{y < m_1 - w_1\} \cup \{m_2 + w_2 < y\} \tag{4.4.4}$$

where m_1 and m_2 are the positions and w_1 and w_2 are the widths of the two boundaries. w_1 and w_2 obtained from eq.4.4.1 are often unrealistically small and a constant width are used instead. In fig.4.5 a constant width of 25Å is marked by the sets of red lines.

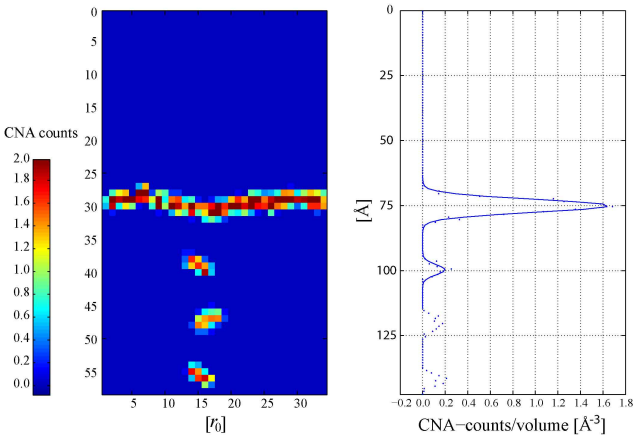

Figure 4.7 Identification of dislocation closest to the grain boundary. First the boundary is identified, then the dislocation. Both are fitted by Gaussians. The figure is reproduced from article H.

4.4.5 Dislocation Tracking

Dislocation tracking can be done in a way similar to the boundary tracking by dividing the simulation-cell into four equally large sections and make projections as illustrated in fig.4.7. The boundary and dislocations are found by fitting Gaussians to the peaks. The reason why Gaussians are used instead of eq.4.4.1 is that dislocation tracking is only performed for one dislocation boundary analyzed by CNA at a time. It is not necessary to define an overall change of intensity from one side of the boundary to the other because every dislocation can be identified separately (and do not contribute to the overall intensity level). An offset is not needed either because the CNA assign zero-values to all atoms in a local fcc-lattice.

The procedure for identifying dislocations is as follows: First the boundary is identified by one Gaussian fit. Then the top-points of the dislocations are identified by making a so-called cubic spline interpolation of the projected data. Finally the dislocations are fitted by separate Gaussian fits where the initial parameters (the initial guesses) are given by the top points. The procedure has only been used to find the dislocation nearest to the boundary, but can in principle be extended to cover all dislocations. This tracking only works as long as the dislocations show up as separate intensity-peaks in the analyzed properties. As shown in section 5.1 only the simulation-cells with edge dislocations (type A–C) have this.

Program	CSM	CAMd
Potential	EAM-Al / LJ	EMT-Cu
Relaxation	MC	MD-minimization
Engine	velocity Verlet	Langevin
Temperature control	Nose-Hoover	Langevin
Pressure control	NA	cell size ajustments
Position averaging	post-processing	built-in
CNA	post-processing	built-in
Speed* (iterations)	$\approx$ 10k it/day (EAM) $\approx$ 50k it/day (LJ)	$\approx$ 70k it/day
Speed* (sim. time)	$\approx$ 0.05 ps/day (EAM) $\approx$ 0.2 ps/day (LJ)	$\approx$ .3ps/day

*the number of iterations per day / simulation time per day apply to a simulation consisting of 100k atoms on a PC with a 3GHz processor and 2GB RAM.

Table 4.1 Comparison between the two simulation programs used, the CSM- and the CAMd-program.

4.5 Comparison Between Simulation Programs

Most of the differences between the CSM- and the CAMd programs have been explained in the sections above. In table 4.1 the main differences are listed. The LJ-potential is simpler than both the EAM- and the EMT-potentials and should therefore be much more efficient computationally. This is indeed the case, which can be seen by comparing the computational speed of the EAM-Al and the LJ potentials. The efficiency, however, also depends strongly on the implementation of the programs, and the EMT-potential is very efficiently implemented in the CAMd-program. Therefore the EMT-Cu potential within the CAMd-program offers the highest computational speed of the three potentials. The CAMd-program also has more features than the CSM-program and most of the simulations performed during this study have therefore been made using this.

4.6 General Discussions

In principle, the structure used here is the same as the triple-junction structure studied by Upmanyu et al. [91] (A simulation-cell with two dislocation boundaries has four triple-junctions, on at each intersection-line between a grain boundary and a dislocation boundary). In the study by Upmanyu et al., however, the triple junctions consisted of three grain boundaries. In the simulations performed during this project, the triple junctions consist of two grain boundaries and one dislocation boundary with identifiable dislocations.

The methodology follows some standard steps for MD simulations of complicated structures: 1) setup, 2) relaxation and 3) simulation (in this case annealing). Steps 2) and 3) are more or less the same for most MD simulations; it is the first step, the setup, that differentiates one simulation from another. In this project the setup is performed by arranging 'building blocks' of fcc-material in the simulation-cell. This is also done in many other simulations, see for example [42, 87, 90, 91]. The novelty of the simulation method presented in this study is the way that interfaces between blocks with low misorientations can be used to form dislocations in a natural way. One of the early findings in the present study was that dislocation structures formed 'by them selves' during relaxation and annealing to accommodate the misorientations across the crystal blocks as reported in article D.

5 Results from Molecular Dynamics Simulations

The aim of performing MD simulations of boundary migration driven by dislocations is to investigate what goes on at the atomic level during the growth-stage of recrystallization as described in section 1.6 page 23. This may lead to new insights regarding the influence of dislocation structures in the deformed matrix on the boundary migration process. This chapter contains the results obtained with the MD simulations that have been preformed during this project. Throughout the chapter the results are discussed and interpreted when appropriate.

Since this is the first time such simulations have been performed, some emphasis will be put on describing the process from a qualitative point of view: In section 5.1 the dislocation structures resulting from the setup-procedure, described in chapter 4, are shown and in section 5.2 it is demonstrated that it is in fact the dislocation structures that are responsible for the boundary migration in these MD simulations. In section 5.3, the mechanism by which grain boundaries absorb dislocations is presented and section 5.4 contains a description of the overall boundary motion.

Sections 5.5 to 5.10 present results on boundary mobilities (section 5.5) and activation energies (section 5.8) and the effect that different dislocation structures have on these quantities. The effects of parameters, such as grain boundary misorientation (section 5.6), driving pressure (section 5.7) and misorientations of the dislocation boundaries (section 5.9) are discussed. A detailed study of how the grain boundary velocity is affected by a dislocation in the vicinity of the grain boundary is presented in section 5.10.

The articles D to H contain various results from the MD simulations using the three potentials described in section 4.2 page 60. During this chapter selected results from these articles are presented and compared. In appendix K, a complete list of all simulations performed is included.

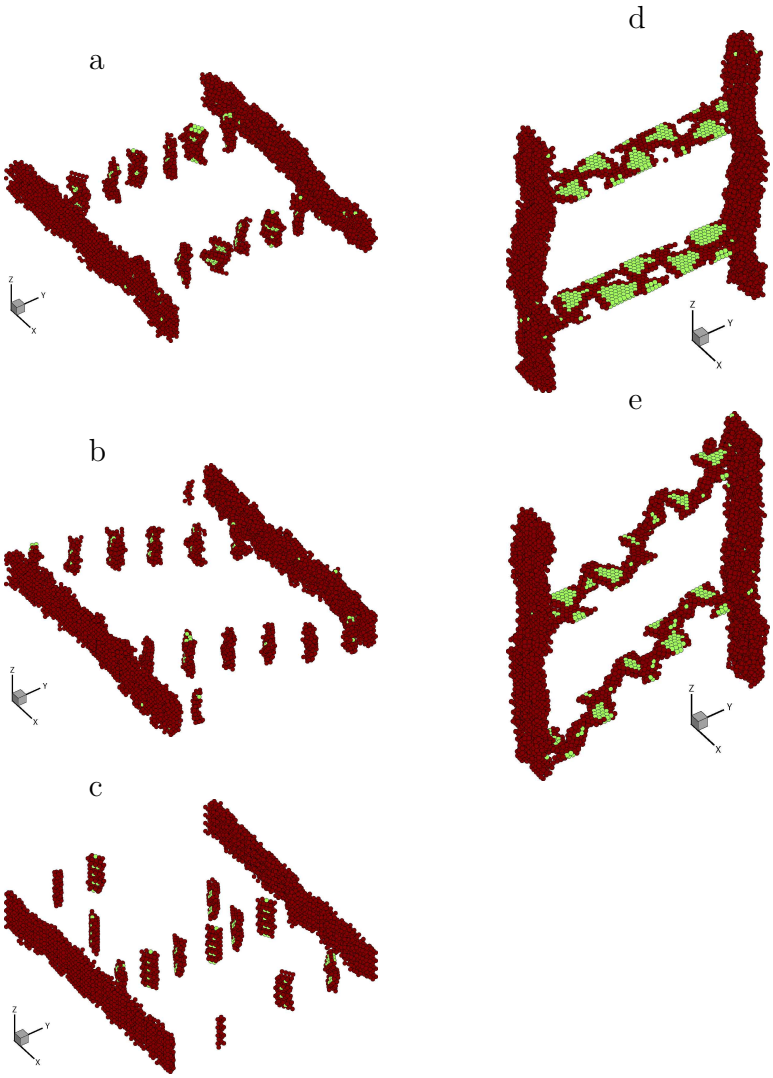

Figure 5.1 Skeletonized images of simulation-cells of different types simulated with the EMT-Cu potential. All atoms situated in a fcc lattice have been made invisible. Colors indicate the local crystal structure: green represents hcp structure, red represents structures different from both fcc and hcp. Grain boundaries and dislocation cores are red, stacking faults are green. (a) A-type: two edge-dislocation boundaries perpendicular to the grain boundaries. (b) B-type: two edge-dislocation boundaries inclined to the grain boundaries. (c) C-type: Three edge-dislocation boundaries with different misorientations perpendicular to the grain boundaries. The middle dislocation boundary has the highest misorientation and consists of six dislocations, the dislocation boundary at the (periodic) boundary of the simulation-cell has four dislocations and the last dislocation boundary has two. (d) D-type: A network of screw dislocations are seen in dislocation boundaries perpendicular to the grain boundaries. (e) E-type: a network of mixed dislocations are seen in dislocation boundaries inclined to the grain boundaries. In (d) and (e) clear stacking faults are seen in between the dislocations. (a) and (d) are reproduced from article H. Fig.4.3 page 66 show the five simulation geometries corresponding to (a–e).

5.1 Simulated Dislocation Structures

Depending on the type of simulation-cell (A-E), the dislocation structure varies as explained in section 4.3.1 page 63. Fig.5.1(a-e) show 'skeletonized' images of the various dislocation structures generated in the simulation-cells during simulations with the EMT-Cu potential. The cells are analyzed by CNA and all fcc atoms made invisible. Because CNA is only available within the CAMd-program, skeletonized images similar to fig.5.1 for the LJ- or EAM-Al potentials have not been made, but the structures simulated using these potentials are very similar to the structure shown in fig.5.1(a) (only A-type simulations have been performed using LJ- and EAM-Al potentials).

Simulation-cells of the A- to C-type are seen in fig.5.1(a-c). All of these contain dislocation boundaries that consist of edge dislocations parallel to the z-direction. It is possible to determine the Burger's vectors and missing atomic half-planes associated with the dislocations as reported in article D. The dislocation spacing for the edge dislocations are well predicted by eq.1.3.1 page 6. Fig.5.1(d) contains screw-dislocation dislocation boundaries and fig.5.1(e) contains dislocation boundaries with mixed-type dislocations. The Burger's vectors and the dislocation spacing for the screw- and edge-dislocation boundaries have not been investigated.

Notice how the dislocations have been arranged in fig.5.1(c). This cell was created using the C-type geometry but the low-angle dislocation boundaries have become somewhat ill-defined. This is because the misorientation across them is only around 3 deg. to begin with and the dislocations spacing within them are therefore quite large (see eq.1.3.1). When the dislocations are widely spaced, the dislocation boundaries are not as stable as dislocation boundaries with higher angles, and the dislocations may thus move. This is what has happened in fig.5.1, where one dislocation has moved from it's original dislocation boundary to the neighboring one.

In simulation-cells of all types, the dislocations split into partial dislocations with stacking faults in between seen as atoms colored in green in fig.5.1. This is most clearly seen for the screw- and mixed-type cells (D- and E-types), where rather large sections of the dislocation boundaries contain stacking faults. There is also a noticeable structural difference between the simulation types A-C and D-E: Individual dislocations are present in A-C while continuous networks of dislocations are seen in D-E. It will be shown below that this difference has a large impact on the boundary migration.

The dislocation densities created in the simulation-cells are of the order of 10^{-3}Å^{-2} equivalent to 10^{17}m^{-2} (dislocation length per unit volume). This is some orders of magnitude higher than values typically seen in deformed metals experimentally [103]. The high dislocation densities are necessary in order to speed up simulations. High driving pressures are typically used in MD simulations of boundary migration driven by grain boundary curvature [89] or other volumetric driving pressures [42, 104].

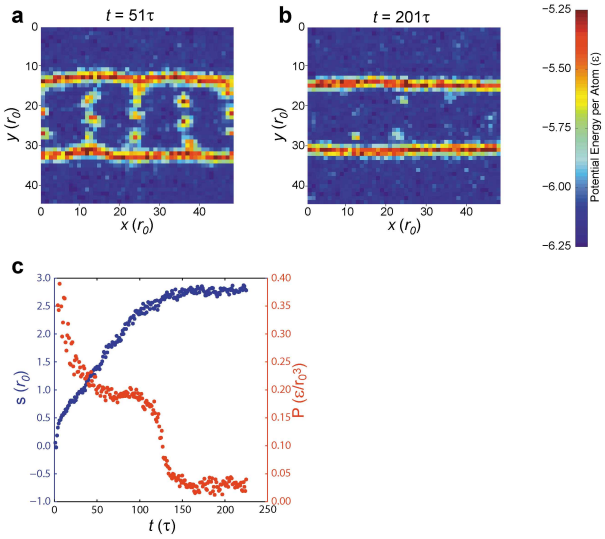

Figure 5.2 Snapshots of a four-boundary A-type LJ simulations at times (a) $t = 51\tau$ and (b) $t = 201\tau$. (c) the average distance travelled by the two boundaries s and the driving pressure P. As annihilations happen, the driving pressure drops and the grain boundaries are arrested. The simulation-cell was not completely relaxed when annealing was started, which resulted in the initial decline in driving pressure. The size of the simulation-cell is $47.6 \times 44.5 \times 7.3 r_0$. The figure is reproduced from article E.

5.2 Dislocations as a Driving Pressure for Boundary Migration

In article E it is shown that dislocation structures are able to drive grain boundaries. Fig.5.2(a) and (b) show two snapshots of a simulation produced by the method described in section 4.4.2 page 71. (c) shows the 'growth plot' for the simulations. The red data points show the driving pressure P defined in eq.4.4.2 page 73 and the blue data points the average distance travelled by the two grain boundaries s.

The simulation is of the A-type using the LJ-potential, but having four dislocation boundaries instead of the normal two. By having four dislocation boundaries, the dislocation boundaries will be closer to each other and the dislocations in neighboring boundaries will apply forces upon each other. Because the Burger's vectors of the dislocations in the two dislocation boundaries are opposite, as described in section 4.3.1 page 63, the dislocations will attract each other. What happens from fig.5.2(a) to (b) is that the dislocations in the dislocation boundaries have moved due to mutual attractions and annihilated. The annihilations remove the dislocations and therefore the driving pressure. This can be seen from fig.5.2(c) where a steep drop in driving pressure is seen at

the time $t = 125\tau$, which is in between the times of the two snapshots in (a) and (b). The growth curve s is monotonically increasing until the annihilations after which it stops completely. This proves that it is the dislocations that are the origin of the boundary migration in this simulation.

The size of the simulation-cell in this example is $47.6 \times 44.5 \times 31.8 r_0$, which is thicker than the normally used simulation-cells. The dislocation annihilations may be a size effect because the dislocations are less constrained in a thick cell. Therefore a thin ($l_z = 7.35 r_0$) version of the simulation has also been simulated. Both simulations exhibited dislocation annihilations and a resulting arrestment of boundary migration.

Dislocation annihilations have been observed in A-type simulations using other potentials as well. Annihilations are observed to happen if the dislocation boundaries are close to each other or if the dislocation boundaries have very low misorientation-angles. Generally, when the dislocations are removed, either by dislocation annihilations or because the boundaries have absorbed them (see section 5.3), the boundary movement stops. This show that it is possible to study boundary migration driven by dislocation structures alone, without any externally imposed driving pressure such as elastic strain[104] or modifications of the interatomic potentials [42].

5.3 Dislocation-Boundary Interactions: Absorbtion Events

Dislocation absorbtion of individual dislocations into the grain boundaries are observed in the simulations employing edge dislocations. No general difference has been observed between simulations of the A-, B- and C-type, and in the following only examples from A-type simulations are shown. The absorption events have been discussed in article E and comparisons between LJ- and EAM-Al potentials are made in article G. In this section results obtained with the EMT-Cu potential, also presented in article H are included for completeness.

Two 'extreme' absorption events are seen in the simulations; these have been named α and β absorptions. An α-type events for the LJ-potential is shown in the first row of fig.5.3. This event can be divided into three stages. In the first stage the grain boundary moves steadily towards the dislocation whilst being almost flat. The second stage happens during a much shorter time-span, in which the grain boundary 'shoots out' in a cusp absorbing the dislocation completely. The cusp represents a large local curvature of the grain boundary associated with increased grain boundary area and energy compared to a flat boundary. In the third stage the system reduces the boundary area by flattening the boundary. This has the effect that the boundary, which is not part of the cusp, is pulled forward. It is noteworthy that the dislocation remains completely fixed while the grain boundary moves towards it and that the shoot-out of the boundary happens in a very localized area near the dislocation.

Within this area the grain boundary moves several interatomic distances while the main portion of the boundary does not move.

In the β-type absorption, seen in the second row of fig.5.3, the dislocation breaks loose from its original position and moves into the grain boundary in a way which does not produce any significant distortion or movement of the grain boundary. The β-type events often happen in LJ-simulations with four dislocation boundaries, i.e. simulations having high driving pressures, and are observed more frequently at high temperatures.

Most often a mixture of α- and β-type events is observed, i.e. the boundary cusps slightly out while the dislocation moves into it. This is for example very often seen in the simulations with the EAM-Al or the EMT-Cu potentials. Two examples of mixed events for the EAM-Al and EMT-Cu potentials are seen in the third and fourth column of fig.5.3.

The absorbtion events in the simulations show a tendency to be more α-type for dislocation boundaries with relatively high misorientations and more β-type for dislocation boundaries with relatively low misorientations. A β-event is characterized by the movement of the dislocation and not the grain boundary. The dislocation is kept in place by the forces acting upon it from the other dislocations in the dislocation boundary[103]. In order for the dislocation to move into the grain boundary it has to 'break loose' from its equilibrium position within the dislocation boundary. The forces acting on the dislocation become weaker as the distances to the neighboring dislocations in the dislocation boundary becomes longer[103]. In low angle dislocation boundaries, the equilibrium distance between dislocations is relatively large, which means that the forces acting on the dislocation being absorbed from the other dislocations are relatively small. Therefore the dislocation being absorbed can more easily move away and into the grain boundary.

The B-type simulations (inclined dislocation boundaries) exhibit dislocations with a strong tendency to move into the boundary, i.e. have a β-type absorption behavior. The dislocation spacing in an inclined dislocation boundary is the same as in the boundaries being perpendicular to the grain boundary, making the 'break away' equally hard in both cases. Edge dislocations, however, move more easily along the direction of their Burger's vectors (glide) than along the direction perpendicular to their Burger's vector (climb) [103]. Since the Burger's vectors of the dislocations in the dislocation boundaries perpendicular to the grain boundary are parallel to the grain boundary the dislocations have to climb in order to move into the grain boundary. This is not necessary for the dislocations in the inclined dislocation boundaries, which may make the movement into the grain boundary easier.

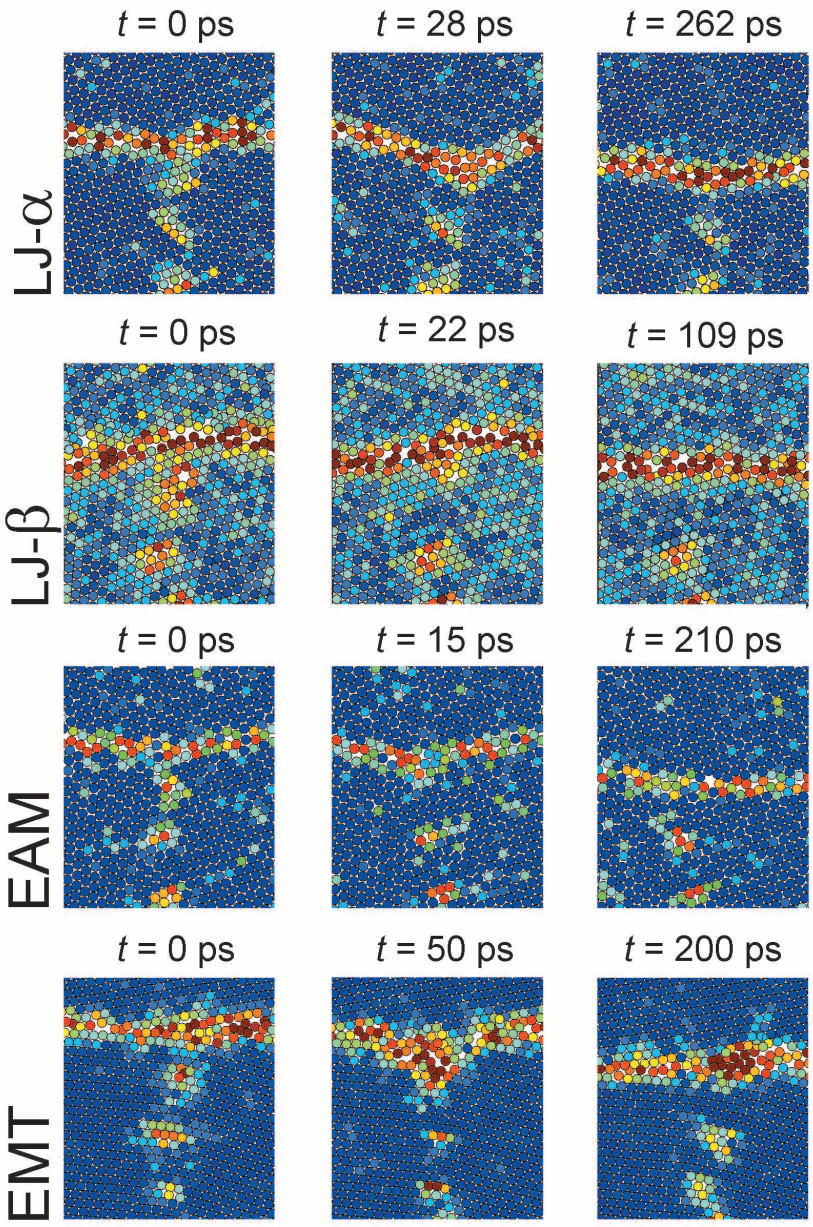

Figure 5.3 Sequences showing dislocation absorption events for edge dislocations in A-type simulation-cells. The columns of images show the situation before, during and after the absorption event. The first row show an α-event in a LJ-simulation, the second show a β-event in a LJ-simulation and the third and fourth show mixed-events in EAM-Al and EMT-Cu simulations. The atoms are colored according to their potential energy. All images have been produced after the atom-positions have been averaged over several snapshots: in the LJ- and EAM-Al images 10 snapshots have been used and in the EMT-images 50 snapshots have been used. The images for the LJ- and EAM-Al potentials are reproduced from article G.

During α-, β- or mixed-type events, edge dislocations are absorbed one at a time in events that happen during short time spans compared to the overall migration process. Most of the time the grain boundaries are not in direct contact with the dislocations but are driven forward slowly by their presence, i.e. by the elastic field that they are producing. Phenomenologically two regimes can be described; one in which the grain boundary is slowly pulled forward by the dislocations and one in which the grain boundary interacts strongly with a single dislocation and absorbs it. This is fundamentally different from for example triple junction migration, where the driving pressure is constant and the shape of the triple junction does not change[91].

Screw- and mixed-type simulation-cells (D- and E-types) do not exhibit absorption events of individual dislocations. This is because the dislocation structures in these cells, as seen in fig.5.1(d-e), are interconnected networks. The grain boundaries will always be in direct contact with the dislocations in the dislocation boundaries. The description with two growth-regimes discussed above does therefore not apply to the simulations of screw- or mixed-dislocation boundaries. Images (not shown here) similar to those shown in fig.5.3 show that the boundary shapes in simulations of the D- and E-types are constant and almost flat.

The mixed-type dislocations have some edge-character, but the behavior of the simulations with mixed dislocations resembles the simulations with screw dislocations very much. This indicates that the structure of the dislocations (individual vs. interconnected network) is probably more important than the type of the dislocation.

When a dislocation meets a grain boundary, it will in general not disappear but get trapped by or move through the grain boundary [36]. This is because a dislocation is associated with some rotation of the crystal lattice, which must be removed before the dislocation disappears. The dislocations do disappear in these simulations because the two grain boundaries in the simulations contain dislocations of opposite Burger's vectors. The rotations associated with the dislocations will therefore also be opposite and cancel out each other.

5.4 Growth

Growth plots like the one in fig.5.2(c) can be constructed for every type of simulation. In fig.5.4, examples of growth plots from the different simulation-types (A-E) are shown. The simulations in the examples are performed using the EMT-Cu potential but similar growth behaviors are seen in simulations performed using the LJ- or the EAM-Al potentials as reported in articles E and G. In the beginning of every EMT-Cu simulation, a transient stage in s occurs due to the slow heating of the system (see section 4.3.3 page 68). This can be observed in fig.5.4. After this, a steady growth stage with almost constant growth rate is seen for all simulations.

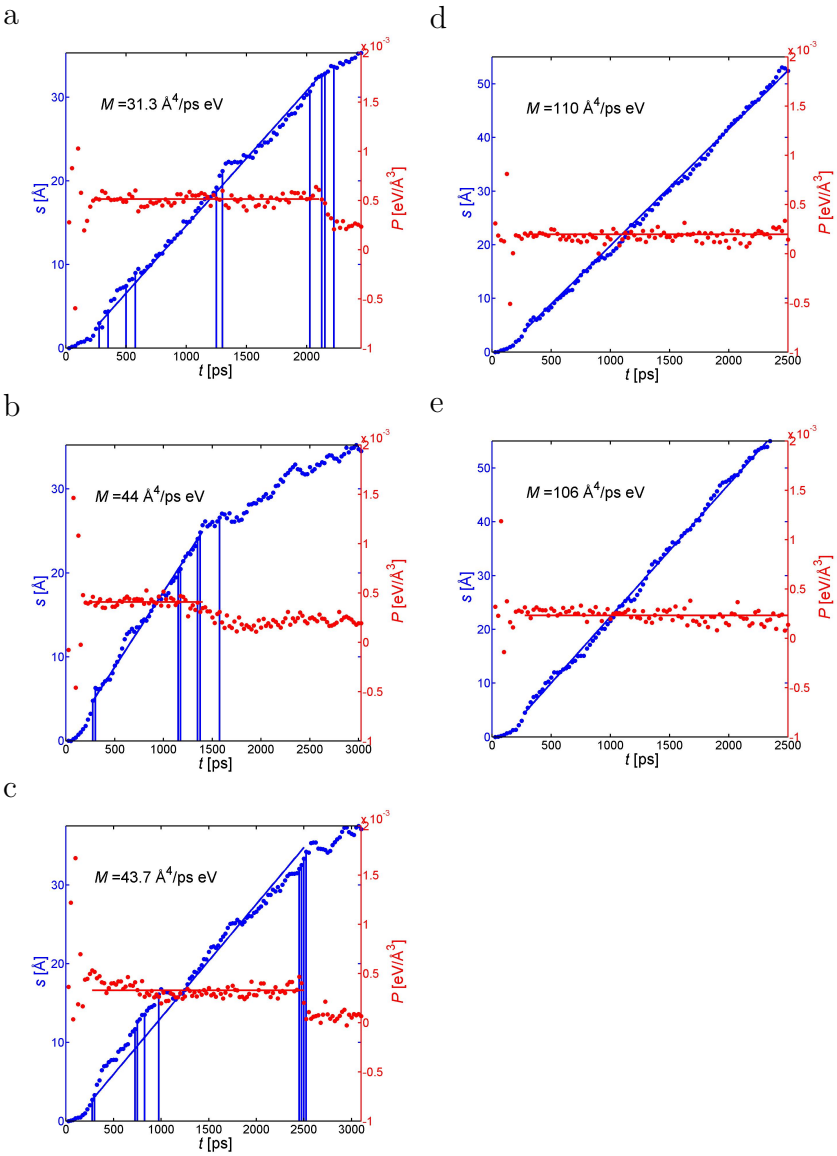

Figure 5.4 Growth plots from (a) A-type, (b) B-type, (c) C-type , (d) D-type and (e) E-type simulations using the EMT-Cu potential. The average distance travelled by the two grain boundaries s and the driving pressure P is plotted as a function of simulation time. In the beginning of any simulation, the growth curve exhibits a transient stage corresponding to the slow heating of the system. The full blue and red lines are fits to extract $< v >$ and $< p >$, see eq.5.5.1. The movement of the grain boundary is irregular in the edge-type cells (a-c). The vertical blue lines in (a) marks dislocation absorption events. The irregularities are less pronounced in the screw- and mixed-type simulations(d-e). (a) and (d) are reproduced from article H.

The growth curves for the edge-types of simulations exhibit irregular fluctuations in the grain boundary velocity. The fluctuations may be caused by local interactions between the migrating grain boundaries and the edge dislocations: The vertical lines in fig.5.4(a-c) indicate the times when a dislocation is absorbed by a grain boundary. There seem to be a close correlation between the fluctuations in s and the dislocation absorption events, i.e. s is increasing rapidly at times where dislocation absorbtion events happen. This is clearly seen in fig.5.4(a) at $t \approx 1300$ps. Not all irregularities are directly related to absorption events, though; see for example fig.5.4(b) at ≈ 700ps.

A cusp on a grain boundary, produced during an absorbtion event, will change the position of the parts of the boundary participating in the cusp. This does; however, not change the value of s significantly. If the part of the boundary that participates in the cusp is excluded in the analysis that determines s, s changes by .1 to .2Å, which is much less than the fluctuations observed in fig.5.4(a-c). This show that it is not the absorption events alone that are causing the fluctuations but the entire grain boundary that is moving faster during interactions with dislocations. This is a very crude way of determining effects of grain boundary-edge dislocation interactions. A more detailed analysis will be given in section 5.10.

The irregularities seem to be much smaller in the screw- and mixed-type simulations, although not completely gone. This is expected because individual interactions with dislocations do not happen in these. Interactions with single dislocations do not happen in these due to the continuous dislocation network.

In fig.5.4(a-c), the driving pressure drops suddenly at some point during the simulation. This indicates that the dislocation density at this time has gone down significantly. The drop in dislocation density happens because dislocations are absorbed by the grain boundary towards the end of the simulation where only few dislocations are left. The drops in P are associated with expected declines in the rate of change of s, i.e. the boundary velocity. For the screw- and mixed-types of simulations, the grain boundaries continue the steady motion all the way to the end of the simulation where the boundaries collapse.

5.5 Mobilities

Although the boundary velocity exhibit irregularities/fluctuations in most cases, the average velocity can be found as $< v >= \Delta s/\Delta t$, where Δs is the distance travelled by the boundary and Δt is the simulation time, both measured from the point where the simulation reaches the target temperature to the point where the driving pressure drops due to the removal of dislocations in the simulation-cell. The *apparent* mobility for each simulation is calculated as:

$$< M >=< v > / < P > \tag{5.5.1}$$

where $< P >$ is the average of the driving pressure calculated in the same time-range as $< v >$. The full blue and red lines, fitted to the data in

fig.5.4, are used to extract the values for $< v >$ and $< P >$. The driving pressure is typically in order of 5×10^{-4} eV/Å^3 in the simulations using the EAM-Al and EMT-Cu potentials, which corresponds to 8×10^7 Pa. This is larger than typical experimental values but in the range of what is seen in experiments; according to Ashby [12] and Smith[84], driving pressures for recrystallization are in the range 10^5 – 10^8 Pa.

The values of the mobilities $< M >$ extracted in these simulations are in the range .5Å^4/ps eV (3×10^{-10}m^4/J s) to 200Å^4/ps eV (1×10^{-7} m^4/J s) depending on the temperature, potential and type of dislocation structure. These values are orders of magnitude larger than typical experimental values, which are in the range 10^{-16} to 10^{-9} m^4/J s. [28, 37, 87, 96]. High mobilities are often seen in MD simulations [42, 81, 87, 108] and are typically associated with the lack of impurities [13, 52]. The impurity content can have a very large influence on the boundary migration rate, changing it by orders of magnitude [13]. Because the simulations here only have one species of atoms they are ultra pure and good quantitative agreement between the simulations and experimental values can not be expected.

The mobility M may not be the best quantity to measure when comparing different simulations due to the strong temperature dependence of M, see eq.1.4.15 page 12. Different potentials may also have different melting points, which makes comparisons difficult. In order to be able to make some quantitative comparison of different potentials after all, simulations near the melting points of the potentials are compared (the simulations in this study are typically performed near the melting point to increase the boundary mobility and thereby reduce the computational effort). In this way the high-temperature behavior is obtained, which gives the maximum grain boundary velocity obtainable. A comparison of A-type simulations with grain boundary misorientation $\theta_b \approx 40$deg. and dislocation boundary misorientation $\theta_d \approx 10$deg. performed with the LJ-, EAM-Al and EMT-Cu potentials is shown in table 5.1. The LJ-simulation is performed at $T = .6\epsilon/k_B$, the EAM-Al simulation at 900K and the EMT-Cu simulation at 1200K. The melting points for the three materials are $.7\epsilon/k_B$, 933K and 1358K.

The data for LJ-Al and LJ-Cu in table 5.1 represent the same simulations, but the numbers are converted to Al- and Cu-units using different conversion factors. The conversion factors used can be found in appendix K. It is clear that the driving pressure in the LJ simulations are hugely overestimated and the mobilities therefore hugely underestimated. It is essentially the value for ϵ (see section 4.2.1 page 60) that determines the energetics of the LJ-potential. If ϵ was chosen smaller, $< P >$ would be estimated more correctly, but then the activation energy would be clearly underestimated (sen section 5.8). Unfortunately, no value for ϵ exists that makes all properties fit simultaneously. This show that the LJ-potential quantitatively performs very poorly. Qualitative similarities between this and the more advanced EAM-Al and EMT-Cu potentials do exist, however, as shown in sections 5.3 and 5.4.

A-type	θ_b deg.	θ_d deg.	$< v >$ 10^{-3}Å/ps	$< P >$ 10^{-5}eV/Å^3	$< M >$ Å^4/ps eV
LJ-Al@.6ϵ/k_B	40.00	10.00	38	350	11
LJ-Cu@.6ϵ/k_B	40.00	10.00	24	540	4.5
EAM-Al@900K	40.00	10.00	110	58	190
EMT-Cu@1200K	40.99	9.85	36	68	53

Table 5.1 Comparison of simulations of the A-type with $\theta_b \approx 40$ and $\theta_d \approx 10$ using the different potentials. LJ-Al and LJ-Cu represent the same data, but numbers are converted to Al- and Cu-units respectively.

	θ_b deg.	θ_d deg.	$< v >$ 10^{-3}Å/ps	$< P >$ 10^{-5}eV/Å^3	$< M >$ Å^4/ps eV
A-type@1200K	24.79	6.01	14	46	30
B-type@1200K	24.79	6.01	14	35	40
C-type@1200K	24.79	6.01	19	41	46
D-type@1200K	24.79	6.01	22	19	118
E-type@1200K	24.79	6.01	25	24	108

Table 5.2 Comparison of simulations with different dislocation structures performed with the EMT-Cu potential. Data is averaged over four simulation runs.

The EAM-Al and the EMT-Cu potentials have quite similar driving pressures but the velocity (and therefore also the mobility for the boundary migration) in the EAM-Al simulation are almost four times larger than for the EMT-Cu simulation. Since both potentials are expected to produce quantitative reliable results, this show that the mobility for boundary migration during recrystallization is higher in Al than in Cu. Reliable experimental results are very sparse, but the available data seem to agree with the results found here: Trautt et al.[87] have compiled a comparison of boundary mobility-values, found both in experiments and in simulations (during grain growth as well as during recrystallization). The mobility-values for Al during recrystallization ranges from 10^{-12} to 10^{-8}m^4/J s. The mobility for Cu found by Vandermeer et al. is 6.3×10^{-16}m^4/J s [96]. One should note that the result from Vandermeer is obtained at a relatively low temperature; still the mobility is lower than any of the Al-mobilities reported in [87].

The mobilities of simulations having different dislocation structures are compared in table 5.2. All simulations are carried out with the EMT-Cu potential at 1200K. The simulations with the three edge structures exhibit similar driving pressures and mobilities. The screw- and mixed-type simulations show a very different behavior: They have higher velocities as well as lower driving pressures which makes the mobilities much higher than for the edge-types. This is a very noticeable result, which shows that the apparent mobility depends strongly on the dislocation structure. An explanation for this will be discussed in section 5.9.

The driving pressures in the edge-type simulations are higher than in the screw- and mixed-type simulations. This could be due to non-equilibrium edge dislocations: Normally dislocations in fcc crystals will have their Burger's vectors along a [110] direction. Because the edge dislocations are forced to have the Burger's vectors along the x-axis (due to the geometry used), this is not be possible in these simulations. In the screw- and mixed-dislocation networks, dislocations with minimum Burger's vectors are allowed to form. Therefore the screw or mixed dislocations will be more relaxed and contain less energy. No fundamental change of the results due to the unrelaxed edge dislocations are expected because the results indicate that the differences between edge- and screw/mixed-type simulations are probably due to the way the dislocations are arranged (as individual dislocations vs. in a dislocation network) rather than the properties of the dislocations themselves.

In the following the effects that several parameters have on the boundary migration are presented. Most of the simulations are carried out using the EMT-Cu potential and are also presented in article H.

5.6 Effects of Changed Grain Boundary Misorientation

The influence of the grain boundary misorientation and the grain boundary inclination on the mobility have been discussed extensively [19, 73, 90]. In this study, simulation-cells of the A-type with a range of grain boundary misorientations have been simulated while maintaining the dislocation boundary misorientation at 9.9deg. The simulations are performed at 1200K. In fig.5.5, the mobility $< M >$ is plotted versus the grain boundary misorientation θ_b. All mobilities measured are from ≈ 50 to $\approx 70 \text{Å}^4/\text{ps eV}$. No clear trend seems to be present; it appears that the data are scattered around a constant value.

This is in contrast to the grain boundary mobility seen in for example curvature driven grain boundary migration simulations [90], where certain boundaries are observed to have much higher mobilities than average. The special $\Sigma 7$ boundary created by a rotation of 38.2 deg. around an [111]-axis is for example known to have very high mobility. The reason why such high-mobility boundaries are not seen in the present simulations may be due to different effects: Firstly the peak in mobility around the $\Sigma 7$ grain boundary is very narrow [90], and none of the simulations performed have a perfect $\Sigma 7$ misorientation. Secondly the special character of any grain boundary is destroyed because the grain boundary meets two parts of the deformed matrix with different orientations. The grain boundary misorientation will therefore always be an average of the misorientations to the two matrix-parts. This is also the case in experiments where a migrating grain boundary during a recrystallization experiment will experience a host of misorientations due to the misorientation-spread in the deformed matrix, whereas a migrating grain boundary during grain growth will experience a very narrow range of misorientations. The concept of special boundaries may therefore not apply for recrystallization, except maybe for small boundary segments in a short time interval.

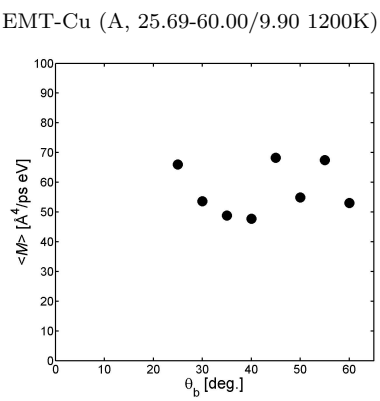

Figure 5.5 Dependence of mobility on grain boundary misorientation. The simulations are of the A-type with a dislocation boundary misorientation of 9.9deg. The mobility $< M >$ is plotted versus the grain boundary misorientation θ_b. No clear trend is seen. The figure is reproduced from article H.

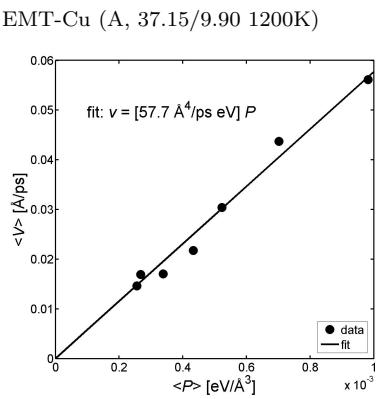

Figure 5.6 Variable driving pressure obtained by varying the dimensions of the simulation-cells. The figure shows the boundary velocity $< v >$ as a function of driving pressure $< P >$. A straight fitted line is seen indicating that eq.1.4.13 holds. The slope of the fitted line, which is 57.7Å^4/ps eV, can be seen as the average mobility of the simulations. The figure is reproduced from article H.

Experiments show that also during recrystallization, some grain boundaries have higher mobilities than average[19, 73]. Especially 40 deg. [111] boundaries were observed to have high mobilities. The reasons for the discrepancy between the present simulations and experiments could be many. The difference in migration rate between special and random boundaries is markedly increased when impurities are present in the metal[13]. Since no experiments are performed with completely pure metals, the grain boundary misorientation may have a strong effect on the migration rate. Surface effects may also play a role. The grain boundaries which showed high boundary migration rates for 40 deg. [111] misorientations in the experiments performed by Bech and Sperry[19] and Rath and Hu[73], were observed at surfaces of the samples but the effect that free surfaces have on the boundary migration rate is very hard to predict. Preferably three-dimensional experimental techniques should be used to obtain the true bulk migration rates. A third possible explanation for the discrepancy between experiments and the simulations presented here could be that many A-type simulations for some reason have mobilities close to each other at 1200K, where the simulation presented in fig.5.5 are also performed. This is discussed in more detail in section 5.8.

Grain boundary migration is often investigated disregarding the actual driving pressure, see for example the study by Gottstein and Shvindlerman [33] that relates the results obtained both to recrystallization and to grain growth, although the driving pressure for boundary migration stems from very different things: minimization of boundary area (grain growth) or the presence of deformation structures (recrystallization). The relatively weak effect of variations in grain boundary misorientation on the boundary migration seen in this study shows that there may be fundamental differences between boundary migration in recrystallization and in grain growth.

5.7 Effects of Changed Driving Pressure

The driving pressure is defined as the potential energy density difference between the deformed and the recrystallizing part of the simulation-cell (see eq.4.4.2 page 73). By changing the dimensions of the simulation-cell, maintaining the type of dislocation boundary, the excess energy density of the deformed part can be changed. If for example the box-length along the x-axis l_x is doubled in an edge-type simulation-cell, the total volume of the deformed part is doubled while the dislocation boundary area is kept at the same value(see figure 4.3). If the excess energy of a dislocation boundary is considered to be independent of the distance to the next dislocation boundary, this will reduce the driving pressure to half of the original value.

A-type simulations where l_x is changed from ≈ 100Å to ≈ 400Å while keeping the grain boundary at a misorientation of 37.2 deg. and the two tilt boundaries at 9.9 deg. have been performed with the EMT-Cu potential. This changes the driving pressure from $\approx 10^{-3} - .25 \times 10^{-3}$ eV/Å^{-3}. Fig.5.6 shows the boundary velocity $< v >$ as a function of driving pressure $< P >$. The data-points can be approximated by a straight line, which indicates that eq.1.4.13 page 11 holds in this case as expected. These results show that when the spacing, but not the structures, of the grain- and dislocation-boundaries are changed, the boundary dynamics follow the same behavior.

5.8 Activation Energies

The mobility is expected to have an Arrhenius temperature dependence as defined in eq.1.4.15 page 12. For most of the simulations performed, an Arrhenius behavior is indeed observed. The data from the simulations is presented in this section. The extracted values for the activation energies E_a are in the range from .20 eV to .65 eV. These are smaller than what is observed in experiments; typical experimental values are at least 1 eV [37, 96]. Low activation energies are expected for metals with low impurity contents [93], which means that the reason why the activation energies in the present study are lower than experimental values is probably the same as the reason why the mobilities are higher than the experimental values, namely the lack of impurities in the simulations.

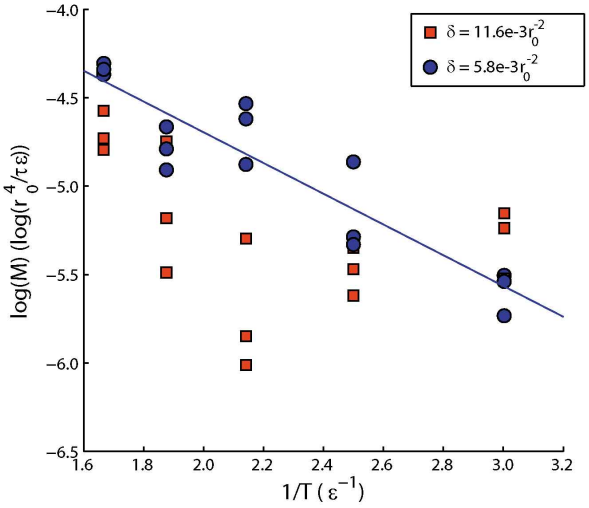

Figure 5.7 Arrhenius plot of mobilities of LJ-simulations with two dislocation boundaries and a dislocation density of $\delta = 5.8 \cdot 10^{-3} r_0^{-2}$ and LJ-simulations with four dislocation boundaries and a dislocation density of $\delta = 11.6 \cdot 10^{-3} r_0^{-2}$. Three data points representing three initially identical simulations are shown for each temperature and dislocation density δ. For the simulations with two dislocation boundaries the data follows a straight line as expected from eq.1.4.15; the slope gives $E_a = .87\epsilon/k_b$. For the simulations with four dislocation boundaries the data cannot be fitted to a straight line. This figure is reproduced from article E.

Simulations of the A-type with two and four dislocation boundaries and cell dimensions of size $60.7 \times 147.3 \times 7.3 r_0$ using the LJ-potential have been carried out and reported in article E. Three repetitions using identical, although differently randomized, simulation-cells were made. An Arrhenius plot of the results is seen in fig.5.7. Each data point represents one simulation.

The data from the simulations with two dislocation boundaries follows a straight line as expected, although with some scatter. For the simulations with four dislocation boundaries, such a fit cannot describe the data. This may be explained by the α- and β-type dislocation absorbtion events. In simulations with low dislocation density only α-type events occur, which is expected to give an Arrhenius behavior with a certain activation energy. However, with a higher dislocation density both α- and β-type events occurs, and each may be assumed to have their own activation energy, which would produce a deviation from the Arrhenius behavior. The high density simulations, where β-type events happen, typically have lower apparent mobilities than the low dislocation simulations as seen in fig.5.7. An explanation for this could be that β-type events remove the dislocations near the grain boundary, which removes the local driving pressure.

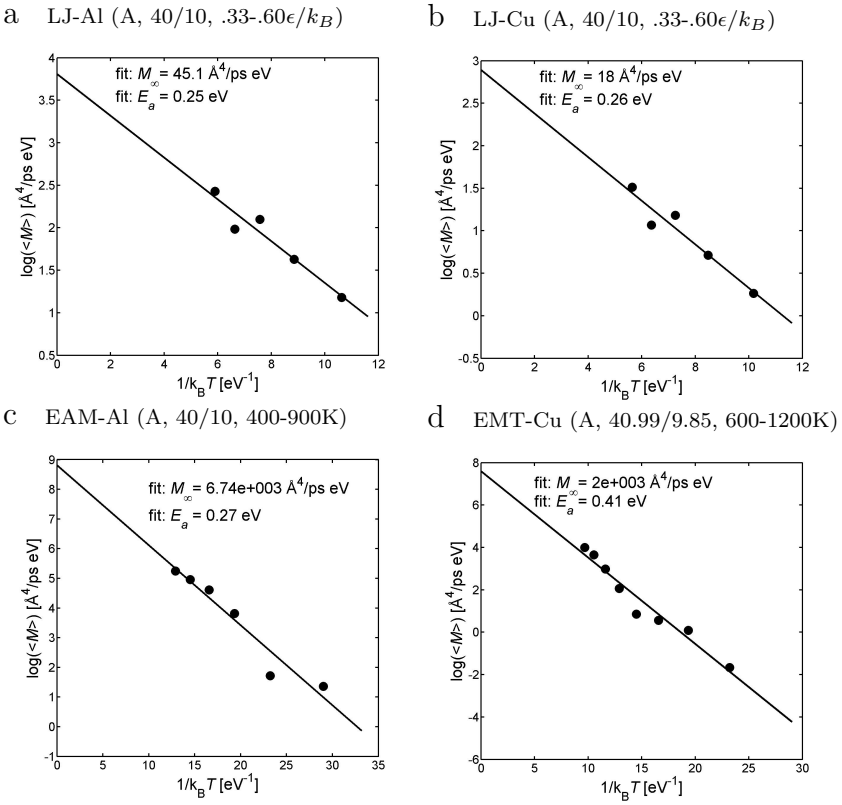

Figure 5.8 Arrhenius plot of A-type simulations with the same misorientations across the grain boundaries $\theta_b \approx 40$deg. and the dislocation boundaries $\theta_d \approx 10$deg. but simulated with different interatomic potentials: (a) LJ-potential converted to Al-units, (b) LJ-potential converted to Cu-units, (c) EAM-Al potential and (d) EMT-Cu potential. The data in (a) and (b) stem from the same simulations; only the unit-conversions are different. All simulations follow an Arrhenius behavior.

It is clear that scatter do exist in the data, especially for the simulations with four dislocation boundaries. The reason for the increased scatter in these simulations may be that the number of α- and β-events that happen during the simulations may vary. If the α- and β-events influence the boundary dynamics differently this may result in different boundary migration rates and mobilities for the different simulations.

Fig.5.8 shows a comparison of the activation-energy-data for the different potentials. The simulations are the same as in table 5.1, meaning that they all have the same grain-boundary and dislocation structure. Fig.5.8(a,b) show the same LJ-data but converted using (a) Al- and (b) Cu-units. The LJ-simulations produce straight lines in the Arrhenius plot with activation energies E_a that are similar to those for the EAM-Al and EMT-Cu potentials, but the infinite temperature values for the

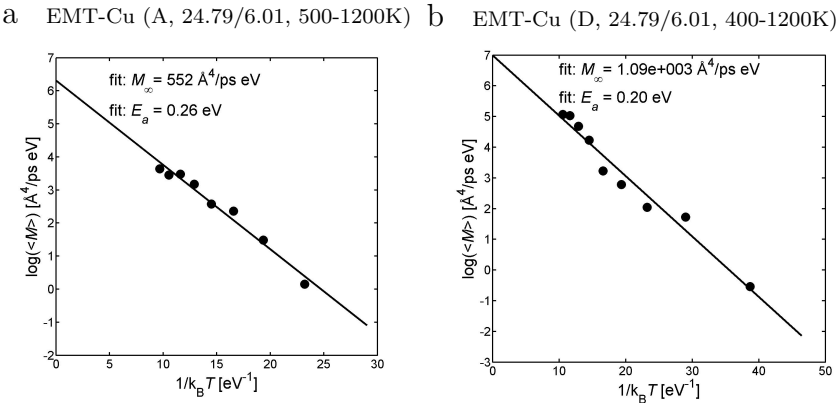

Figure 5.9 Arrhenius plots for (a) A-type and (b) D-type simulations with $\theta_b = 24.79$ and $\theta_d = 6.01$ simulated at temperatures up to 1200K. The A-type simulations have lower mobilities and higher activation energies compared to the D-type simulations. This figure is reproduced from article H.

mobility M_∞ deviates by several orders of magnitude. If the value of the LJ-energy parameter ϵ (see section 4.2.1) was decreased, M_∞ could be made similar to the results from the EAM-Al or EMT-Cu potentials, but E_a would then be reduced correspondingly. This shows, as with the results for the mobilities in table 5.1, that the LJ-potential do not produce quantitative reliable results, although the overall qualitative behavior is captured.

E_a is lower for the EAM-Al potential than for the EMT-Cu potential. Since the potentials are assumed to produce quantitative reliable results, this shows that the typical energy barrier that atoms have to cross in order for the grain boundary to migrate is lower for Al than for Cu. This corresponds well with experimental results [93]. M_∞ is higher for the EAM-Al than for the EMT-Cu simulations, which corresponds well with the higher mobilities seen in the EAM-Al than in the EMT-Cu simulations (section 5.5).

Fig.5.9 shows Arrhenius plots of A- and D-type simulations with the same grain boundary and dislocation boundary misorientations simulated at temperatures up to 1200K. Again straight lines are seen. The values for E_a for the two simulation-types are quite similar: $E_a = .26$ eV for the A-type and $E_a = .20$ eV for the D-type. M_∞ for the two types of simulation-cells differs by a factor of two. This shows that the change in dislocation structure do not have a large effect on the activation energy, although the dislocation structure influence the mobility greatly as shown in section 5.5.

The activation energy from the A-type simulations in fig.5.9(a) is different than the activation energy from the A-type simulations in fig.5.8(d) although the simulations are performed using the same potential (EMT-Cu). The difference between the simulations is the grain- and dislocation-

a EMT-Cu (A, 40.34/6.01, 700-1200K)

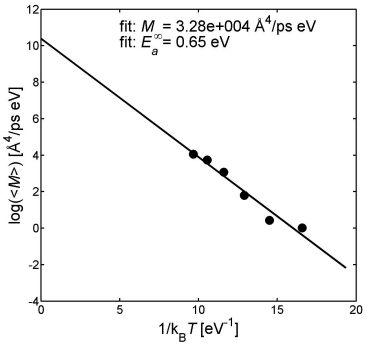

Figure 5.10 Arrhenius plots for A-type simulations with $\theta_b = 40.34$ and $\theta_d = 6.01$ simulated at 700-1200K.

boundary misorientations: The data in fig.5.9(a) is from simulations with grain- and dislocation-boundary misorientations of 24.79 and 6.01 deg. while the data in fig.5.8(d) is from simulations with misorientations of 40.99 and 9.85 deg. It is noticeable that $E_a[24.79/6.01]$ is much smaller than $E_a[40.99/9.85]$. This show that the activation energy may depend on the misorientations of the grain boundary and the dislocation boundary.

Fig.5.10 shows A-type simulations with misorientations of 40.34 and 6.01 deg. using the EMT-Cu potential. Here an even higher activation energy is seen than in both fig.5.8(d) and fig.5.9(a). This verifies that some grain boundaries may indeed have higher activation energies than other (compare fig.5.9(a) with fig.5.10) and the dislocation structure itself may influence the activation energy (compare fig.5.8 with fig.5.10).

It is interesting that all the A-type simulations using the EMT-Cu potential shown in fig.5.8(d), 5.9(a) and 5.10 have mobilities in the same range ($< M > \approx 50 \text{Å}^4/\text{ps eV}$) at 1200K, which is also in the same range as the mobilities seen in fig.5.5 at 1200K. This seemingly show that the low dependence of mobility on the grain boundary misorientation is due to the effect, that all grain boundaries have similar mobilities at high temperatures (1200k). If simulations with different misorientations across dislocation- and grain-boundaries have different activation energies, the mobilities at lower temperatures will be different. Typically experiments are performed at lower temperatures. In these simulations larger differences in the mobilities may therefore be seen at lower temperatures.

It is, however, *not correct* that all A-type simulations have the same high temperature mobility. This was the case for the simulations in fig.5.5, 5.8(d), 5.9(a) and 5.10, but the dislocation-boundary misorientation can have a great influence on the mobility, which will be clear from the next section.

5.9 Effects of Changed Misorientation of Dislocation Boundaries

A way to change the driving pressure, different from varying the simulation dimensions as done in section 5.7, is by changing the misorientation of the dislocation boundaries, which will change the dislocation boundary energy. Simulations where the misorientation of the dislocation boundaries are varied from 2.6 to 19.1 deg. in A-type simulation-cells and from 4.2 to 19.0 in D-type simulation-cells have been performed. Fig.5.11(a) and fig.5.11(b) show the dislocation boundary energy per unit area $< \gamma >$, defined as $< \gamma_A >=< P > \times(L_x/2)$ for the edge-simulations and $< \gamma_D >=< P > \times(L_z/2)$ for the screw-simulations. The full lines are fits to the Read-Shockley formula eq.1.3.4 page 7. Good agreements between the RS-formula and the simulated boundary energies are seen. Although the RS-formula is not expected to work for misorientations above 10 deg., it often fits data up to much higher misorientations quite well as discussed in section 1.3.1. The maximum for a RS-curve, fitted to data from a symmetric [111]-tilt boundary, is often seen to be around 40 deg. [65, 101], which is also reflected in the fit in fig.5.11(a): $\gamma_{\max} = \exp(A-1) = 40.0$deg.

In fig.5.11(c) and fig.5.11(d) the boundary velocity $< v >$ is plotted as a function of driving pressure $< P >$. According to eq.1.4.13 page 11 this should be a straight line. It is a straight line for the screw-type simulations, as shown by the linear fit in fig.5.11(d), but it is clearly not for the edge-type simulations. In fig.5.11(c), the data is fitted by $< v >\propto< P >^2$. That $< v >$ increases with $< P >^2$ is rather unexpected. This may be explained on the basis of local interactions between the grain boundary and the nearest dislocation as will be shown in section 5.10. The fits in fig.5.11(c-d) are forced to go through zero as it is assumed that the velocity is zero only when the driving pressure is zero. One could also assume that a minimum driving pressure was needed in order to make the boundaries move. This is not done here.

Fig.5.11(e) and (f), that show the mobility $< M >$ vs. $< P >$, reflect the behavior of $< v >$ vs. $< P >$ for the A- and D-type simulations. $< M >$ increases linearly with $< P >$ for the A-type simulations but are fairly constant for the D-type simulations (a slight increase in $< M >$ is seen as $< P >$ increases).

The difference in the grain boundary mobility between edge- and screw/mixed-type simulations seen here and in section 5.5 is very large. The different behavior is probably due to different interactions between migrating grain boundaries and dislocations. During an absorption-event in an edge-type simulation, the dislocation is removed. This will reduce the local driving pressure and therefore slow down the migration rate of the grain boundary. The actual driving pressure experienced by the grain boundaries may therefore not be represented well by the average driving pressure $< P >$. In the case of the screw or mixed dislocation simulations, the network of dislocations created ensures that it is not possible to remove the dislocations close to the grain boundary. Therefore the local driving pressure will be more or less constant throughout the simulation and will be well represented by $< P >$.

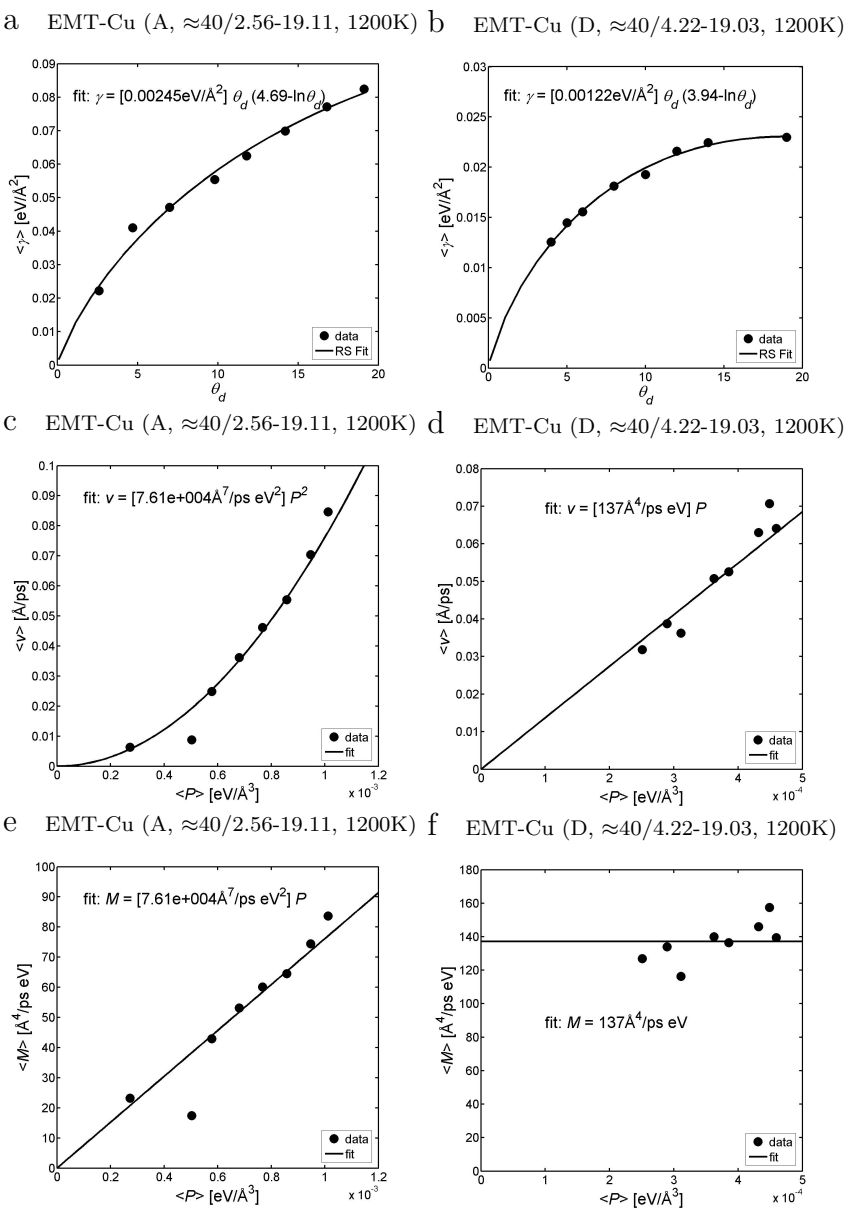

Figure 5.11 Effect of variations in misorientation across dislocation boundaries. (a) and (b) show the dislocation boundary energy per unit area $< \gamma >$ as a function of dislocation boundary misorientation θ_d for (a) A-type simulations with boundaries containing edge dislocations and (b) D-type simulations containing screw dislocations. The full lines are fits using the Read-Shockley formula eq.1.3.4. (c) and (d) show the boundary velocity $< v >$ as a function of driving pressure $< P >$ for simulations with (c) edge and (d) screw dislocations. The edge dislocation-simulations are fitted by $v \propto P^2$, whereas the screw dislocation-simulations are fitted by $v \propto P$. (e) and (f) show the mobility $< M >$ as a function of $< P >$ for (e) the edge simulations and (f) the screw simulations (f). A linear correlation is seen for the edge simulations and an almost constant mobility is seen for the screw simulations. This figure is reproduced from article H.

The mobilities for the A-type simulations approach that for the D-type simulations when the misorientations across the dislocation boundaries are increased. As the misorientation increases, the distance between the dislocations decrease. At very high misorientations, it becomes impossible to distinguish the dislocations from each other and the absorption process for the edge-type simulations is no longer a valid description: At high dislocation-boundary misorientations, the grain boundaries will always be in the process of absorbing a dislocation; no intermediate situations with grain boundaries approaching, but not 'touching', dislocations exist. This is similar to what goes on in the screw-type simulations.

5.10 Grain Boundary Velocity Dependence on Local Structure

The differences in the grain boundary mobility between edge- and screw-type simulations are very large. This indicates that the apparent grain boundary mobility not only depends on the grain boundary type but also the structure of the dislocations providing the driving pressure as discussed above. In the case of screw- or mixed-type simulations the local driving pressure is more or less constant, but in edge-type simulations the local driving pressure depends on the positions of the edge dislocations.

The distance from the grain boundary to the nearest edge dislocation d can be measured by identifying the position of the grain boundary and the position of the dislocation by the method shown in fig.4.7. The instantaneous velocity v of the boundary adjacent to the dislocation versus d in edge simulations is plotted in fig.5.12. We see that v increases as d decreases. The plot is generated by analyzing and averaging ≈ 300 absorption events. This is necessary because the uncertainty associated with the instantaneous grain boundary velocity is very large. All of the the analyzed events stem from the same A-type simulation geometry using grain boundaries with misorientations of 24.79 deg. and dislocation boundaries with 6.01 deg. Although fig.5.12 shows the correlation between v and d for one specific type of simulation only, the general shape of the curve is expected to be the same for grain boundaries and edge dislocation boundaries with other misorientations as well. The overall velocity is expected to depend on the driving pressure, i.e. a higher $< P >$ must give a higher velocity at all values of d. The increase of v associated with low values of d, on the other hand, could be seen as the effect of the nearest dislocation, i.e. the local presence of dislocations. Interestingly this effect is quite significant: v increases more than a factor of two when the distance from the grain boundary center to the dislocation core changes from 30Å to 10Å (at $d = 10$Å the dislocation is on the verge of being absorbed by the grain boundary). This means that grain boundaries will move much faster when an edge dislocation is close to the boundary than when the dislocation is further from the boundary.

EMT-Cu (A,≈24.79/6.01, 1200K)

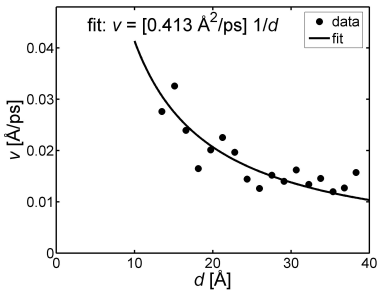

Figure 5.12 Instantaneous local boundary velocity v versus distance to nearest dislocation d. The full is a fit using eq.5.10.2.

The following suggests how the behavior of the edge-type simulations seen in fig.5.11 may be seen as a result of local interactions. Assuming that the contribution to the grain boundary velocity can be divided into a background contribution B depending on $< P >$ and a contribution L from the local presence of dislocations:

$$v = BL \tag{5.10.1}$$

If it is assumed that the local contribution is inversely proportional to the distance between the grain boundary and the nearest dislocation d, the following expression for the velocity applies:

$$v \propto \frac{B}{d} \tag{5.10.2}$$

The data in fig.5.12 have been fitted by this equation. The fit is quite good, although some deviations are seen for high values of d. If it is further assumed that B is proportional to $< P >$:

$$v \propto \frac{< P >}{d} \tag{5.10.3}$$

The dislocation spends little time close to the grain boundary because the boundary moves rapidly. Also the grain boundary may cusp out or the dislocation may move into the boundary. Most of the time the dislocation will be at a distance that corresponds to the the spacing between the dislocations D in the dislocation boundary. For low-angle tilt boundaries $D \approx b/\theta_d$ (see eq.1.3.1). If we assume that $< \gamma >$ roughly depends linearly on θ_d in the range of misorientations simulated:

$$< P > \propto < \gamma > \propto \theta_d \propto 1/D \tag{5.10.4}$$

By combining eq.5.10.3 and 5.10.4 and assuming that $< d >$ will be close to D, we obtain:

$$< v > \propto < P >^2 \tag{5.10.5}$$

which is what we have seen for the edge dislocation simulations.

The simple calculation above shows how local interactions may play an important role in the determination of the boundary migration rate. The calculation assumes that the dislocation spacing plays a significant role for the grain boundary migration rate because it assumes that the average distance to the nearest dislocation $< d >$ is equal to the dislocation spacing D. This is of course not exact, but it is certain that a smaller value of D will yield a smaller value for $< d >$.

Smith et al. discussed mechanisms for boundary migration [84]. They found that a grain boundary migrates with a velocity that is proportional to the square of the driving pressure when a so-called step mechanism controls the migration. They also argued that this happens during recrystallization. Whether the step mechanism takes place in these simulations is outside the scope of the present paper, but the result of Smith et al. shows that boundary migration with $v \propto P^2$ may take place during recrystallization.

For the simulation with screw dislocations, some dislocation is always present at the boundary, and no local effect can be defined. The local driving pressure experienced by the grain boundaries is therefore the same as the overall driving pressure and the relationship $< v > \propto < M >$ is seen.

In figure 5.6, a linear correlation between $< v >$ and $< P >$ is seen for simulations where different driving pressures are created by different edge-dislocation densities. The appropriateness of a linear correlation between $< v >$ and $< P >$ in this case (and not $< v > \propto < P >^2$ as seen in the edge-dislocation simulations with varied dislocation boundary misorientations) can be argued as follows: The simulations in figure 5.6 all have the same dislocation boundary misorientation and therefore the same local contribution to the driving pressure L. Only the background B, which is assumed proportional to $< P >$, changes due to the changes in the simulation size. Therefore, if eq.5.10.1 holds, $< v > \propto B \propto < P >$.

5.11 General Discussions

Although very detailed information about interactions between grain boundaries and dislocations is obtained using the MD simulations, the simulation-cells are very much simplified compared to experimental situations, and the simulations can not be considered as a detailed study of any totally realistic experiment. In other words the simulations do not imitate any experiments directly. They do, however, capture essential features of boundary migration during recrystallization: migrating grain boundaries driven by dislocation structures. By changing various parameters it can be investigated which factors are expected to play the largest roles for boundary migration during recrystallization, and therefore what future experimental studies should aim for.

Quantitative measures, such as the mobility M or the activation energy E_a depend strongly on the applied potential. Especially the values of v and P obtained with the LJ potential are very far from the values obtained with the more realistic EAM-Al and EMT-Cu potentials. This study clearly shows that if numbers are important, the LJ potential is not usable.

The A-type simulations using LJ, EAM-Al and EMT-Cu potentials show qualitatively similar results, namely dislocations being absorbed by migrating grain boundaries and irregular growth. The EAM-Al and EMT-Cu potentials have a somewhat higher tendency to produce mixed-events that the LJ potential, but mixed events are also often seen in LJ simulations. The similarities indicate that the qualitative features of boundary migration driven by dislocations are determined much by crystallographic/structural effects rather than inter-atomic effects. The method developed should therefore be broadly applicable to other potentials as well.

The deformed microstructure plays an important role in boundary migration during recrystallization, as we have seen in these simulations, but it is somewhat unexpected that the type of dislocation structure influences the boundary mobility, because the mobility is a property typically associated with the migrating grain boundary alone. That the dislocation structures directly influence the mobility can have important effects on the recrystallization process as a whole. If certain deformation structures are formed along certain crystallographic directions and those microstructures are able to pull boundaries along more rapidly than other, this may lead to differences in the measured boundary mobilities. The structure of the dislocations, being organized as individual dislocations or in dislocation-networks, has a large impact on the apparent mobility in the simulations performed here. This could also be the case in experiments. If, for example, the two sets of dislocation boundaries seen in fig.1.5 page 6 have different dislocation structures, which influence the migrating grain boundaries differently, recrystallization along the one set of boundaries may be more rapid than along the other.

6 Conclusions

Recent experimental studies have shown that growth during recrystallization is a much more inhomogeneous process than previous thought. Present recrystallization models do not take growth-inhomogeneities into account because their origin and effects on recrystallization-kinetics and -microstructure are largely unknown. This thesis investigates growth-aspects of recrystallization in metals by the use of simulations. The aim is not to mimic any particular metal-sample, but to gain a fundamental understanding of how growth-inhomogeneities can occur and what their effects can be. Two simulation methods have been adopted for this: Geometric simulations and molecular dynamics simulations.

Geometric Simulations

The geometric simulations test what happens if certain assumptions concerning the nucleation- and growth parameters are made and should be considered the numerical solutions to problems like the Johnson-Mehl-Avrami-Kolmogorov (JMAK) model that are too complicated to solve analytically. Besides the kinetic data, the geometric simulations also provide microstructural information. A significant extension of an existing method for geometric simulations has been developed during this project. The main development compared to the existing method is the development of a refinement procedure that can recalculate certain volumes of the simulation-cell in which the original method produced wrong results. By using the new method, situations where grains have a variety of growth-properties can be simulated.

Various simulations of spherically growing grains with *distributions of growth rates* have been performed. By assuming that a grain-radius is given by $r = At^{1-\alpha}$, distributions of A and α have been simulated.

The kinetics are fundamentally unchanged by distributions in A: V_V and S_V have the same time-dependencies (apart from a constant factor) for all simulations with A-distributions and the data can be made to collapse onto a single master curve in the JMAK-plot. Distributions in α, on the other hand, change the kinetics significantly and produce upward-curved graphs in the JMAK-plot resulting in changing values over time of the JMAK-parameter p because grains with different growth rates will dominate the kinetics at different times. Understanding how growth rate distributions influence the JMAK-kinetics are very important from a practical point of view because experimental data are often interpreted using JMAK-analyses. The results show that growth rate distributions must be taken into account in such interpretations of experiments.

The microstructural paths (MP) for all simulations of either A- or α-distributions are identical. This means that MP-modelling can be used to predict the kinetics for any growth rates distribution.

Distributions in either A or α have a large impact on the microstructure of the fully recrystallized structure. This can be seen qualitatively in plane sections of the simulation-cells or quantitatively in distributions of $d/ < d >$, where d is a line scan grain-intercept length and $< d >$ is the mean intercept length. Some of the simulated growth rate distributions have grains with d-values more than six times the average (usually d is not above three times the average). Understanding the influence of growth rate distributions on the recrystallized grain size distributions is very important because the grain size distributions is essential for controlling material properties.

Random anisotropic growth, where the grains are shape-preserved and have preferred growth directions that are randomly oriented in space, have been simulated. Ellipsoids in three dimensions and ellipses in two dimensions with aspect ratios up to 16 have been studied and the kinetics data compared to models assuming aligned anisotropic growth corresponding to the assumptions of the JMAK model.

The kinetics are surprisingly not affected strongly by random anisotropy in three dimensions. V_V, S_V and R_V can be accurately predicted by models employing JMAK-assumptions up to an aspect ratio of four. Aspect ratios beyond four are rarely seen in recrystallization, which means that the JMAK model can be used for anisotropic growth during recrystallization.

When representing data using microstructural paths, aspect ratios up to eight can be predicted by the models. This shows that MP-modelling can be used to predict the kinetics for random anisotropic growth to a large extend just as it could be used to predict the kinetics for growth rate distributions.

The effects of random anisotropy in two dimensions are much stronger. The JMAK-like models can only predict the results from the simulations up to an aspect ratio of two for the kinetic data and up to an aspect ratio of four for the MP-representation of data. This show that two-dimensional model can not be extended to three dimensions just like that.

The ability for grains to grow around each other is crucial for the microstructure and the kinetics. This is the reason that the three-dimensional simulations performed here produce less deviations from 'normal' behavior than three-dimensional simulations performed previously by others. It is also the inability of grain in two-dimensional simulations to grow around each other that makes these simulations deviate more from 'normal' behavior than three-dimensional simulations.

Large changes in the microstructures in the fully recrystallized simulations are seen as an effect of anisotropic growth in both two and three dimensions, although more complicated structures are seen in three dimensions. The grain shapes after total recrystallization also exhibit com-

plicated shapes, which is a consequence of grains that have grown around each other. This shows that even though the kinetics may be predicted by JMAK- or MP-models, the microstructure and thereby the properties of a metal may vary strongly depending on the growth anisotropy.

Molecular Dynamics Simulations

A new method for performing MD simulations of boundary migration has been developed during this PhD project. The method differs from other methods in the way atoms are set up to produce grain- and dislocation-boundaries. Dislocations are formed 'naturally' during the simulations to accommodate the misorientations between the crystal-lattices that are introduced in the setup. The simulations performed show that the grain boundaries are migrating driven by the presence of dislocations and as the grain boundaries migrate, they absorb the dislocations. This is the fundamental process of recrystallization and the simulations presented in this thesis represent *the first MD simulations of recrystallization.*

The simulations have been performed using three different interatomic potentials: the Lennard-Jones (LJ) pair potential, an embedded atom method (EAM) Al potential and an effective medium theory (EMT) Cu potential. The LJ-potential produce quantitative results that deviate much from the two other, more realistic potentials and can not be used if reliable numbers are required. However, the three potentials give the same qualitative results, showing that the method is general applicable for the simulation of boundary migration during recrystallization.

Grain-boundary- and dislocation-properties can be varied by changing the details of the set-up. Dislocation boundaries with two different types of dislocation structures have been observed to form during the simulations: 1) edge dislocations arranged in tilt boundaries. The directions of the edge dislocations are parallel and the dislocations appear as individual entities that are not in direct contact with each other. 2) screw or mixed dislocations arranged in twist or mixed boundaries. The dislocations are arranged in interconnected dislocation networks where all dislocations are in direct contact with the neighboring dislocations.

The dislocation-type is not expected to play a major role in these simulations, but the different types of dislocations are arranged in different dislocation structures and the dislocation-structures have a major effect on the interactions between grain boundaries and dislocations, the growth-curves of the grain boundaries and their mobility.

The migrating grain boundaries absorb the edge dislocations one at a time in what has been termed absorbtion events. Different absorbtion events have been observed: α-type events, where the grain boundary cusps out and 'eats' the dislocation, β-type events, where the dislocation moves into the boundary without any distortion of the grain boundary or mixed events where the grain boundary cusps out slightly while the dislocation moves into the grain boundary. Screw- and mixed-types dislocations are not absorbed individually because they are arranged as interconnected dislocation networks. The grain boundary migration is

significantly more irregular in the edge-type than in the screw/mixed-type simulations due to the presence of absorption events in the edge- but not in the screw/mixed-type simulations. This shows that the behavior of the grain boundaries depends very much on the local dislocation configurations that are pulling the boundaries.

The average boundary velocity $< v >$ increases linearly with the average driving pressure $< P >$ for simulation where $< P >$ is changed by varying the dislocation density while keeping the type of dislocation boundaries the same. $< v >$ also increases linearly with $< P >$ in simulations where $< P >$ is changed by varying the misorientation across screw-dislocation boundaries. These results are in accordance with the expectations. For simulations with edge type boundaries, where $< P >$ is changed by varying the misorientation across edge-dislocation boundaries, $< v >$ increases proportional to $< P >^2$, which is very unexpected. This correlation may be explained on the basis of local interactions as it is shown that the instantaneous grain boundary velocity in an edge-type simulation depends on the distance from the grain boundary to the nearest dislocation.

The apparent mobilities, calculated as $< M >=< v >/< P >$, are significantly higher in the screw/mixed-type simulations than in the edge-type simulations. This may also be related to the way that grain boundaries interact with dislocations. In screw/mixed-type simulations the grain boundaries are constantly in close contact with the dislocations and a constant local driving pressure for boundary migration is obtained. In the edge-type simulations the local driving pressure and instantaneous velocity varies over time due to the individual dislocation absorption events.

The grain boundary misorientation does not affect the mobility to any significant degree, probably because the grain boundary 'sees' different misorientations for different parts of the deformed matrix. This is in contrast to the common knowledge that the grain boundary mobility depends strongly on grain boundary misorientation, obtained from simulations of other types of boundary migration, such as grain growth. The results indicate that it may not be possible to study boundary migration without considering the underlying physical process.

Generally the MD simulations show that local growth inhomogeneities during recrystallization can occur at very small length scales due to differences in dislocation structures. Mesoscopic inhomogeneities observed experimentally may therefore ultimately be an effect of differences in the dislocation structures in the deformed matrix and the deformed matrix must be treated as inhomogeneous in recrystallization modelling.

Overall Conclusions

Overall, the geometric simulations show that the introduction of growth-inhomoge-neities into a simple recrystallization-model can affect the recrystallization kinetics and microstructure significantly, which makes it very important to understand the origin of inhomogeneities. The MD simulations show that the grain boundary migration during recrystallization is strongly affected by the dislocation structures providing the driving pressure due to differences in the local interactions between the migrating grain boundaries and the dislocation structures. Some types of dislocation structures may drive the migrating grain boundaries many times faster than other types and produce changes in the grain boundary morphology. The effects that the dislocation structures have must be taken into account in order to create realistic recrystallization models, and through that improve the processing and properties of metals.

7 Outlook

This chapter describes some of the questions that have arisen during the work of this PhD-project and ideas of how to proceed. Some comments are also included on how the methods developed here could be used for further studies.

The geometric simulations show that distributions in the growth parameters can have large impacts on the transformation kinetics and the microstructure, but experiments are needed to establish the extent to which such distributions are seen in experiments: Are the distributions present, able to make an impact on the microstructure and the recrystallization kinetics? Very few experiments that focus on growth irregularities have been carried out, probably because such experiments are very difficult to perform: the experimentalist must follow the growth of each grain individually during the process, preferably with a resolution on the microstructural level. The further development of powerful experimental techniques such as the 3DXRD-microscope and electron microscopy may make this possible in the near future.

The geometric simulations are closely related to analytical models to which they provide numerical solutions. One of the main challenges when developing analytical JMAK-type models is how to handle impingement of grain boundaries. In the original JMAK model[14, 15, 16, 43, 47], impingement happen in a certain way due to the random placement of nuclei. This was also the case in later models by Cahn[22] and Vandermeer[97], where nucleation was assumed to be random on randomly placed lines or planes. Two stages of impingement could therefore be treated: Impingement within the lines/planes and impingement between the lines/planes. For aligned anisotropic growth, the fundamental impingement relations are not changed as shown by Kolmogorov[47]. For random anisotropic growth, however, this is not the case. The reason is that the fast growing directions of the grains get impinged quicker than the slow directions. This reduces the transformation rate and lowers the Avrami parameter p. One way to formalize this problem of complicated impingement is the *impingement function* $\phi = \frac{\mathrm{d}V_V}{\mathrm{d}V_X}$[75]. ϕ will have values between zero and one depending on the severity of the impingement (0 is most severe). Rios et al. [75] have used the impingement function to investigate clustered nucleation. The impingement function could also be used in connection with random anisotropic growth and perhaps aid the efforts to model impingement analytically in this case.

A different way to use the geometric simulations could be in a more direct connection with experiments, for example 3DXRD-measurements[51]. Depending on how the 3DXRD-microscope is used, different levels of detail are obtained. There is always a trade-off between speed and accuracy. In some experiments, like the one performed by Lauridsen et al.[51], the volumes and grain-centers of recrystallizing grains are detected, but the microstructure is not. The geometric simulations could be used to reconstruct microstructures of the experiments by performing simulations, where the nuclei are placed according to the experimental results. This would of-course only give rough estimates of the real microstructures but it is a way to visualize the measured experimental data and could give information on impingement (which is not detected in the experiment).

The geometric algorithm developed is very versatile. It is the hope of the author that it will also be used by others to study geometric aspects of phase transformation-like processes.

Very detailed analyses of the atomic movements during grain boundary migration have been performed by MD simulations of stress-driven boundary migration by Zhang et al. [105, 106, 107]. Zhang et al. found among other things that atoms moving in string-like configurations, which resembles what have been seen in MD simulations of supercooled liquids [82], facilitate the grain boundary migration. Certain energy barriers have to be crossed before the string of atoms can move and the activation energy for boundary migration is therefore associated with these barriers. The simulation geometries used by Zhang et al. is very similar to the geometries used in this study and the analysis-apparatus used by Zhang could be applied to simulations such as the ones presented in this thesis. It would be very interesting to investigate if the atomic movements within the boundaries are altered by the interactions with dislocations or not; would for example the string-like motion be more or less pronounced if interactions with dislocations took place? Boundary migration is often discussed by disregarding the origin of the actual driving pressure, which could be curvature, stress or the presence of dislocations. Detailed analyses of atomic movements could establish whether or not this is a sound assumption.

The MD simulations carried out in this study show that the microstructure of the deformed matrix has a dominating effect on boundary migration during recrystallization, other than 'just' providing the driving pressure. Some structures may be able to pull the grain boundaries along quicker than others. This is something that may not be very surprising when taking into account the complicated deformation-structures driving recrystallization, but interactions between migrating grain boundaries and the deformation structures on a very fine-scaled level is something that has seldom been studied experimentally. Detailed characterizations of the microstructures in many metals and alloys have been made under static conditions, but capturing the actual interactions between migrating grain and dislocations is something that is very very hard.

Even though experimental studies of interactions between migrating grain boundaries and dislocation structures may be hard to carry out, they are necessary if the origin of the irregularities observed during recrystallization, such as those described in section 1.4.7, is to be found. One way to go ahead could be to try to correlate the detailed knowledge available regarding deformation microstructures with experiments of recrystallization: Are there for example fast growth directions in experiments and are these correlated with the microstructures in the deformed material? The advancement of x-ray techniques may also lead to new experimental possibilities which we have not seen yet.

The MD simulations presented in this study are the first of their kind and a selection of parameters has been studied. These parameters, however, only represent a tiny fraction of the huge parameter space that in principle can be studied with the method. More simulations would for example be needed to establish the influence of the grain boundary character (misorientation and inclination) on the activation energy. Detailed studies of the simulation-cells with mixed dislocations could also be performed to investigate the differences (if any) between these and simulations of screw simulations. Finally, larger simulation-cells with more complicated/realistic microstructures could be performed to test if the findings in the simplified simulation-geometries in this study are valid for more realistic systems. One idea could be to initially simulate the deformation of a polycrystal using MD and then use the structure obtained in an annealing simulation. Experimental data from for example transmission electron microscopy (TEM) investigations could also be used as input for simulations. If the deformation structures (either produced by MD or TEM) have certain preferred directions, MD-anneals with the structure oriented differently could establish if certain growth directions are indeed faster in more realistic scenarios.

This study show that the deformed matrix can not be treated as a continuum as done in most present recrystallization models. Future modelling work should focus on incorporating effects related to the deformation structures within the deformed matrix. It is at the present moment not fully understood why the growth inhomogeneities described in the introduction of this thesis occur. Further experimental and theoretical work is surely needed for this.

Bibliography

Authored Publications

[1] **Article A** P. R. Rios, R. B. Godiksen, S. Schmidt, D. Juul Jensen, and R. A. Vandermeer. Analytical expression for the evolution of interfacial area density between transformed grains during nucleation and growth transformations. *Scripta Materialia*, 54(8):1509–1513, Apr 2006.

[2] **Article B** R. B. Godiksen, S. Schmidt, and D. J. Jensen. Effects of distributions of growth rates on recrystallization kinetics and microstructure. *Scripta Materialia*, 57(4):345–348, Aug 2007.

[3] **Article C** R. B. N. Godiksen, P. R. Rios, R. A. Vandermeer, S. Schmidt, and D. Juul Jensen. Three-dimensional geometric simulations of anisotropic growth during transformation phenomena. Accepted for publication in *Scripta Materialia*, doi:10.1016/j.scriptamat.2007.10.003, Oct 2007.

[4] **Article D** R. B. Godiksen, Z. T. Trautt, M. Upmanyu, S. Schmidt, and D. Juul Jensen. Towards atomic level simulations of recrystallisation - setting up suitable geometry. *Materials Science and Technology*, 21(12):1373–1375, Dec 2005.

[5] **Article E** R. B. Godiksen, Z. T. Trautt, M. Upmanyu, J. Schiøtz, D. Juul Jensen, and S. Schmidt. Simulations of boundary migration during recrystallisation using molecular dynamics. *Acta Materialia*, 55:6383–6391, 2007.

[6] **Article F** R. B. Godiksen, S. Schmidt, and D. Juul Jensen. Atomistisk simulering af rekrystallisation. *Proceedings of Dansk Metallurgisk Selskabs Vintermøde*, 27–37, 2007.

[7] **Article G** R. B. Godiksen, Z. T. Trautt, M. Upmanyu, S. Schmidt, and D. Juul Jensen. Simulation of recrystallization using molecular dynamics; effects of the interatomic potential. *Materials Science Forum*, 558-559:1081–1086, 2007.

[8] **Article H** R. B. N. Godiksen, S. Schmidt, and D. Juul Jensen. Molecular dynamics simulations of grain boundary migrationduring recrystallization employing different types of dislocationstructures to produce the driving pressure. *Submitted to Modelling and Simulation of MaterialsScience and Engineering*, 2007.

[9] **Article I** S. F. Nielsen, G. Beckmann, R. B. Godiksen, K. Haldrup, H. F. Poulsen, and J. A. Wert. Measurement of the components of plastic displacement gradients in three dimensions. *Proceedings of SPIE*, 5535:485–492, 2004.

[10] **Article J** S. Schmidt, R. B. Godiksen, and D. Juul Jensen. Bulk investigations of grain boundary migration during recrystallization utilizing the 3dxrd microscope. *Proceedings from Phase Transformations in Inorganic Materials '05*, :583, 2005.

Cited Publications

[11] M. P. Allen and D. J. Tildesley. *Computer Simulation of Liquids*. Oxford University Press, 2004.

[12] M. F. Ashby. The influence of particles on boundary mobility. *Proceedings from the 1st Risø International Symposium on Metallurgy and Materials Science*, 1:325–336, 1980.

[13] K. T. Aust and J. W. Rutter. Grain boundary migration in high-purity lead and dilute lead-tin alloys. *Transactions of the American Institute of Mining and Metallurgical Engineers*, 215(1):119–127, 1959.

[14] M. Avrami. Kinetics of phase change I - general theory. *Journal of Chemical Physics*, 7:1103–1112, 1939.

[15] M. Avrami. Kinetics of phase change II - transformation-time relations for random distribution of nuclei. *Journal of Chemical Physics*, 8:212–224, 1940.

[16] M. Avrami. Kinetics of phase change III - granulation, phase change, and microstructure. *Journal of Chemical Physics*, 9:177–183, 1941.

[17] Z. H. Barber. *Introduction to Materials Modelling*. Maney Publications, 2005.

[18] M. I. Baskes. Many-body effects in fcc metals: A Lennard-Jones embedded-atom potential. *Physical Review Letters*, 83(13):2592–2595, Sep 1999.

[19] P. A. Beck, P. R. Sperry, and H. Hu. The orientation dependence of the rate of grain boundary migration. *Journal of Applied Physics*, 21(5):420–425, 1950.

[20] D. P. Birnie and M. C. Weinberg. Kinetics of transformation for anisotropic particles including shielding effects. *Journal of Chemical Physics*, 103(9):3742–3746, Sep 1995.

[21] E. M. Bringa, A. Caro, Y. M. Wang, M. Victoria, J. M. McNaney, B. A. Remington, R. F. Smith, B. R. Torralva, and H. Van Swygenhoven. Ultrahigh strength in nanocrystalline materials under shock loading. *Science*, 309(5742):1838–1841, Sep 2005.

[22] J. W. Cahn. The kinetics of grain boundary nucleated reactions. *Acta Metallurgica*, 4(5):449–459, 1956.

[23] R. W. Cahn. Recovery and recrystallization. In R. W. Cahn and P. Haasen, editors, *Physical Metallurgy*, pages 1595–1671. Elsevier Science Publishers, 1983.

[24] Y. B. Chun, S. L. Semiatin, and S. K. Hwang. Monte Carlo modeling of microstructure evolution during the static recrystallization of cold-rolled, commercial-purity titanium. *Acta Materialia*, 54(14):3673–3689, Aug 2006.

[25] A. S. Clarke and H. Jonsson. Structural changes accompanying densification of random hard-sphere packings. *Physical Review e*, 47(6):3975–3984, Jun 1993.

[26] R. T. Dehoff. Microstructural evolution during recrystallization. *Proceedings from the 7th Risø International Symposium on Metallurgy and Materials Science*, 7:35–52, 1986.

[27] R. D. Doherty, A. R. Rollett, and D. J. Srolovitz. Structural evolution during recrystallization. *Proceedings from the 7th Risø International Symposium on Metallurgy and Materials Science*, 7:53–67, 1986.

[28] R. Le Gall, G. Liao, and G. Saindrenan. In-situ sem studies of grain boundary migration during recrystallization of cold-rolled nickel. *Scripta Materialia*, 41(4):427–432, Jul 1999.

[29] F. Gao, Y. Zhang, M. Posselt, and W. J. Weber. Atomic-level simulations of epitaxial recrystallization and amorphous-to-crystalline transition in 4H-SiC. *Physical Review B*, 74(10), Sep 2006.

[30] N. A. Gjostein and F. N. Rhines. Absolute interfacial energies of [001] tilt and twist grain boundaries in copper. *Acta Metallurgica*, 7(5):319–330, 1959.

[31] A. M. Gokhale. Calculation of the product phase grain-boundary area during solid-state transformations. *Metallurgical Transactions A-Physical Metallurgy and Materials Science*, 19(9):2123–2131, Sep 1988.

[32] G. Gottstein and L. S. Shvindlerman. On the orientation dependence of grain-boundary migration. *Scripta Metallurgica et Materialia*, 27(11):1515–1520, Dec 1992.

[33] G. Gottstein and L. S. Shvindlerman. On the true dependence of grain-boundary migration rate on driving force. *Scripta Metallurgica et Materialia*, 27(11):1521–1526, Dec 1992.

[34] N. Hansen. New discoveries in deformed metals. *Metallurgical and Materials Transactions A*, 32A:2917–2935, 2001.

[35] H. W. Hesselbarth and I. R. Gobel. Simulation of recrystallization by cellular automata. *Acta Metallurgica et Materialia*, 39(9):2135–2143, Sep 1991.

[36] J. P. Hirth, R. C. Pond, and J. Lothe. Spacing defects and disconnections in grain boundaries. *Scripta Materialia*, 55:5428–5437, 2007.

[37] Y. Huang and F. J. Humphreys. Measurements of grain boundary mobility during recrystallization of a single-phase aluminium alloy. *Acta Materialia*, 47(7):2259–2268, May 1999.

[38] Y. Huang and F. J. Humphreys. The pinning of grain boundaries during the recrystallization of an Al-0.3Mn-0.15Si alloy. *Thermec'2003, Pts 1-5*, 426-4:501–506, 2003.

[39] F. J. Humphreys. Modelling microstructural evolution during annealing. *Modelling and Simulation in Materials Science and Engineering*, 8:893–910, 2000.

[40] F. J. Humphreys and M. Hatherly. *Recrystallization and Related Annealling Phenomena*. Elsevier Ltd., Oxford, 2004.

[41] K. W. Jacobsen, P. Stoltze, and J. K. Norskov. A semi-empirical effective medium theory for metals and alloys. *Surface Science*, 366(2):394–402, Oct 1996.

[42] K. G. F. Janssens, D. Olmsted, E. A. Holm, S. M. Foiles, S. J. Plimpton, and P. M. Derlet. Computing the mobility of grain boundaries. *Nature Materials*, 5(2):124–127, Feb 2006.

[43] W. A. Johnson and R. F. Mehl. Reaction kinetics in processes of nucleation and growth. *Transactions of the American Institute of Mining and Metallurgical Engineers*, 135:416, 1939.

[44] D. Juul Jensen. Growth of nuclei with different crystallographic orientations during recrystallization. *Scripta Metallurgica et Materialia*, 27(5):533–538, Sep 1992.

[45] D. Juul Jensen. Simulation of recrystallization microstructures and textures: Effects of preferential growth. *Metallurgical and Materials Transactions A-Physical Metallurgy and Materials Science*, 28(1):15–25, Jan 1997.

[46] D. Juul Jensen, E. M. Lauridsen, and R. A. Vandermeer. In-situ determination of grain boundary migration during recrystallization. *Proceedings of TMS annual meeting, science and technology of interfaces*, :361–374, 2002.

[47] A. N. Kolmogorov. On the statistical theory of metal crystallization (english translation). In *Selected Works*, pages 188–193. Kluwer, Boston, 1991.

[48] B. J. Kooi. Monte Carlo simulations of phase transformations caused by nucleation and subsequent anisotropic growth: Extension of the Johnson-Mehl-Avrami-Kolmogorov theory. *Physical Review B*, 70(22), Dec 2004.

[49] B. J. Kooi. Extension of the Johnson-Mehl-Avrami-Kolmogorov theory incorporating anisotropic growth studied by Monte Carlo simulations. *Physical Review B*, 73(5):054103, Feb 2006.

[50] K. Kremer and G. S. Grest. Dynamics of entangled linear polymer melts - a molecular-dynamics simulation. *Journal of Chemical Physics*, 92(8):5057–5086, Apr 1990.

[51] E. M. Lauridsen, H. F. Poulsen, S. F. Nielsen, and D. Juul Jensen. Recrystallization kinetics of individual bulk grains in 90cold-rolled aluminium. *Acta Materialia*, 51(15):4423–4435, Sep 2003.

[52] A. Lens, C. Maurice, and J. H. Driver. Grain boundary mobilities during recrystallization of Al-Mn alloys as measured by in situ annealing experiments. *Materials Science and Engineering A-Structural Materials Properties Microstructure and Processing*, 403(1-2):144–153, Aug 2005.

[53] M. I. F. Macedo, C. A. Bertran, and C. C. Osawa. Kinetics of the gamma ->alpha-alumina phase transformation by quantitative X-ray diffraction. *Journal of Materials Science*, 42(8):2830–2836, Apr 2007.

[54] K. W. Mahin, K. Hanson, and J. W. Morris. Comparative-analysis of the cellular and Johnson-Mehl microstructures through computer-simulation. *Acta Metallurgica*, 28(4):443–453, 1980.

[55] K. Marthinsen, O. Lohne, and E. Nes. The development of recrystallization microstructures studied experimentally and by computer-simulation. *Acta Metallurgica*, 37(1):135–145, Jan 1989.

[56] M. A. Martorano, M. A. Fortes, and A. F. Padilha. The growth of protrusions at the boundary of a recrystallized grain. *Acta Materialia*, 54(10):2769–2776, Jun 2006.

[57] M. A. Martorano, H. R. Z. Sandim, M. A. Fortes, and A. F. Padilha. Observations of grain boundary protrusions in static recrystallization of high-purity bcc metals. *Scripta Materialia*, 56(10):903–906, May 2007.

[58] J. L. Meijering. Interface area, edge length, and number of vertices in crystal aggregates with random nucleation. *Philips Research Reports*, 8(4):270–290, 1953.

[59] M. I. Mendelev and B. Bokstein. Molecular dynamics study of vacancy migration in al. *Materials Letters*, 61(14-15):2911–2914, Jun 2007.

[60] M. I. Mendelev, D. J. Srolovitz, G. J. Ackland, and S. Han. Effect of fe segregation on the migration of a non-symmetric sigma 5 tilt grain boundary in al. *Journal of Materials Research*, 20(1):208–218, Jan 2005.

[61] N. Metropolis and S. Ulam. The Monte Carlo method. *Journal of the American Statistical Association*, 44(247):335–341, 1949.

[62] G. Monnet. Mechanical and energetical analysis of molecular dynamics simulations of dislocation-defect interactions. *Acta Materialia*, 55:5081–5088, 2007.

[63] M. Mrovec, Y. Cheng, C. Elsasser, and P. Gumbsch. Atomistic simulations of dislocation-grain-boundary interactions in tungsten. *Proceedings of third international conference on multiscale materials modeling*, :213–216, 2006.

[64] P. Mukhopadhyay, M. Loeck, and G. Gottstein. A cellular operator model for the simulation of static recrystallization. *Acta Materialia*, 55(2):551–564, Jan 2007.

[65] A. A. Nazarov, O. A. Shenderova, and D. W. Brenner. On the disclination-structural unit model of grain boundaries. *Materials Science and Engineering A-Structural Materials Properties Microstructure and Processing*, 281(1-2):148–155, Apr 2000.

[66] E. Nes, H. E. Vatne, T. Pettersen, T. Furu, and K. Marthinsen. Modelling of recrystallization applied to industrial processing of aluminium alloys. *Proceedings of the 21st Risø International Symposium on Materials Science*, 21, 2000.

[67] A. J. Patrinos, I. P. Antoniades, and G. L. Bleris. Monte-Carlo and molecular-dynamics investigation of [001] twist boundaries in Cu3Au at t=0 K. *Physical Review B*, 52(13):9291–9299, Oct 1995.

[68] U. R. Pedersen, N. P. Bailey, J. C. Dyre, and T. B. Schrøder. Crystallization of the Wahnström binary Lennard-Jones liquid. *cond-mat.mtrl-sci*, arXiv:0706.0813v2:1–4, Jul 2007.

[69] T. Pusztai and L. Granasy. Monte Carlo simulation of first-order phase transformations with mutual blocking of anisotropically growing particles up to all relevant orders. *Physical Review B*, 57(22):14110–14118, Jun 1998.

[70] D. Raabe. Cellular automata in materials science with particular reference to recrystallization simulation. *Annual Review of Materials Research*, 32:53–76, 2002.

[71] B. Radhakrishnan and T. Zacharia. Monte carlo simulation of stored energy driven interface migration. *Modelling and Simulation in Materials Science and Engineering*, 11(3):307–319, May 2003.

[72] D. C. Rapaport. *The Art of Molecular Dynamics Simulation*, volume 2. Cambridge University Press, Cambridge, 2004.

[73] B. B. Rath and H. Hu. Driving-force dependence of rate of boundary migration in zone-refined aluminum crystals. *Transactions of the Metallurigal Society of AIME*, 245:1243–1252, Jun 1969.

[74] W. T. Read and W. Shockley. Dislocation models of crystal grain boundaries. *Physical Review*, 78(3):275–289, 1950.

[75] P. R. Rios, L. O. Pereira, F. F. Oliveira, W. L. S. Assis, and J. A. Castro. Impingement function for nucleation on non-random sites. *Acta Materialia*, doi:10.1016/j.actamat.2007.04.003, 2007.

[76] A. D. Rollett. Overview of modeling and simulation of recrystallization. *Progress in Materials Science*, 42:79–99, 1997.

[77] J. C. Russ and R. T. Dehoff. *Pratical Stereology*, volume 2. Plenum Press, New York, 1999.

[78] T. O. Saetre, O. Hunderi, and E. Nes. Computer-simulation of primary recrystallization microstructures - the effects of nucleation and growth-kinetics. *Acta Metallurgica*, 34(6):981–987, Jun 1986.

[79] J. Schiotz and K. W. Jacobsen. A maximum in the strength of nanocrystalline copper. *Science*, 301(5638):1357–1359, Sep 2003.

[80] S. Schmidt, S. F. Nielsen, C. Gundlach, L. Margulies, X. Huang, and D. Juul Jensen. Watching the growth of bulk grains during recrystallization of deformed metals. *Science*, 305(5681):229–232, Jul 2004.

[81] B. Schonfelder, G. Gottstein, and L. S. Shvindlerman. Comparative study of grain-boundary migration and grain-boundary self-diffusion of [001] twist-grain boundaries in copper by atomistic simulations. *Acta Materialia*, 53(6):1597–1609, Apr 2005.

[82] T. B. Schroder, S. Sastry, J. C. Dyre, and S. C. Glotzer. Crossover to potential energy landscape dominated dynamics in a model glass-forming liquid. *Journal of Chemical Physics*, 112(22):9834–9840, Jun 2000.

[83] M. P. Shepilov and D. S. Baik. Computer-simulation of crystallization kinetics for the model with simultaneous nucleation of randomly-oriented ellipsoidal crystals. *Journal of Non-Crystalline Solids*, 171(2):141–156, Aug 1994.

[84] D. A. Smith, C. M. F. Rae, and C. R. M. Grovenor. Grain boundary migration. *Papers presented at the 1979 ASM Materials Science Seminar*, :337–371, 1979.

[85] Z. Sukosd, K. Hannesson, G. Wu, and D. Juul Jensen. 3d spatial distribution of nuclei in 90% cold rolled aluminium. *Materials Science Forum*, 558-559:345–350, 2007.

[86] Y. Suwa, Y. Saito, and H. Onodera. Phase field simulation of stored energy driven interface migration at a recrystallization front. *Materials Science and Engineering A-Structural Materials Properties Microstructure and Processing*, 457(1-2):132–138, May 2007.

[87] Z. T. Trautt, M. Upmanyu, and A. Karma. Interface mobility from interface random walk. *Science*, 314(5799):632–635, Oct 2006.

[88] S. M. Ulam and J. Vonneumann. On combination of stochastic and deterministic processes - preliminary report. *Bulletin of the American Mathematical Society*, 53(11):1120–1120, 1947.

[89] M. Upmanyu, G. N. Hassold, A. Kazaryan, E. A. Holm, Y. Wang, B. Patton, and D. J. Srolovitz. Boundary mobility and energy anisotropy effects on microstructural evolution during grain growth. *Interface Science*, 10(2-3):201–216, Jul 2002.

[90] M. Upmanyu, D. J. Srolovitz, L. S. Shvindlerman, and G. Gottstein. Misorientation dependence of intrinsic grain boundary mobility: Simulation and experiment. *Acta Materialia*, 47(14):3901–3914, Oct 1999.

[91] M. Upmanyu, D. J. Srolovitz, L. S. Shvindlerman, and G. Gottstein. Molecular dynamics simulation of triple junction migration. *Acta Materialia*, 50(6):1405–1420, Apr 2002.

[92] M. Upmanyu, Z. T. Trautt, and B. B. Kappes. Anisotropy in grain boundary thermo-kinetics: Atomic-scale computer simulations. *Materials Science Forum*, 467-470:715–726, 2004.

[93] R. A. Vandermeer. Kinetic aspects of nucleation and growth in recrystallization. *Proceedings of the 21st Risø International Symposium: Recrystallization - Fundamental Aspects and Relations to Deformation Microstructure.*, 21:179–200, 2000.

[94] R. A. Vandermeer. Microstructural descriptors and the effects of nuclei clustering on recrystallization path kinetics. *Acta Materialia*, 53(5):1449–1457, Mar 2005.

[95] R. A. Vandermeer and H. Hu. On the grain-growth exponent of pure iron. *Acta Metallurgica et Materialia*, 42(9):3071–3075, Sep 1994.

[96] R. A. Vandermeer, D. Juul Jensen, and E. Woldt. Grain boundary mobility during recrystallization of copper. *Metallurgical and Materials Transactions A-Physical Metallurgy and Materials Science*, 28(3A):749–754, Mar 1997.

[97] R. A. Vandermeer and R. A. Masumura. The microstructural path of grain-boundary-nucleated phase-transformations. *Acta Metallurgica et Materialia*, 40(4):877–886, Apr 1992.

[98] R. A. Vandermeer, R. A. Masumura, and B. B. Rath. Microstructural paths of shape-preserved nucleation and growth transformations. *Acta Metallurgica et Materialia*, 39(3):383–389, Mar 1991.

[99] R. A. Vandermeer and B. B. Rath. Modeling recrystallization kinetics in a deformed iron single-crystal. *Metallurgical Transactions A-Physical Metallurgy and Materials Science*, 20(3):391–401, Mar 1989.

[100] A. F. Voter and S. P. Chen. Accurate interatomic potentials for Ni, Al and Ni_3Al. *Mater.Res.Soc.Symp.Proc.*, 82:175, 1987.

[101] G. J. Wang and V. Vitek. Relationships between grain-boundary structure and energy. *Acta Metallurgica*, 34(5):951–960, May 1986.

[102] C. M. Wayman. Phase transformations, nondiffusive. In R. W. Cahn and P. Haasen, editors, *Physical Metallurgy*, pages 1031–1074. Elsevier Science Publishers, 1983.

[103] J. Weertman and J. R. Weertman. *Elementary Dislocation Theory*. Oxford University Press, Inc., 1992.

[104] H. Zhang, M. I. Mendelev, and D. J. Srolovitz. Computer simulation of the elastically driven migration of a flat grain boundary. *Acta Materialia*, 52(9):2569–2576, May 2004.

[105] H. Zhang and D. J. Srolovitz. Simulation and analysis of the migration mechanism of sigma 5 tilt grain boundaries in an fcc metal. *Acta Materialia*, 54(3):623–633, Feb 2006.

[106] H. Zhang, D. J. Srolovitz, J. F. Douglas, and J. A. Warren. Characterization of atomic motion governing grain boundary migration. *Physical Review B*, 74(11), Sep 2006.

[107] H. Zhang, D. J. Srolovitz, J. F. Douglas, and J. A. Warren. Atomic motion during the migration of general [001] tilt grain boundaries in ni. *Acta Materialia*, 55(13):4527–4533, Aug 2007.

[108] H. Zhang, M. Upmanyu, and D. J. Srolovitz. Curvature driven grain boundary migration in aluminum: molecular dynamics simulations. *Acta Materialia*, 53(1):79–86, Jan 2005.

List of Figures

List of Tables

A Analytical expression for the evolution of interfacial area density between transformed grains during nucleation and growth transformations

P.R. Rios, R.B. Godiksen, S. Schmidt, D. Juul Jensen, R.A. Vandermeer, *Scripta Materialia* **54**, 1509–1513 (2006).

Available online at www.sciencedirect.com
SCIENCE DIRECT
Scripta Materialia 54 (2006) 1509–1513
Scripta MATERIALIA
www.actamat-journals.com

Analytical expression for the evolution of interfacial area density between transformed grains during nucleation and growth transformations

P.R. Rios [a,*], R.B. Godiksen [b], S. Schmidt [b], D. Juul Jensen [b], R.A. Vandermeer [b]

[a] *Universidade Federal Fluminense, Escola de Engenharia Industrial Metalúrgica de Volta Redonda, Av. dos Trabalhadores, 420, Volta Redonda, RJ 27255-125, Brazil*

[b] *Center for Fundamental Research: Metal Structures in Four Dimensions, Materials Research Department, Risø National Laboratory, DK-4000 Roskilde, Denmark*

Received 31 May 2005; received in revised form 15 November 2005; accepted 23 December 2005
Available online 25 January 2006

Abstract

This paper shows that interfacial area density between transformed grains during nucleation and growth transformations and the contiguity are useful descriptors of microstructural evolution. These descriptors are evaluated analytically and compared with results from computer simulation. Usage of these descriptors makes microstructural path analysis even more reliable and robust.

Keywords: Microstructure; Modeling; Kinetics; Recrystallization; Phase transformations

1. Introduction

In opaque solids like metals and alloys, quantitative microscopy continues to be an important experimental technique to study the kinetics of nucleation and growth phase transformations and transformation-like phenomena such as the annealing process of recrystallization. Over a range of reaction times, experimental geometrical descriptors can be used to characterize the kinetics of the transformation process [1].

Volume fraction transformed, V_V, is the most often measured descriptor. Another useful one is the interfacial area density separating transformed regions from untransformed ones, i.e. the free-to-migrate interfacial area density, $S_V^{\alpha\beta}$. As shown by Cahn and Hagel [2] an average interface migration rate or growth rate, $\langle v \rangle$, for a transformation can be obtained from the measured time dependence of these two descriptors, i.e.

$$\langle v \rangle = \frac{1}{S_V^{\alpha\beta}} \frac{dV_V}{dt} \tag{1}$$

The V_V and $S_V^{\alpha\beta}$ parameters are just two of a number of geometrical descriptors that may be useful in describing the microstructural path [3] of a transformation. Another potentially useful descriptor is the interfacial area density between two transformed grains, $S_V^{\beta\beta}$. $S_V^{\beta\beta}$ is the impinged boundary area density of the transformation product grains. When added together $S_V^{\alpha\beta}$ and $2S_V^{\beta\beta}$ yield the total grain boundary area density, S_V^T, associated with the grains of the transformation product. Another related parameter, the contiguity ratio $C_{\beta\beta}$, defined as

$$C_{\beta\beta} = \frac{2S_V^{\beta\beta}}{S_V^{\alpha\beta} + 2S_V^{\beta\beta}} = \frac{2S_V^{\beta\beta}}{S_V^T} \tag{2}$$

is the fraction of the total grain boundary area of the new, transformed grains shared (impinged upon) by other new grains. This parameter may be useful for characterizing the extent to which the new product grains are nucleated randomly or in colonies or clusters [4]. Attempts to develop

* Corresponding author.
E-mail address: prrios@metal.eeimvr.uff.br (P.R. Rios).

1359-6462/$ - see front matter © 2006 Acta Materialia Inc. Published by Elsevier Ltd. All rights reserved.
doi:10.1016/j.scriptamat.2005.12.037

analytical geometrical models of the microstructural path of phase transformations and recrystallization by relating V_V to a nucleation rate, a growth rate, a new grain shape and the reaction time, t, began with the work of Kolmogorov [5], Johnson and Mehl [6] and Avrami [7] (KJMA). These were simple models that regarded the nucleation rate and the growth rate to be constants where the product grains grew with a spherical shape. The KJMA models were based on the critical, statistical assumption that the transforming grains be distributed randomly throughout the volume of material. The simple KJMA kinetics formulations may be summarized analytically in general terms by the Avrami equation [7] which may be written as

$$V_V = 1 - \exp(-Bt^k) \tag{3}$$

where B and k are constants that depend on the precise geometrical model selected.

Gokhale and DeHoff [8] and later Vandermeer et al. [9] (VMR) expanded on the work of KJMA and derived kinetic relationships for $S_V^{\alpha\beta}$ versus time and V_V. These relationships are

$$S_V^{\alpha\beta} = (1 - V_V)Kt^m \tag{4}$$

and

$$S_V^{\alpha\beta} = C(1 - V_V)(-\ln(1 - V_V))^q \tag{5}$$

where K, C, m and q are constants that depend on the precise nature of the geometrical model under consideration. VMR [9] retained the basic, critical assumption that the transformation product be distributed randomly in a statistical sense throughout the volume. The VMR formalism, however, relaxed some of the other KJMA assumptions. Thus, as long as the nucleation rate and the growth rate could both be subsumed to be power-law functions of reaction time and the new grains preserved their shape during transformation, Eq. (3)–(5) were valid [9]. The VMR models which may be characterized as "relaxed" KJMA models are able to treat time-dependent nucleation and growth rates as well as cases where nucleation is site-saturated.

A natural development of the microstructural path method would be to add $S_V^{\beta\beta}$ and $C_{\beta\beta}$ to the existent descriptors, $S_V^{\alpha\beta}$ and V_V. A more complete microstructural description would make the method even more reliable and robust. In 1953, Meijering [10] calculated $S_V^{\beta\beta}$ at the end of complete transformation of one phase to another for two nucleation models: site saturation, and constant nucleation rate. Meijering further assumed that the nucleation was spatially uniformly random, and that in the extended structure, the product phase particles were spherical and their growth rate was a constant. Meijering's results were generalized by Gokhale [11]. Gokhale obtained expressions for other growth rate and nucleation rate functional forms, again under assumptions that the nucleation is spatially uniform random, and in the extended structure, the particles are spherical. In a second paper [12], Gokhale also derived expressions for the total grain edge length and quadruple points per unit volume to complete the description of microstructural evolution. Tong et al. in a recent paper [13] obtained $S_V^{\beta\beta}$ as a function of time for the same cases analyzed by Meijering.

The work presented in this paper seeks to expand the microstructural path formalism including $S_V^{\beta\beta}$ and $C_{\beta\beta}$. Gokhale's [11] relationships were also valid for a time dependent nucleation and time dependent velocity. Here, time dependent nucleation and time dependent velocity is introduced with the help of VMR formalism. In the VMR formalism, nucleation rate and growth rate must be simple power law functions. VMR allows growing regions to be of certain non-spherical shapes, specifically, prolate and oblate spheroids that maintain a constant ratio of major to minor axis during growth. Hence, analytical relationships that would be companions to Eqs. (3)–(5) will be used for $S_V^{\beta\beta}$ and $C_{\beta\beta}$. These relationships will be illustrated by comparing them with results of computer simulations based on a number of KJMA and "relaxed" KJMA assumptions. The computer simulation results of the present paper are potentially useful because they provide the framework to solve the problem for spatially non-uniform or clustered nucleation of the product phase, which occurs so often.

2. Derivation of analytical expressions

In what follows, for brevity, $S_V^{\alpha\beta}$ are written as S_V and $S_V^{\beta\beta}$ as S_β.

The relationship below is our starting point [11]:

$$\frac{S_\beta}{S_{\beta F}} = \frac{\int_0^{V_E} S_E \exp(-V_E)\mathrm{d}V_E}{\int_0^{\infty} S_E \exp(-V_E)\mathrm{d}V_E} \tag{6}$$

where $S_{\beta F}$ is the interface area between transformed regions at the end of transformation. For spherical shapes, $S_{\beta F}$ can be calculated from Meijering [10] or Gokhale [11]. For non-spherical shapes, $S_{\beta F}$, must be obtained from computer simulation or from experimental measurement.

Eq. (6) can be obtained by dividing Eq. (50) by Eq. (51) or Eq. (63) by Eq. (64) from Gokhale's paper [11]. See also Eqs. (13) and (15) of Tong et al. [13].

In order to integrate Eq. (6), it is necessary to know the relationship between S_E and V_E. For example, when the reaction is site-saturated and the growing regions are spherical:

$$S_E = (36\pi N_V)^{\frac{1}{3}} V_E^{\frac{2}{3}} \tag{7}$$

where N_V is the number of nuclei per unit of volume.

A more general approach would be to follow VMR and assume a relationship of the form

$$S_E = C(V_E)^q \tag{8}$$

Resulting in

$$\frac{S_\beta}{S_{\beta F}} = \frac{\int_0^{V_E} (V_E)^q \exp(-V_E)\mathrm{d}V_E}{\int_0^{\infty} (V_E)^q \exp(-V_E)\mathrm{d}V_E} \tag{9}$$

This integral can be written in terms of the incomplete gamma function, Γ:

$$\frac{S_\beta}{S_{\beta F}} = \left(1 - \frac{\Gamma(q+1, V_E)}{\Gamma(q+1)}\right) = \left(1 - \frac{\Gamma(q+1, -\ln(1-V_V))}{\Gamma(q+1)}\right) \quad (10)$$

Using S_V from Eq. (5) the contiguity, $C_{\beta\beta}$ is given by

$$C_{\beta\beta} = \frac{2S_{\beta F}\left(1 - \frac{\Gamma\left(q+1, \ln\left(\frac{1}{1-V_V}\right)\right)}{\Gamma(q+1)}\right)}{C(1-V_V)\left(\ln\left(\frac{1}{1-V_V}\right)\right)^q + 2S_{\beta F}\left(1 - \frac{\Gamma\left(q+1, \ln\left(\frac{1}{1-V_V}\right)\right)}{\Gamma(q+1)}\right)} \quad (11)$$

From Eqs. (10) and (11), by specifying C and q one can obtain particular cases. For example, comparing Eqs. (7) and (8): $C = (36\pi N_V)^{1/3}$ and $q = 2/3$ the site-saturation case is immediately recovered. VMR found the values of C and q for the case in which the growing regions are spheroids. They assumed mathematical time dependencies for the nucleation rate I and for the growth rate G:

$$I = N_1 t^{\delta-1} \quad (12)$$

$$G = rPt^{r-1} \quad (13)$$

where N_1, P, r and δ are constants. The values of C and q are given by

$$q = \frac{2r+\delta}{3r+\delta} \quad (14)$$

$$C = \frac{(K_S N_1 P^2 \Gamma(s))}{(K_V N_1 P^3 \Gamma(x))^{\frac{2r+\delta}{3r+\delta}}} \quad (15)$$

where K_V and K_S are constant shape factors; $K_V = 4\pi/3$ and $K_S = 4\pi$ for spherical shape; they have a more general form for oblate and prolate spheroids with a constant ratio of major/minor axis [8]; $\Gamma(s) = \Gamma(2r+1)\Gamma(\delta)/\Gamma(2r+\delta+1)$ and $\Gamma(x) = \Gamma(3r+1)\Gamma(\delta)/\Gamma(3r+\delta+1)$.

It could be useful to write Eqs. (10) and (11) as a function of time. This can be done recalling from VMR that

$$V_E = \ln\left(\frac{1}{1-V_V}\right) = K_V \Gamma(x) N_1 P^3 t^{3r+\delta} \quad (16)$$

Eq. (16) can be inserted into Eqs. (10) and (11) to yield $S_\beta/S_{\beta F}$ and $C_{\beta\beta}$ as a function of time.

3. Comparison with computer simulations

The simulation assumed that the nuclei were randomly located and that the growing regions had a spherical shape in extended space, so the shape factors were $K_S = 4\pi$ and $K_V = 4\pi/3$. The simulation method was analogous to that employed in Ref. [14]. Four simple cases were simulated:

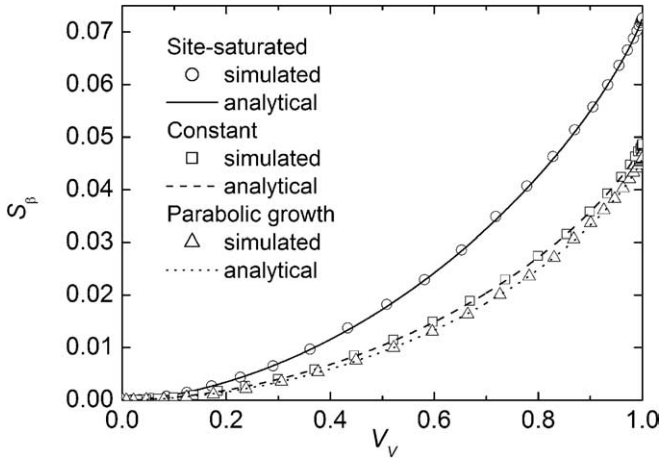

Fig. 1. Interfacial area density between transformed grains, S_β, plotted against volume fraction transformed, V_V. The three simulation cases are represented: I—site-saturated, II—constant nucleation rate with constant growth rate and III—constant nucleation rate with parabolic growth rate. Agreement between computer simulation and analytical expression is excellent.

(I) Site-saturated nucleation, $q = 2/3$, comprising two growth conditions:
  (I.1) constant growth rate, $G =$ constant and
  (I.2) parabolic growth, $r = 1/2$, $G \propto t^{-1/2}$, in Eq. (13).

Case I.1 and I.2 give identical theoretical results. Computer simulation confirmed this. In what follows, both cases will be represented by I.1 and referred to as "site-saturated".

(II) Constant nucleation rate and constant growth rate: $G =$ constant and $q = 3/4$;

(III) Constant nucleation rate and parabolic growth rate: $G \propto t^{-1/2}$ and $q = 4/5$.

Our simulations can be extended to transformations involving spatially non-random nucleation, for example, preferential nucleation at grain boundaries, edges or vertices. This point is now under investigation.

Fig. 1 shows the result for S_β as a function of volume fraction for all three cases.

Figs. 2 and 3 show the normalized interfacial area density between transformed grains, $S_\beta/S_{\beta F}$, and the contiguity, $C_{\beta\beta}$ plotted against volume fraction transformed. In Fig. 2 site-saturated nucleation is compared with constant nucleation rate. In Fig. 3 constant nucleation rate with constant growth rate is compared with constant nucleation rate with parabolic growth rate.

4. Discussion

The analytical expressions for normalized interfacial area density between transformed grains, $S_\beta/S_{\beta F}$ and contiguity, $C_{\beta\beta}$, give interesting insights on the behavior of nucleation and growth reactions.

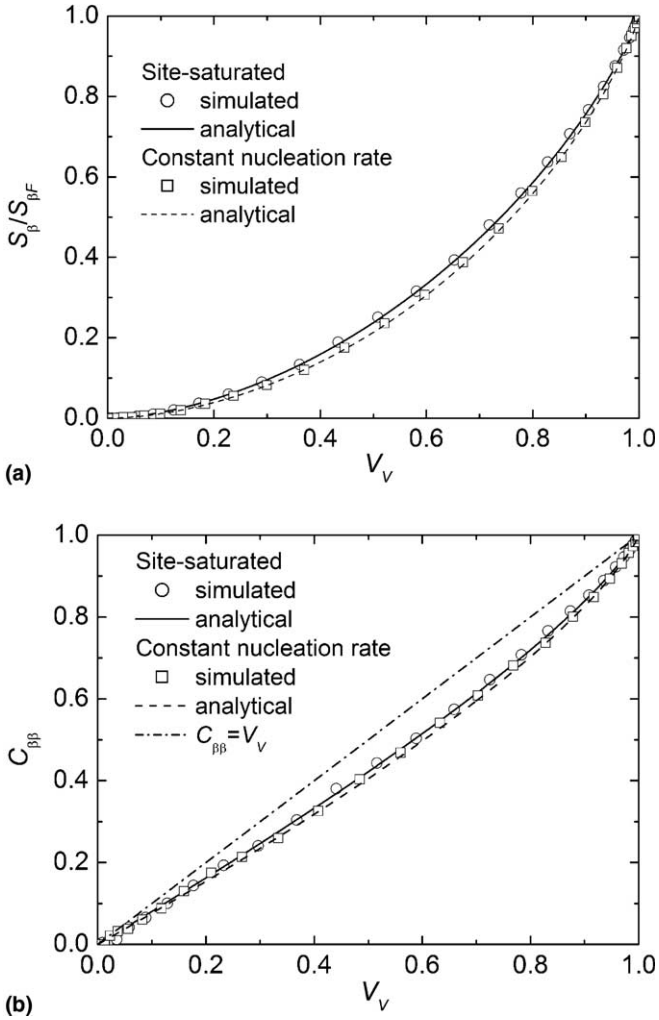

Fig. 2. Normalized interfacial area density between transformed grains, $S_\beta/S_{\beta F}$ (a) and contiguity, $C_{\beta\beta}$ (b) plotted against volume fraction transformed, V_V, for: I—site-saturated and II—constant nucleation rate with constant growth rate. Agreement between computer simulation and analytical expression is excellent. A straight line, $C_{\beta\beta} = V_V$, was also plotted in (b) for comparative purposes.

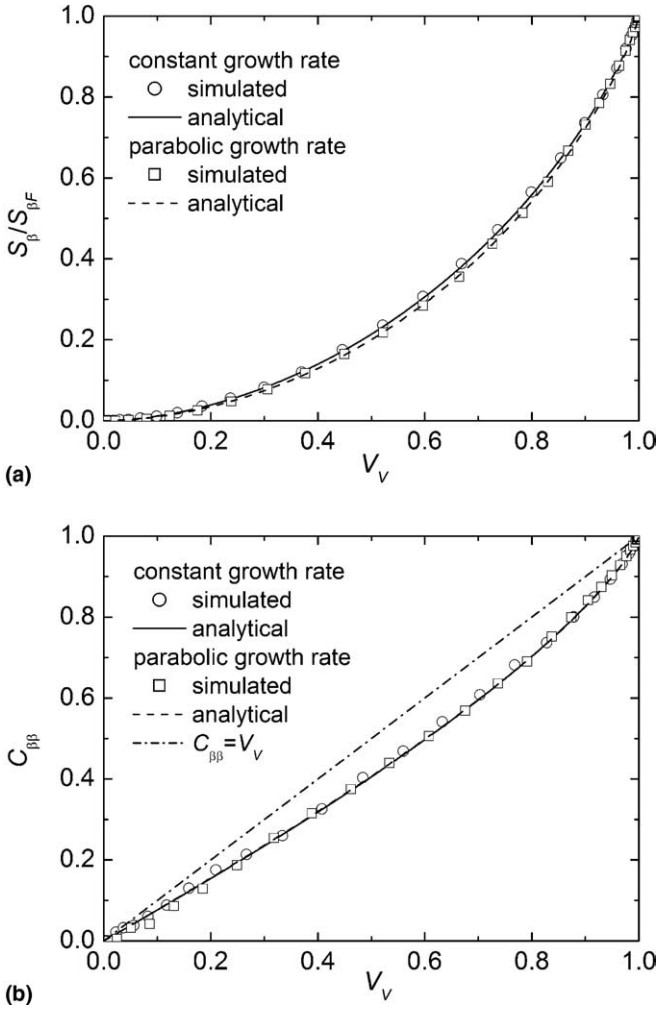

Fig. 3. Normalized interfacial area density between transformed grains, $S_\beta/S_{\beta F}$ (a) and contiguity, $C_{\beta\beta}$ (b) plotted against volume fraction transformed, V_V, for: II—constant nucleation rate with constant growth rate and III—constant nucleation rate with parabolic growth rate. Agreement between computer simulation and analytical expression is excellent. A straight line, $C_{\beta\beta} = V_V$, was also plotted in (b) for comparative purposes.

Fig. 1 shows that $S_{\beta F}$ depends on the nucleation and growth kinetics. $S_{\beta F}$ simulated here can be compared with analytical values obtained from Meijering [10]. For site-saturation nucleation and constant velocity [10] $S_{\beta F} = 2.91 N_V^{1/3}$, the calculated value was equal to 0.073, identical to the simulated result, also, 0.073. For constant nucleation rate and constant velocity: $S_{\beta F} = 2.479(I/G)^{1/4}$, the calculated value of $S_{\beta F}$ was equal to 0.049, identical to the simulated result, also, 0.049.

For site-saturated nucleation $q = 2/3$ and the theory predicts that $S_\beta/S_{\beta F}$ should be the same, independently of growth kinetics or growing shape. Figs. 2(a) and 3(a) further suggest that it is also not so sensitive to small deviations in q. For the three simulated cases: $q = 2/3$, 3/4 and 4/5 the curves remained quite close even though nucleation and growth kinetics were significantly different. In practice, knowledge of $S_{\beta F}$ that can be easily measured from a planar section and suitable choice or fitting of q can be used to generate the whole S_β vs. V_V curve.

Another point shown in Figs. 2(b) and 3(b) is that the analytical expression for the contiguity as a function of V_V is not a straight line. A straight line is not too bad an approximation for V_V below, say, 0.2, but it is only fair for larger values of V_V.

Overall, the results suggest that $S_\beta/S_{\beta F}$ and $C_{\beta\beta}$ are not strongly affected by the nucleation and growth kinetics as previously remarked on by Gokhale [11]. The potential implication of this is that the randomness of nuclei location has more effect on these parameters than details of the kinetics. Figs. 1–3 can be used in practice to check trends observed in the usual S_V vs. V_V plots that are normally fitted by Eq. (5). If data follows the theoretical expressions in both cases this gives a higher reliability and robustness to the analysis of nucleation and growth of the transformed

regions. In case of disagreement, other assumptions need to be tested, for example, the possibility that the nuclei are not randomly located could be considered. It is important to point out that in order to calculate the contiguity using Eq. (11) one needs to know $S_{\beta F}$, as said above it can be calculated for spherical shape [10,11], otherwise one needs computer simulation or experimental determination. It is worthy of note that analytical results provided here are only valid for spatially uniform random nucleation, the contiguity parameter calculated from Eq. (11) cannot provide any information about the spatial clustering of nuclei. Moreover, one must bear in mind that the VMR formalism is limited to cases in which the nucleation and growth kinetics may be described by simple power laws and the growing regions are prolate and oblate spheroids that maintain a constant ratio of major to minor axis during growth.

5. Summary and conclusions

Analytical expressions for normalized interfacial area density between transformed grains, $S_\beta/S_{\beta F}$, and contiguity, $C_{\beta\beta}$ were presented [11,13] and showed good agreement with computer simulations. The use of $S_\beta/S_{\beta F}$ and $C_{\beta\beta}$ plots such as those shown in Figs. 1–3 in conjunction with the usual S_V vs. V_V plots and their corresponding analytical expressions, Eqs. (5), (10) and (11), can provide a higher reliability and robustness to the microstructural path analysis and to its conclusions regarding nucleation and growth of the transformed regions.

Acknowledgements

One of the authors (PRR) is grateful to Conselho Nacional de Desenvolvimento Científico e Tecnológico, CNPq, and to Fundação de Amparo à Pesquisa do Estado do Rio de Janeiro, FAPERJ, for his financial support. The authors (RG,SS, DJJ and RAV) gratefully acknowledge the Danish National Research Foundation for supporting the Center for Fundamental Research: Metal Structures in Four Dimensions, within which part of this work was performed.

References

[1] Vandermeer RA, Rath BB. Metall Trans 1989;20A:391.
[2] Cahn JW, Hagel WC. In: Zackey ZD, Aaronson HI, editors. Decomposition of austenite by diffusional processes. New York (NY): Interscience; 1960. p. 131.
[3] DeHoff RT. The dynamics of microstructural change. Treatise on materials science and technology, vol. 1. New York (NY): Academic Press; 1972. p. 247.
[4] Vandermeer RA. Acta Mater 2005;53:1449.
[5] Kolmogorov AN. Izv Akad Nauk USSR-Ser Matemat 1939;1:355.
[6] Johnson WA, Mehl RF. Trans AIME 1939;135:416.
[7] Avrami MJ. J Chem Phys 1939;7:1103.
[8] Gokhale AM, DeHoff RT. Metall Trans A 1985;16A:559.
[9] Vandermeer RA, Masumura RA, Rath BB. Acta Metall Mater 1991;39:383.
[10] Meijering JI. Phillips Res Rep 1953;8:270.
[11] Gokhale AM. Metall Trans A 1988;19A:2123.
[12] Gokhale AM. Metall Trans A 1989;20A:349.
[13] Tong WS, Rickman JM, Barmak K. Acta Mater 2000;48:1181.
[14] Juul Jensen D. Metall Mater Trans A 1997;28A:15.

B Effects of distributions of growth rates on recrystallization kinetics and microstructure

R.B. Godiksen, S. Schmidt, D. Juul Jensen, *Scripta Materialia* **57**, 345–348 (2007).

Available online at www.sciencedirect.com
ScienceDirect
Scripta Materialia 57 (2007) 345–348
Scripta MATERIALIA
www.elsevier.com/locate/scriptamat

Effects of distributions of growth rates on recrystallization kinetics and microstructure

Rasmus B. Godiksen,* Søren Schmidt and Dorte Juul Jensen

Center for Fundamental Research: Metal Structures in Four Dimensions, Materials Research Department, RisøNational Laboratory, Technical University of Denmark, 4000 Roskilde, Denmark

Received 30 March 2007; revised 18 April 2007; accepted 19 April 2007
Available online 1 June 2007

The effects on recrystallization kinetics and microstructure of growth rate distributions rather than a single growth rate for recrystallizing grains were investigated by geometric simulations. The grains were set to grow as spheres with radii $r = At^{1-\alpha}$. The results show that distributions in A and α may produce significant changes in the microstructure and texture, whereas only distributions in α may change the overall evolution in kinetics represented by $V_V(t)$ by completely changing the shape of the kinetics curve.

Keywords: Recrystallized microstructure; Recrystallization kinetics; Modeling; Geometric simulation

Plastically deformed metals may undergo recrystallization when annealed. Recrystallization is defined as the nucleation and growth of new almost defect-free grains within the deformed defect-filled material. The driving force for recrystallization is the energy stored in the deformed microstructure. The boundaries surrounding recrystallizing grains will migrate through the deformed material until they impinge upon other recrystallizing grains. This process may in turn transform the entire deformed microstructure into a fully recrystallized polycrystalline grain structure [1].

The classic model used to interpret recrystallization kinetics was devised by Johnson and Mehl [2], Avrami [3–5] and Kolmogorov [6], and is now often called the JMAK model. This model is applicable not only for recrystallization but for any transformation on any length scale where a material changes from one 'phase' to another by nucleation and growth.

The JMAK model assumes that the nucleation of new grains happens randomly in space (site saturated or at a constant nucleation rate), that the grains grow as spheres and that all grains grow at a common constant growth rate. The JMAK model can be used to predict the volume fraction V_V of transformed material as a function of time.

The assumptions made in the JMAK model are highly simplified compared with what is observed in recrystallization experiments. Grains typically do not nucleate randomly but at special locations in the deformed matrix, e.g. near the grain boundaries or triple junctions of the deformed grains [7,8]. Non-random nucleation produces changes in the transformation kinetics due to early impingement on the grain boundaries or along the triple junctions. This can be modeled as a reduction in the dimensionality of the growth from three dimensions in the case of random nucleation to one or two dimensions in the cases of grain boundary- and triple junction nucleation [9].

Experiments also show that grains typically do not grow as spheres but very irregularly. Different parts of the grain boundary may migrate at different rates [10], producing anisotropic grain shapes, and grains may exhibit facets or protrusions during growth [11–13]. Anisotropic growth in two dimensions has been studied, and it has been shown that mutual blocking/shielding between anisotropic growing grains strongly affects the transformation (see e.g. [14]). The influence of grain shapes on the recrystallization kinetics studied in three dimensions is an issue for future investigations.

In-situ studies show that wide growth rate distributions exist, with some grains growing much faster than average. Reasons for this may relate to inhomogeneities in the deformed microstructure or

* Corresponding author. Tel.: +45 4677 5730; fax: +45 4677 5758; e-mail: rasmus.godiksen@risoe.dk

1359-6462/$ - see front matter
doi:10.1016/j.scriptamat.2007.04.036

orientation-dependent growth rates. Generally, every grain is observed experimentally to have its own recrystallization kinetics [15,16], but the effects of growth rate distributions on recrystallization kinetics and microstructure are largely unknown.

In this investigation, we study the effect of growth rate distributions on recrystallization kinetics and microstructure evolution by simulations. Following the JMAK model, we assume site-saturated nucleation, that the nuclei are distributed randomly in space and that grains grow as spheres until impingement, but we model collections of grains with distributions of growth rates. We use the JMAK assumptions of random nucleation and spherical growth, even though experiments show that these are oversimplified, as discussed above, because we want to study the simplest possible cases containing growth rate distributions without any other complications, and thus be able to isolate the effects of growth rate distributions.

As done in Ref. [16], we assume that the time dependence of the unimpinged radius of the individual grains is given by $r = At^{1-\alpha}$, where A is the growth rate at $t = 1$ and α the growth rate decline ($0 \leqslant \alpha < 1$).

The investigations are performed by so-called geometric simulations. These should be considered as numerical solutions of JMAK-like problems that are too complex to solve analytically. Also, the simulations provide temporal microstructural information that is not available in the analytical JMAK framework. The simulations should not be taken as precise predictions for certain materials but serve the purpose of exploring what will happen when distributions of growth parameters are present.

Before each simulation is started every grain is awarded an individual set of parameters: position of nucleus, nucleation time, A and α. The algorithm used solves the numerical problem in a discretized simulation volume; the discretization used is a division of the volume into cubic voxels. Nucleation is introduced by assigning nucleation time $t_N = 0$ (site saturation) and growth parameters to random voxels. The strategy for calculating the growth is to make an initial solution by the method described in Ref. [17], where no blocking between growing grains occurs, and subsequently refining the initial solution to handle problematic voxels: in the initial solution every voxel is recrystallized by the grain giving the smallest recrystallization time: $t_V = \min_N((r_{NV}/A_N)^{1/(1-\alpha_N)} + t_N)$, where r_{NV} is the distance from the nucleus of the grain N to the voxel V. In this solution no blocking is taken into account because grains cannot screen each other's growth. The initial solution may have grains that grow through each other, which is clearly unphysical, but often the method produces quite good solutions (in some cases, exact solutions) and requires very short simulation times.

The problematic voxels are those that cannot be recrystallized by direct growth from a nucleus, e.g. voxels that are recrystallized by a fast growing grain that has to grow around a slow growing grain to reach the voxels. These are dealt with in a refinement method where voxels are recrystallized in a time step sequence: at each time step only those voxels with recrystallized neighbors are allowed to recrystallize themselves. All already recrystallized voxels in a given time step are in principle allowed to act as new nuclei, with the properties inherited from their parent nucleus and nucleation time equal to their recrystallization time. Only those recrystallized voxels in a neighborhood around an unrecrystallized voxel are considered for computational reasons. Also, only those neighboring voxels that can reach the unrecrystallized voxel by a straight unbroken path can lead to its recrystallization. If no recrystallized voxels fulfills these criteria, the unrecrystallized voxel is shifted to the next time step and the analysis is performed again. This method is illustrated in Figure 1. The refinement method makes it possible for grains to grow around each other due to the time-step approach; it assures that the recrystallization times are correct and that no grains can grow through each other.

Analysis of the simulations are carried out at various time steps using line scans along the x-, y- and z-axes. Volume fractions are found as $V_V = L_{rex}/L_{tot}$, where L_{rex} is the length of the scan lines that pass through recrystallized material and L_{tot} is the total length of all lines. Intercept lengths d are found as the chords through the grains produced by the scan lines.

All simulations have been performed in a volume of 200^3 voxels containing $N = 1000$ nuclei. For each type of distribution, three simulations with different seeds of nuclei positions and growth parameters have been performed to increase the data quality.

Table 1 lists the distributions simulated; the functions $n(A)$ and $n(\alpha)$ describe probability densities in A and α for the distributions used. JMAK simulations are included for comparison purposes. The width of the bell-shaped distributions in α generally narrows as p and q increase, so that p1q1 has a broader distribution than p10q10, as seen in Table 1.

Distributions in growth parameters have a big impact on the recrystallized microstructure, as seen in Figure 2,

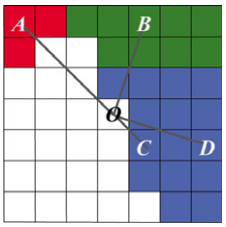

Figure 1. Neighborhood around the unrecrystallized voxel O under consideration. The figure shows a two-dimensional neighborhood, but in the algorithm three-dimensional neighborhoods are used. White squares represent not yet recrystallized voxels and colored squares represent already recrystallized voxels belonging to three different grains. Recrystallization paths from some of the neighbor voxels A, B, C, D to O are shown as lines. In the algorithm recrystallization paths from all recrystallized neighbors to the unrecrystallized voxel under consideration are investigated. Voxel A cannot recrystallize O because the path is broken by unrecrystallized voxels. Voxel B cannot recrystallize O because the path is broken by recrystallized voxels from another grain. Voxels C and D from the same grain can both recrystallize O by unbroken paths, and O will therefore be recrystallized by the grain that C and D belongs to. The recrystallization time for O is calculated as the shortest time for growth from voxels C or D using the recrystallization times for C and D combined with the distances from C and D to O.

Table 1. Distributions used for $r = At^{1-\alpha}$

JMAK	$A = 1,\ \alpha = 0$	
A uniform	$n(A) = 1/2$ $0 \leqslant A < 2,\ \alpha = 0$	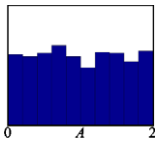
A log-normal	$n(A) = \frac{1}{A\sigma\sqrt{2\pi}}\exp\frac{-(\ln A-\mu)^2}{2*\sigma^2}$ $0 < A,\ \alpha = 0$	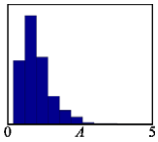
$1/A$[a]	$n(A) = \frac{1}{\ln 100}\frac{1}{A}$ $.05 < A < 5,\ \alpha = 0$	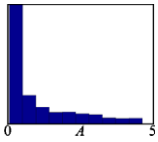
α uniform	$n(\alpha) = 1$ $0 \leqslant \alpha < 1,\ A = 1$	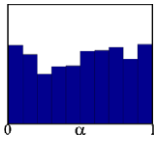
α p1q10-bell[b]	$n(\alpha) = 132 \cdot \alpha(1-\alpha)^{10}$ $0 \leqslant \alpha < 1,\ A = 1$	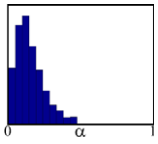
α p1q1-bell[c]	$n(\alpha) = 6 \cdot \alpha(1-\alpha)$ $0 \leqslant \alpha < 1,\ A = 1$	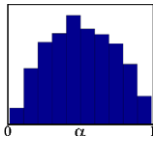
α p10q10-bell[d]	$n(\alpha) = 3879 \times 10^3 \cdot \alpha^{10}(1-\alpha)^{10}$ $0 \leqslant \alpha < 1,\ A = 1$	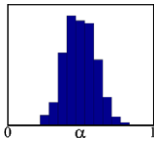
α p5q1.5-bell[e]	$n(\alpha) = 87.98 \cdot \alpha^5(1-\alpha)^{1.5}$ $0 \leqslant \alpha < 1,\ A = 1$	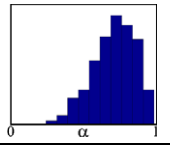

All distributions are normalized so that $\int n(x) = 1$ and $\langle A \rangle = 1$. Histograms show examples of distributions.

[a] $n(A) = \frac{c}{A^m}$, used with parameter $m = 1$ [16].

[b] $C\alpha^p(1-\alpha)^q$, used with parameters $p = 1$ and $q = 10$ [16].

[c] $C\alpha^p(1-\alpha)^q$, used with parameters $p = 1$ and $q = 1$ [16].

[d] $C\alpha^p(1-\alpha)^q$, used with parameters $p = 10$ and $q = 10$ [16].

[e] $C\alpha^p(1-\alpha)^q$, used with parameters $p = 5$ and $q = 1.5$ [16].

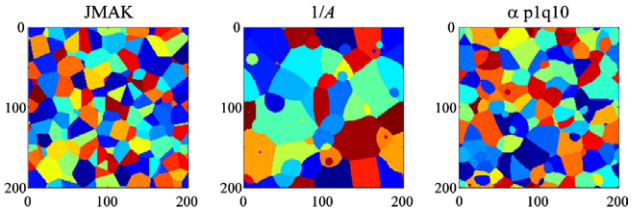

Figure 2. Sections from three simulations: JMAK conditions (left), $1/A$ (middle) and α p1q10 distribution (right). For explanation see Table 1. Different colors mark different grains.

which shows the fully recrystallized microstructure from three simulations: JMAK conditions, $1/A$ and p1q10-bell. The simulations have been performed with the same nucleation density and therefore, the same number of grains (ensured by the site saturation condition), but the recrystallized microstructures are clearly very different for the three simulations. Note that the grain boundaries in the JMAK simulations are straight, but curved boundaries occur in the $1/A$ and p1q10 simulations due to neighboring grains with different growth rates. Very small grains are observed especially in the $1/A$ simulation. These would not normally be seen in experiments because such small grains would tend to disappear very quickly by grain growth (surface reduction) mechanisms if such processes were possible. In our simulation this is not allowed to happen.

The difference in the recrystallized microstructure can be quantified by measuring the distributions of grain intercept lengths d. The distributions for all simulations normalized by the mean intercept length $\langle d \rangle$ are shown in Figure 3. A clear difference between the JMAK simulation and all distributions both in A and α are seen: the JMAK simulation has a typical intercept length (the peak of the intercept distribution) close to the mean intercept length, whereas data from all simulations employing distributions of either A or α have typical intercept lengths that are smaller than the mean length. Also, the simulations with growth rate distributions show extended tails in their distributions, clearly seen in the inset of Figure 3. In other words, growth rate distributions have very significant effects on the homogeneity of the recrystallized microstructure. No general difference is observed between A and α distributions; both A and α distributions show extended tails to various degrees, depending on the distribution details. If growth rates are correlated with grain orientations, recrystallization textures may arise from growth rate distributions because grains with some orientations will grow to sizes much larger than average and their orientations consequently dominate the recrystallization texture. Therefore, heterogeneities in the recrystallized microstructure are expected in situations where texture arises from growth rate distributions.

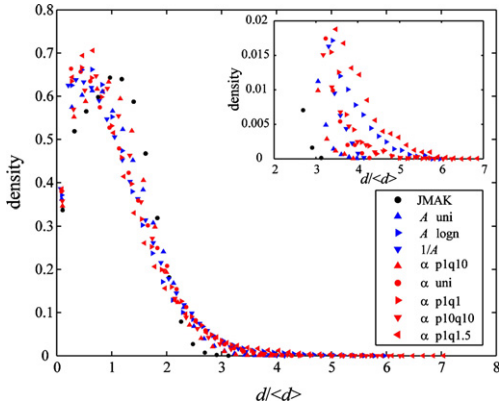

Figure 3. Distributions of line scan intercepts d normalized to the mean intercept length $\langle d \rangle$. The inset shows a close-up of the intercept distribution tails.

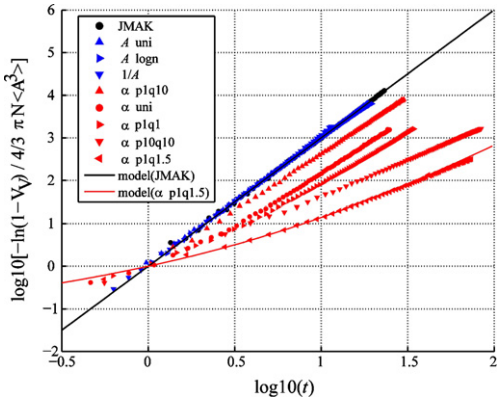

Figure 4. Averaged and pre-factor-normalized growth kinetics for all simulations. Full lines are drawn for the analytical JMAK solution and the numerical solution for the p5q1.5 distribution presented in Ref. [16]. Normalization is done by dividing $\ln(1 - V_V)$ with $4/3\pi N\langle A^3\rangle$, where N is the number of grains and $\langle A^3\rangle$ is the average of A^3 for all grains in the simulation. It should be mentioned that the normalization works only in cases of random nucleation.

The overall recrystallization kinetics can be investigated by plotting V_V in the so-called Avrami plot. Figure 4 shows a pre-factor-normalized version of the standard Avrami plot for all simulations. As seen in the figure, all simulations with distributions in A collapse onto a single line, indicating that any distribution solely in A can only change the pre-factor of $V_V(t)$. In Ref. [16] it was predicted that the $1/A$ distribution would not fundamentally change the growth kinetics compared with the JMAK model, only the pre-factor of $V_V(t)$. This seems to be true in general for all distributions solely in A.

A change in the distribution of α seems to have a significant impact on the growth kinetics. It appears that distributions with the majority of grains having an α near 1 deviate more strongly from the JMAK model than distributions with a majority of αs near 0. This makes sense since the JMAK model can be considered having a delta-function distribution of α centered at $\alpha = 0$.

The data for the various α distributions in Figure 4 exhibits upwards curvatures to various degrees. We interpret this in the context of 'the dominating grains': V_V from a collection grains with equal parameters A and α would produce a straight curve with a slope of $3(1 - \alpha)$ if plotted in Figure 4. A very small slope in Figure 4 indicates that the dominating grains have high α values and a slope near 3 indicates that $\alpha \approx 0$. An upward curved data series indicates that the dominating grains initially have high α values but grains with low α values take over later on. This is plausible because the grain radius is given by $r = At^{1-\alpha}$, which means that the high-α grains grow fast initially but lose pace as time passes, while the low-α grains more or less maintain the same growth rate throughout the simulation.

Using this interpretation, we see that the curvature observed in Figure 4 must be related to the width of the distribution. A very narrow distribution cannot produce grains with significantly different α-parameters. Therefore, the dominating grains will all have almost the same growth properties. By comparing the data from p1q1 and p10q10, we see that they initially start out with the same slope but deviate later on. p1q1, which is the broader of the two distributions, curves upward more than p10q10, as expected from the above arguments.

In summary, the recrystallization microstructure and texture may change significantly as a result of growth rate distributions. If the radius of recrystallizing grains are given by $r = At^{1-\alpha}$, distributions of both A and α may produce significant deviations in microstructure and grain size distribution from JMAK behaviour. Distributions of A do not change the overall growth kinetics represented by V_V apart from a pre-factor, but distributions in α do. The changed kinetics can be interpreted in context of the dominating grains. Grains with different αs may dominate at different times, producing upward curved data series in the Avrami plot. These results underline the importance of considering growth rate distributions when analyzing recrystallization kinetics and microstructure development.

The authors thank R.A. Vandermeer for very useful discussions and gratefully acknowledge the Danish National Research Foundation for supporting the Center for Fundamental Research, Metal Structures in Four Dimensions, within which this work was performed.

[1] R.W. Cahn, in: R.W. Cahn, P. Haasen (Eds.), Physical Metallurgy, Elsevier Science Publishers, Amsterdam, 1983, pp. 1595–1671.
[2] W.A. Johnson, R.F. Mehl, Trans. Am. Inst. Min. Metall. Eng. 135 (1939) 416.
[3] M. Avrami, J. Chem. Phys. 7 (1939) 1103.
[4] M. Avrami, J. Chem. Phys. 8 (1940) 212.
[5] M. Avrami, J. Chem. Phys. 9 (1941) 177.
[6] A.E. Kolmogorov, Bull. Acad. Sci. URSS 1 (1937) 355.
[7] P.A. Beck, P.R. Sperry, H. Hu, J. Appl. Phys. 21 (1950) 420.
[8] R.A. Vandermeer, P. Gordon, Trans. Am. Inst. Min. Metall. Eng. 215 (1959) 577.
[9] R.A. Vandermeer, R.A. Masumura, Acta Metall. Mater. 40 (1992) 877.
[10] S. Schmidt, S.F. Nielsen, C. Gundlach, L. Margulies, X. Huang, D. Juul Jensen, Science 305 (2004) 229.
[11] M.A. Martorano, M.A. Fortes, A.F. Padilha, Acta Mater. 54 (2006) 2769.
[12] R.B. Godiksen, Z.T. Trautt, M. Upmanyu, J. Schiotz, S. Schmidt, D. Juul Jensen, submitted for publication.
[13] D. Juul Jensen, D. Rowenhorst, S. Schmidt, Proc. Rex GG III, in press.
[14] T. Pusztai, L. Granasy, Phys. Rev. B 57 (1998) 14110.
[15] E.M. Lauridsen, H.F. Poulsen, S.F. Nielsen, D. Juul Jensen, Acta Mater. 51 (2003) 4423.
[16] D. Juul Jensen, E.M. Lauridsen, R.A. Vandermeer, Proc. TMS Annu. Meet. (2002) 361.
[17] D. Juul Jensen, Metall. Mater. Trans. A 28 (1997) 15.

C Three-Dimensional Geometric Simulations of Anisotropic Growth during Transformation Phenomena

R.B. Godiksen, P.R.Rios, R.A.Vandermeer S. Schmidt, D. Juul Jensen, Accepted for publication in *Scripta Materialia*, doi:10.1016/j.scriptamat.2007.10.003 (2007).

Available online at www.sciencedirect.com
ScienceDirect
Scripta Materialia xxx (2007) xxx–xxx
Scripta MATERIALIA
www.elsevier.com/locate/scriptamat

Three-dimensional geometric simulations of random anisotropic growth during transformation phenomena

Rasmus B. Godiksen,[a,*] Paulo R. Rios,[b] Roy A. Vandermeer,[a] Søren Schmidt[a] and Dorte Juul Jensen[a]

[a] *Center for Fundamental Research: Metal Structures in Four Dimensions, Materials Research Department, RisøNational Laboratory, Technical University of Denmark, 4000 Roskilde, Denmark*
[b] *Universidade Federal Fluminense, Escola de Engenharia Industrial Metalurgica de Volta Redonda, Av. dos Trabalhadores, 420, Volta Redonda, RJ 27255-125, Brazil*

Received 12 July 2007; revised 3 October 2007; accepted 3 October 2007

In this paper, the effects of anisotropic growth during transformation processes are investigated by geometric simulations of randomly oriented shape preserved ellipsoids in three dimensions and the applicability of idealized models are tested. Surprisingly, the results show that the models can predict the results for random ellipsoids up to aspect ratios of at least four, making the effects of random anisotropic growth less pronounced than what has previously been predicted from two-dimensional simulations or other, more restrictive three-dimensional simulations.

Keywords: Phase transformations; Recrystallization; Geometric simulations; Modelling; Analytical methods

Many processes in materials, such as crystallization from melts, recrystallization of deformed materials or solid state phase transformations are governed by the nucleation and growth of individual regions (grains) consisting of one phase (the product) within another phase (the matrix). The driving force for the nucleation and growth of the grains depends on the actual process, but is generally associated with the free energy release due to the conversion from matrix to product phase. The product grains will grow as long as their grain boundaries are free to migrate into yet untransformed matrix material, but when one grain boundary impinges upon another the migration stops. In very many cases, the growth is observed to be anisotropic (e.g. [1–3]).

Nucleation and growth kinetics are often interpreted using the JMAK model, developed by Johnson, Mehl [4], Avrami [5–7] and Kolmogorov [8]. The popularity of the JMAK model for interpreting experimental data from nucleation and growth phenomena is probably due to the simple and generic nature of the model, which enables the use of it in many scientific areas. The aim of the present work is to analyze the potential and pitfalls of using JMAK to analyze random anisotropic growth.

In this study we will use a numerical simulation scheme to investigate a system that exhibits anisotropic growth where different grains have different preferred growth directions. The preferred growth directions are chosen randomly for the different grains and we will therefore term this *random anisotropic growth*. In this paper we will investigate the simplest possible case of random anisotropic growth, which allows us to study random anisotropic growth without other complications.

Investigations of random anisotropic growth by modelling and simulation have been carried out, primarily in two dimensions [9–11], but three-dimensional simulations have also been carried out [12,13]. In the latter three-dimensional simulations, growing grains were either completely two-dimensional (flat) [13] or not allowed to grow around each other [12]. In the simulations presented here grains are three-dimensional and are allowed to grow around each other, which is what is observed experimentally in, for example, recrystallization. Simulations, in both two and three dimensions, predict that the transformation kinetics departs from the JMAK solution during random anisotropic growth, something

* Corresponding author. Tel.: +45 4677 5730; fax: +45 4677 5758; e-mail: rasmus.godiksen@risoe.dk

1359-6462/$ - see front matter © 2007 Published by Elsevier Ltd. on behalf of Acta Materialia Inc.
doi:10.1016/j.scriptamat.2007.10.003

that is ascribed to blocking, i.e. the fast growth directions being blocked faster than the slow ones [9].

The JMAK model assumed that all grains nucleate at random locations and grow until impingement [4–8]. The nucleation rate may be time-dependent and the growth rate time- or direction-dependent, as shown by Kolmogorov [8] and Christian [14], but all grains are required that have the same growth rate in a particular direction at a particular time. Anisotropic growth can be included in the JMAK model because the growth rate may be dependent on direction, but since the growth rate of all grains will have the same directional dependence, this could be called *aligned anisotropic growth*. Extensions to the JMAK model have been developed enabling, for example, nucleation along grain edges or triple junctions [15], parabolic growth [14] or distributions of the growth rates [16,17] to be dealt with. The original JMAK model is used to predict the volume fraction transformed V_V, but extensions have been made to describe other microstructural parameters, such as the free surface fraction S_V [18], the impinged surface fraction R_V [19] and the contiguity [20]. The concept of the microstructural path (MP), developed by DeHoff [21] and adopted by Vandermeer [18], describes the transformation process as the (multidimensional) path that a process follows over time through a microstructural parameter-space, for example $\mathrm{MP}(t) = [V_V(t), S_V(t), Crr(t)]$.

At this point random anisotropic growth cannot be dealt with properly in a JMAK framework and the effect that three-dimensional random anisotropic growth has on the transformation kinetics when grains are allowed to grow around each other is unknown. The original JMAK model is, however, used in situations that lie outside the original assumptions of the model, and JMAK might be able to describe random anisotropic growth as well. The purpose of this paper is to test to what extend the classic JMAK model and extensions for S_V and R_V can be used for random anisotropic growth.

The essential element of the JMAK model is the so-called extended volume fraction $V_X = \sum_{i=1}^{N} V_i / V_{\mathrm{total}}$, where N is the number of grains and V_i is the unimpinged volume of grain i, i.e. the volume of the grain if it were allowed to grow completely undisturbed. V_X is therefore defined as the volume fraction that would exist if grains did not impinge and could grow through each other. Using the JMAK assumptions, the relation between V_V and V_X can be shown to be [4,6,8]:

$$V_V = 1 - \exp(-V_X) \tag{1}$$

S_V can be predicted by the model of DeHoff [21] and Vandermeer et al. [18]:

$$S_V = S_X(1 - V_V) \tag{2}$$

where S_X is the extended surface fraction defined in a similar way as V_X. This formula requires that the nuclei are randomly distributed. If Eq. (1) is also used, Eq. (2) can be rewritten as:

$$S_V = S_X \exp(-V_X) \tag{3}$$

R_V can be predicted by a model proposed by Gokhale [22] and utilized for aligned anisotropic growth by Rios et al. [19]:

$$R_V = R_{VF} \frac{\int_0^{V_X} S_X \exp(-V_X)\,\mathrm{d}V_X}{\int_0^{\infty} S_X \exp(-V_X)\,\mathrm{d}V_X} \tag{4}$$

where R_{VF} is the value for R_V in the fully transformed sample. R_{VF} for spherical grains can be found theoretically by $R_{VF} = 2.91(N/V_{\mathrm{total}})^{1/3}$, as shown by Meijering [23]. The formulas Eqs. (1)–(4) are applicable for aligned anisotropic growth; the shape of the grains enter into the calculation of V_X and S_X. In summary, exact formulas exist for V_V, S_V and R_V under JMAK conditions with aligned anisotropic growth, but it is unclear how to deal with random anisotropic growth.

In this paper we investigate grains that grow as randomly oriented prolate (needles) or oblate (plates) ellipsoids in three dimensions, as well as ellipses in two dimensions for comparison. The changes in V_V, S_V and R_V as a result of shape changes are investigated as well as the extent to which the existing models Eqs. (1)–(4) can be used to make predictions about random anisotropic growth.

The investigations are carried out by geometric computer simulations, where grains with predefined growth rates and shapes grow from nuclei until they impinge upon other grains. The simulation method used here is an extension of the method developed in Ref. [24] and is described in Ref. [17]. The simulation is executed in time steps in a discretized simulation volume of cubic voxels, where in each time step voxels with transformed neighbors are allowed to transform. The growing grains retain their growth rates in every direction and parts of the sample transformed by a certain grain act as new starting points from which the grain can continue to grow with the same properties as the original nucleus of the grain. In this way grains are allowed to grow around each other.

The simulation method can be used with a variety of growth parameters, such as non-random nucleation, preferred growth directions and distributions of growth rates [17]. The method produces numerical solutions to problems involving nucleation and growth of grains with predefined properties, and should be considered as numerical solutions of JMAK-like problems that are too complex to solve analytically. Also the simulation provides temporal and structural information that is not available in analytical models such as Eqs. (1)–(4).

In this investigation the grain kinetics is identical to the JMAK model apart from the random orientation. We have chosen to maintain the oversimplistic assumption of random nucleation and constant growth rate to be able to clearly identify the effects of randomly oriented non-spherical grain shapes. Prolate ellipsoids with aspect rations 1:1:16, 1:1:8, 1:1:4, 1:1:2 and 2:2:3 and oblate ellipsoids with aspect rations 16:16:1, 8:8:1, 4:4:1, 2:2:1 and 3:3:2 have been simulated. Simulations employing spherical growth were also carried out for comparison. Each simulation consists of 100 nuclei in a cubic simulation cell with periodic boundary conditions along x, y and z directions and a side length of 232 voxels, giving a total of approximately 12.5×10^6 voxels.

In two dimensions ellipses, instead of ellipsoids, are simulated. The aspect ratios of the simulated two-dimensional ellipses were 1:16, 1:8, 1:4, 1:2 and 2:3,

Please cite this article in press as: R.B. Godiksen et al., Scripta Mater. (2007), doi:10.1016/j.scriptamat.2007.10.003

and simulations using circles were also simulated. The ellipses were oriented randomly in the plane, making the simulations similar to the ones performed by Pusztai and Granasy [10]. Each two-dimensional simulation consists of 100 nuclei in a square simulation cell side length 500 pixels giving a total of 250×10^3 pixels.

Every three-dimensional simulation was repeated six times with different seeds (positions of nuclei and orientations of grains) and every two-dimensional simulation was repeated 12 times to improve statistics.

For the simulations of spheres in three dimensions the growth rate is set to 1 voxel per time unit, giving a volume of $v_s(t) = 4/3\pi t^3$ voxels. By scaling the aspect ratios a:b:c of an ellipsoid so that $a \cdot b \cdot c = 1$, the volume of the ellipsoid becomes $v_e(t) = 4/3\pi(a \cdot b \cdot c)t^3 = 4/3\pi t^3$; the same as for the sphere. The growth rates of the ellipsoids in the simulations are chosen to make $V_X(t)$ the same for all simulations. The same is done for the simulations in two dimensions.

The volume fractions as a function of time for all three-dimensional simulations are plotted in Figure 1, together with the predictions made by the JMAK model (Eq. (1)). Since V_X is the same for all the ellipsoids simulated, as explained above, Eq. (1) gives the same predictions for all simulations. The data and the model predictions coincide almost exactly for aspect ratios of up to four and Eq. (1) is therefore useable in three dimensions for phenomena with random ellipsoidal growth up to this aspect ratio.

In the inset of Figure 1 the so-called Avrami parameter defined as

$$p(t) = \frac{\mathrm{d}[\log(-\ln(1 - V_V(t)))]}{\mathrm{d}[\log(t)]} \quad (5)$$

which is plotted as a function of V_V. For the JMAK model, where every grain nucleates at $t = 0$ in three dimensions, $p(t) = 3$, which is indicated by the full line in the inset. Deviations in p from the JMAK are clearly seen for the simulations with aspect ratios greater than four. The time-averaged Avrami parameters $\langle p(t) \rangle$ ('$\langle\ \rangle$' meaning 'average of') during the entire growth processes are listed in Table 1. Up to an aspect ratio of four the deviations in $\langle p(t) \rangle$ from JMAK behavior are less than 3%. We see that the deviations from JMAK behavior are stronger for the oblate ellipsoids than for the prolate grains, which may be due to the greater blocking potential of plates compared with needles in three dimensions.

Table 1. Average Avrami parameters $\langle p(t) \rangle$ for simulations of prolate and oblate ellipsoids in three dimensions and ellipses in two dimensions

Aspect ratio (a/b)	3d-Prolate ellipsoids (a:b:b)	3d-Oblate ellipsoids (a:a:b)	2d Ellipses (a:b)
1	2.95	2.95	2.03
1.5	3.02	2.97	1.98
2	3.00	2.96	1.96
4	2.97	2.92	1.80
8	2.73	2.62	1.60
16	2.57	2.27	1.38

The volume fractions from two-dimensional simulations of ellipses as well as circles are shown in Figure 2 and the Avrami parameter p is shown in the inset of Figure 2. p should be two for the JMAK model where all grains nucleate at $t = 0$ in two dimensions.

By comparing Figures 1 and 2 it is seen that the deviations from JMAK behavior are much more pronounced in two than in three dimensions. $\langle p(t) \rangle$ for the two-dimensional simulations (see Table 1) also shows much stronger deviations than for three dimensions: for an aspect ratio of eight, for example, $\langle p(t) \rangle$ is reduced by nearly 20% in two dimensions, whereas the three-dimensional simulations show a reduction of around 10–15%. The stronger effect of random anisotropic growth in two dimensions is due to the more efficient blocking between grains: in two dimensions, the major axis of all ellipses will be in the same plane and will therefore impinge quickly, but in three dimensions the major axis of, for example, prolate ellipsoids will typically be out of plane and thus not impinge as quickly.

The MP S_V vs. V_V and R_V vs. V_V for all three-dimensional simulations together with model predictions calculated from Eqs. (1)–(4) are plotted in Figure 3. Model predictions have to be calculated for each aspect ratio because the surface area depends on the aspect ratio. For S_V we see that the model predictions work rather well for aspect ratios up to eight. For aspect ratios of 16 the model cannot predict the simulated data. For R_V the model predictions are even better; here only the oblate grains with an aspect ratio of 16:16:1 cannot be described by the model. It is expected, however, that the model predictions are better for R_V since Eq. (4) uses R_{VF} from the simulations as input.

The MPs for all aspect ratios have the same shape and can be made to coincide by simple scaling, which

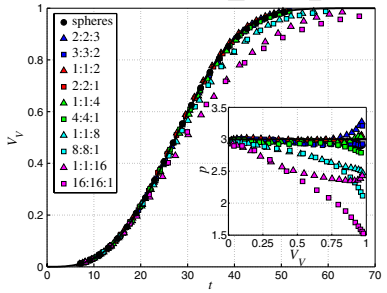

Figure 1. $V_V(t)$ for three-dimensional simulations as well as the predictions of the JMAK model Eq. (1) (full line). The inset show the Avrami parameter p defined in Eq. (5) for the simulations.

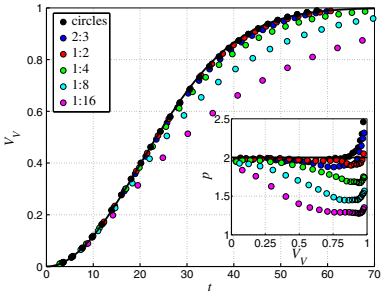

Figure 2. $V_V(t)$ for two-dimensional simulations as well as the predictions of the JMAK model Eq. (1) (full line). The inset show the Avrami parameter p defined in Eq. (5) for the simulations.

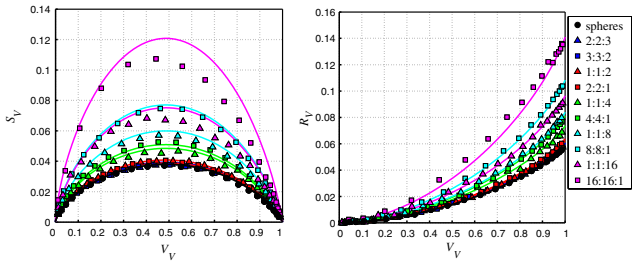

Figure 3. MP $S_V(t)$ vs. $V_V(t)$ and $R_V(t)$ vs. $V_V(t)$ for three-dimensional simulations together with model predictions Eqs. (1)–(4) (full lines). The MP for all ellipsoids have the same shape and can be made to coincide by a single fitting parameter.

shows that the MP of the ellipsoids are very similar, although the aspect ratios differ a lot. A plot of the supplementary material online shows the scaled data.

In two dimensions the MP derived from models for S_V and R_V works well up to an aspect ration of four but breaks down for aspect ratios of 1:8 and 1:16. Therefore S_V and R_V (like V_V) exhibit increased sensitivities to random anisotropic growth in two dimensions compared with three dimensions. A figure similar to Figure 3 for the two-dimensional MP can be found in the supplementary material online.

The contiguity *Crr* is, as described above, defined as the fraction of the total boundary area that is impinged, and can be used to describe the randomness of the nuclei [20,25]. Figure 4 shows the MP for *Crr* vs. V_V for all three-dimensional simulations. As seen, the data coincide, which is expected due to the random placement of the nuclei, and the spherical model fits well. Interestingly, the models using aligned ellipsoids do not work very well. The contiguity for the two-dimensional simulations show the same tendency, although the deviations of the models are larger (see the supplementary material online).

Simulations where randomly oriented anisotropic grains can grow around each other have to the best of our knowledge not been simulated in three dimensions before. The final grain shapes of fully recrystallized grains are very complicated, with clear signs of interactions with other grains. Many parts of the grains would not have been transformed by the particular grains if they were not allowed to grow around each other, and consequently the grain shapes would have been very different (see the supplementary material online).

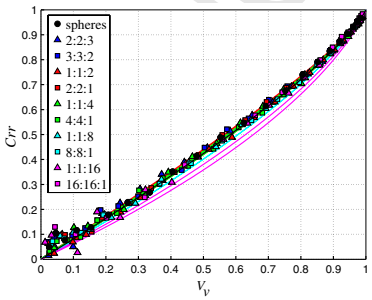

Figure 4. MP *Crr*(*t*) vs. $V_V(t)$ for three-dimensional simulations together with model predictions Eqs. (1)–(4) (full lines).

The ability for grains to grow around each other also influences the transformation kinetics. The results reported in Ref. [12], where no growing around was allowed, showed larger deviations between random ellipsoidal and spherical growth in three dimensions than are reported here: an aspect ratio of five clear reductions in p were observed in Ref. [12], whereas we did not observe any significant change up to an aspect ratio of four. This difference may be ascribed to the possibility for grains to grow around each other.

In summary, the model Eq. (1) is able to predict the evolution of V_V very well up to aspect ratios of four for three-dimensional randomly oriented prolate and oblate ellipsoidal growth, although it models aligned growth. Predictions of the MP for S_V and R_V vs. V_V based on the models Eqs. (1)–(4) are even better; here predictions hold up to aspect ratios of eight. The MPs for *Crr* vs. V_V are identical for all aspect ratios, probably due to the random placement of the nuclei.

In some phenomena, e.g. recrystallization, aspect ratios beyond four are very rarely seen and the models Eqs. (1)–(4) will therefore be almost accurate. For other phenomena, such as martensitic transformations, where high aspect ratios may occur, new models may be needed.

The deviations from model behavior (Eqs. (1)–(4)) are more pronounced in two dimensions than in three (in two dimensions the models break down at aspect ratios of four or more), which is due to the stronger blocking effect in two dimensions. Therefore care has to be taken when using results from two-dimensional simulations/models in connection with three-dimensional nucleation and growth phenomena.

The authors gratefully acknowledge the Danish National Research Foundation for supporting the Center for Fundamental Research, Metal Structures in Four Dimensions, within which this work was performed.

Supplementary data associated with this article can be found, in the online version, at doi:10.1016/j.scriptamat.2007.10.003.

[1] S. Schmidt, S.F. Nielsen, C. Gundlach, L. Margulies, X. Huang, D. Juul Jensen, Science 305 (2004) 229.
[2] C.M. Wayman, in: R.W. Cahn, P. Haasen (Eds.), Physical Metallurgy, Elsevier Science Publishers, 1983, pp. 1031–1074.
[3] M.I.F. Macedo, C.A. Bertran, C.C. Osawa, J. Mater. Sci. 42 (2007) 2830.
[4] W.A. Johnson, R.F. Mehl, Trans. Am. Inst. Min. Metall. Eng. 135 (1939) 416.
[5] M. Avrami, J. Chem. Phys. 7 (1939) 1103.
[6] M. Avrami, J. Chem. Phys. 8 (1940) 212.
[7] M. Avrami, J. Chem. Phys. 9 (1941) 177.
[8] A.N. Kolmogorov, in: Selected Works, Kluwer, Boston, MA, 1991, pp. 188–193.
[9] D.P. Birnie, M.C. Weinberg, J. Chem. Phys. 103 (1995) 3742.
[10] T. Pusztai, L. Granasy, Phys. Rev. B 57 (1998) 14110.
[11] B.J. Kooi, Phys. Rev. B 70 (2004) 054103.
[12] M.P. Shepilov, D.S. Baik, J. Non-Cryst. Solids 171 (1994) 141.

[13] B.J. Kooi, Phys. Rev. B 73 (2006).
[14] J.W. Christian, The Theory of Transformations in Metals and Alloys, Part1 (1975).
[15] J.W. Cahn, Acta Metall. 4 (1956) 449.
[16] E.M. Lauridsen, H.F. Poulsen, S.F. Nielsen, D. Juul Jensen, Acta Mater. 51 (2003) 4423.
[17] R.B. Godiksen, S. Schmidt, D. Juul Jensen, Scripta Mater. 57 (2007) 345.
[18] R.A. Vandermeer, R.A. Masumura, B.B. Rath, Acta Metall. Mater. 39 (1991) 383.
[19] P.R. Rios, R.B. Godiksen, S. Schmidt, D. Juul Jensen, R.A. Vandermeer, Scripta Mater. 54 (2006) 1509.
[20] R.A. Vandermeer, Acta Mater. 53 (2005) 1449.
[21] R.T. Dehoff, in: N. Hansen, D. Juul Jensen, T. Leffers, B. Ralph (Eds.), Proceedings from 7th Riso International Symposium on Metallurgy and Materials Science, 1986, pp. 35–52.
[22] A.M. Gokhale, Metall. Trans. A 19 (1988) 2123.
[23] J.L. Meijering, Philips Res. Rep. 8 (1953) 270.
[24] D. Juul Jensen, Metall. Mater. Trans. A 28 (1997) 15.
[25] P.R. Rios, L.O. Pereira, F.F. Oliveira, W.L.S. Assis, J.A. Castro, Acta Mater. (2007), doi:10.1016/j.actamat.2007.04.003.

D Towards atomic level simulations of recrystallization - setting up suitable geometry

R.B. Godiksen, Z.T. Trautt, M. Upmanyu, S. Schmidt, D. Juul Jensen, *Materials Science and Technology* **21**, 1373–1375 (2005).

Towards atomic level simulations of recrystallisation – setting up suitable geometry

R. B. Godiksen*[1], Z. T. Trautt[2], M. Upmanyu[2], S. Schmidt[1] and D. Juul Jensen[1]

During recrystallisation, high angle grain boundaries migrate through deformed microstructure containing dislocations arranged, for example, in dislocation boundaries. A simple method for designing geometries suitable for atomistic simulations of migrating boundaries during recrystallisation is developed. Preliminary studies show that the method can be used to generate simulation cells with both high angle grain boundaries and small angle dislocation boundaries.

Keywords: Recrystallisation, Atomistic simulation, Molecular dynamics simulation, Grain boundary migration, Deformation microstructure, Simulation geometry design

Introduction

During recrystallisation of deformed metals, new essentially dislocation free grains nucleate and grow while consuming the deformed material. The boundaries surrounding the new grains sweep through the entire deformed matrix altering the orientation of every part of the sample.[1] High angle boundaries migrate at a faster rate than low angle boundaries,[2] and recrystallisation will therefore mainly involve migration of high angle grain boundaries.

Many different factors, such as misorientation across grain boundaries, boundary inclination, particles in the material and structure of the deformed matrix might influence the mobility of, and the driving force for, the migration of boundaries. To understand how different factors influence the migrating boundaries at a fundamental level, information about the atomic mechanisms involved is needed.

Molecular dynamics simulations have been used extensively to understand properties of metals during plastic deformation, for example, to investigate the maximum strength of copper,[3] stacking fault energies and slip mechanisms in various metals[4] and the atomic mechanisms for emission of dislocations from grain boundaries.[5]

Atomistic simulations of boundary migration have also been performed using molecular dynamics simulations,[6] but these have been focused on curvature driven boundary migration. To our knowledge the only atomistic simulations dealing with recrystallisation directly are performed using two dimensional molecular dynamics simulations.[7]

Our aim is to create simulation cells for atomistic simulations suitable to simulate segments of migrating grain boundaries in three dimensions under conditions that capture some of the essential aspects of recrystallisation.

Recent experiments have shown that growing grains exhibit irregular shapes and abrupt movement of grain boundaries, indicating that local inhomogeneities in the microstructure of the deformed matrix may play an important role in recrystallisation.[8]

The microstructure of the deformed matrix depends on both the type of metal and the kind of deformation, but some common features do exist. The dislocations introduced during deformation are typically not randomly distributed. They accumulate in dislocation boundaries, which separate regions with a relatively low dislocation density. Two different types of boundaries are often seen: extended nearly planar boundaries and almost randomly oriented cell boundaries. In almost all cases a sample does not solely contain one type of boundaries, but the two types coexist in it.[9]

Method for designing simulation cells

The simulation cells must be designed in such a way that certain features characteristic of recrystallisation are included. Both high angle grain boundaries between the recrystallising grain and the deformed matrix and small angle dislocation boundaries subdividing the deformed matrix should be present because these, as described in the previous section, are key features of recrystallisation.

Our simulation cells are designed in the following way: First, a rectangular three dimensional simulation box with periodic boundary conditions in all directions is created. Afterwards perfect lattices with certain crystal orientations compared with the axes of the box are made and the blocks of this are cut out and placed inside the simulation box. The blocks are designed in such a way that they fill the entire simulation box. At the interfaces between the blocks, atoms may overlap. If a pair of atoms is closer than $0{\cdot}6r_0$, where r_0 is the intermolecular distance (the distance between two neighbouring atoms

[1]Center for Fundamental Research: Metal Structures in Four Dimensions, Risoe National Laboratory, 4000 Roskilde, Denmark
[2]Simulation and Theory of Atomic-scale Material Phenomena (STAMP), Colorado School of Mines, Golden, CO 80401, USA

*Corresponding author, email rasmus.godiksen@risoe.dk

Published by Maney on behalf of the Institute
Received 30 August 2005; accepted 13 September 2005
DOI 10.1179/174328405X71620

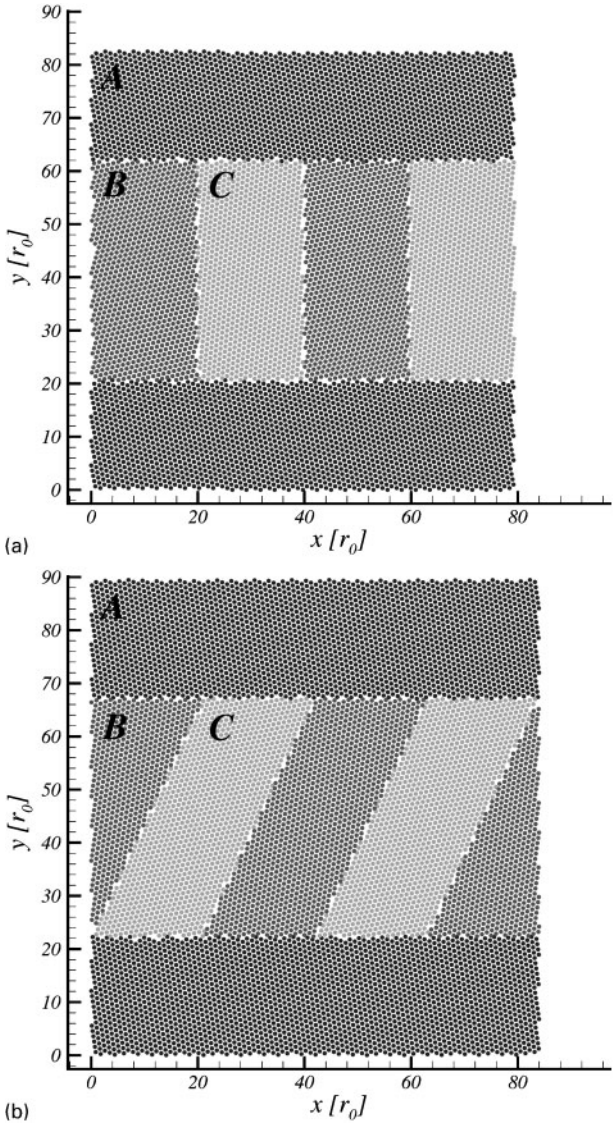

1 Cross-sections of unrelaxed simulation cells with *a* small and high angle interfaces perpendicular to each other and *b* small angle interfaces inclined to high angle interfaces; crystal blocks in both *a* and *b* are all rotated around common [111] direction along *z*-axis, initially having [$\bar{1}1\bar{0}$] direction along *x*-axis; in *a* rotation angle is −19·1° for recrystallising grain *A*, 14·1° for *B* and 24·1° for *C* matrix part. In *b* angle is −21·6° for *A*, 21·6° for *B* and 11·6° for *C* respectively

in a close packed plane in equilibrium), one of them is removed. Examples of simulation cells are shown in Fig. 1.

In the cells shown in Fig. 1, all crystal blocks have their (111) plane normals along the z-direction. The cross-sections of the cells shown in the figures are the (111) planes at $z=0$; the geometry for all other values of z being identical to this. Every rotation of the blocks is made around this common [111] axis. The misorientation between the recrystallised part and the deformed matrix in both cells are 38·2° on average. This angle is chosen because simulations have shown this to have low activation energy for curvature driven boundary migration.[6] Although a different type of driving force is acting in this case, the activation energy for migration of these boundaries might also be low here. All misorientations between neighbouring parts of the deformed matrix are 10°. Distributions of misorientations across small angle boundaries are present in most samples, but 10° is a realistic value for the misorientation of small angle boundaries in medium to high strain deformed microstructures.

The size of the simulation cell is determined in such a way that the crystal lattices are matched up perfectly by the periodic boundary conditions. The size of the simulation cell shown in Fig. 1*a*, in intermolecular distances, is $79{\cdot}37 \times 82{\cdot}49 \times 22{\cdot}05$ and the size of the cell in Fig. 1*b* is $84{\cdot}00 \times 89{\cdot}45 \times 22{\cdot}05$. If the lengths are converted to the lengths typical for aluminum (lattice constant 4·05) this corresponds to $22{\cdot}73 \times 23{\cdot}62 \times 6{\cdot}31$ nm and $24{\cdot}06 \times 25{\cdot}62 \times 6{\cdot}31$ nm. The cells contain 202356 and 232443 atoms respectively – less than 1% were removed owing to the overlap at the interfaces of crystal blocks.

Simulation details

The simulations are carried out using a standard Lennard–Jones (LJ) pair potential

$$U_{ij} = 4\varepsilon \left(\left(\frac{\sigma}{r_{ij}} \right)^{12} - \left(\frac{\sigma}{r_{ij}} \right)^{6} \right) \quad (1)$$

where U_{ij} is the contribution to the potential energy owing to the interaction of atom i and j with a mutual distance r_{ij}. Dimensionless units are used throughout; the energy parameter ε is set to 1 and the distance parameter σ is set to $2^{1/6}$, giving an equilibrium energy of -1 and an equilibrium distance r_0 of 1.

The potential is truncated at a cutoff distance $r_c = 2{\cdot}1 r_0$ and modified by a spline fit beyond r_0, so that it goes to zero smoothly at $r = r_c$. The atomic mass is set to $m_{at} = 1$ for convenience, and the simulations are performed in *reduced units* – time is reported in units of $\tau = (m_{at} r_o^2/\varepsilon)^{1/2}$, and the temperature is reported in units of ε/k_B, k_B being the Boltzmann constant.

Initially the simulation cell is relaxed when using a constant number of atoms, pressure and temperature Metropolis Monte Carlo algorithm (NPT-MC),[10] which performs displacements of individual atoms as well as variations of the box dimensions. The dimensions of the box can be varied individually along the x-, y- and z-directions. The relaxed simulation cell is then used as the initial configuration for the time integrator. The removal of overlapping atoms described above together with this relaxation process prevents local melting during the time integration caused by high potential energy of close lying atoms.

The time integration is performed using a constant number of atoms, volume and temperature velocity Verlet molecular dynamics algorithm (NVT-MD). For efficiency, interpolated table lookups, neighbour lists and a cell method are used for potential and force calculations.[10] The thermostat is a damped Berendsen velocity rescaling algorithm, with damping time $t_d = 0{\cdot}2\tau$. Details on the simulation method can be found elsewhere.[7]

Results and discussion

The method for designing simulation cells presented in the present paper only produces crystal blocks with different orientations cut in certain shapes. If the

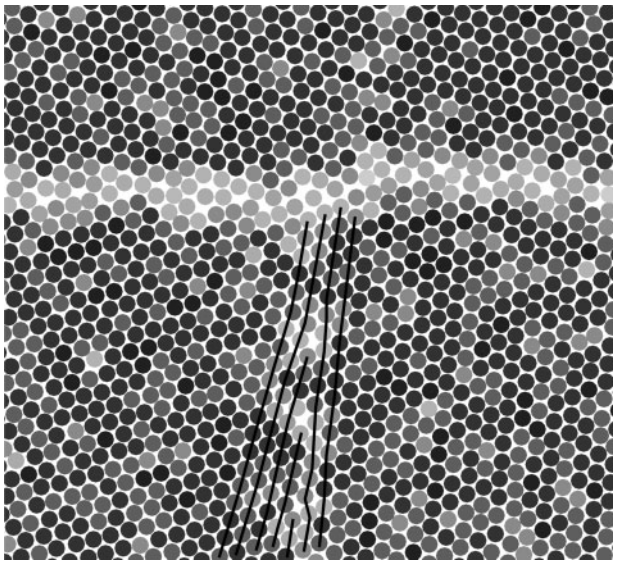

2 Snapshot form simulation of geometry with small and high angle interfaces perpendicular to each other; intensity indicates potential energy, light being high energy and dark being low; small angle interface has developed into dislocation boundary; dislocations along this can be identified by increased energy and ending rows of atoms; high angle interface has developed into grain boundary with thickness of three to four interatomic distances

method is to be sound, realistic boundaries must form at the interfaces between the crystal blocks during simulation.

A preliminary simulation of the geometry shown in Fig. 1*a* has been performed. Initially the simulation was relaxed by a NPT-MC run with $\sim 2 \times 10^6$ single atom movements and $\sim 2 \times 10^4$ box length variations. Following this a NVT-MD was run for 100τ at $T=0{\cdot}17$ (melting temperature is $T_m=0{\cdot}69$). At this point realistic high angle grain boundaries and small angle dislocation boundaries had formed.

Figure 2 shows part of the (111) plane at $z=0$ of the cell at $t=100\tau$. Intensity indicates potential energy; bright is high energy and dark is low. Dislocations have formed along the small angle interface, identifiable by localised excess in potential energy and by the presence of ending rows of atoms. These rows endings exist for all values of z, their positions in x and y are almost identical. Owing to the periodic boundary conditions these ending rows constitutes extra half planes giving the dislocations edge character. No dislocations have formed along the high angle interface. Instead, a grain boundary of a more or less constant thickness, roughly three to four interatomic distances, has formed. It should be noted that dislocations actually form after a few τ.

This preliminary simulation shows that the way of designing simulation cells presented above is capable of producing high angle grain boundaries and small angle dislocation boundaries, which are essential features observed in metals during recrystallisation.

In the cells created here the dislocation density is of the order of 10^{17} m^{-2}, which should be enough to drive recrystallisation because the typical dislocation density is around 10^{16} m^{-2} for heavily deformed materials.[2] Simulations run for longer times will show if the high angle grain boundaries migrates through the deformed matrix consuming the dislocations located in the small angle boundaries. If this is the case such investigations will hopefully provide information on the basic atomic mechanisms of recrystallisation.

Summary

A simple method for designing simulation cells for three dimensional atomistic simulations with structures important for recrystallisation has been developed. Initial simulations show that high angle grain boundaries as well as small angle dislocation boundaries form during simulation runs of the cells designed with this method.

Acknowledgements

The authors gratefully acknowledge the Danish National Research Foundation for supporting the Center for Fundamental Research: Metal Structures in Four Dimensions, within which part of this work was performed. The authors would also like to thank Wolfgang Pantleon, Center for Fundamental Research: Metal Structures in Four dimensions, and Jakob Schiøtz, Center for Atomic-scale Materials Physics (CAMP), Technical University of Denmark, for very fruitful discussions.

References

1. R. W. Cahn: in 'Physical metallurgy', (eds. R. W. Cahn and P. Haasen), Vol. II, 1595–1671; 1983, Amsterdam, North Holland, Elsevier Science Publishers.
2. F. J. Humphreys and M. Hatherly: 'Recrystallization and related annealling phenomena', 2004, Oxford, UK, Elsevier Ltd.
3. J. Schiøtz and K. W. Jacobsen: *Science*, 2003, **301**, 1357–1359.
4. H. Van Swygenhoven, P. M. Derlet and A. G. Frøseth: *Nature Mater.*, 2004, **3**, 399–403.
5. H. Van Swygenhoven, P. M. Derlet and A. Hasnaoui: *Phys. Rev. B*, 2002, **66**, 024101.
6. M. Upmanyu, D. J. Srolovitz, L. S. Shvindlerman and G. Gottstein: *Acta Mater.*, 1999, **47**, 3901–3914.
7. M. Upmanyu, Z. T. Trautt and B. B. Kappes: *Mater. Sci. Forum*, 2004, **467–470**, 715–726.
8. S. Schmidt, S. F. Nielsen, C. Gundlach, L. Margulies, X. Huang and D. Juul Jensen: *Science*, 2004, **305**, 229–232.
9. N. Hansen: *Metall. Mater. Trans. A*, 2001, **32A**, 2917–2935.
10. M. P. Allen and D. J. Tildesley: 'Computer simulation of liquids', 2004, Oxford, UK, Oxford University Press.

E Simulations of Boundary Migration during Recrystallization using Molecular Dynamics

R.B. Godiksen, Z.T. Trautt, M. Upmanyu, J. Schiøtz, D. Juul Jensen, S. Schmidt, *Acta Materialia* **55**, 6383–6391 (2007).

Available online at www.sciencedirect.com
ScienceDirect
Acta Materialia 55 (2007) 6383–6391
Acta MATERIALIA
www.elsevier.com/locate/actamat

Simulations of boundary migration during recrystallization using molecular dynamics

Rasmus B. Godiksen [a,*], Zachary T. Trautt [b], Moneesh Upmanyu [b], Jakob Schiøtz [c], Dorte Juul Jensen [a], Søren Schmidt [a]

[a] Center for Fundamental Research: Metal Structures in Four Dimensions, Materials Research Department, Risø National Laboratory, Technical University of Denmark, 4000 Roskilde, Denmark
[b] Simulation and Theory of Atomic-Scale Material Phenomena (STAMP), Division of Engineering, Materials Science Program, Colorado School of Mines, Golden, CO 80401, USA
[c] Danish National Research Foundation's Center for Individual Nanoparticle Functionality (CINF), Department of Physics, NanoDTU, Technical University of Denmark (DTU), 2800 Kgs. Lyngby, Denmark

Received 8 February 2007; received in revised form 24 July 2007; accepted 26 July 2007
Available online 25 September 2007

Abstract

We have applied an atomistic simulation methodology based on molecular dynamics to study grain boundary migration in crystalline materials, driven by the excess energy of dislocation arrangements. This method is used to simulate recrystallization in metals. The simulations reveal that the migration process is not uniform as assumed in many recrystallization models, but that the grain boundaries migrate in an irregular fashion and exhibit a strong dependence on the local presence of dislocations, which can distort the local migration process significantly.

Keywords: Molecular dynamics; Recrystallization; Grain boundary migration

1. Introduction

During recrystallization new, essentially dislocation-free grains appear and grow at the expense of the surrounding defect-filled deformed matrix as illustrated in Fig. 1a. The grain boundaries surrounding a recrystallizing grain travel through the deformed matrix, removing defects and thereby lowering the energy of the sample. The newly nucleated grains that are most prone to grow generally have crystallographic orientations that are different from the local matrix [1], and grains having a misorientation angle close to 40° around an [1 1 1]-axis to the deformed matrix are observed to have grain boundaries with high mobilities in many common metals [2–5]. The factors that determine the dynamics of the boundary motion stem from the interplay between the grain boundaries surrounding the recrystallizing grains and the dislocations in the deformed matrix.

The way in which dislocations are organized in the deformed matrix has been studied extensively [6–9]. It has been found that dislocations typically are not randomly distributed but accumulate at dislocation boundaries, which separate regions of relatively low dislocation density [8]. A typical microstructure observed by transmission electron microscopy (TEM) is shown in Fig. 1b. The microstructure is dominated by extended, almost planar dislocation boundaries. The misorientation angle across these boundaries can reach values above 10° for metals deformed to medium and high strain and the sign of the misorientation angle is typically opposite from one boundary to the next [8].

Although there are fairly large misorientation angles across the elongated dislocation boundaries, they are not

* Corresponding author. Tel.: +45 4677 5730; fax: +45 4677 5758.
E-mail address: rasmus.godiksen@risoe.dk (R.B. Godiksen).

1359-6454/$30.00
doi:10.1016/j.actamat.2007.07.055

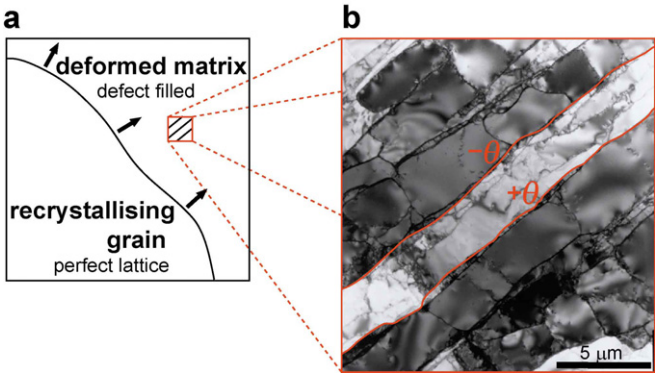

Fig. 1. Recrystallization and the deformed matrix: (a) Sketch illustrating the recrystallization process: the boundary surrounding the recrystallizing grain sweeps through the deformed matrix, leaving behind a nearly perfect crystal lattice (arrows indicate the direction of boundary motion). (b) Close-up micrograph of a typical deformed microstructure. The micrograph shows the substructure within a single grain in a 40% cold-rolled Al sample observed by TEM. Intensity reflects crystallographic orientation. The microstructure is dominated by extended, almost planar dislocation boundaries. Two of these are highlighted by red lines. The crystallographic misorientation angles across the extended dislocation boundaries are observed to be up to 10° and alternating [8], which means that if the misorientation across a particular extended boundary corresponds to a positive rotation $+\theta$ around a given axis, the misorientations of the neighbouring boundaries correspond to a negative rotations $-\theta$ around the same axis. Dislocation boundaries with smaller misorientations are also seen between the extended planar dislocation boundaries dividing the microstructure into smaller cells.

to be confused with conventional grain boundaries, because the structures in the two types of boundaries and the ways in which they are created are very different. Dislocation boundaries are created during deformation while grain boundaries are the interfaces surrounding grains formed during annealing. Structurally it is possible to create an unbroken atomic path through a dislocation boundary, where all the atoms along the path are placed perfectly in the local crystal lattice. The lattice may be elastically distorted but no crystal defects exist in the path. Such a path cannot be made through a grain boundary; here the crystal structure will change abruptly when passing through the boundary.

The most common experimental technique used to study microstructural changes during recrystallization is electron microscopy, which allows detailed characterization of the microstructure and crystallographic orientations but not the dynamics, except at surfaces, which may not be representative of bulk behaviour. Recently, three-dimensional X-ray diffraction (3DXRD) has made it possible, for example, to follow in situ the growth kinetics of individual grains [10] and even the boundary dynamics of individual growing grains deeply embedded in the metal during recrystallization [11]. These types of measurements have, contrary to common knowledge, shown that even during recrystallization in weakly deformed single crystals, grain boundaries surrounding newly nucleated grains move very heterogeneously and the boundary motion is strongly dependent on the local microstructure [11]. Recrystallization models, such as cellular automata [12,13] and geometric models [14–16], assume very simplified growth dynamics and do not account for these observations. Simulation techniques, such as molecular dynamics (MD) and Monte Carlo (MC), have the necessary spatial and temporal resolution to obtain atomic-scale information on migrating grain boundaries and may be able to provide new insight into the atomic motion of recrystallizing grain boundaries and provide new input parameters for recrystallization models.

Here we present a method for simulating the migration of grain boundaries using the MD technique applying the "natural" driving force for recrystallization, namely the presence of dislocations, something that previously has been thought "challenging, if not impossible" [17].

MD has been used extensively to study metals, especially during plastic deformation [18,19]. Grain boundary migration driven by energy reduction has also been investigated, but prior simulations have been performed using different driving forces, and therefore represent processes other than recrystallization. Examples of such are simulations of curvature-driven boundary migration [20], triple-junction migration [21], stress-driven boundary migration [22,23] or boundary migration driven artificially by altered interatomic potentials [17]. Curvature-driven and triple junction simulations are related to grain growth, where the driving force is the reduction of grain boundary energy. Stress-driven and artificially driven boundary migration simulations make use of volumetric driving forces, where the excess energy driving the boundaries is distributed homogeneously over volumes of the sample. In the present work we want to study recrystallization. The interaction between the grain boundaries and the dislocation structures may be a key issue in understanding the heterogeneities observed in recrystallization experiments and therefore dislocation structures must be included in the simulations. The only simulations known to the authors that directly apply a driving force due to the excess energy associated with the presence of dislocations have been performed in two dimensions, using only one layer of atoms [24].

2. Simulation strategy

In the investigation presented here simulations are carried out using standard MC and MD techniques [25]. Each simulation represents a small area of a grain boundary migrating through a deformed matrix consisting of extended dislocation boundaries. The intersections between the grain boundaries and the dislocation boundaries happen at right angles. This resembles the triple junction configuration used in, for example, Ref. [21], with the important difference that in the present study one of the boundaries is a dislocation boundary that consists of individual dislocations. As will be shown below, this alters the local grain boundary migration dynamics significantly.

Compared to microstructures observed experimentally, the simulation cells are somewhat simplified, which allows for a thorough analysis of the migration process, while still capturing the essential features of recrystallization.

2.1. Potential

The potential used is a Lennard–Jones (LJ) pair potential. LJ is the standard potential to use for investigations where the focus is on fundamental issues, rather than studying the properties of a specific material. The results produced here should give a phenomenological description; however, the simulation method can readily be used with other potentials without further modification.

The potential energy of interaction between two atoms i and j with a mutual distance r_{ij} is given by:

$$U_{ij} = 4\epsilon((\sigma/r_{ij})^{12} - (\sigma/r_{ij})^{6}). \quad (1)$$

$\sigma = (1/2)^{1/6} r_0$, where r_0 is the equilibrium interatomic distance and ϵ is the bonding energy between two atoms. The potential is truncated at a cutoff distance $r_c = 2.1 r_0$ and modified by a spline fit beyond r_0, so that it goes to zero smoothly at $r = r_c$.

Scaled units are used throughout, mass is given in units of m_0, the mass of one atom, length in units of r_0, energy in units of ϵ, time in units of $\tau = (m_0 r_0^2/\epsilon)^{1/2}$, temperature in units of ϵ/k_B, where k_B is Boltzmann's constant. During a simulation m_0, r_0, ϵ and k_B are set to 1 for convenience, but appropriate values can be inserted to make approximate quantitative comparisons between results obtained with the LJ potential and real materials.

2.2. Overall simulation procedure

The simulation procedure consists of three stages; setup of atoms, relaxation using MC, and annealing using MD. The procedure can be viewed as an extension of previously applied methods, where other setups were used to produce curvature-driven boundary migration [20,21].

During setup, atoms are arranged to produce crystallographic interfaces with certain misorientations across them, and during relaxation and early annealing the interfaces between the crystal blocks develop into grain boundaries or dislocation boundaries depending on the misorientations [26]. The dislocations within one dislocation boundary all have the same Burgers vector and the dislocations within neighbouring dislocation boundaries have Burgers vectors of the same size but opposite sign, resulting in parallel dislocation boundaries with alternating misorientations. The dislocation density (dislocation length per unit volume) in the deformed matrix part of the simulation cell due to the dislocation boundaries varies from simulation to simulation but is generally around $10^{-2} r_0^{-2}$, which corresponds to dislocation densities around $10^{17}\,\mathrm{m}^{-2}$, some orders of magnitude higher than observed experimentally [27]. The higher dislocation density is necessary to obtain high migration rates so that simulations can be carried out with reasonable computational resources.

2.3. Setup

The setup used here has been described in outline elsewhere [26], but in short, face-centred cubic (fcc) crystal blocks with different crystallographic orientations are "patched" together in the simulation cell, where periodic boundary conditions are applied along the x, y and z-directions. Fig. 2 shows an example of a simulation cell as set up.

Initially blocks of atoms arranged in perfect fcc crystal structures are created with a [1 1 1] direction along the z-axis, rotated around this to create different crystallographic orientations, cut to fit, and placed in the simulation volume. The simulation volume is chosen so that the crystal lattice blocks match up perfectly at the periodic boundaries. The orientation of the crystal blocks can be varied to produce different boundary misorientations and inclinations, although in this study we have chosen to simulate

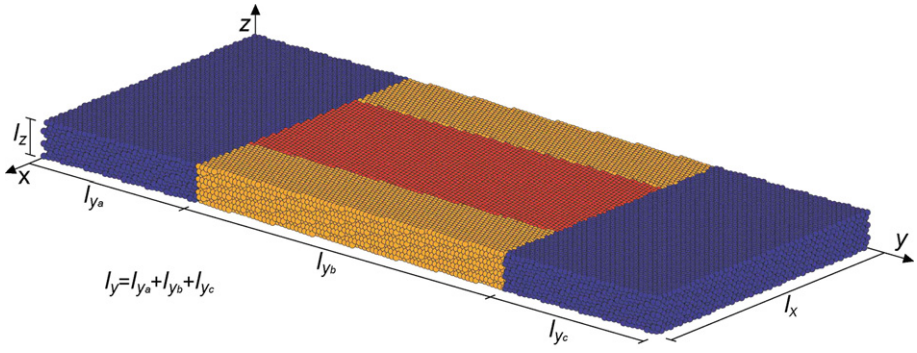

Fig. 2. Simulation cell as set up. Colours indicate crystallographic orientations of the crystal blocks. All blocks have a common [1 1 1] crystallographic direction parallel to the z-axis, but are rotated by different amounts around this. The misorientation between the blue and the red block is 45°, the misorientation between the blue and orange is 35° and the misorientation between the red and the orange is 10°. Blue represents the recrystallizing grain, the red and orange represent the deformed matrix. The simulation cell contains $\approx 9.3 \times 10^4$ atoms.

only one set of boundary misorientations. The deformed matrix is represented by a number of blocks, where neighbouring blocks differ by 10° in orientation, resulting in an array of low-angle dislocation boundaries when simulated. The recrystallizing grain is represented by a perfect crystal block[1] that has an orientation which differs from the matrix blocks by 35° or 45° depending on which part of the deformed matrix is adjacent to the recrystallizing grain. This grain boundary misorientation is chosen because 40° [1 1 1] boundaries are known from experiments to have a high mobility [2–5].

Two types of simulation cells with different dimensions have been used: (A) $60.7 \times 147.3 \times 7.3 r_0$ and (B) $47.6 \times 44.5 \times 31.8 r_0$. A-type simulation cells with two or four dislocation boundaries have been used, giving dislocation densities in the deformed matrix of 5.8×10^{-3} or $11.6 \times 10^{-3} r_0^{-2}$. B-type simulation cells have only been made with four dislocation boundaries, giving a dislocation density of $14.8 \times 10^{-3} r_0^{-2}$. The simulation cells all consist of $\approx 10^5$ atoms, and the computational time was around a month on a single processor per simulation.

2.4. Relaxation

When set up, the atoms may overlap at the interfaces between crystal blocks. If the overlap is too large the increased energy may lead to local "melting". This is avoided by removing atoms that are closer than $0.4 r_0$ and relaxing the remaining atoms. For this relaxation a constant number of atoms, pressure and temperature (NPT) Metropolis MC algorithm is used [25]; this relaxes both atom positions and box dimensions. The MC simulations are run at the same temperature as the MD anneals (see below) for the particular simulations.

Simulation cells are relaxed using approximately 5×10^6 atom movements and 5×10^4 box movements. The settings are chosen because our experience has shown us that local melting is avoided when these are applied.

2.5. Annealing

Annealing is performed using a constant number of atoms, volume and temperature (NVT) velocity verlet MD algorithm [25]. A damped Berendsen velocity rescaling algorithm is used for temperature control.

Simulations of the A-type cells have been performed at temperatures: $T = 0.33$, 0.40, 0.47, 0.53 and $0.60\epsilon/k_B$, in order to extract activation energies. Simulations of the B-type cells have only been simulated at $T = 0.40\epsilon/k_B$. The melting temperature $T_m \approx 0.66\epsilon/k_B$ for a LJ crystal.

Three repeated simulations of each temperature and dislocation density have been made to improve the statistics for the A-type cells. Two repeated simulations have been made for the B-type cells.

Simulations, both A- and B-types, were run for up to $2 \times 10^3 \tau$ in time-steps of $10^{-3}\tau$.

3. Results and discussion

3.1. Overall boundary motion

The simple geometry of the simulation cells makes it possible to follow the overall migration of the grain boundaries. Fig. 3 shows data from an A-type simulation. The grain boundaries and dislocations are clearly seen as high-energy areas in Fig. 3a. The potential energy in the simulation cell as a function of the y-position is plotted in Fig. 3b. The grain boundaries are clearly seen as peaks. Fig. 3c shows a typical growth curve (blue) of the average distance travelled by the two boundaries s. An irregular growth is observed with both forward and backward motion, although an average trend, which can be approximated rather well by a straight line, is observed. Irregular growth in some form is observed in most of our simulation runs. The growth is clearly more irregular than that which is observed in MD simulations of boundary migration applying other driving forces [17,20,21,28]. The pronounced irregular growth might be due to the driving force being localized in the dislocations rather than being smeared out over the volume or the boundary, which is the case for simulations applying other driving forces.

The dislocations possess an excess free energy in the deformed matrix, creating a driving pressure for boundary migration. The driving pressure P is defined as the difference in the free energy density between the deformed and recrystallized parts of the sample: $P = F_m/V_m - F_g/V_g$, where the subscripts m and g for the free energy F and volume V indicate deformed matrix and recrystallizing grain.

The free energy in the simulation is given by: $F = U - TS$, where U is the internal (potential) energy, T is the temperature and S is the entropy. The free energy difference per unit volume between the deformed and the recrystallized part of the simulation cell is: $\Delta F = \Delta U - T\Delta S$ since T is constant throughout the simulation cell. The entropy difference between the deformed and recrystallized parts of the simulation cell arises solely from the presence of the dislocations in the deformed part. The change in the entropy contribution ($T\Delta S$) to the free energy of introducing dislocations into a lattice is very small compared to the change in internal energy ΔU [27] and ΔU is a good approximation to ΔF in our simulations. Therefore we use the following approximation for the driving pressure:

$$P = U_m/V_m - U_g/V_g \tag{2}$$

P is plotted as the red curve in Fig. 3c. After an initial equilibration, P reaches a level where it becomes more or less stable for the rest of the simulation.

[1] Actually there are two blocks, but they are connected by the periodic boundary conditions and therefore act as one.

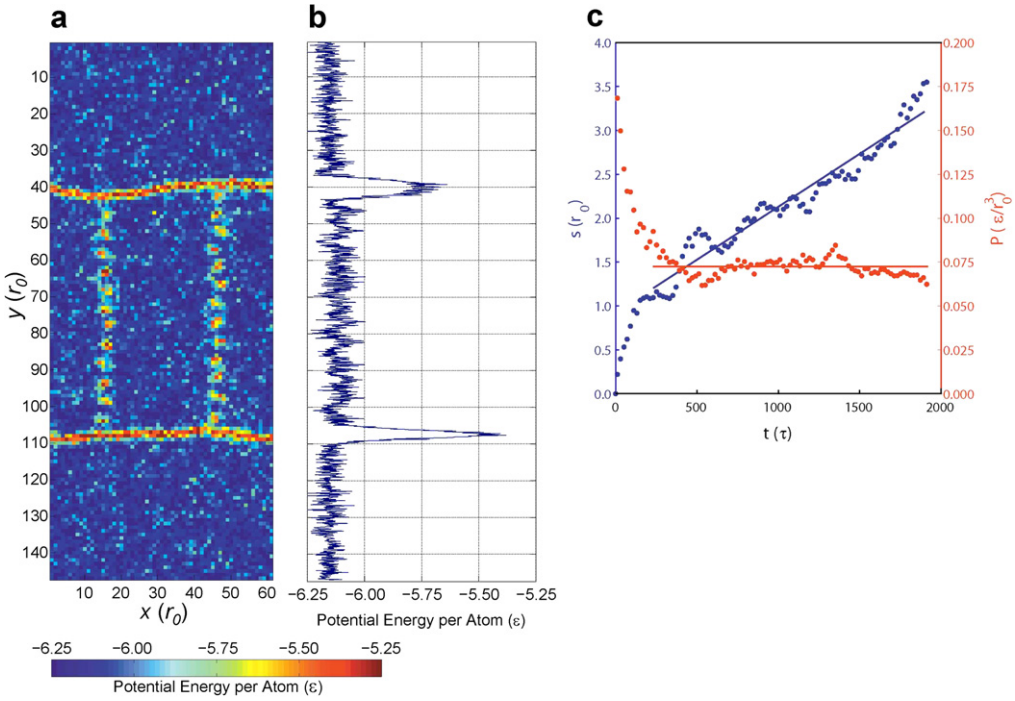

Fig. 3. Analysis of an A-type simulation. (a) The simulation cell seen from above. The entire simulation cell is divided into bins of size $r_0 \times r_0 \times l_z$, and every atom is assigned to the appropriate bin. The integrated potential energy per atom in each bin is calculated and the bins coloured accordingly. Energy is reported in units of ϵ, the natural energy unit for LJ systems. (b) Average bin-energy as a function of y. The actual positions of the boundaries are determined by identifying the value y_c for which the interval $[y_c - r_0/2; y_c + r_0/2]$ has the largest average potential energy. By following y_c for the two grain boundaries over time, the average distance travelled s can be found: $s(t) = 1/2(|y_{c1}(t) - y_{c1}(0)| + |y_{c2}(t) - y_{c2}(0)|)$. (c) s and driving pressure P as a function of simulation time. Time is reported in units of τ, the natural time unit for LJ systems, which approximately corresponds to 10^{-12} s. Fits are made by zero-order (P) and first-order (s) polynomials for $\tau > 200$.

3.2. Dislocation absorbtion into the grain boundary

Two types of dislocation absorbtion into the grain boundary are observed in our simulations as the boundaries progress, hereafter called α-type and β-type events. The α-type is shown in Fig. 4a–c. This event can be divided into three stages. In the first stage (Fig. 4a) the grain boundary moves steadily towards the dislocation whilst being almost flat. The second stage (Fig. 4b) happens during a much shorter time-span, in which the grain boundary "shoots out" in a cusp, absorbing the dislocation completely. The cusp represents a large local curvature of the grain boundary associated with an excess grain boundary energy compared to a flat boundary. In the third stage (Fig. 4c) the system reduces the boundary area by flattening the boundary. This has the effect that the boundary, which is not part of the cusp, is dragged forward. Fig. 4d–g shows the shooting out on an atomic level. It is noteworthy that the dislocation remains completely fixed while the grain boundary moves towards it, and that the shoot-out of the boundary happens in a very localized area near the dislocation. Within this area the grain boundary moves several interatomic distances while the main portion of the boundary does not move.

In the β-type absorption the dislocation breaks loose from its original position and moves into the grain boundary in a way that does not produce any significant distortion or movement of the grain boundary. The β-type events only happen in simulations with high dislocation densities and are observed more frequently at high temperatures. Often a mixture of α- and β-type events is observed, i.e. the boundary cusps slightly out while the dislocation slides into it.

During both the α- and the β-type events, dislocations are absorbed one at a time in events that happen during short time spans compared to the overall migration process. Most of the time the grain boundaries are not in direct contact with the dislocations but are driven slowly forward by their presence. Phenomenologically two regimes can be described; one in which the grain boundary is slowly dragged forward by the dislocations and on in which the grain boundary interacts strongly with a single dislocation and absorbs it. A grain boundary may thus locally experience very different driving forces over time. This is fundamentally different from, for example, triple junction migration, where the driving force is constant and the shape of the triple junction does not change [21].

3.3. Dislocation annihilations

During simulations, dislocation annihilations may occur, emptying the matrix part of the simulation cell of dislocations. Fig. 5a and b shows a simulation before (a) and after (b) several annihilations in a B-type simulation.

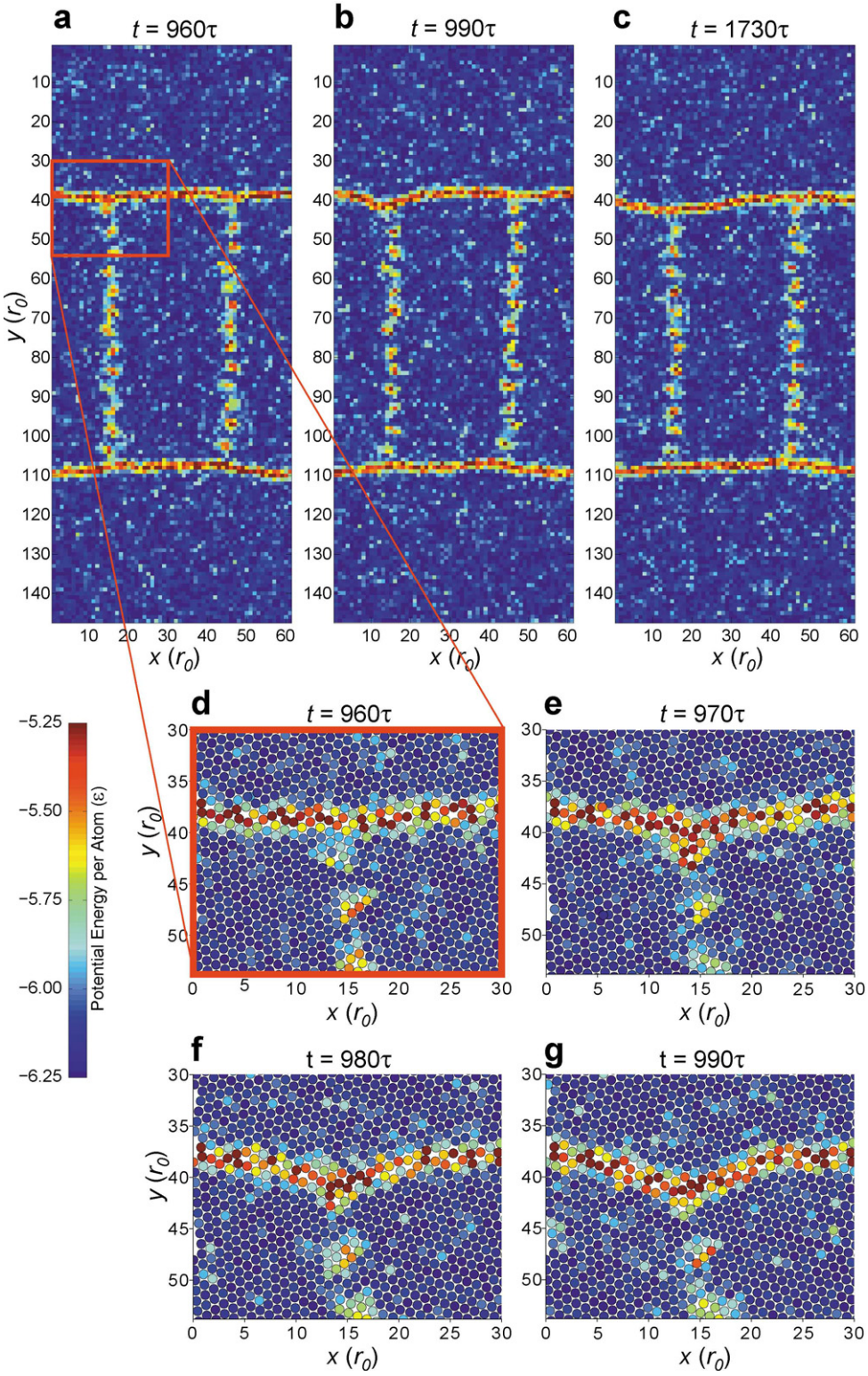

Fig. 4. Time sequence from an A-type simulation showing a dislocation being absorbed during an α-type event: (a) the boundary approaches the dislocation; (b) the boundary "shoots out" in a cusp absorbing the dislocation; (c) the rest of the boundary is dragged along (a–c are coloured in the same way as Fig. 3a). (d–g) The atomistic details of one layer of atoms during the shoot-out. The positions and energies of the atoms shown are averaged over 10τ using 10 snapshots. This is done in order to remove thermal noise which would otherwise make the grain boundary and dislocations difficult to identify by potential energy alone.

In Fig. 5c the driving pressure P and the average distance travelled s are plotted as a function of simulation time. After an initial drop due to equilibration of the simulation cell, P levels off at a value $P \approx 0.2\epsilon r_0^{-3}$ but then falls to almost zero at $\tau \approx 125$ due to dislocation annihilations. The boundaries migrate steadily until this point, but do

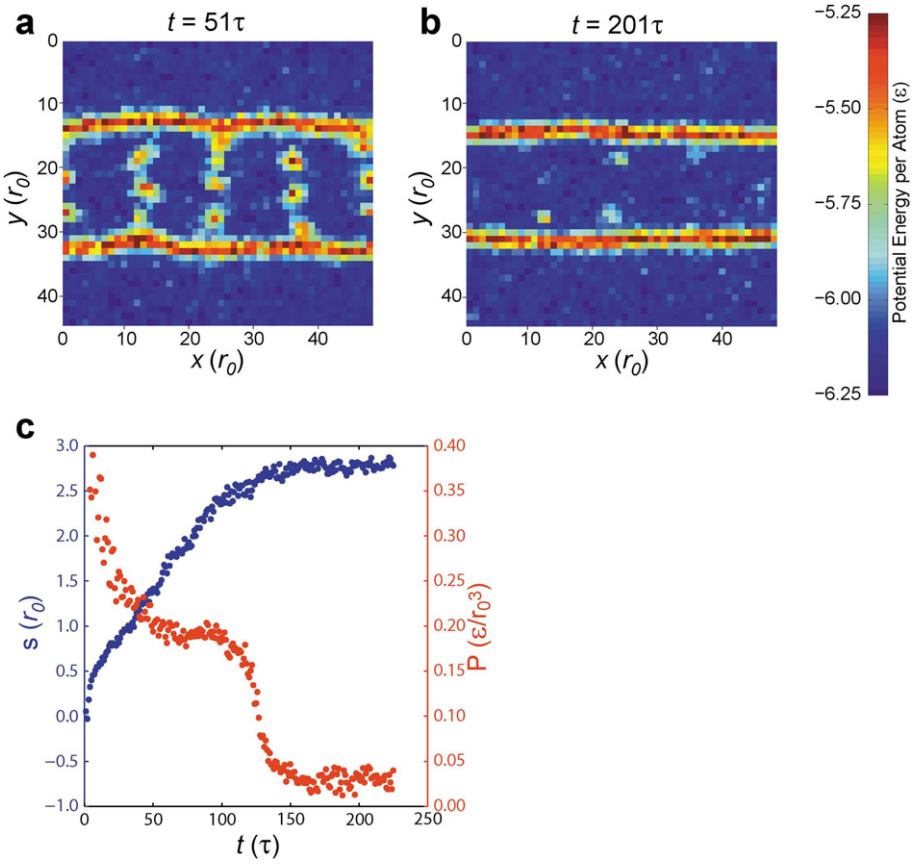

Fig. 5. A B-type simulation exhibiting dislocation annihilations. Snapshots before (a) and after (b) several dislocation annihilations (a and b are coloured in the same way as Fig. 3a). In (b) the matrix material no longer contains dislocations, but debris from the dislocation annihilations is still present. (c) Average distance travelled by grain boundaries s and driving pressure P plotted as a function of simulation time.

not move thereafter. This shows that the driving force for the grain boundary migration is indeed the excess energy due to the presence of dislocations.

In simulations where annihilations do not take place, the positions of the dislocations in the dislocation boundary remain fixed, the misorientations across the dislocation boundaries do not change, and the driving pressure is therefore more or less constant as seen in Fig. 3.

3.4. Mobility and activation energy

Grain boundary velocities v, driving pressures P and mobilities M, defined as

$$M = v/P, \tag{3}$$

are calculated for the A-type simulations for all temperatures and dislocation densities. Due to the irregular motion of the grain boundaries, mobilities are calculated as averages over time. The velocity varies significantly with time as seen in Fig. 3c, but there are also large variations in average velocity, and therefore mobility, between simulations with identical initial conditions.

An Arrhenius behaviour for M is generally assumed:

$$M = M_0 \exp(-E_a/k_B T), \tag{4}$$

where E_a is the activation energy and k_B is Boltzmann's constant [29]. As seen in Fig. 6, $\log M$ from low dislocation density simulations plotted as a function of $1/T$ follows a straight line as expected, although with some scatter. However, for the high-density simulations such a fit cannot describe the data. An explanation for this might rest in the α- and β-type dislocation absorbtion events. In simulations with low dislocation density, only α-type events occur, which gives a simple activation energy and an Arrhenius behaviour. However, with a higher dislocation density, a mixture of α- and β-type events occurs, and each may be assumed to have a different activation energy, which would produce a deviation from the Arrhenius behaviour. The high-density simulations, where β-type events happen, typically have lower mobilities than the low dislocation simulations as seen in Fig. 6. An explanation for this could be that during β-type events much of the local driving pressure is removed by the dislocation moving into the grain boundary. On the other hand, the driving pressure calculated over the entire deformed part of the simulation cell P only changes a little, because just one of the many dislocations is removed. This means that P may overestimate the real driving pressure experienced locally by the grain boundary and M is therefore underestimated.

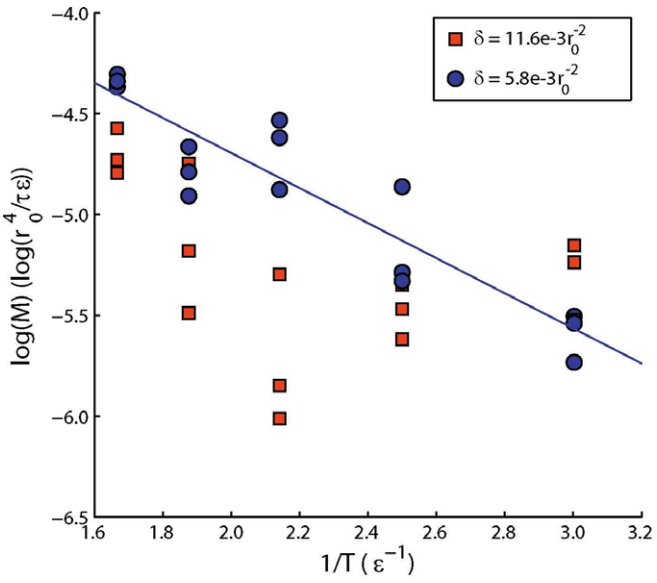

Fig. 6. Mobilities as a function of dislocation density and temperature. Three data points representing three initially identical simulations are shown for each temperature and dislocation density δ. For the low-δ simulations the data follows a straight line as expected; the slope is $-0.87\epsilon/k_b$. For the high-δ simulations the data cannot be fitted to a straight line. The high-δ simulations generally have lower mobilities than the low-δ simulations.

Migration rates, mobilities and activation energies for the A-type low dislocation density simulations can be converted from LJ units into, for example, "copper units" as done by Schönfelder et al. [22] and these estimates can be compared to experiments or simulations of specific metals. The migration rates calculated from our simulations correspond to values from 0.5 to 3 m s^{-1}, which by far exceed values measured in recrystallization experiments [10,30], but high migration rates are to be expected here due to the very high dislocation densities.

The mobilities found correspond to values from 10^{-9} to 4×10^{-9} m s^{-1} Pa^{-1}. These are orders of magnitude larger than values typically obtained in recrystallization experiments on metals [30–32], although mobilities as high as 10^{-10} m s^{-1} Pa^{-1} have been reported [30]. Impurities greatly reduce the mobilities of grain boundaries, and the discrepancies between simulations and experiments may be ascribed to the lack of impurities in MD simulations [33,34]. The mobilities found in our simulations are lower than the mobilities found in all other simulations according to Trautt et al. [33], who have compared mobilities extracted from several simulations and experiments at temperatures 0.8–0.9T_m.

The activation energy found corresponds to 0.14 eV atom^{-1}, when converted, which is around one order of magnitude smaller than that which is typically found in recrystallization experiments [30,31]. MD simulations of boundary migration applying other types of driving force exhibit similar discrepancies compared to experiments [22,35].

4. Conclusions

The simulations presented here show that grain boundary migration during recrystallization, i.e. driven by the presence of dislocations, can be simulated and analysed using MD.

These first results show that the nature of the migration process is not homogeneous, as typically assumed in recrystallization models, but exhibits irregular migration rates, which are generally not seen in MD simulations of grain boundary migration caused by other driving forces.

Furthermore, the boundary morphology is dependent on the local presence and behaviour of dislocations. Two types of dislocation absorption events are observed, called α- and β-type events. During α-type events the dislocations remains stationary during the entire absorption process and the grain boundary cusps out. During β-type event the dislocation moves into grain boundary with no significant distortion or movement of the boundary. These are extreme situations. Often a mixture of the two is observed.

The mobilities found in the simulations correspond to values from 10^{-9} to 4×10^{-9} m s^{-1} Pa^{-1} when converted from LJ to copper units. These values are higher than experimental values but lower than values extracted from all other MD simulations of boundary migration known to the authors.

The activation energies found for the simulations with low dislocation density ($\delta = 5.8\times10^{-3}r_0^{-2} = 4.4\times10^{16}$ m^{-2}) corresponds to 0.14 eV atom^{-1}. This value is smaller than typical experimental values, but in fairly good agreement with other MD simulations of boundary migration caused by other driving forces. The activation energy for the high dislocation density ($\delta = 11.6\times10^{-3}r_0^{-2}$) simulations cannot be extracted due to a non-Arrhenius behaviour, which could indicate that two different activated processes associated with the α- and β-type absorption events are taking place simultaneously.

Future investigations using this method will study the influence of different parameters such as the interaction potential, the structure of the deformed matrix, the dislocation density, the misorientation angle across grain boundaries and the boundary inclination.

Acknowledgements

The authors would like to thank J. Dyre, N. Hansen, K.W. Jacobsen, W. Pantleon, H.F. Poulsen, B. Ralph and R.A. Vandermeer for very useful discussions. R.B.G., S.S. and D.J.J. gratefully acknowledge the Danish National Research Foundation for supporting the Center for Fundamental Research, Metal Structures in Four Dimensions, within which this work was performed; Z.T.T. and M.U. acknowledge support from Structural Metallics Program, Office of Naval Research, Department of Defense, Award No. N00014-06-1-0207 titled "Particle

Strengthened Interfaces'', and Alcoa Technical Center; J.S. acknowledges the Danish National Research Foundation for supporting the Center for Individual Nanoparticle Functionality.

References

[1] Juul Jensen D. Acta Metall Mater 1995;43:4117.
[2] Beck PA, Sperry PR, Hu H. J Appl Phys 1950;21:420.
[3] Liebmann B, Lücke K, Masing G. Zeit Metall 1956;47:57.
[4] Aust KT, Rutter JW. Trans Inst Min Metall Eng 1959;215:119.
[5] Yoshida H, Liebmann B, Lucke K. Acta Metall 1959;7:51.
[6] Hansen N, Juul Jensen D. Phil Trans R Soc A 1999;357:1447.
[7] Driver JH, Juul Jensen D, Hansen N. Acta Metall Mater 1994;42:3105.
[8] Hansen N. Metall Mater Trans A 2001;32A:2917.
[9] Liu Q, Huang X, Lloyd DJ, Hansen N. Acta Mater 2002;50:3789.
[10] Lauridsen EM, Poulsen HF, Nielsen SF, Juul Jensen D. Acta Mater 2003;51:4423.
[11] Schmidt S, Nielsen SF, Gundlach C, Margulies L, Huang X, Juul Jensen D. Science 2004;305:229.
[12] Hesselbarth HW, Gobel IR. Acta Metall Mater 1991;39:2135.
[13] Marx V, Reher FR, Gottstein G. Acta Mater 1999;47:1219.
[14] Marthinsen K, Lohne O, Nes E. Acta Metall 1989;37:135.
[15] Vandermeer RA. In: 16th Riso Int Symp; 1995. p. 193–213.
[16] Rios PR, Godiksen RB, Schmidt S, Juul Jensen D, Vandermeer RA. Scripta Mater 2006;54:1509.
[17] Janssens KGF, Olmsted D, Holm EA, Foiles SM, Plimpton SJ, Derlet PM. Nat Mater 2006;5:124.
[18] Bringa EM, Caro A, Wang YM, Victoria M, McNaney JM, Remington BA, et al. Science 2005;309:1838.
[19] Schiøtz J, Jacobsen KW. Science 2003;301:1357.
[20] Upmanyu M, Srolovitz DJ, Shvindlerman LS, Gottstein G. Acta Mater 1999;47:3901.
[21] Upmanyu M, Srolovitz DJ, Shvindlerman LS, Gottstein G. Acta Mater 2002;50:1405.
[22] Schönfelder B, Gottstein G, Shvindlerman LS. Acta Mater 2005;53:1597.
[23] Zhang H, Srolovitz DJ. Acta Mater 2006;54:623.
[24] Upmanyu M, Trautt ZT, Kappes BB. Mater Sci Forum 2004;467–470:715.
[25] Allen MP, Tildesley DJ. Computer simulation of liquids. Oxford: Oxford University Press; 2004.
[26] Godiksen RB, Trautt ZT, Upmanyu M, Schmidt S, Juul Jensen D. Mater Sci Tech 2005;21:1373.
[27] Weertman J, Weertman JR. Elementary dislocation theory. Oxford: Oxford University Press; 1992.
[28] Zhang H, Mendelev MI, Srolovitz DJ. Acta Mater 2004;52:2569.
[29] Humphreys FJ, Hatherly M. Recrystallization and related annealling phenomena. Oxford: Elsevier; 2004.
[30] Huang Y, Humphreys FJ. Acta Mater 1999;47:2259.
[31] Vandermeer RA, Juul Jensen D, Woldt E. Metall Mater Trans A 1997;28:749.
[32] Gall RL, Liao G, Saindrenan G. Scripta Mater 1999;41:427.
[33] Trautt ZT, Upmanyu M, Karma A. Science 2006;314:632.
[34] Lens A, Maurice C, Driver JH. Mater Sci Eng A 2005;403:144.
[35] Zhang H, Upmanyu M, Srolovitz DJ. Acta Mater 2005;53:79.

F Atomistisk Simulering af Rekrystallisation

R.B. Godiksen, S. Schmidt, D. Juul Jensen, *Proceedings of Dansk Metallurgisk Selskabs Vintermøde*, 27–37 (2007).

Atomistisk Simulering af Rekrystallisation

Rasmus B. Godiksen, Søren Schmidt, Dorte Juul Jensen

Grundforskningscenteret: Metalstrukturer i Fire Dimensioner
Afdeling for Materialeforskning
Forskningscenter Risø

rasmus.godiksen@risoe.dk, soeren.schmidt@risoe.dk, dorte.juul.jensen@risoe.dk

Bidrag til

Dansk Metallurgisk Selskabs

Vintermøde, Middelfart, januar 2007, Metallurgi, Design og Innovation,
ISBN 87-87535-37-8
Eds. Pobl Brøndsted, Peter Kjeldseen, Marcel A.J. Somers

Abstract

We have used an atomistic simulation methodology based on molecular dynamics to study recrystallization; one of the most important processes of metal working. During recrystallization, grains with perfect crystal structure grow within the defect-filled material, driven by the presence of the surrounding defects. In this paper we show how the movement (migration) of interfaces between the growing grains and the surroundings can be simulated and analyzed. The simulations reveal that the migration process is not uniform, as assumed in most recrystallization models, but the grain boundaries migrate in an irregular manner and exhibit a strong dependence on the *local* presence of defects, which can distort the grain boundary shape significantly. This indicates that the details of the migration process depend on the defect structure itself and not only on magnitude of the driving force. Knowledge on how defect structures influence the migrating grain boundaries may be used to improve metal manufacturing processes involving recrystallization and improve material properties as well.

Resume

Vi har anvendt *molecular dynamics*-teknikken til at studere rekrystallisation, en af de vigtigste processer i metalforarbejdning. Under rekrystallisation gror korn med perfekt krystalstruktur i et defektfyldt metal, drevet af tilstedeværelsen af de omgivende defekter. I denne artikel præsenteres en metode til at simulere og analysere bevægelsen af grænseflader mellem krystalkornene og omgivelserne. Simuleringerne viser, at processen ikke er uniform, som antaget i de fleste rekrystallisationsmodeller, men at korngrænserne bevæger sig irregulært og er stærkt påvirket af den *lokale* tilstedeværelse af defekter, som kan ændre korngrænsernes form. Dette indikerer, at detaljerne i korngrænsebevægelsen afhænger af selve defektstrukturen, og ikke bare den gennemsnitlige kraft hvorved defekterne trækker i grænserne. En bedre forståelse af hvordan defektstrukturer påvirker korngrænsebevægelsen under rekrystallisation kan føre til store forbedringer af metalforarbejdningsprocesser, som involverer rekrystallisation, og derigennem tilvejebringe materialer med bedre egenskaber.

Motivation

Innovation indenfor moderne materialeteknologi kræver en helhedsorienteret tilgang, hvor materiale-anvendelser, -egenskaber, -strukturer samt bearbejdningsprocesser ses samlet, fordi den traditionelle trail-and-error tilgang er for ineffektiv. Videnskabeligt arbejde indenfor materialeteknologi er desuden nødvendigt for at tilvejebringe en grundlæggende vidensbase, som kan inddrages når nye materialer skal designes. Uden denne vidensbase ville det være svært at udvikle nye materialer, med andre egenskaber, end dem som allerede findes på markedet. Denne artikel præsenterer et eksempel på et stykke videnskabeligt arbejde, hvis formål er at bidrage til forståelsen af principperne bag den grundlæggende proces *rekrystallisation*, som har enorm betydning for metalfremstilling. Et metal ændrer egenskaber drastisk når det rekrystalliserer, og derfor kan en bedre forståelse af rekrystallisation potentielt lede til store forbedringer af materialeegenskaber gennem ændrede bearbejdningsprocesser (*1*). I denne artikel beskrives hvorledes rekrystallisation kan studeres vha. *molecular dynamics* (MD) teknikken, hvilket ikke har været gjort før. Med MD simuleres de enkelte atomers bevægelser, hvilket giver mulighed for meget detaljerede studier af materialer, der kan være med til at belyse grundlæggende processer i materialer.

Rekrystallisation

Når et stykke metal deformeres plastisk induceres defekter i krystalgitteret, som primært er linjedefekter, såkaldte *dislokationer*. Dislokationerne er typisk ikke tilfældigt fordelt i metallet, men organiserer sig i *dislokationsstrukturer*. Dannelsen og bevægelsen af dislokationer, er det som gør, at metaller kan deformeres plastisk. Jo flere dislokationer der er til stede, jo sværere er det for dem at bevæge sig, og derved bliver materialet hårdere, et fænomen som er kendt som deformationshærdning. Ulempen ved deformationshærdning er, at metallet typisk samtidigt bliver sprødt.

En del af det arbejde, som udføres på et stykke metal under deformation, bliver lagret i defekterne. Hvis metallet efterfølgende varmebehandles (udglødes), kan en del af defekterne fjernes. Dette vil have den modsatte effekt på metallets egenskaber i forhold til deformation, nemlig at metallet igen bliver blødere og mere smidigt/formbart. Ved passende proceskombinationer bestående af deformation og udglødning kan materialer med ønskede egenskaber tilvejebringes.

Udglødning kan inddeles i tre overordnede processer; *recovery*, *rekrystallisation* og *kornvækst*. Under recovery reduceres antallet af frie dislokationer. En del fjernes simpelthen, mens andre organiserer sig yderligere i strukturer som reducerer spændingerne i metallet. Under rekrystallisation opstår nye defektfri områder, kaldet *korn*, som vokser på bekostning af det omgivne defektfyldte materiale. Disse korn har oftest en stor krystallografisk

misorientering[1] sammenlignet med den omgivne matrix (*2*). *Korngrænser* fra korn, som har en misorientering på omkring 40º, er særligt mobile i mange almindelige metaller (*3*, *4*). Kornene vokser ved, at korngrænsen mellem kornet og den omgivne dislokationsfyldte *matrix* bevæger sig ud igennem matricen og absorberer defekterne. Tilbage bliver en perfekt gitterstruktur. Kornet har grundet dets perfekte gitterstruktur en lavere energi end den omgivne matrix og rekrystallisation er drevet af den energireduktion, som følger af, at de bevægende korngrænser konverterer defektfyldt materiale til defektfrit. En principskitse af rekrystallisation er vist i fig.1a. Rekrystallisation stopper når hele den deformerede matrix er blevet absorberet af nye korn. Den resulterende polykrystal kan ved yderligere opvarmning bringes til at gennemgå kornvækst, hvor store korn vokser på bekostning af små, og det samlede korngrænseareal derved reduceres. Rekrystallisation og kornvækst bliver ofte forvekslet idet begge processer involverer bevægende korngrænser. Forskellen består, lettere

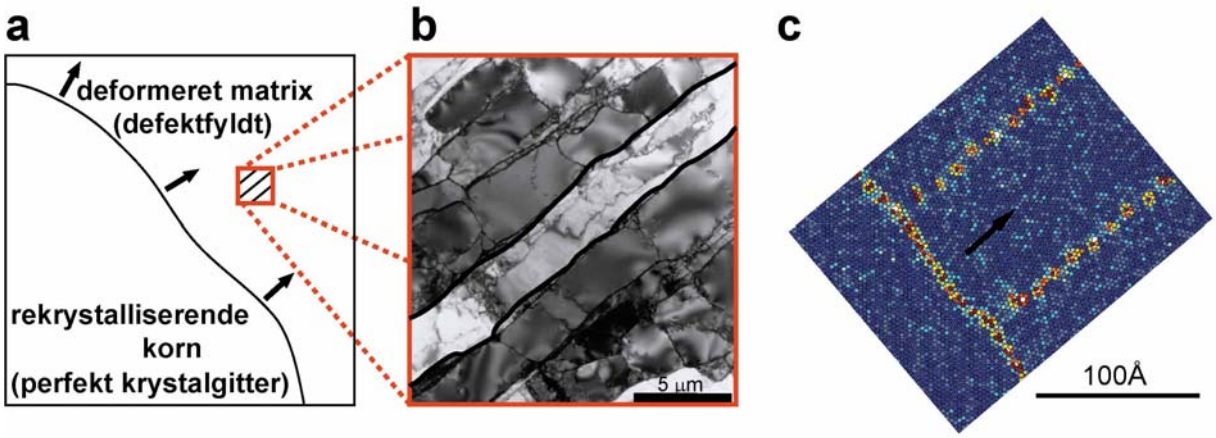

Figur 1 a *Principskitse af rekrystallisation. Det rekrystalliserede korn med perfekt gitterstruktur vokser på bekostning af den defektfyldte deformerede matrix. Kornene vokser ved, at korngrænsen bevæger sig, hvorved defekterne i matricen fjernes og energien reduceres.* ***b*** *Eksempel på mikrostruktur i den deformerede matrix fra en kold-valset aluminiumsprøve, reduceret med 40 % i tykkelse, observeret med transitions elektron mikroskopi (TEM). Intensitetsforskelle angiver forskelle i den krystallografiske orientering af forskellige dele af materialet. Mørke streger angiver dislokationsvægge, og lange, næsten plane dislokationsvægge kan ses (To af disse er tegnet kraftigt op). Misorienteringen henover disse er højere end over de tværgående dislokationsvægge, der opdeler mikrostrukturen i mindre celler.* ***c*** *Øjebliksbillede af et snit fra en MD simulering. Et lag atomer farvet efter deres potentielle energi er vist. En massiv korngrænse og to dislokationsvægge, opbygget af individuelle dislokationer, ses som områder med højere energi. Under simuleringen bevæger korngrænsen sig i den i pilen angivne retning og absorberer dislokationerne i dislokationsvæggene.*

[1] Misorienteringen mellem to krystalgitre er den vinkel som kræves for at rotere det ene krystalgitter således, at det vil falde oven i det andet.

forsimplet, i den drivende kraft: Under rekrystallisation driver den overskydende energi lokaliseret i dislokationsstrukturer korngrænserne, mens minimering af korngrænseenergi driver kornvækst.

De underliggende processer i rekrystallisation opstår i samspillet mellem korngrænser og dislokationsstrukturer. Dislokationsstrukturer er blevet studeret nøje, og det viser sig, at dislokationer typisk akkumuleres i *dislokationsvægge*, som adskiller områder med relativt lav dislokationstæthed (*5, 6*). Et typisk eksempel på en deformationsstruktur observeret med transmissions elektron mikroskopi (TEM) er vist i fig.1b. Mikrostrukturen er fremkommet ved kold-valsning, men den er repræsentativ for mange andre deformationstyper (*6*). Det dominerende træk ved mikrostrukturen er de lange, næsten plane dislokationsvægge, som ved høje deformationsgrader typisk kan have misorienteringer på 10º og i visse tilfælde endda højere (*6*).

Vi har ønsket i stor detalje at simulere hvorledes en korngrænse bevæger sig, når den bliver drevet af den overskydende energi, som er deponeret i dislokationsvæggene. Fig.1c viser et enkelt lag atomer fra en af vores simuleringer. Hvis læseren forestiller sig fig.1a og fig.1b kombineret forstås hvorfor vi har valgt den opbygning af vores simuleringer, som er vist i fig.1c, nemlig korngrænser som bevæger sig ind igennem en struktur bygget op af langstrakte dislokationsvægge.

MD

MD teknikken er konceptuelt simpel. Metoden bygger på Newtons bevægelsesligning for klassisk mekanik, idet hvert atom bevæger sig ifølge Newtons 2. lov: $\boldsymbol{F}=m\boldsymbol{a}$. Atomerne vekselvirker gennem et potentiale, som definerer kraften på hvert enkelt atom som funktion af positionen alle de andre atomer. I praksis benyttes kun de nærmeste naboatomer til at udregne kraften for at reducere beregningstiden. Kendes atomernes startpositioner, starthastigheder og potentialet, er bevægelsen fuldstændigt determineret i al fremtid af Newtons 2. lov. I praksis løses bevægelsesligningen iterativt, dvs. i tidsskridt, hvor kraften på atomerne i hvert tidsskridt beregnes og atomerne flyttes derefter. Teknikken nyder stor udbredelse og der findes flere måder at udføre iterationerne på, samt en mængde tricks og kneb, som bruges til at optimere simuleringerne (*7*).

MD har været brugt i stor udstrækning til at studere materialer, herunder metaller (*7*). De fleste simuleringer har fokuseret på atomistiske processer under deformation (*8, 9*), men også bevægelse af korngrænser er blevet simuleret. Dog har den drivende kraft virkende på korngrænserne i disse simuleringer altid været andre end den vi er interesseret i. Som eksempler kan nævnes simuleringer hvor et korngrænseareal minimeres (kornvækst) (*10, 11*),

bevægelse af korngrænser drevet ved elastisk spænding (*12*) eller ved kunstigt modificerede potentialer (*13*). Der kan være en tendens til at ignorere årsagen til den drivende kraft og fokusere mere på grænsens bevægelse, uafhængigt af hvad der driver den. En af vores pointer er, at bevægelses-processen ikke uden videre kan adskilles fra årsagen til drivende kraft, hvilket vi vil forsøge at sandsynliggøre med resultaterne fra vores simuleringer.

Metode

Metoden, som benyttes her, er bygget op af tre trin: 1) *opsætning*, 2) *relaksation* og 3) *udglødning*. Trin 3) er den egentlige simulering af rekrystallisation, men 1) og 2) er også vigtige elementer i metoden.

1) **Opsætning**. Først bygges blokke, hvor atomerne sættes op i passende krystalgitre. I vores tilfælde er gitrene af typen *kubisk fladecentreret* (fcc), som er den gittertype atomerne i mange almindelige metaller, så som aluminium og kobber, sidder i. Blokkene bygges således, at gitterets orientering i forhold til simuleringscellen er passende (se nedenfor). Blokkene placeres derefter i simuleringscellen; et eksempel kan ses i fig.2. De forskellige blokke repræsenterer det rekrystalliserende korn hhv. den deformerede matrix. Forskellene i krystallografisk orientering blokkene imellem medfører en misorientering over grænsefladerne imellem blokkene. Misorienteringen mellem de blokke, som repræsenterer det rekrystalliserende korn og de blokke, som

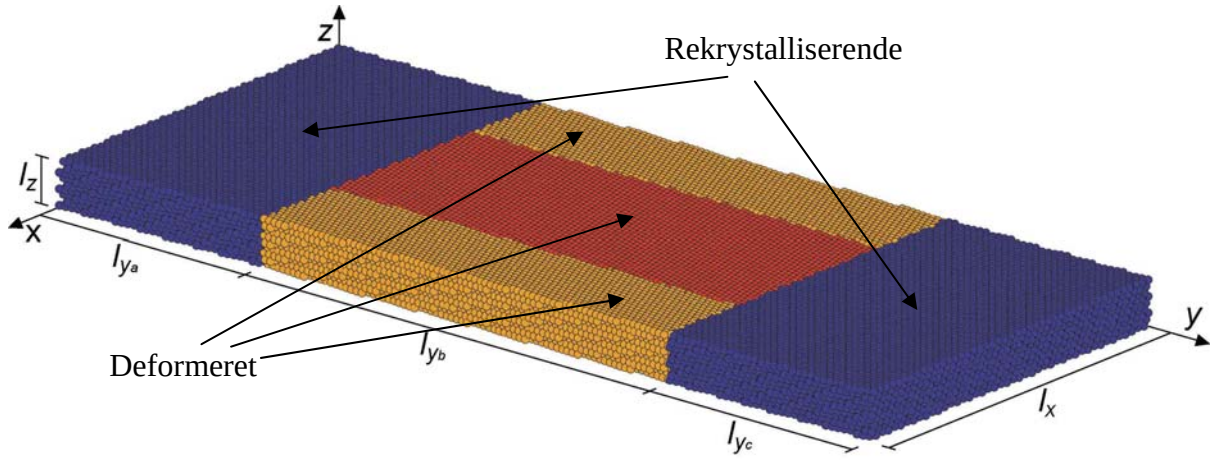

Figur 2 *Simuleringscelle efter opsætning. Blokke med forskellig krystallografisk orientering er illustreret ved forskellige farvetoner, således at de mørke blokke i enderne af cellen repræsenterer det rekrystalliserende korn, og de to lysere blokke repræsenterer den deformerede matrix. Den krystallografiske misorientering mellem blokkene svarer til, at krystalgitteret i de to blokke som repræsenterer den deformerede matrix, er roteret 35º hhv. 45º omkring z-aksen i forhold til det rekrystalliserende korn. Periodiske randbetingelser benyttes i x-, y- og z-retningerne, således at atomerne tæt på en af cellens sider også vekselvirker med atomerne på den modsatte side af cellen.*

repræsenterer den deformerede matrix, er i gennemsnit 40º omkring en krystallografisk [111]-akse, som er sammenfaldende med z-aksen. Misorienteringen mellem de to blokke, som repræsenterer den deformerede matrix, er 10º omkring den samme akse. Grænsefladerne vil under de to efterfølgende trin i metoden udvikle sig til enten korngrænser eller plane dislokationsvægge alt efter deres misorientering. En af de attraktive egenskaber ved denne metode er netop, at grænsefladerne (af sig selv) udvikler sig til de konfigurationer, som med lavest mulig energi imødekommer misorienteringen. På den måde kan både korngrænser og dislokationsvægge skabes blot ved at variere på misorienteringen mellem blokkene.

2) **Relaksation**. Atomer ved grænsefladerne mellem blokkene kan i visse tilfælde være placeret meget tæt på atomer i naboblokke. Sker dette vil den potentielle energi af atomerne være særdeles høj. For at undgå at denne fører til lokal smeltning under MD simuleringen, må strukturen relakseres kontrolleret. Dette gøres i to trin. I de atom-par hvor afstanden mellem atomer er mindre end ½ normal inter-atomar afstand fjernes det ene atom. Derefter relakseres hele simuleringscellen vha. en simpel *Monte Carlo* (MC) algoritme, hvor atomerne et ad gangen forskydes i en tilfældig retning på en sådan måde at forskydninger som sænker energien accepteres og forskydninger som hæver energien kun accepteres med en vis sandsynlighed (*14*). Ved at udføre mange, dvs. 10-50 forskydninger pr. atom, kan den overskydende energi i simuleringscellen fjernes. Under relaksationen kan simuleringscellens dimensioner også relakseres således at det fri volumen, som evt. kan opstå ved at fjerne overlappende atomer, fjernes.

3) **Udglødning**. Den centrale del af simuleringen er udglødningen, som foretages vha. en standard *velocity verlet* MD algoritme (*14*). Simuleringen foretages under konstant volumen og temperatur.

Antallet af atomer i en simuleringscelle er ca. 10^5 og det benyttede potentiale er det såkaldte *Lennard-Jones* (LJ). LJ er et meget simpelt potentiale, der kun afhænger af afstanden mellem par af atomer. Det tager ikke højde for f.eks. retningsafhængigheder af vekselvirkninger eller mange-atom effekter (*14*). Dette potentiale er velegnet når man ønsker at studere generelle fænomener som kan vedrøre en række materialer frem for at studere egenskaber af et bestemt materiale.

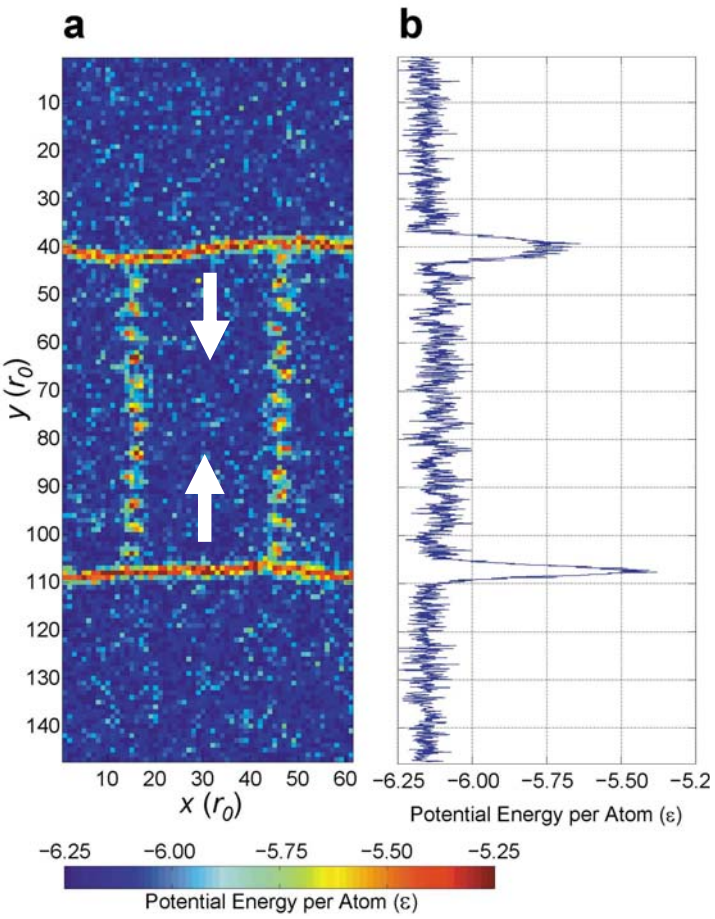

Figur 3 a *Simuleringscelle set oppefra. Gennemsnittet af den potentielle energi af atomer med samme x- og y-positioner er udregnet og figuren farvet derefter. Figuren viser således gennemsnits-energien langs z-aksen. Korn-grænser parallelt med x-aksen og dislokationsvægge (med individuelle dislokationer) parallelt med y-aksen kan ses som områder med ændret farve. Enhederne på akserne er givet ved den inter-molekylære afstand* r_0 *og pilene angiver bevægelsesretningen af grænserne.* ***b*** *Gennemsnits-energi af atomer med samme y-position. De to korngrænser kan identificeres som toppunkter på kurven. Energien er angivet i arbitrære enheder* ε*.*

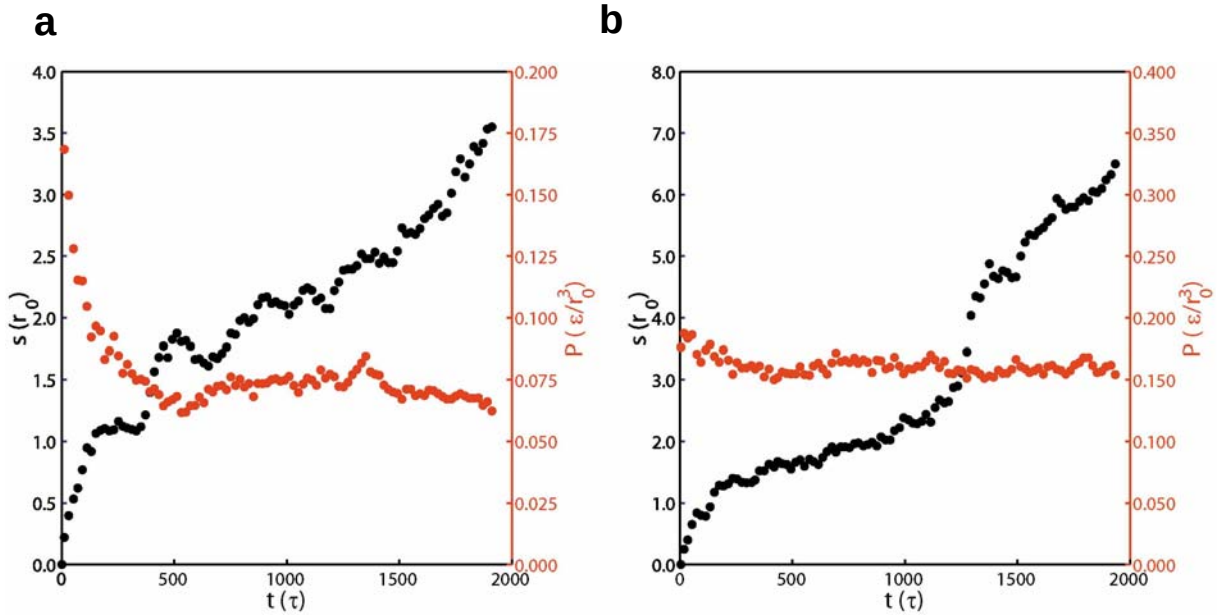

Figur 4 a,b *Vækstkurve samt drivende tryk. Vækstkurven er konstrueret ved at afbilde den gennemsnitlige bevægelse af de to korngrænser som funktion af tiden (i arbitrære enheder* τ*).*

Resultater og Diskussion

Delvist under relaksationen og delvist under udglødningen udvikler grænsefladerne mellem krystalblokkene sig som nævnt til krongrænser og dislokationsvægge. Et eksempel på en simuleringscelle, hvor dette har fundet sted, kan ses i fig.3a. Under udglødningen bevæger korngrænserne sig igennem cellen i pilenes retninger mens de absorberer dislokationerne i den del af cellen, som repræsenterer den deformerede matrix.

På grund af den enkle geometri af simuleringscellen, er det let at identificere korngrænserne og dislokationsvæggene. Positionerne af korngrænserne findes simpelthen ved at projektere energien af atomerne ind på y-aksen som vist i fig.3b og identificere toppunkterne. Ved at følge korngrænsernes positioner over tid, kan vækstkurver for det rekrystalliserende korn konstrueres.

Fig.4 viser vækstkurver fra to forskellige simuleringer. Som det ses er begge kurver irregulære, forstået på den måde, at korngrænsen ikke bevæger sig jævnt. Fig.4a viser en vækstkurve med flere på hinanden følgende fremad- og bagudrettede bevægelser, mens fig.4b viser en vækstkurve, hvor der eksisterer flere vækststadier. Irregulær vækst er så vidt vi ved ikke set i computersimuleringer af bevægelse af korngrænser, hvor korngrænserne drives frem ved andre metoder (*11-13, 15*), hvilket indikerer, at typen af drivende kraft har indflydelse på selve processen. Fig.4 viser også energitæthedsforskellen mellem den del af simuleringscellen, som repræsenterer den deformerede matrix og den del, som repræsenterer det rekrystalliserende korn. Denne størrelse kaldes det drivende tryk, fordi energitæthed har samme enhed som tryk. Det ses tydeligt fra fig.4b, at bevægelsen varierer stærkt på trods af et konstant drivende tryk, hvilket ikke stemmer overens med den sædvanlige antagelse om, at bevægelseshastighed og drivende tryk er proportionelle (i det mindste ikke på dette atomare niveau). Vi mener, at den irregulære vækst som ses her indikerer, at den lokale fordeling af den drivende kraft (dislokationerne), og ikke bare størrelsen af den, må have indflydelse på detaljerne i bevægelsen.

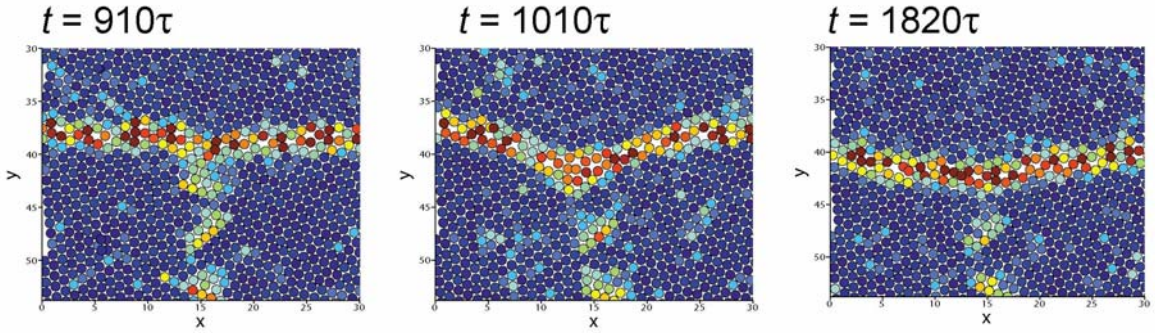

Figur 5 *Sekvens af en absorptionsproces. Det ses hvordan en korngrænse, som indledningsvist er flad, skyder ud i en spids, i det øjeblik dislokationen bliver absorberet. Efterfølgende flader korngrænsen igen ud til en form, som svarer til udgangspunktet.*

MD simuleringerne muliggør, at bevægelse af korngrænser kan studeres i stor detalje. Fig.5 viser en korngrænse imens den absorbere en af dislokationerne i en dislokationsvæg. Processen kan deles op i tre trin: 1) Indledningsvist er grænsen flad og bevæger sig langsomt mod dislokationen i en homogen proces. 2) Korngrænsen skyder pludseligt ud i en spids, og absorberer dislokationen totalt, hvorved energien, som er associeret med dislokationen, elimineres. Dette sker dog på bekostning af en øget korngrænseenergi, som opstår fordi korngrænsens længde øges. 3) Den øgede korngrænseenergi fjernes gradvist ved at korngrænsen langsomt rettes ud igen indtil den opnår en facon svarende til udgangspunktet. Absorptionsprocessen viser tydeligt hvorledes tilstedeværelsen af dislokationer påvirker korngrænsebevægelsen. Således kan grænsebevægelsen under rekrystallisation, hvor bevægelsen er drevet af dislokationsstrukturer, ikke forventes at være den samme som under kornvækst, hvor bevægelsen er drevet af reduktion i korngrænseoverflade. Korngrænsebevægelse må studeres i den rette kontekst, altså med den rette type drivende kraft.

Konklusion

Med dette arbejde har vi påvist, at det kan lade sig gøre at simulere rekrystallisation på et fundamentalt niveau ved hjælp af MD teknikken. Resultaterne viser, at korngrænsebevægelse under rekrystallisation kan være stærkt irregulær, hvilket adskiller disse simuleringer fra andre typer simuleringer af bevægende korngrænser foretaget med MD. Vi mener, at irregulariteterne skyldes tilstedeværelsen af dislokationer, som påvirker korngrænseformen under processen. Gennem kommende studier vil vi forsøge at forstå, hvorledes variationer i dislokationsstrukturerne påvirker den overordnede grænsebevægelsesproces, så vi kan få yderligere indsigt i hvordan korn vokser i den deformerede struktur under rekrystallisation. En ny viden, som på sigt kan bidrage til en bedre kontrol med forarbejdningsprocesser, så ønskede materialeegenskaber kan opnås.

Tak

Zachary Trautt og Moneesh Upmanyu, Colorado School of Mines, skal have en stor tak for deres hjælp til at få simuleringerne op at køre. Jakob Schiøtz og Karsten Jacobsen, DTU, fortjener også en særlig tak for gode råd til hvordan rekrystallisation kan simuleres med MD. Vi vil også gerne takke venner af og medarbejdere i Grundforskningscenteret: Metalstrukturer i Fire Dimensioner, især Roy Vandermeer, Brian Ralph, Wolfgang Pantleon, Henning Friis Poulsen, Niels Hansen og Jeppe Dyre. Endelig vil vi takke Danmarks Grundforskningsfond for at støtte Grundforskningscenteret: Metalstrukturer i Fire Dimensioner i hvilket dette arbejde blev udført.

Reference Liste

1. F. J. Humphreys, M. Hatherly, *Recrystallization and Related Annealling Phenomena* (Elsevier Ltd., Oxford, 2004).

2. D. Juul Jensen, *Acta Metallurgica et Materialia* **43**, 4117 (1995).

3. P. A. Beck, P. R. Sperry, H. Hu, *Journal of Applied Physics* **21**, 420 (1950).

4. K. T. Aust, J. W. Rutter, *Transactions of the American Institute of Mining and Metallurgical Engineers* **215**, 119 (1959).

5. N. Hansen, D. Juul Jensen, *Philosophical Transactions of the Royal Society of London Series A-Mathematical Physical and Engineering Sciences* **357**, 1447 (1999).

6. N. Hansen, *Metallurgical and Materials Transactions A* **32A**, 2917 (2001).

7. D. C. Rapaport, *The Art of Molecular Dynamics Simulation* (Cambridge University Press, Cambridge, ed. 2, 2004).

8. J. Schiotz, K. W. Jacobsen, *Science* **301**, 1357 (2003).

9. E. M. Bringa *et al.*, *Science* **309**, 1838 (2005).

10. H. Zhang, N. Upmanyu, D. J. Srolovitz, *Acta Materialia* **53**, 79 (2005).

11. M. Upmanyu, D. J. Srolovitz, L. S. Shvindlerman, G. Gottstein, *Acta Materialia* **50**, 1405 (2002).

12. H. Zhang, M. I. Mendelev, D. J. Srolovitz, *Acta Materialia* **52**, 2569 (2004).

13. K. G. F. Janssens *et al.*, *Nature Materials* **5**, 124 (2006).

14. M. P. Allen, D. J. Tildesley, *Computer Simulation of Liquids* (Oxford University Press, 2004).

15. M. Upmanyu, D. J. Srolovitz, L. S. Shvindlerman, G. Gottstein, *Acta Materialia* **47**, 3901 (1999).

G Simulation of Recrystallization using Molecular Dynamics; Effects of the Interatomic Potential

R.B. Godiksen, Z.T. Trautt, M. Upmanyu, S. Schmidt, D. Juul Jensen, *Materials Science Forum* **558–559**, 1081–1086 (2007).

Materials Science Forum Vols. 558-559 (2007) pp. 1081-1086
online at http://www.scientific.net

Simulation of Recrystallization using Molecular Dynamics; Effects of the Interatomic Potential

Rasmus B. Godiksen[1,a], Zachary T. Trautt[2,b], Moneesh Upmanyu[2,c], Søren Schmidt[1,d] and Dorte Juul Jensen[1,e]

[1]Center for Fundamental Research: Metal Structures in Four Dimensions, Materials Research Department, Risø National Laboratory, 4000 Roskilde, Denmark

[2]Simulation and Theory of Atomic-Scale Material Phenomena (STAMP), Division of Engineering, Materials Science Program, Colorado School of Mines, Golden, Colorado 80401, USA

[a]rasmus.godiksen@risoe.dk, [b]ztrautt@mines.edu, [c]mupmanyu@mines.edu, [d]soeren.schmidt@risoe.dk, [e]dorte.juul.jensen@risoe.dk

Keywords: molecular dynamics simulation, boundary migration, dislocation structures, interatomic potentials, Aluminum, EAM, Lennard-Jones.

Abstract

Recrystallization is governed by the migration of high angle grain boundaries traveling through a deformed material driven by the excess energy located primarily in dislocation structures. A method for investigating the interaction between a migrating grain boundary and dislocation boundaries using molecular dynamics (MD) was recently developed. During simulations migrating high angle grain boundaries interact with dislocation boundaries, and individual dislocations from the dislocation boundaries are absorbed into the grain boundaries. Results obtained previously, using a simple Lennard-Jones (LJ) potential, showed surprisingly irregular grain boundary migration compared to simulations of grain boundary migration applying other types of driving forces. Inhomogeneous boundary-dislocation interactions were also observed in which the grain boundaries locally acquired significant cusps during dislocation absorption events. The study presented here makes comparisons between simulations performed using a LJ- and an embedded atom method (EAM) aluminum potential. The results show similarities which indicate that it is the crystallographic features rather than the atomic interactions that determine the details of the migration process.

Introduction

Metallic properties are to a very large extent determined by the microstructures within the metals, and understanding the fundamental microstructural evolution of metals during processing, such as deformation and annealing, is a key issue within metallurgy. Recrystallization, where grains with near-perfect crystal lattices form and grow at the expense of the surrounding defect-filled deformed material, is a process that drastically changes the microstructure of metals during annealing. Essentially every part of a metal sample changes crystallographic orientation during recrystallization [1]. Recrystallization is governed by the migration of high angle grain boundaries that sweep up deformation-introduced defects, driven by the energy reduction associated with the defect removal. In this study we simulated the fundamental interactions between migrating grain boundaries and defect structures during recrystallization using the MD technique with an EAM aluminum potential. Previously we carried out simulations using the same simulation setup but with a simplistic LJ-potential [2]. This article poses the question if the observed effects in the LJ study were a consequence of the simplistic potential used or actual effects of local crystallography.

Recrystallization Using Molecular Dynamics

An MD algorithm calculates the trajectory in space and time of every atom in the simulated volume, which enables very detailed dynamical investigations of a variety of problems, for example

different types of grain boundary migration phenomena [3,4,5]. The downside of this level of detail is the computational power needed to do the calculations, which limits the size and period that can be simulated. Typically only nanometer-sized volumes can be simulated and only for a few nanoseconds. Since nuclei of recrystallizing grains have to be above a critical size of typically a few micrometers to grow, it is impossible to simulate an entire recrystallizing grain within a matrix of a deformed material using MD. In this study we simulate a small section of a migrating grain boundary, separating the recrystallizing grain from the matrix.

During recrystallization grain boundaries migrate, driven by the presence of defects in the deformed matrix. The driving force is determined by the defect structure in the deformed matrix, which typically consists of dislocations organized in dislocation boundaries [6]. The basic process of recrystallization is the interplay between the migrating grain boundaries and the dislocations.

During the simulations presented here, the grain boundary moved and absorbed dislocations. The simulations were not set up to exactly mimic the complicated microstructure in the deformed matrix, but to capture essential features.

Method

The method, that has been used previously with the LJ-potential, is described in detail elsewhere [2,7]; this section summarizes the most important aspects. The method consists of three stages; setup, relaxation and annealing. In the setup stage, the atoms is placed in the simulation volume as blocks with an fcc crystal structure. The interfaces between the blocks will, during relaxation and annealing, develop into grain- and dislocation boundaries. The grain boundaries are chosen to be pure tilt 40º<111> and the dislocation boundaries pure tilt 10º<111>. During relaxation, atoms that are overlapping are removed and the energy of the entire simulation volume relaxed using a short Monte Carlo (MC) simulation run. This is done to avoid a local excess of potential energy. The actual simulation of recrystallization happens in the annealing stage. During this, the MD trajectories of the atoms collectively facilitate the grain boundary migration.

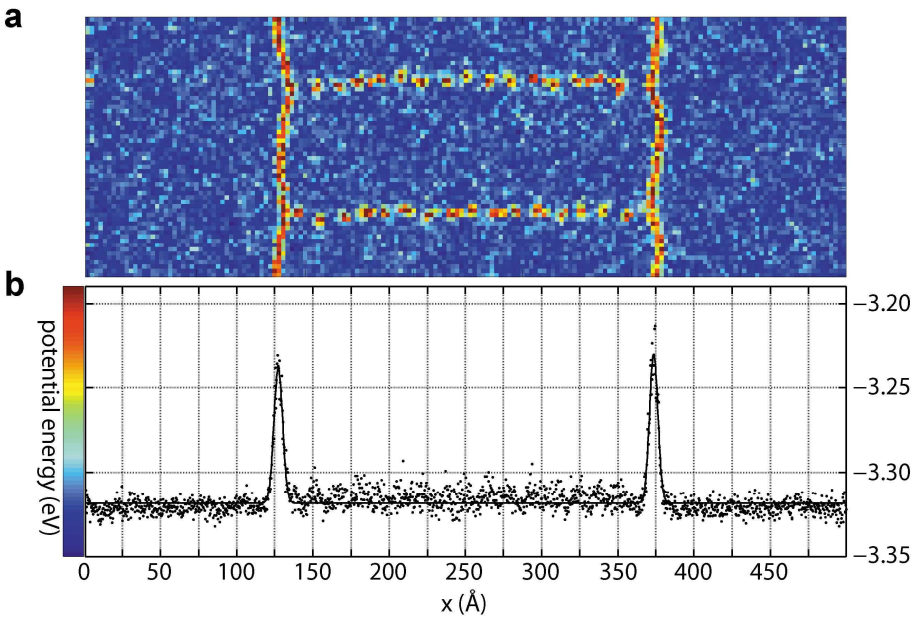

Figure 1 a Averaged simulation cell seen along the *z*-direction for an EAM-simulation. The simulation volume has been divided into boxes of size 2.86Å×2.86Å×21Å, the average energy of the atoms within a box has been calculated and the figure colored accordingly. **b** Energy profile along the *x*-direction; dots represent data points, full lines, fits. Clear peaks are visible representing the grain boundaries. Also a somewhat higher potential energy within the matrix part compared to the grain part of the simulation cell can be seen.

In the annealing stage we used a standard constant volume and temperature velocity verlet MD algorithm [8] and the EAM-potential of Voter and Chen [9]. The simulations were set up in a rectangular box of size: x=399Å, y=173Å, z=21Å, which consisted of $\approx 110*10^3$ atoms. Periodic boundary conditions were applied in the x-, y- and z-directions. We performed simulations at temperatures: T=100, 200,..., 900K. A simulation cell seen from the z-direction is shown in fig.1a. The simulation volume is divided into

boxes of one interatomic distance (2.86Å). The average potential energy of the atoms within each box has been calculated and the box colored accordingly. This makes the structures in the simulation cell stand out very clearly; grain boundaries as well as individual dislocations in the dislocation boundaries are seen. All simulations presented here have a dislocation density of $7*10^{16}m^{-2}$ (length of dislocation per unit volume), orders of magnitude larger than what is typically observed experimentally. We choose this high dislocation density to reduce the simulation time. The potential energy profile shown in fig.1b, obtained by calculating the potential energy of the atoms as a function of *x*, shows the position of the two grain boundaries in the simulation cell as energy peaks. By fitting the peaks by a Gaussian function and using the mean value as the position of the grain boundary, the boundary positions are defined with high precision.

Results and Discussion

During simulations, the grain boundaries move, sweeping up dislocations. The process can be analyzed both qualitatively as well as quantitatively. In [2] is was reported that the morphology of migrating grain boundaries in a LJ-system was inhomogeneous involving large grain boundary curvatures during dislocation absorption events and the overall grain boundary migration process was very irregular with varying migration rates. Quantitatively the extracted activation energies were smaller than what has been found experimentally.

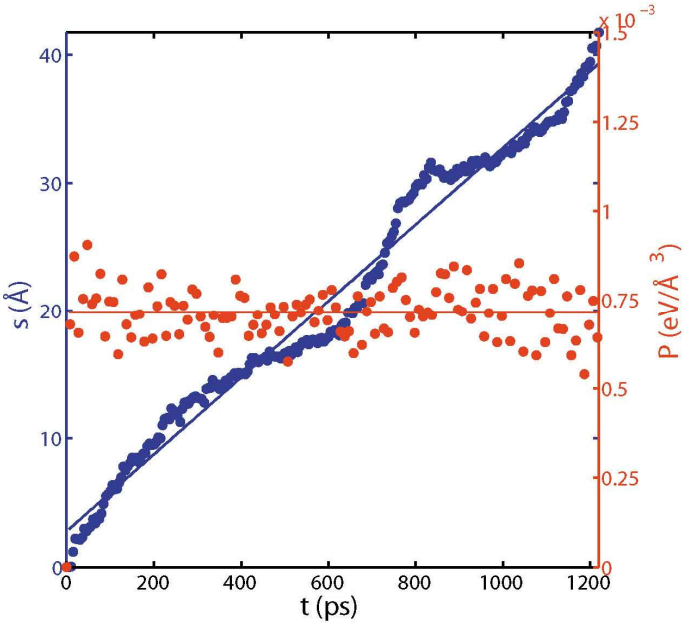

Figure 2 Average distance travelled by grain boundaries *s* and driving pressure *P* for the 600K EAM-simulation plotted as a function of time. Straight lines are fits to data used to extract the average velocity and driving pressure.

The simulations presented here, which used an EAM-system, produced migration rates from zero at low temperatures to around $10ms^{-1}$ at 900K. Simulations at 100K, 200K, and 300K did not produce grain boundary movement at all and the simulation at 400K only produced grain boundary movement in the first couple of hundred picoseconds; after this initial movement of a few Å, the grain boundary stopped and remained fixed for the rest of the simulation.

At higher temperatures the overall grain boundary migration process observed in the EAM-simulations was irregular in the same way as it was in the LJ-simulations. The average distance traveled by the two grain boundaries *s* and the driving pressure *P* for the 600K simulation are shown in fig.2. It is seen that *P* remains constant throughout the entire simulation, although there is some scatter. The growth rate on the other hand varies quite significantly. These types of irregularities become less pronounced at higher temperature, where the migration rate is higher and dislocations are swept up more rapidly, indicating that the localization of the driving force in the dislocations affects the migration process, something that was not as clear in the LJ-simulations due to the somewhat smaller distances traveled by the grain boundaries in those simulations. The variations in the growth rate observed in the simulations presented here are more pronounced than observed in the MD simulations of grain boundary migration driven by other types of driving forces [4,5,10]. This was also the case for the LJ-simulations, which proves that the detailed description of the migration process depends on the type of force acting on the grain boundary.

The mobility, defined as $M=v/P$, where v is the migration rate and P is the driving force, can be calculated by taking as v and P the average values represented by the fits in fig.2. Generally an Arrhenius behavior for the mobility is assumed; $M / M_0 = exp(-E_a / k_B T)$, where M_0 is the mobility at infinite temperature, E_a is the (apparent) activation energy and k_B the Boltzmann constant. As seen in fig.3 mobilities from the simulations follow the Arrhenius behavior quite well.

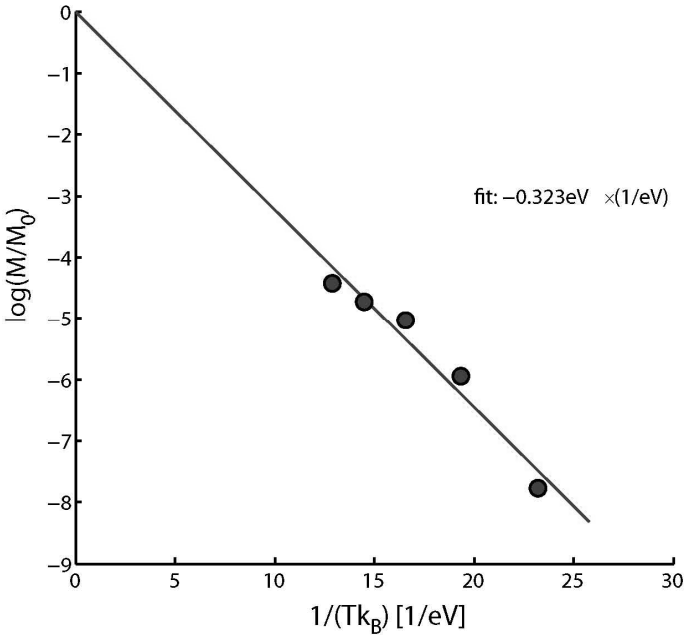

Figure 3 Arrhenius plot of average mobilities for the EAM-simulations. Data from simulations at 100K-400K are not included since no clear grain boundary migration is seen in these cases.

The activation energy extracted from the fit is 0.32eV. The activation energy extracted from the LJ study, converted by fitting the LJ-units to the length, mass, and cohesive energy of aluminum, is 0.25eV [2]. Activation energies found in experiments are much larger; typically activation energies for aluminum and aluminum alloys are 1-2eV [11,12,13]. Our findings here reject the possibility that the discrepancy in activation energy between the LJ-simulations and experiments is due to an oversimplified potential; it must be a result of something else. Solute drag may be rate controlling in experiments [12], and since both the LJ- and EAM-simulations contained no solute particles, this could be the explanation for the discrepancy.

Two types of dislocation absorption events, named α- and β-type events, were observed in the LJ study [2]. The α-type event is characterized by a cusp in the grain boundary that 'shoots out' very quickly and absorbs the dislocation without the dislocation moving. After the dislocation has been absorbed the grain boundary flattens in a process much slower than the 'shooting out'. The β-type event is characterized by the dislocation moving into the grain boundary without any significant grain boundary distortion. The left column of images in fig.4 shows an α-type event from a LJ-simulation and the middle column of images show a β-type event.

In the EAM-simulations only one type of absorption event was observed. It is neither a pure α- nor a pure β-type but it has a mixed character. In the right column of images in fig.4 a dislocation absorption event from the EAM-simulations is shown. A cusp in the grain boundary develops as the grain boundary absorbs the dislocation, but the cusp is not as pronounced as for the α-type in the LJ-simulation. It is seen that the dislocation core is not located in the same position in the 15ps-image as it was in the 0ps-image, which means that the dislocation has moved towards the grain boundary at the same time as the grain boundary cusped. It should be mentioned that the distance moved by the dislocation is smaller than that typically observed in the LJ β-events. A third difference between LJ and EAM is in the structure of grain boundaries; the LJ grain boundaries are thicker and seem to contain more free volume than EAM grain boundaries.

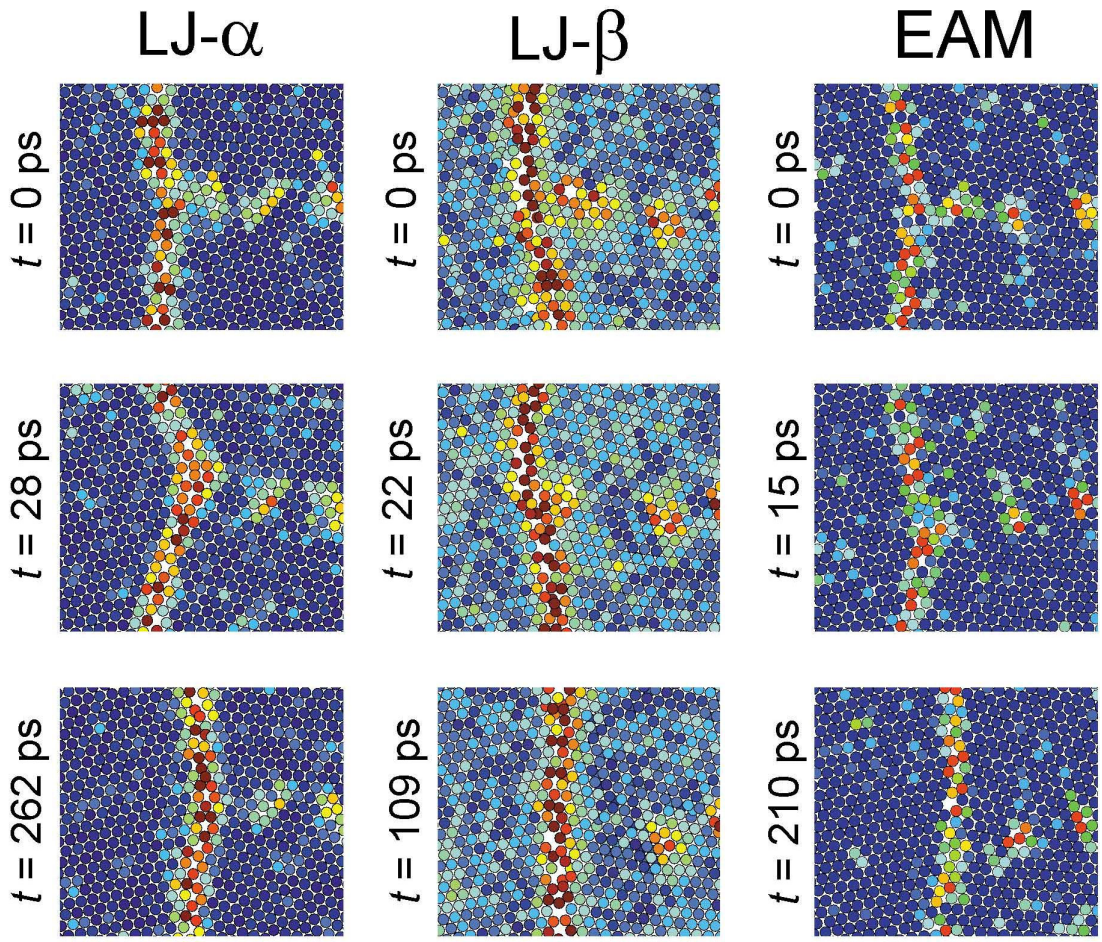

Figure 4 Dislocation absorption events in LJ-simulations (α-type left column, β-type middle column) and an EAM-simulation (right column). Atoms are colored according to their potential energy; blue represents low potential energy, red high. Atom positions and energies are averaged over several simulation snapshots to average out fluctuations in energy.

Conclusions

The EAM-simulations presented here show both differences and similarities with otherwise identical simulations using the LJ-potential.

The dislocation absorption events in the EAM-simulations are neither identical to the LJ α-type nor the β-type events. The EAM events produce cusps like the LJ α-type events, but there are several qualitative differences: The distortion in the grain boundary morphology during dislocation absorption events is less pronounced for EAM-events. The dislocations being absorbed do not move during the LJ α-type events. During EAM-events, the dislocations move into the grain boundary simultaneously with the cusp formation on the grain boundary. It is also worth mentioning that the EAM grain boundary is thinner than the LJ boundary, containing less free volume.

Grain boundary migrations in the EAM- and LJ-simulations have the same overall behavior. They exhibit the same type of irregularities, where grain boundary migration rates changes over time; probably due to the inhomogeneous distribution of the driving force originating from individual dislocations. The activation energies for grain boundary migration using the EAM- and the LJ-potentials are quite similar; LJ: 0.25eV, EAM: 0.32eV. We will not put too much emphasis on the almost identical values of the activation energies, but instead emphasize the very large discrepancy between the values from simulations and experiments, which apparently cannot be understood from the nature of the interatomic potential.

Although there are differences between the EAM- and LJ-simulations, the overall results do not depend much on the interatomic potential, indicating that the results stem primarily from crystallographic effects.

Acknowledgements
The authors would like to thank J. Dyre, N. Hansen, K.W. Jacobsen, W. Pantleon, H.F. Poulsen, B. Ralph, J. Schiøtz and R.A. Vandermeer for very useful discussions. RBG, SS and DJJ gratefully acknowledge the Danish National Research Foundation for supporting the Center for Fundamental Research, Metal Structures in Four Dimensions, within which this work was performed; ZTT and MU acknowledge support from Structural Metallics Program, Office of Naval Research, Department of Defense and Award No. N00014-06-1-0207 titled '*Particle Strengthened Interfaces*', and the Alcoa Technical Center.

References

[1] R.W. Cahn, in: *Physical Metallurgy*, edited by R.W. Cahn and P. Haasen, Elsevier Science Publishers (1983), p. 1595
[2] R.B. Godiksen, Z.T. Trautt, M. Upmanyu, J. Schiøtz, S. Schmidt and D. Juul Jensen, submitted to Acta Mater. (2007)
[3] M. Upmanyu, G.N. Hassold, A. Kazaryan, E.A. Holm, Y. Wang, B. Patton and D.J. Srolovitz: Interface Science Vol. 10 (2002), p. 201
[4] H. Zhang, M.I. Mendelev and D.J. Srolovitz: Acta Mater. Vol. 52 (2004), p. 2569
[5] K.G.F. Janssens, D. Olmsted, E.A. Holm; S.M. Foiles, S.J. Plimpton and P.M. Derlet: Nature Mater. Vol. 5 (2006), p. 124
[6] N. Hansen: Metall. Mater. Trans. A Vol. 32A (2001), p. 2917.
[7] R.B. Godiksen, Z.T. Trautt, M. Upmanyu, S. Schmidt and D. Juul Jensen: Mater. Sci. Tech. Vol. 21 (2005), p. 1373
[8] M.P. Allen and D.J. Tildesley: *Computer Simulation of Liquids* (Oxford University Press, 2004)
[9] A.F. Voter and S.P. Chen: Mater Res Soc Symp Proc Vol. 82 (1987), p. 175
[10] M. Upmanyu, D.J. Srolovitz, L.S. Shvindlerman and G. Gottstein: Acta Mater. Vol. 47 (1999), p. 3901
[11] Y. Huang and F.J. Humphreys: Acta Mater. Vol. 47 (1999), p. 2259
[12] R.A. Vandermeer and D. Juul Jensen: Acta Mater. Vol. 49 (2001), p. 2083
[13] A. Lens, C. Maurice and J.H. Driver: Mater. Sci. Eng. A Vol. 403 (2005), p. 144

H Molecular dynamics simulations of grain boundary migration during recrystallization employing different types of dislocation structures to produce the driving pressure

R. B. N. Godiksen, S. Schmidt, D. Juul Jensen, submitted to *Modelling and Simulation of Materials Science and Engineering.*

Molecular dynamics simulations of grain boundary migration during recrystallization employing different types of dislocation structures to provide the driving pressure

R B N Godiksen, S Schmidt and D Juul Jensen

Center for Fundamental Research: Metal Structures in Four Dimensions, Materials Research Department, Risø National Laboratory, Technical University of Denmark, 4000 Roskilde, Denmark

E-mail: dorte.juul.jesen@risoe.dk

Abstract. Molecular dynamics simulations of grain boundary migration, where the driving pressure P is the excess stored energy due to dislocation structures, have been performed. This represents recrystallization in metals. Two types of dislocation structures have been simulated: (a) twist dislocation boundaries, where screw dislocations are arranged in interconnected dislocation networks, (b) Tilt dislocation boundaries, where edge dislocations are arranged as parallel arrays. The velocity v and mobility M of the migrating boundaries have been calculated from the simulations. v and M are higher in twist-type simulations than in tilt-type simulations, although the activation energies are similar in the two cases. $v \propto P$ is observed for tilt-simulations where the driving pressure is changed by varying the density of dislocation boundaries and for twist-simulations where the driving pressure is changed by varying the misorientation across dislocation boundaries. When the misorientations across edge dislocation boundaries are varied, however, the simulations show $v \propto P^2$. This may be explained by local interactions between the grain boundaries and the dislocations. Misorientation-variations across grain boundaries have also been simulated, but the mobilities show little dependence on this. These simulations show that variations in the dislocation structures may play a dominant role in recrystallization dynamics and that local effects are very important.

PACS numbers: 81.10.Jt, 87.10.Tf, 61.72.Lk, 61.72.Mm

Submitted to: *Modelling Simulation Mater. Sci. Eng.*

1. Introduction

When a metal is deformed plastically, huge amounts of defects are introduced into the crystal lattice in the form of vacancies and dislocations. The defects created increase the free energy stored in the metal. If the metal is subsequently subjected to annealing, the defects may reorganize and disappear during various processes. In the first stages of annealing, typically termed *recovery*, most of the vacancies disappear by diffusion. The dislocations will, during deformation and recovery, arrange themselves in dislocation boundaries, which are low energy configurations compared to free dislocations. Some dislocations may also annihilate or move into grain boundaries or free surfaces and disappear during recovery. If annealing is continued, *recrystallization* may set in. During recrystallization new almost defect-free grains nucleate and grow within the deformed material. The growth, which is governed by the migration of the grain boundaries surrounding the new grains, is driven by the excess energy present in the defect structures in the surrounding deformed material. Large microstructural changes happen during recrystallization because essentially every part of the recrystallizing metal is transformed [1]. After total recrystallization, the majority of defects has been absorbed by the migrating grain boundaries, and the metal has obtained a polycrystalline microstructure consisting of grains with near-perfect crystalline lattices.

Recent experiments have demonstrated that recrystallization is a much more inhomogeneous process than normally assumed in typical recrystallization models. For example, by using the so-called three-dimensional X-ray diffraction (3DXRD) technique Lauridsen et al. found that the volume of every recrystallizing grain evolved differently over time [2]. Schmidt et al. found, also using 3DXRD techniques, that different boundary-parts of a single recrystallizing grain may exhibit different growth rates at different times during the recrystallization process [3]. Schmidt et al. also observed that the shape of a recrystallizing grain boundary may be irregular. Similarly, Martorano et al. found that on the very fine scale protrusions (local bulges on the grain boundary) may form during recrystallization [4]. Such protrusions were also seen by Beck et.al [5] and Vandermeer and Gordon [6] but were not discussed in any great detail or used in subsequent models.

All of these inhomogeneities are expected to be caused by the structures in the deformed material. Understanding how the migrating boundaries of the recrystallizing grains are driven by and interact with the structures in the deformed metal may be essential for understanding the observed recrystallization inhomogeneities.

Experimental or theoretical techniques with very high spatial and temporal resolutions are necessary in order to analyze the interactions between migrating grain boundaries and dislocations. So far no suitable experimental technique exists for in-situ observations. The molecular dynamics (MD) simulation technique has very high spatial and temporal resolutions because it simulates the motion of individual atoms. MD simulations of migrating grain boundaries driven by curvature [7, 8], the migration of triple-junctions [9], elastic strain [10] or a synthetic driving pressure [11] have been performed. All of these simulations exhibit homogeneous boundary migration in the sense that the boundary at some point obtains a stable shape, which it keeps throughout the rest of the simulation. MD simulations of boundary migration during recrystallization do not exhibit homogeneous grain boundary migration in general. In [12] is was found that migrating grain boundaries may be perturbed when interacting with dislocations in dislocation boundaries.

The investigation performed in [12] was carried out with one type of grain boundary interacting with one type of dislocation boundary only. In this study we will perform a parameter study of dislocation driven boundary migration to investigate how different types of dislocation- and grain boundaries influence the grain boundary morphology, the migration rate, the mobility and the activation energy of the grain boundaries. Two types of dislocation structures are investigated: (1) dislocation boundaries consisting of interconnected screw dislocation networks (pure twist boundaries), (2) dislocation boundaries consisting of individual edge dislocations (pure tilt boundaries). Simulations where temperature, grain boundary misorientation, driving pressure and dislocation boundary misorientation are varied have been performed.

In section 2, the theoretical background for the study is given and in section 3 we describe how the simulations are carried out and analyzed. In section 4 we present the results which are then discussed and compared to experimental work and other simulations in section 5. Finally, in section 6, the conclusions are drawn.

2. Background

MD simulations of boundary migration have among other things been used to extract driving pressures, velocities and mobilities for migrating grain boundaries. Generally the following relationship is assumed:

$$v = MP \tag{1}$$

v is the velocity, P is the driving pressure and M is the mobility for the boundary. M is expected to depend on the five degrees of freedom of the boundary (three for the misorientation relationship between the crystal lattices on each side of the boundary plus two for the inclination of the boundary). Since boundary migration is a thermally activated process, the mobility is expected to have an Arrhenius temperature dependence:

$$M = M_\infty \exp\left(\frac{-E_a}{k_b T}\right) \tag{2}$$

M_∞ is the mobility when extrapolated to infinite temperature, E_a is the activation energy, k_b is the Boltzmann constant and T is the temperature.

The microstructure at the onset of recrystallization is composed primarily of dislocation boundaries created during deformation and recovery. For low angle dislocation boundaries, the elastic energy generated by the dislocations can be calculated using the Read-Shockley formula [13]:

$$\gamma = \gamma_0 \theta [A - \ln(\theta)] \tag{3}$$

where γ is the energy of the dislocation boundary per unit area, θ is the misorientation across the dislocation boundary and γ_0 and A are constants. Although this formula is only valid for low-angle dislocation boundaries, it often fits data up to much higher misorientations quite well [13, 14, 15]. The driving pressure for recrystallization can be found by integrating the energy of all dislocation boundaries within a certain volume of the deformed metal. The driving pressures in the simulations performed in this study are taken as the potential energy density difference

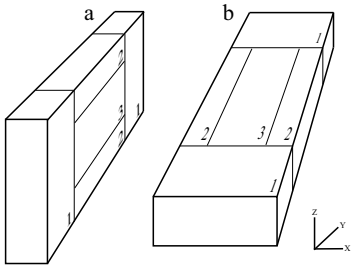

Figure 1. Setup geometries for (a) twist simulation cell with screw dislocation boundaries and (b) tilt simulation cell with edge dislocation boundaries. Atom-blocks are marked by numbers: 1 belongs to recrystallizing grain, 2 and 3 belong to deformed material.

between the part of the simulation representing the the deformed matrix and the part of the simulation representing the recrystallizing grain:

$$P = \frac{U_{matrix}}{V_{matrix}} - \frac{U_{grain}}{V_{grain}} \tag{4}$$

The true driving pressure for recrystallization is the free energy density difference between the deformed matrix and the recrystallizing grain, but because dislocation structures are causing the energy difference and the entropy contribution due to the introduction of dislocations in a metal is very small[16], the potential energy difference is assumed equivalent to the free energy difference in our simulations.

3. MD Methods

The MD technique, applied in this study, solves the classical Newtonian equations of motion for the simulated atoms iteratively [17]. The motion is governed by the interaction-potential between the atoms. In this study a so-called effective medium theory (EMT) interaction-potential for copper is used [18].

The simulation methodology applied has been used before, and is described in detail in [12, 19]. The purpose of the methodology is not to simulate an entire recrystallization process, but to simulate the fundamental process during recrystallization, namely migrating grain boundaries driven by the presence of dislocations. In the simulations, the dislocations are organized in dislocation boundaries because such dislocation-microstructures are typically present in metals at the onset of recrystallization. The simulation methodology consists of three steps: setup, relaxation and annealing:

3.1. Setup

During setup the atoms are placed inside the simulation cell. One simulation cell typically consists of 10^5 atoms. Blocks of atoms arranged in fcc-crystal lattices are generated and put into the simulation cell. The dimensions of the blocks are chosen such that they fill out the entire volume of the simulation cell. In order for the simulations to generate grain- and dislocation boundaries, the orientation of the crystal lattice in each block must be different. We have simulated grain boundaries with misorientations $\gtrsim 20$ deg. and dislocation boundaries with misorientations $\lesssim 20$

deg. When the misorientation across an interface is $\gtrsim 20$ deg., an amorphus layer will be formed at the interface, i.e. individual dislocations will be indistinguishable. All crystal blocks in the present simulations have the [111]-direction along the z-axis and are rotated by different amounts around this. If an interface has the normal vector perpendicular to the rotation axis it is a tilt boundary and if it has the normal vector parallel to the rotation axis it is a twist boundary.

Figure 1 shows the two types of simulation setups (simulation geometries) used. (a) The screw-type geometry contains pure twist dislocation boundaries, and therefore only screw dislocations. (b) The edge-type geometry contains pure tilt dislocation boundaries, and therefore only edge dislocations. The numbers in figure 1 indicate the blocks placed in the simulation cells. Blocks numbered 1 represent the recrystallizing grains while blocks numbered 2 or 3 represent the deformed material. The migrating grain boundaries are the interfaces between the blocks numbered 1 and the combo of blocks numbered 2 and 3. As discussed in [12], this geometry i chosen because it captures dominating features of typical deformation microstructures. The dislocation boundaries are the interfaces between blocks numbered 2 and 3. In most of the simulations, the misorientations of the migrating grain boundaries are on average ≈ 40 deg., because grain boundaries with this misorientation are known to have high mobilities [5, 20]. Fast boundaries reduce the simulation time. The misorientation between blocks marked 1 and 2 is different from the misorientation between blocks marked 1 and 3, but the average misorientation is around 40 deg.

The misorientations of the dislocation boundaries are different in the different simulations. Periodic boundary conditions are applied to the simulation cell along the x-, y- and z-axes to avoid surface effects. This also means that blocks with equal numbers in figure 1 can be considered as the same block. The simulation cells are thinned in directions of high symmetry, i.e. the z-direction for the edge-type simulation cell and in the x-direction for the screw-type cell. No size effects due to this have been observed in the simulations.

The way the simulation cells are set up ensures that near-constant driving pressures are obtained. This is because the driving pressure in a simulation depends on the dislocation density in the dislocation boundaries, given by the dislocation spacing. The dislocation spacing within the dislocation boundaries stays constant during the course of the simulation because the dislocations are absorbed at the rate by which the grain boundaries move forward (one dislocation is absorbed when the grain boundary has travelled a distance equal to the dislocation spacing).

The distance between dislocation boundaries are made small compared to the spacing between dislocation boundaries typically seen in deformed metals. This create higher driving pressures, but the high driving pressures are necessary in order to run the simulations within a reasonable amount of computational time.

Different series of simulations have been performed in order to investigate different aspects of dislocation driven boundary migration. These are listed in table 1. The 'E_a edge' and 'E_a screw' series contain simulations of the edge- and screw-type simulation cells at different temperatures in order to extract activation energies (see section 4.3). The series 'θ_b edge' contains simulations where the misorientation across the grain boundaries is varied (see section 4.4). The 'P edge' series contains simulation of the edge-type where the misorientation across all interfaces are kept constant but the driving pressure is changed by varying the size of the simulation cell (see section 4.5). Finally, the series 'θ_d edge' and 'θ_d screw' contain simulations where the misorientation across the dislocation boundaries are varied (see section 4.6).

name	cell type	T [K]	θ_b [deg.]	θ_d [deg.]	N [x1000]	l_x [Å]	l_y [Å]	l_z [Å]
E_a edge	b	100–1300	24.8	6.0	106	172	295	25
E_a screw	a	100–1300	24.8	6.0	107	25	295	175
θ_b edge	b	1200	25–60	9.9	78–96	≈ 100	≈ 400	25
P edge	b	1200	37.2	9.9	77–309	103–410	355	25
θ_d edge	b	1200	≈ 40	2.6–19.1	≈ 108	162	314	25
θ_d screw	a	1200	≈ 40	4.2–19.0	100–200	29–60	≈ 400	100

Table 1. Simulations performed. T is the temperature, θ_b is the grain boundary misorientation, θ_d is the dislocation boundary misorientation, N is the number of atoms, l_x, l_y and l_z are the simulation cell dimensions.

3.2. Relaxation

Atoms at the interface between two blocks may overlap after the crystal-blocks have been set up. If the MD simulation is started right away, these atoms may produce large excess energies, which may lead to local melting at the interfaces. In order to avoid this, atoms that are closer than a certain cut-off distance are removed. In order to relax the structure of the remaining atoms, a 'high friction' MD minimization-scheme is performed using the 'As Soon As Possible' (ASAP) MD program[21].

3.3. Annealing

The final step in a simulation is the MD run, i.e. the annealing. The simulations are performed using the ASAP MD program[21].

At the beginning of every simulation the temperature is increased relatively slowly (100K/5000 iterations) to obtain a controlled heating to the target temperature. When the target temperature is reached, the simulation is run at this temperature using Langevin dynamics. Pressure is kept constant near zero by adjusting the dimensions of the simulation cell for every 100 iterations. One iteration correspond to 5×10^{-15}s.

3.4. Common Neighbor Analysis – CNA

CNA is used to analyze the local structure around atoms and to identify for example fcc, hcp and other structures [22]. In ASAP, atoms are assigned the value 0 if they are in a fcc neighborhood, 1 if they are in a hcp neighborhood and 2 if they are in neither fcc or hcp. Atoms near stacking faults in fcc metals show up as hcp atoms in the CNA implemented in ASAP.

In order for CNA to work, the atom positions must be very close to their equilibrium positions (local energy minima). An easy way to identify these, is to average the atomic positions from several consecutive iterations in the MD integrator because most of the atomic movements are vibrations around the atoms' minimum energy configurations. Every atomic configuration shown in this paper is produced by averaging positions from 50 consecutive iterations.

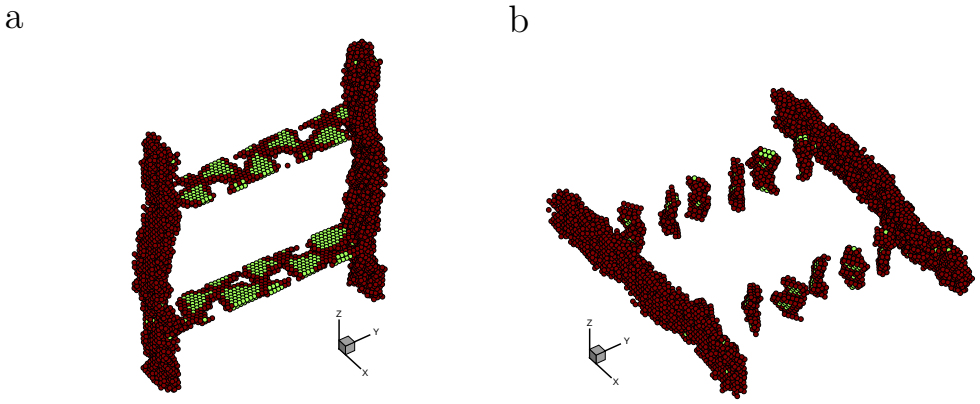

Figure 2. Skeletonized simulation cells, obtained by making atoms in a fcc neighborhood invisible. (a) Screw dislocation network in a screw-type simulation cell. (b) Edge dislocations running parallel to the z-direction in an edge-type cell. Colors indicate the local crystal structure: green represents hcp structure, red represents structures different from both fcc and hcp. Grain boundaries and dislocation cores are red, stacking faults are green. Some splitting into partial dislocations occur in the edge-type cell while rather large areas containing stacking faults are observed in between partial dislocations in the screw-type cell.

4. Results

4.1. Dislocation Structure

The dislocation structures formed in the edge- and screw-type simulation cells can be observed by making all atoms in a local fcc environment, i.e. atoms with CNA-values of zero, invisible. Figure 2 shows such 'skeletonized' simulation cells. The grain boundaries are seen as massive red atom-arrangements and dislocations are seen as smaller red strings of atoms. In both edge- and screw- simulation cells, dislocations split into partial dislocations with stacking faults in between. This is most clearly seen in the screw-type simulation cell in figure 2.

The dislocation densities created in the simulation cells are of the order of 10^{-3}Å^{-2} equivalent to 10^{17}m^{-2} (dislocation length per unit volume). This is some orders of magnitude higher than values typically seen in deformed metals experimentally [16], and is the result of the close spacing chosen for the dislocation boundaries mentioned above.

4.2. Boundary Migration

The grain boundaries absorb the dislocation as they migrate during the simulation. The interactions between migrating grain boundaries and edge dislocations were simulated using a Lennard-Jones potential and discussed in great detail in [12] but shall be summarized here for clarity. When a grain boundary approach an edge dislocation being parallel to the boundary, the boundary may cusp out and absorb the dislocation in a process much faster than the overall migration of the boundary. This was named an α-type absorption event in [12]. This type of events also takes place in the present simulations. Figure 3(a-c) show an α-event from the present simulations. Three images taken at different times during the simulation are shown: (a) Initially, the

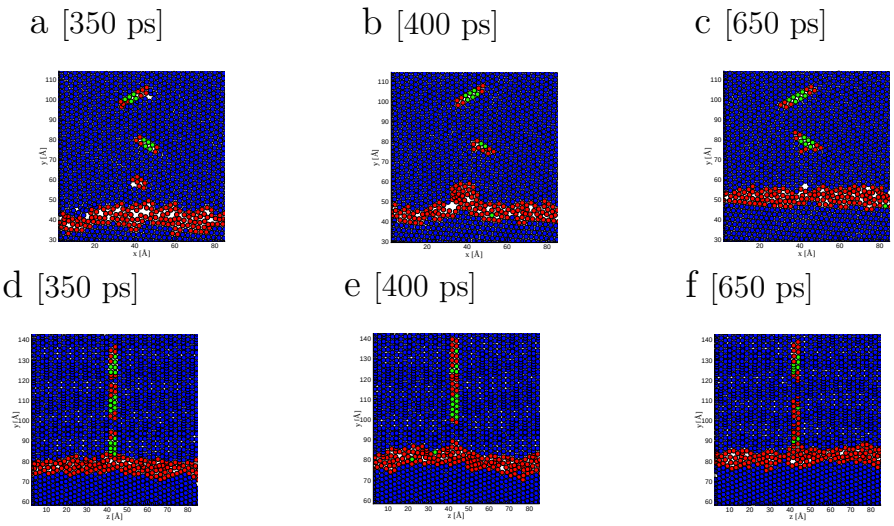

Figure 3. . An α-type absorption event in an edge-type simulation (a-c) and the corresponding structure of the grain- and dislocation boundaries in a screw-type simulation (d-f) seen at the atomistic level. One layer of atoms is seen, colored according to the CNA: Red and green represent the same as in figure 2, blue represents local fcc-structure. Voids or overlaps may be seen as the result of atoms being misplaced compared to the observed layer. (a) The grain boundary approaches the dislocation slowly. (b) At some point the boundary cusps out and absorbs the dislocation. (c) The boundary flattens and returns to its initial shape. (d-f) The structure is more or less flat during the entire migration process. Notice that the dislocations in the screw dislocation network move during the simulation.

grain boundary is almost flat and approaches the dislocation slowly. (b) At some point, the boundary shoots out in a cusp and absorbs the dislocation. This happens very quickly compared to the overall timescale of the simulation. (c) The grain boundary flattens after having absorbed the dislocation and obtains the same shape as before the absorption event.

The dislocation being absorbed will in many cases move towards the grain boundary at the same time as the cusp is formed by grain boundary. This was called a mixed event in [12]. In some extreme cases the grain boundary morphology is completely unaffected by the dislocation moving into it. This was called a β-event in [12].

For the screw dislocation simulations such events are not seen. The interconnected network of dislocations ensures that the grain boundaries are continuously in contact with the dislocations. Figure 3(d-f) show how the grain- and dislocation-boundaries interact in a screw-type simulation. It is seen that the shape of the grain boundary is fairly constant. It can also be seen that the dislocations in the screw dislocation network are not stationary but move during the simulation.

The positions of the grain boundaries can easily be found due to the simple geometries of the simulation cells. Figure 4(a) shows a part of the x-y-plane of an edge-type simulation, where the CNA-values of the atoms are averaged over small rectangular volumes. The dislocations are seen as localized areas of increased intensity while the grain boundary shows up as an broad line of high intensity perpendicular to the y-axis. By projecting the CNA-values of the atoms of a simulation cell onto

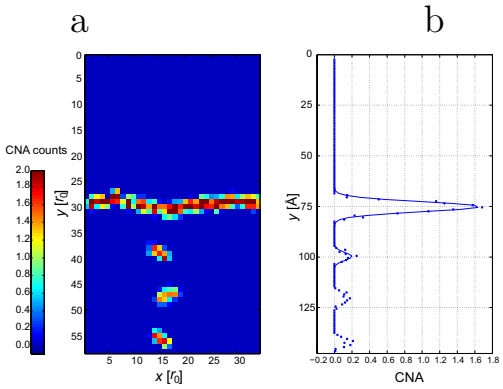

Figure 4. Boundary and dislocation tracking. (a) Edge-type simulation cell seen from the z-direction. The image is colored according to CNA values. A grain boundary and three dislocations are seen. (b) The CNA-values of all atoms are projected onto the y-axis, which makes identification of the positions of the grain boundary and the dislocations possible. The full lines indicate Gaussian fits.

the y-axis, the grain boundary and dislocations clearly stand out as high intensity peaks. In figure 4(b) such a projection is shown. Gaussians are fitted to the peaks of the grain boundary and one of the dislocations. The positions (y-coordinates) of the grain boundary and the dislocation are defined as the mean values of the Gaussian fits. Grain boundary tracking using the same methodology is possible in the screw-type simulations, but dislocation tracking is not possible. The complicated dislocation networks, with dislocations being along different directions, makes it impossible to identify the positions of the dislocations by making projections in any direction.

Growth curves can be created by tracking the grain boundary position over time. The average distance s travelled by the two grain boundaries in an edge-type simulation cell and the driving pressure P are plotted as a function of time in figure 5(a). The growth curve exhibits irregular fluctuations in the grain boundary velocity that are not coupled to changes in the driving pressure; no changes in P are seen at the times where s fluctuates. The fluctuations in s seem to be caused by local interactions between the migrating grain boundaries and the dislocations: The vertical lines in figure 5(a) indicate the times when a dislocation is absorbed by a grain boundary. There seems to be a direct correlation between the fluctuations in s and the dislocation absorption events, i.e. s is increasing fast at times where dislocation absorbtion events happen. This is most clearly seen at $t \approx 1300$ps.

A cusp on a grain boundary, produced during an absorbtion event, changes the position of the parts of the boundary participating in the cusp. This does, however, not change the value of s significantly. If the part of the boundary that participates in the cusp is excluded in the analysis, s only changes by .1 to .2Å, which is much less than the fluctuations observed in figure 5(a). This means that the fluctuations indicate when a grain boundary as a whole moves faster, which happens during absorption events as shown above.

Toward the end of the edge simulation, the velocity drops. This drop is associated with a drop in the driving pressure, which indicates that the dislocation density has gone down significantly. The drop in dislocation density happens because the grain boundaries are very close to each other at the end of the simulation and only few

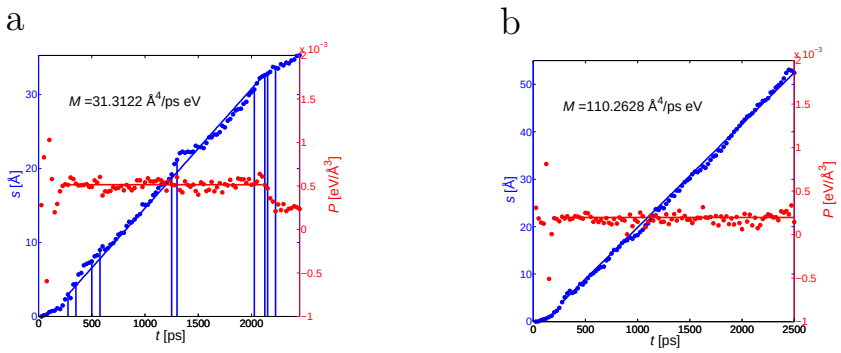

Figure 5. Growth curves from (a) an edge-type simulation cell and (b) a screw-type simulation cell. The average distance travelled by the two grain boundaries s and the driving pressure P is plotted as a function of simulation time. In the beginning of any simulation, the growth curve exhibit a transient stage corresponding to the slow heating of the system. The movement of the grain boundaries are irregular in the edge-type cell, which is probably due to interactions with dislocations. The vertical lines marks dislocation absorption events. The irregularities are less pronounced in the screw-type simulation.

dislocations are left. The disappearance of one dislocation will therefore change the dislocation density significantly.

Figure 5(b) shows a growth curve for a screw-type simulation. The irregularities seem to be much smaller, although not completely gone. Interactions with single dislocations do not happen in the screw-simulations due to the continuous dislocation network.

4.3. Mobilities and Activation Energies

Although the boundary velocity exhibit irregularities/fluctuations in most cases, the average velocity can be found as $< v >= \Delta s/\Delta t$, where Δs is the distance travelled by the boundary and Δt is the simulation time, both measured from the point where the simulation reaches the target temperature to the point where the driving pressure changes due to the removal of the last dislocations in the simulation cell. The apparent mobility for each simulation is calculated as $< M >=< v > / < P >$, where $< P >$ is the average of the driving pressure calculated in the same range as $< v >$.

Figure 6(a) shows $\log < M >$ vs. $(k_B T)^{-1}$ for the 'E_a edge' series of simulations (see table 1). The data-points for $T \leq 400$K are excluded because insufficient movement of the grain boundaries took place during these simulations. The low limit for the mobilities that can be 'measured' in these simulations is given by the time that a simulation is allowed to run because the distance moved by the grain boundaries has to be of a certain magnitude to extract mobilities. In this study the maximum simulation times are of the order of one month on a standard 3GHz single processor PC. The data-point for $T = 1300$K is excluded because melting occurred. Figure 6(b) shows the same plot, but for the 'E_a screw' series of simulations. Here the data-points for $T \leq 200$K and $T = 1300$K are excluded for the same reasons as in the edge-type simulations.

The mobilities extracted from these simulations are in the range .5 – 38Å^4/ps eV (3×10^{-10} – 2.4×10^{-8} m^4/J s) for edge simulations and .5 – 160Å^4/ps eV (3×10^{-10} – 1.00×10^{-7} m^4/J s) for screw simulations. It is noticeable that large differences exist

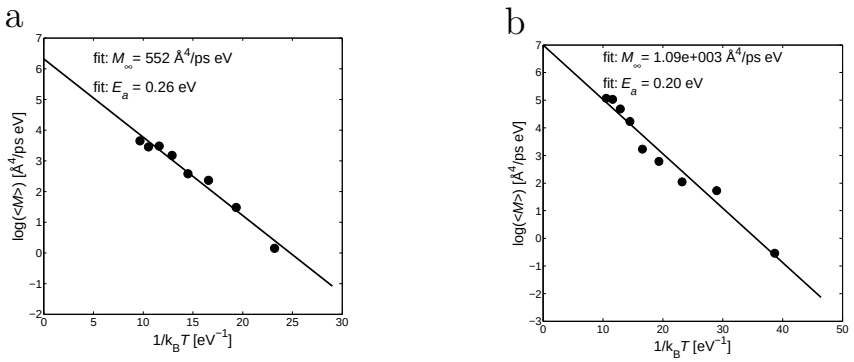

Figure 6. $\log M$ vs. $(k_B T)^{-1}$ for the simulations with dislocation boundaries containing (a) edge and (b) screw dislocations. The slope of the curves indicate the activation energy E_a for the two types of dislocation boundaries. The simulations containing edge dislocations have lower mobilities and higher activation energies compared to the simulations containing screw dislocations.

between the mobilities in the two simulation-types. At all temperatures the mobilities measured in the edge-type simulations are lower than the mobilities measured in the screw-type simulations. The mobilities at 1200 K for example is around 38Å^4/ps eV for the edge-type simulations and 160Å^4/ps eV for the screw-type simulations.

The mobility is typically assumed to follow an Arrhenius behavior given by equation (2). In both figure 6(a) and figure 6(b), a straight line is seen which indicates that equation (2) is obeyed. The slope of the curve gives the activation energy: $-E_a$. As indicated on the plots, E_a for the two types of simulations are similar: $E_{a-edge} = .26$ eV, $E_{a-screw} = .20$ eV. M_∞ for the two types of simulation cells differs by a factor of two.

4.4. Effects of Variations in Grain Boundary Misorientation

The influence of the grain boundary misorientation and the boundary inclination on the mobility have been discussed extensively [7, 5, 23]. In this study we have simulated a range of grain boundary misorientations while maintaining the dislocation boundary misorientation in the series 'θ_b edge' (see table 1). In figure 7, the mobility $< M >$ is plotted versus the grain boundary misorientation θ_b. Some differences do exist, but there does not seem to be any clear trend.

4.5. Effects of Variations in Driving Pressure

The driving pressure is defined as the potential energy density difference between the deformed and the recrystallizing part of the simulation cell (see equation (4)). The energy difference stems from the dislocations in the dislocation boundaries that are present within the deformed part of the simulation and of course not in the recrystallized part. By changing the dimensions of the simulation cell, maintaining the type of dislocation boundary, the excess energy density of the deformed part can be changed. If for example the box-length along the x-axis l_x is doubled in an edge-type simulation cell, the total volume of the deformed part is doubled while the dislocation boundary area is kept at the same value(see figure 1). The excess energy of a dislocation boundary is believed to be fairly independent of the distance to the

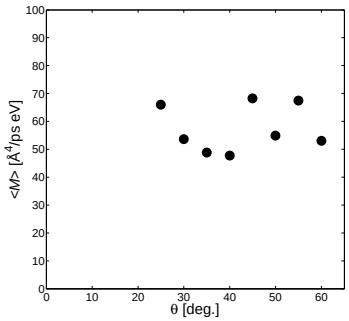

Figure 7. Dependence of mobility on grain boundary misorientation in edge-type simulations: The mobility $< M >$ is plotted versus the grain boundary misorientation θ_b. No clear trend is seen.

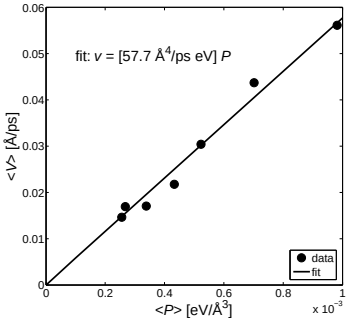

Figure 8. Variable driving pressure obtained by varying the dimensions of the edge-type simulation cells. The figure shows the boundary velocity $< v >$ as a function of driving pressure $< P >$. A straight line is seen indicating that equation (1) holds.

next dislocation boundary, this will reduce the excess energy density, i.e. the driving pressure, to approximately the half of the original values.

In the simulation series 'P edge' (see table 1), l_x is changed from ≈ 100Å to ≈ 400Å while keeping the grain boundary at a misorientation of 37.2 deg. and the two tilt dislocation boundaries at 9.9 deg. This changes the driving pressure from $\approx 10^{-3}$ to $.25 \times 10^{-3}$ eV/Å^{-3}. Figure 8 shows the boundary velocity $< v >$ as a function of driving pressure $< P >$. The data-points can be approximated by a straight line, which indicates that equation (1) holds.

4.6. Effects of Variations in Dislocation Density within Dislocation Boundaries

Another way to change the driving pressure is by varying the misorientation of the dislocation boundaries. This will change the dislocation boundary energy according to the Read-Shockley formula, equation (3). In the simulation series called 'θ_d edge' and 'θ_d screw' (see table 1) the misorientations of the dislocation boundaries are varied from 2.6 to 19.1 deg. (edge) and 4.2 to 19.0 (screw). Figure 9(a) and figure 9(b) show the dislocation boundary energy per unit area. The full lines are fits to the Read-Shockley formula. Good agreements between the Read-Shockley formula and

the simulated boundary energies are seen.

In figure 9(c) and figure 9(d) the boundary velocity $< v >$ is plotted as a function of driving pressure $< P >$. According to equation (1) this should be a straight line. It is a straight line for the screw-type simulations, as shown by the linear fit in figure 9(d). But this is clearly not the case for the edge-type simulations. In figure 9(c) the data is fitted by $< v > \propto < P >^2$. This surprising behavior will be discussed in detail below. The fits in figure 9(c-d) are forced to go through zero as it is assumed that the velocity is zero only when the driving pressure is zero. One could also assume that a certain minimum driving pressure was needed in order to make the boundaries move. This is not done here.

Figure 9(e) and figure 9(f), that shows the mobility $< M >$ vs. $< P >$, also reflects this. $< M >$ increases linearly with $< P >$ for the edge simulations but are fairly constant for the screw simulations (a slight increase in $< M >$ is seen as $< P >$ increases though).

The mobilities for the edge simulations approach that for the screw simulations when the misorientations across the dislocation boundaries are increased. As the misorientation increases, the distance between the dislocations decrease. When the distance between the dislocations decreases, the dislocation boundary becomes more 'solid' and the grain boundary will locally experience a more constant driving pressure without individual dislocation absorbtion events. This is similar to what goes on in the screw-type simulations.

5. Discussion

In this study an EMT interatomic potential was used. Previous simulations of edge-type simulation cells using Lennard-Jones (LJ) and Embedded Atom Method (EAM) Al potentials show qualitatively similar results, namely dislocations being absorbed by migrating grain boundaries in α-, β- and mixed-type events[12, 24]. The similarity indicates that the type of potential used might not be very important for the grain boundary-dislocation interactions. On the other hand, quantitative measures such as M or E_a may depend strongly on the applied potential as discussed below.

The values of M extracted in these simulations are in the range 3×10^{-10} – 1.00×10^{-7} m^4/J s depending on the temperature and type of dislocation structure. These values are orders of magnitude larger than typical experimental values, which are in the range 10^{-12} – 10^{-8} m^4/J s. [20, 25, 26, 27]. The extracted values for E_a are .20 eV for the screw- and .26 eV for the edge-type simulations. These are smaller than what is observed in experiments, typical experimental values are in the order of 1 eV [20, 25]. High mobilities and low activation energies are often seen in MD simulations [8, 10, 11, 27] and are typically associated with the lack of impurities [28]. The impurity content can have a very large influence on the boundary migration rate, changing it by orders of magnitude [29]. Because the simulations here only have one species of atoms they are ultra pure and good quantitative agreement between the simulations and experimental measurements can not be expected. MD simulations of dislocation driven boundary migration performed with other interatomic potentials show mobilities and activation energies in the same general range, but differences do exist: The simulations in [12], performed using a LJ-potential, produced mobilities for edge-type simulations in the range 1×10^{-9} – 4×10^{-9} m^4/J s when converted to Cu-units. The activation energy extracted was .14 eV when converted to Cu-units[12]. It is important to note that the energies and mobilities extracted from from LJ-simulations

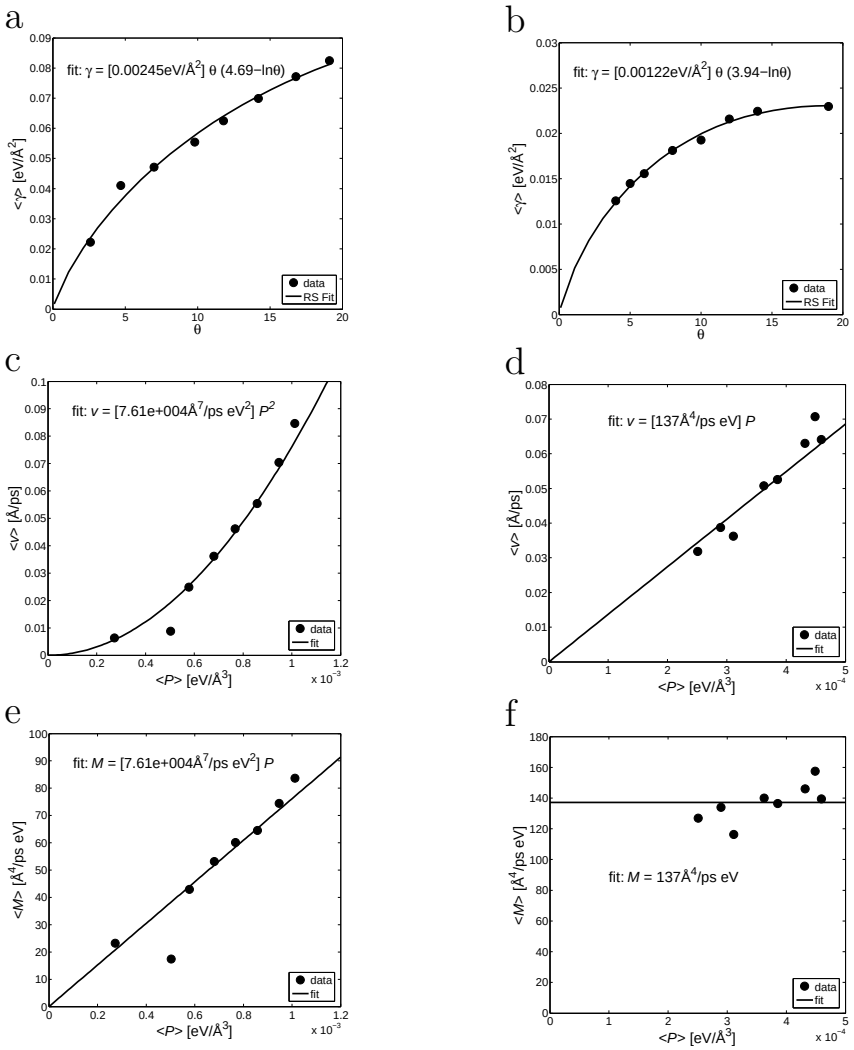

Figure 9. Effect of dislocation density within dislocation boundaries. (a) and (b) show the dislocation boundary energy per unit area $< \gamma >$ as a function of boundary misorientation θ for simulations with boundaries containing edge (a) and screw (b) dislocations. The full lines are fits using the Read-Shockley formula, equation (3). (c) and (d) show the boundary velocity $< v >$ as a function of driving pressure $< P >$ for simulations with edge (c) and screw (d) dislocations. The edge dislocation-simulations are fitted by $v \propto P^2$, whereas the screw dislocation-simulations are fitted by $v \propto P$. (e) and (f) show the mobility $< M >$ as a function of $< P >$ for edge (e) and screw-simulations (f). A linear correlation is seen for the edge-simulations and an almost constant mobility is seen for the screw-simulations.

are associated with large errors due to inaccurate reproductions of energetic properties of metallic systems by the LJ-potential[30]. In [24] the activation energy was found to be .32 eV for edge-type simulations using an EAM-Al potential. Although activation energies for Al and Cu of course should not be compared directly, it is noteworthy that E_a obtained in [24] is of the same order of magnitude as E_a found in this study.

In [12] and [24] the average misorientation across the simulated migrating grain boundaries were 40 deg. ([111]-tilt). Different misorientations may have an influence on M, although this study shows that M is not affected strongly by variations in the grain boundary misorientation, as seen in figure 7. This is in contrast to the grain boundary mobility in for example curvature driven grain boundary migration [7], where certain boundaries were observed to have much higher mobilities than average. The special $\Sigma 7$ boundary created by a rotation of 38.2 deg. around an [111]-axis is for example known to have very high mobility. The reason why such high mobility boundaries are not seen in our simulations may be that the special character of any grain boundary is destroyed because the grain boundary meets two parts of the deformed matrix with different orientations. The grain boundary misorientation will therefore always be an average of the misorientations to the two matrix-parts and each segment of the boundary will in all cases have a misorientation away from, for example, the exact $\Sigma 7$.

The driving pressure is typically around 5×10^{-4} eV/Å^3 in our simulations, which corresponds to 8×10^7 Pa. This is large but within what is seen in experiments, e.g. according to Ashby [31] and Smith et al. [32], the driving pressure for recrystallization is in the range 10^5 – 10^8 Pa. The simulations with edge dislocations exhibit larger driving pressures, i.e. larger dislocation boundary-energies, than the simulations with screw dislocations for the same dislocation boundary misorientations. This could be due to non-equilibrium edge dislocations. Normally dislocations in fcc crystals will have their Burger's vectors along a [110] direction. Because the edge dislocations are forced to have the Burger's vectors along the x-axis defined by the simulation geometry, this is not possible in these simulations. In the screw dislocation networks, which can be seen in figure 2(b), dislocations with minimum Burger's vectors are allowed to form. Therefore the screw dislocation will be more relaxed and contain less energy. We do not expect that the unrelaxed edge dislocations fundamentally change the results; we believe that the differences between edge- and screw-type simulations are mainly due to the way the dislocations are arranged: as individual dislocations vs. in a dislocation network.

The difference in the grain boundary mobility between edge- and screw-type simulations is very large. This indicate that the apparent grain boundary mobility does not only depend on the grain boundary type but also the structure of the dislocations providing the driving pressure. The different behavior may be due to different interactions between migrating grain boundaries and dislocations. During an absorption-event in an edge-type simulation, the dislocation is removed. If the dislocation moves into the boundary in a β-event, the dislocation will be removed without the boundary moving. This will reduce the local driving pressure and therefore slow down the migration rate of the grain boundary. The local driving pressure experienced by the grain boundaries may therefore not be the same as the average driving pressure $< P >$ calculated over the entire deformed part of the simulation. In the case of the screw dislocation simulations, the network of dislocations created ensure that it is not possible to remove the dislocations close to the grain boundary. Therefore the local driving pressure will be more or less constant throughout the simulation and equal to $< P$.

As shown in figure 5, the boundary velocity is more or less constant for the screw-type simulations but fluctuates for the edge-type simulations. This is due to the differences in dislocation structures: In screw-type simulations the grain boundaries are in direct contact with the dislocation all the time whereas in edge-type simulations

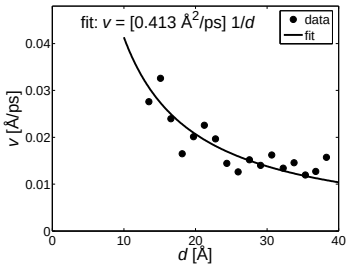

Figure 10. Instantaneous boundary velocity v versus distance to nearest dislocation d. The full is a fit using equation (6).

the boundary velocity fluctuate as individual dislocations are absorbed. It is therefore interesting to investigate how the grain boundary velocity changes as a function of the position of the dislocation that are about to be absorbed. The distance from the grain boundary to the nearest edge dislocation d can be measured by identifying the position of the grain boundary and the position of the dislocation by the method shown in figure 4. The instantaneous velocity v of the boundary adjacent to the dislocation versus d in edge simulation is plotted in figure 10. We see that v increases as d decreases. The plot is generated by analyzing and averaging ≈ 300 absorption events. This is necessary because the uncertainties associated with the instantaneous grain boundary velocity are very large. All of the analyzed events stem from the same simulation geometry using grain boundaries with misorientations of 24.8 deg. and dislocation boundaries with 6.0 deg. ('E_a edge' simulation series). Although figure 10 shows the correlation between v and d for one specific type of simulation only, the general shape of the curve is expected to be the same for grain boundaries and edge dislocation boundaries with other misorientations as well. The overall velocity is expected to depend on the driving pressure, i.e. a higher $< P >$ must give a higher velocity at all values of d. The increase of v associated with low values of d, on the other hand, could be seen as the effect of the nearest dislocation, i.e. the local presence of dislocations. Interestingly this effect is quite significant: v change more than a factor of two in figure 10. This means that grain boundaries will move much faster when an edge dislocation is close to the boundary than when the dislocation is far from the boundary.

In the following we show how the behavior of the edge-type simulations seen in figure 9 may be seen as a result of local interactions. Assuming that the contribution to the grain boundary velocity can be divided into a background contribution B depending on $< P >$ and a contribution L from the local presence of dislocations:

$$v = BL \tag{5}$$

If we assume that the local contribution are inversely proportional to the distance $L \propto 1/d$ to the boundary we have the following velocity:

$$v \propto \frac{B}{d} \tag{6}$$

The data in figure 10 have been fitted by equation (6). The fit is quite good, although some deviations are seen for high values of d. If we further assume that B is proportional to $< P >$ we have that:

$$v \propto \frac{< P >}{d} \tag{7}$$

The dislocation spends little time close to the grain boundary because the boundary moves fast. Also the grain boundary may cusp out or the dislocation may move into the boundary. Most of the time the dislocation will be at a distance that correspond to the the spacing between the dislocations D in the dislocation boundary. For low-angle tilt boundaries $D \approx b/\theta$, where θ is the misorientation and b is the size of the Burger's vector[16]. If we assume that $< \gamma >$ depends linearly on θ in the range of misorientations simulated:

$$< P > \propto < \gamma > \propto \theta \propto 1/D \tag{8}$$

By combining equation (7) and (8) and assuming that $< d >$ will be close to D, we obtain:

$$< v > \propto < P >^2 \tag{9}$$

which is what we have seen for the edge dislocation simulations. The simple calculation above shows how local interactions may play a role in the determination of the boundary migration rate. The model assumes that the dislocation spacing plays a significant role for the grain boundary migration rate: If the dislocation spacing is smaller, the grain boundary will much more often experience a strong driving pressure due to local dislocations.

Smith et al. discussed mechanisms for boundary migration [32]. They found that a grain boundary migrates with a velocity that is proportional to the square of the driving pressure when a so-called step mechanism controls the migration. They also argued that this happens during recrystallization. Whether the step mechanism takes place in these simulations is outside the scope of the present paper, but it is reassuring that the result of Smith et al. shows that boundary migration with $v \propto P^2$ may take place during recrystallization.

For the simulation with screw dislocations, some dislocation is always present at the boundary, and no local effect can be defined. The local driving pressure experienced by the grain boundaries is therefore the same as the overall driving pressure and the relationship $< v > \propto < P >$ is seen.

In figure 8, a linear correlation between $< v >$ and $< P >$ is seen for simulations where different driving pressures are created by different edge-dislocation densities. The appropriateness of a linear correlation between $< v >$ and $< P >$ in this case (and not $< v > \propto < P >^2$ as seen in the edge-dislocation simulations with varied dislocation boundary misorientations) can be argued as follows: The simulations in figure 8 all have the same dislocation boundary misorientation and therefore the same local contribution to the driving pressure L. Only the background B, which is assumed proportional to $< P >$, changes due to the changes in the simulation size. Therefore, if equation (5) holds, $< v > \propto B \propto < P >$.

6. Conclusions

We have simulated grain boundary migration driven by the excess energy of dislocation structures using MD. Two different types of dislocation boundaries have been used to represent the dislocation structure prior to recrystallization: (a) edge dislocations arranged parallel to the grain boundary and (b) screw dislocations arranged in an interconnected network.

The boundary migration is generally more irregular in the edge dislocation-simulations than in the screw dislocation-simulations. This may be because the grain

boundary in the former case absorbs one dislocation at a time whereas the boundary in the latter case continuously interacts with the dislocation network. The difference is not likely to be due to the difference in dislocation type, but rather the difference in the dislocation arrangement.

The average misorientation across the grain boundary do not have a large effect on the mobility, in contrast to what is seen in for example curvature driven boundary migration where some misorientations have much higher mobilities than average. Likewise, no significant change in mobility is seen when the driving pressure is changed by changing the distance between dislocation boundaries, as long as the type of dislocation boundary is kept the same.

The mobilities are quite different for the edge- and the screw-type of simulations. The mobilities at 1200 K is around 38Å^4/ps eV for the edge dislocation simulations and 160Å^4/ps eV for the screw. The activation energies are similar: .26 eV for the edge- and .20 for the screw-type simulations.

Edge- and screw dislocation simulations behave very differently if the misorientations across the dislocation boundaries are changed. In both cases $< v >$ increases when $< P >$ increases, as expected, but whereas screw-type simulations exhibit the expected $< v > \propto < P >$ behavior, the edge-type simulations exhibit a $< v > \propto < P >^2$ behavior. This may be explained by assuming that the migration rate have a contribution from the overall dislocation structure and a contribution from the local presence of dislocations.

The simulations performed show that the dislocation structure, present at the onset of recrystallization, may have a significant impact on the migration rates, the mobilities and the activation energies of the grain boundaries of the recrystallizing grains. Further experimental and theoretical studies should investigate if variations in the deformation microstructure can explain the irregularities observed in recrystallization experiments.

Acknowledgements

The authors would like to thank W. Pantleon, B. Ralph, and R.A. Vandermeer for very useful discussions and J. Schiøtz for help with the simulations. The authors gratefully acknowledge the Danish National Research Foundation for supporting the Center for Fundamental Research, Metal Structures in Four Dimensions, within which this work was performed.

References

[1] R. W. Cahn. Recovery and recrystallization. In R. W. Cahn and P. Haasen, editors, *Physical Metallurgy*, pages 1595–1671. Elsevier Science Publishers, 1983.

[2] E. M. Lauridsen, H. F. Poulsen, S. F. Nielsen, and D. Juul Jensen. Recrystallization kinetics of individual bulk grains in 90cold-rolled aluminium. *Acta Materialia*, 51(15):4423–4435, Sep 2003.

[3] S. Schmidt, S. F. Nielsen, C. Gundlach, L. Margulies, X. Huang, and D. Juul Jensen. Watching the growth of bulk grains during recrystallization of deformed metals. *Science*, 305(5681):229–232, Jul 2004.

[4] M. A. Martorano, H. R. Z. Sandim, M. A. Fortes, and A. F. Padilha. Observations

of grain boundary protrusions in static recrystallization of high-purity bcc metals. *Scripta Materialia*, 56(10):903–906, May 2007.

[5] P. A. Beck, P. R. Sperry, and H. Hu. The orientation dependence of the rate of grain boundary migration. *Journal of Applied Physics*, 21(5):420–425, 1950.

[6] R. A. Vandermeer and P. Gordon. The influence of recovery on recrystallization in aluminium. In L. Himmel, editor, *Recovery and recrystallization of metals*, page 211. 1963.

[7] M. Upmanyu, D. J. Srolovitz, L. S. Shvindlerman, and G. Gottstein. Misorientation dependence of intrinsic grain boundary mobility: Simulation and experiment. *Acta Materialia*, 47(14):3901–3914, Oct 1999.

[8] H. Zhang, M. Upmanyu, and D. J. Srolovitz. Curvature driven grain boundary migration in aluminum: molecular dynamics simulations. *Acta Materialia*, 53(1):79–86, Jan 2005.

[9] M. Upmanyu, D. J. Srolovitz, L. S. Shvindlerman, and G. Gottstein. Molecular dynamics simulation of triple junction migration. *Acta Materialia*, 50(6):1405–1420, Apr 2002.

[10] B. Schonfelder, G. Gottstein, and L. S. Shvindlerman. Comparative study of grain-boundary migration and grain-boundary self-diffusion of [001] twist-grain boundaries in copper by atomistic simulations. *Acta Materialia*, 53(6):1597–1609, Apr 2005.

[11] K. G. F. Janssens, D. Olmsted, E. A. Holm, S. M. Foiles, S. J. Plimpton, and P. M. Derlet. Computing the mobility of grain boundaries. *Nature Materials*, 5(2):124–127, Feb 2006.

[12] R. B. Godiksen, Z. T. Trautt, M. Upmanyu, J. Schiøtz, S. Schmidt, and D. Juul Jensen. Simulations of boundary migration during recrystallisation using molecular dynamics. *Acta Materialia*, 55:6383–6391, 2007.

[13] W. T. Read and W. Shockley. Dislocation models of crystal grain boundaries. *Physical Review*, 78(3):275–289, 1950.

[14] N. A. Gjostein and F. N. Rhines. Absolute interfacial energies of [001] tilt and twist grain boundaries in copper. *Acta Metallurgica*, 7(5):319–330, 1959.

[15] A. J. Patrinos, I. P. Antoniades, and G. L. Bleris. Monte-Carlo and molecular-dynamics investigation of [001] twist boundaries in Cu3Au at t=0 K. *Physical Review B*, 52(13):9291–9299, Oct 1995.

[16] J. Weertman and J. R. Weertman. *Elementary Dislocation Theory*. Oxford University Press, Inc., 1992.

[17] M. P. Allen and D. J. Tildesley. *Computer Simulation of Liquids*. Oxford University Press, 2004.

[18] K. W. Jacobsen, J. K. Norskov, and M. J. Puska. Interatomic interactions in the effective-medium theory. *Physical Review B*, 35(14):7423–7442, May 1987.

[19] R. B. Godiksen, Z. T. Trautt, M. Upmanyu, S. Schmidt, and D. Juul Jensen. Towards atomic level simulations of recrystallisation - setting up suitable geometry. *Materials Science and Technology*, 21(12):1373–1375, Dec 2005.

[20] Y. Huang and F. J. Humphreys. Measurements of grain boundary mobility during recrystallization of a single-phase aluminium alloy. *Acta Materialia*, 47(7):2259–2268, May 1999.

[21] J. Schiøtz. Asap - as soon as possible md program used within the ase - atomistic simulation environment. asap and ase are available at http://www.camd.dtu.dk/software.aspx. ( ), 2007.

[22] A. S. Clarke and H. Jonsson. Structural changes accompanying densification of random hard-sphere packings. *Physical Review e*, 47(6):3975–3984, Jun 1993.

[23] B. B. Rath and H. Hu. Driving-force dependence of rate of boundary migration in zone-refined aluminum crystals. *Transactions of the Metallurigal Society of AIME*, 245:1243–1252, Jun 1969.

[24] R. B. Godiksen, Z. T. Trautt, M. Upmanyu, S. Schmidt, and D. Juul Jensen. Simulation of recrystallization using molecular dynamics; effects of the interatomic potential. *Materials Science Forum*, 558-559:1081–1086, 2007.

[25] R. A. Vandermeer, D. Juul Jensen, and E. Woldt. Grain boundary mobility during recrystallization of copper. *Metallurgical and Materials Transactions A-Physical Metallurgy and Materials Science*, 28(3A):749–754, Mar 1997.

[26] R. Le Gall, G. Liao, and G. Saindrenan. In-situ sem studies of grain boundary migration during recrystallization of cold-rolled nickel. *Scripta Materialia*, 41(4):427–432, Jul 1999.

[27] Z. T. Trautt, M. Upmanyu, and A. Karma. Interface mobility from interface random walk. *Science*, 314(5799):632–635, Oct 2006.

[28] A. Lens, C. Maurice, and J. H. Driver. Grain boundary mobilities during recrystallization of Al-Mn alloys as measured by in situ annealing experiments. *Materials Science and Engineering A-Structural Materials Properties Microstructure and Processing*, 403(1-2):144–153, Aug 2005.

[29] K. T. Aust and J. W. Rutter. Grain boundary migration in high-purity lead and dilute lead-tin alloys. *Transactions of the American Institute of Mining and Metallurgical Engineers*, 215(1):119–127, 1959.

[30] M. I. Baskes. Many-body effects in fcc metals: A Lennard-Jones embedded-atom potential. *Physical Review Letters*, 83(13):2592–2595, Sep 1999.

[31] M. F. Ashby. The influence of particles on boundary mobility. *Proceedings from the 1st Risø International Symposium on Metallurgy and Materials Science*, 1:325–336, 1980.

[32] D. A. Smith, C. M. F. Rae, and C. R. M. Grovenor. Grain boundary migration. *Papers presented at the 1979 ASM Materials Science Seminar*, :337–371, 1979.

I Measurement of the components of plastic displacement gradients in three dimensions

S. F. Nielsen, G. Beckmann, R. B. Godiksen, K. Haldrup, H. F. Poulsen and J. A. Wert, Developments in X-Ray Tomography IV. Edited by Ulrich Bonse, *Proceedings of SPIE*, **5535**, 485–492, (2004).

Measurement of the components of plastic displacement gradients in three dimensions

S.F. Nielsen[*a], F. Beckmann[b], R.B. Godiksen[c], K. Haldrup[c], H.F. Poulsen[c] and J.A. Wert[c]
[a] Materials Research Department, Risø National Laboratory, 4000 Roskilde, Denmark
[b] GKSS-Forschungszentrum Geesthacht, 21502 Geesthacht, Germany
[c] Center for Fundamental Research: Metal Structures in Four Dimensions, Risø National Laboratory, 4000 Roskilde, Denmark

ABSTRACT

A method for non-destructive characterization of plastic deformation in bulk materials is presented. The method is based on X-ray absorption microtomography investigations using X-rays from a synchrotron source. The method can be applied to materials that contain marker particles, which have an atomic number significantly different from that of the matrix material. Data were acquired at the dedicated microtomography instrument at beamline BW2 at HASYLAB / DESY, for a cylindrical aluminium sample containing W particles with an average particle diameter of 7 μm. The minimum detectable size of the maker particles is 1-2 μm with the present spatial resolution at HASYLAB. The position (x,y,z) of all the detected marker particles within 1 mm^3 was determined as function of strain. The sample was deformed in stepwise compression along the axis of the cylinder. A tomographic scan was performed after each deformation step. After a series of image analysis steps to identify the centre of mass of individual particles and alignment of the successive tomographic reconstructions, the displacements of individual particles could be tracked as a function of external strain. The particle displacements are then used to identify local displacement gradient components, from which the local 3D plastic strain tensor can be determined. This allows us to map the strain components as a function of location inside a deforming metallic solid.

Keywords: Synchrotron radiation, Plastic deformation, X-ray tomography, Discrete tomography, Image analysis

1. INTRODUCTION

As metals predominantly deform plastically, and the local deformation in most cases is heterogeneous, it is of obvious interest to characterize the spatial variations of the plastic strain as a function of external strain. This is true on the macroscopic scale, where the heterogeneity is a function of the geometry of the specimen and the mode of deformation and it is also true on the meso-scale, where grain orientations, inclusions, pores and cracks may influence the field. Depending on the deformation process and the material there can be local plastic strain variations down to the μm-scale, which are important for the mechanical properties of the material.

Spatial variations in plastic deformation have mainly been studied experimentally by observing scratches, etch patterns or grids placed on the surface [1-6]. The spatial resolution of these methods depends on the size and the distance between recognizable features before and after a given deformation increment. Two-dimensional grids or marker wires within samples have in the past been used to study deformation processes within bulk material [7,8]. A two-dimensional grid inside a sample can be introduced by welding two pieces together around a grid. In [7] the grid was made by machining a network of grooves in one aluminium piece and afterwards weld it together with another. A similar network of grooves was machined on the outer surface of the sample. The sample was afterwards deformed by rolling and after the deformation the two aluminium pieces were separated. When comparing the side surface and the centre of the width of the sample a substantial difference of the local deformation is observed.

* soeren.faester.nielsen@risoe.dk; phone +45 4677 5762; fax +45 4677 5758; risoe.dk

Developments in X-Ray Tomography IV, edited by Ulrich Bonse, Proc. of SPIE Vol. 5535
(SPIE, Bellingham, WA, 2004) · 0277-786X/04/$15 · doi: 10.1117/12.559641

The spatial resolution of these methods is in the order of 0.1 mm, which is insufficient to study local meso-scale deformation. At the same time these methods demand drilling holes or welding material together around a grid, which most likely will change the material properties, and the application of these methods is therefore limited.

In the present paper, a novel method is presented to determine the plastic deformation in bulk material with a spatial resolution in the μm range. X-rays from a synchrotron radiation source are used to perform absorption tomography on a sample that contains marker particles with high absorption contrast. The displacements of individual particles are identified as a function of imposed strain and the components of the local plastic deformation gradient are determined in the subsequent analysis.

2. EXPERIMENTAL PROCEDURE

A sample was made by compacting aluminium powder mixed with 1 vol.% tungsten powder. The size of both types of powder particles was in the range of 1-10 μm. The powder mixture was cold compressed (30 MPa) and hot compressed (60 MPa) at 825 K for five minutes. The result was a compact sample with a relatively homogeneous distribution of W particles (Fig. 1). A cylinder with a diameter of 1 mm and a height of 2 mm was cut from the material and investigated tomographically before and after compression to macroscopic strains of 2.7, 6.2 and 9.5%.

Tomography refers to the cross-sectional imaging of an object from either transmission or reflection data collected by illuminating the object from many different directions. This technique has had a tremendous impact in diagnostic medicine because is has enabled the medical doctors to view internal organs with unprecedented precision. The first medical application utilized x-rays for forming images of tissues based on their x-ray attenuation coefficient. However, medical imaging has also been successfully accomplished with radioisotopes, ultrasound, and magnetic resonance; the imaged parameter being different in each case. If the absorption contrast is recorded on a 2D detector then the image will be a projection of the sample absorption from a given incident beam direction. By combining projections of the absorption from different angles, the absorption can be calculated in the bulk of the sample and this calculation is called a tomographic reconstruction. From the tomographic reconstruction, one can at will produce cuts or volume renderings of the object.

Advantages of using synchrotron radiation for tomographic investigations are that the divergence of the beam is small and the intensity is high. This combination makes it possible to use monochromatic X-rays to perform micro-tomography showing a spatial resolution of 1-2 μm.
The experiment described here was performed at HASYLAB [9] with an X-ray energy of 24 keV. The spatial resolution in the reconstructed volumes is 2 μm.

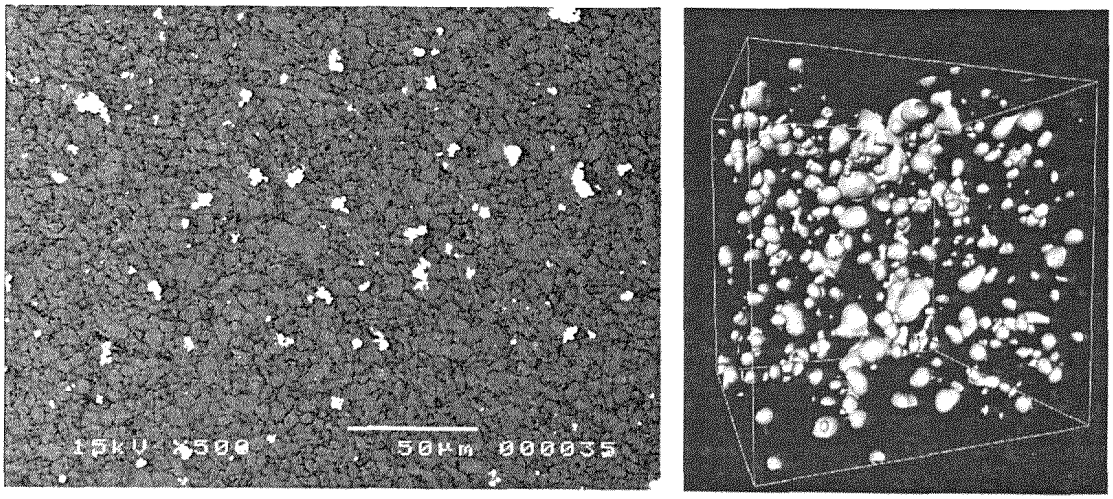

Fig. 1. Left: Scanning electron microscopy image of the W particles (white) and the Al grains (gray). Right: Tomographic reconstruction of the cylindrical specimen. For further details see Ref. [10].

3. RESULTS

The sample was deformed step-wise to enable identification of the marker particles both before and after a deformation step from the distance they are displaced. This approach is possible as long as the particles are displaced less than the average distance between the particles in one deformation step, otherwise it will be necessary to use pattern recognition techniques in order to identify the marker particles. When the positions of the marker particles are known both before and after a deformation increment, the displacement field can be determined. Fig. 2 shows a three-dimensional image of the displacement of all the particles in the sample after 9.5% compression.

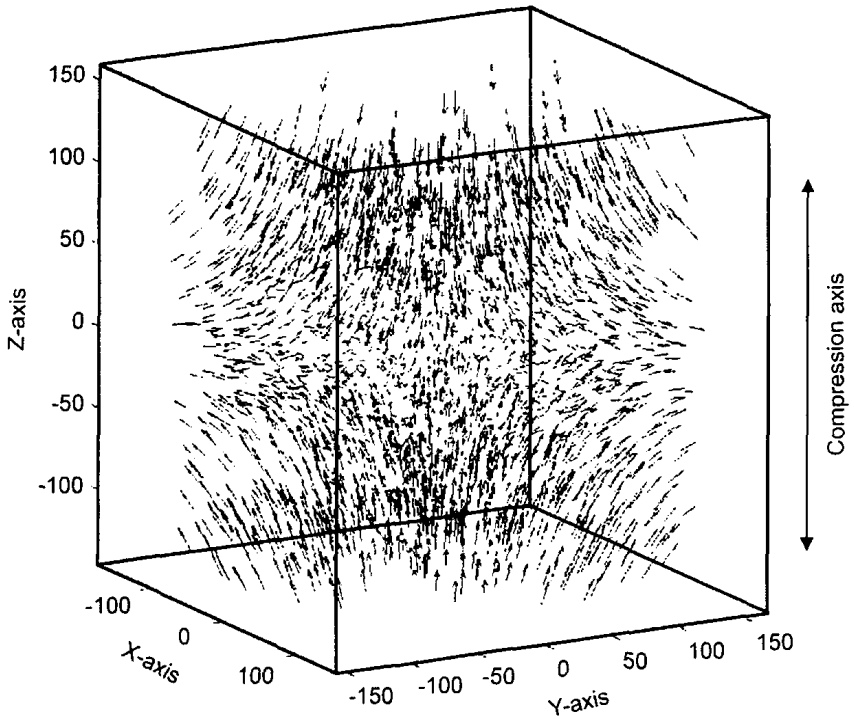

Fig. 2. A three-dimensional image of the displacement of the marker particles after compression to 9.5%. The numbers on the axes are in units of pixels of 1.5 μm. For further details see Ref. [10].

The nine components of the displacement gradient tensor are defined by:

$$e_{ij} = \left(\frac{\partial u_i}{\partial x_j} \right) \quad \forall\, i,j \tag{1}$$

where u_i are the particle displacement components and x_j are the position components.

The displacement gradient tensor was determined for each particle by a least-squares fit to the relative displacement of the eight nearest neighbours. The nine components of e_{ij} were in this way determined at the position (x,y,z) of all the marker particles. The local e components for all the matched particles in the observed volume can than be represented as distributions (see Fig. 3)

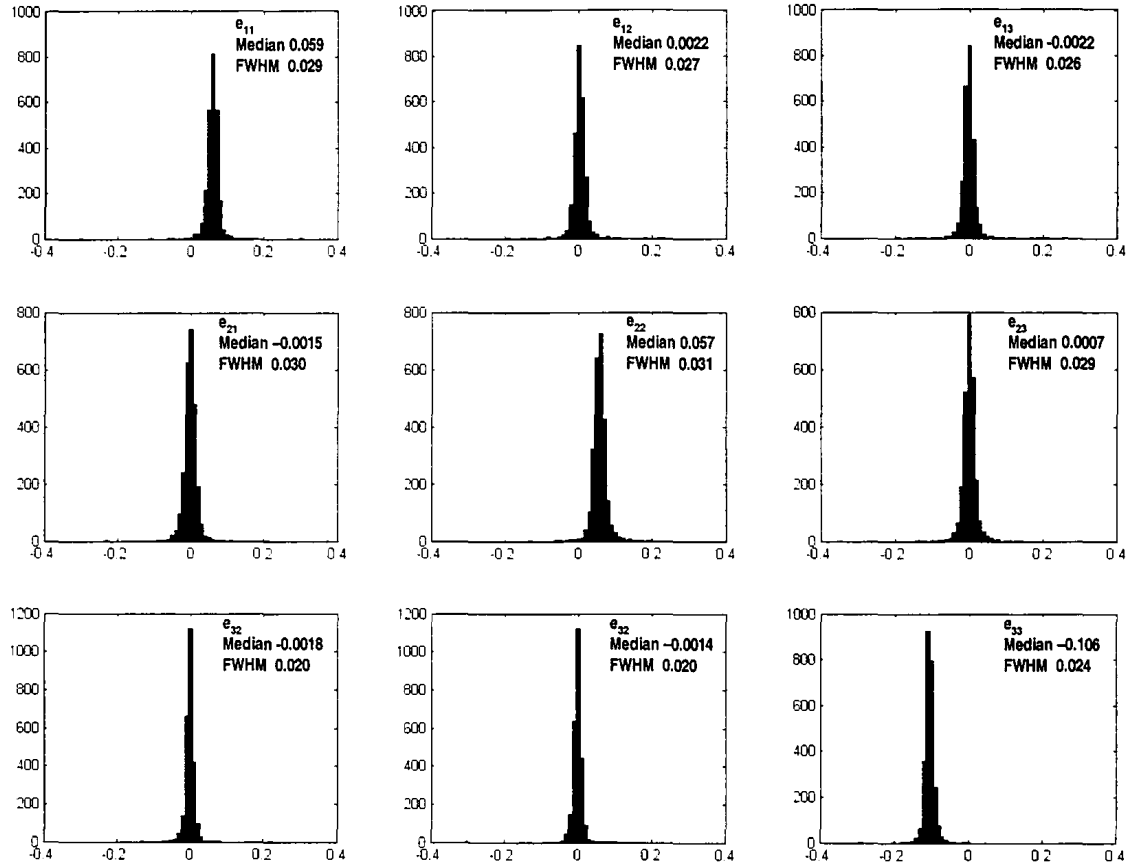

Fig. 3. The nine displacement gradient tensor components plotted as histograms of all the matching particles in the initial and final data sets.

The trace of the displacement gradient tensor should be zero for all the particles as a result of volume conservation during the plastic deformation. The distribution of the calculated quantity $(e_{11}+e_{22}+e_{33})/3$ has a FWHM of 0.020 (see Fig. 4). This constitutes an upper limit on the instrumental resolution. The distributions of each of the displacement gradient components are broader than 0.020 and their widths can therefore be seen as a convolution of an instrumental effect and a "real" fluctuation. This indicates real plastic strain fluctuations on the order of 0.01 to 0.02 for the present experimental conditions.

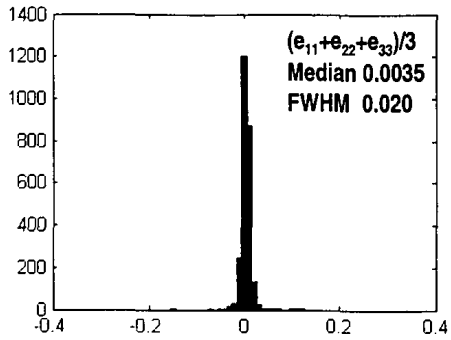

Fig. 4. The FWHM of the quantity $(e_{11}+e_{22}+e_{33})/3$ constitute an upper limit on the instrumental resolution as the trace of the displacement gradient tensor should be zero due to volume conservation during deformation.

The displacement gradient tensor components are fixed to the positions of the marker particles, an irregular grid, and this makes it difficult to visualize the displacement gradient tensor in three dimensions. One suitable visualization method is to interpolate each *e*-component on a regular grid and to assign each grid point the average value of that *e*-

component for all the particles that lie within a radius of half the distance between the grid points. The nine *e*-components can now be visualized by plotting them layer by layer. Fig. 5 shows a very homogeneous straining which is as expected for a powder metallurgical sample of aluminium grains with approximately the same size as the marker particles. Never the less there are small variations of strain (see e.g. Fig. 5 near x = 200 μm, y = 400 μm and z = 120 μm).

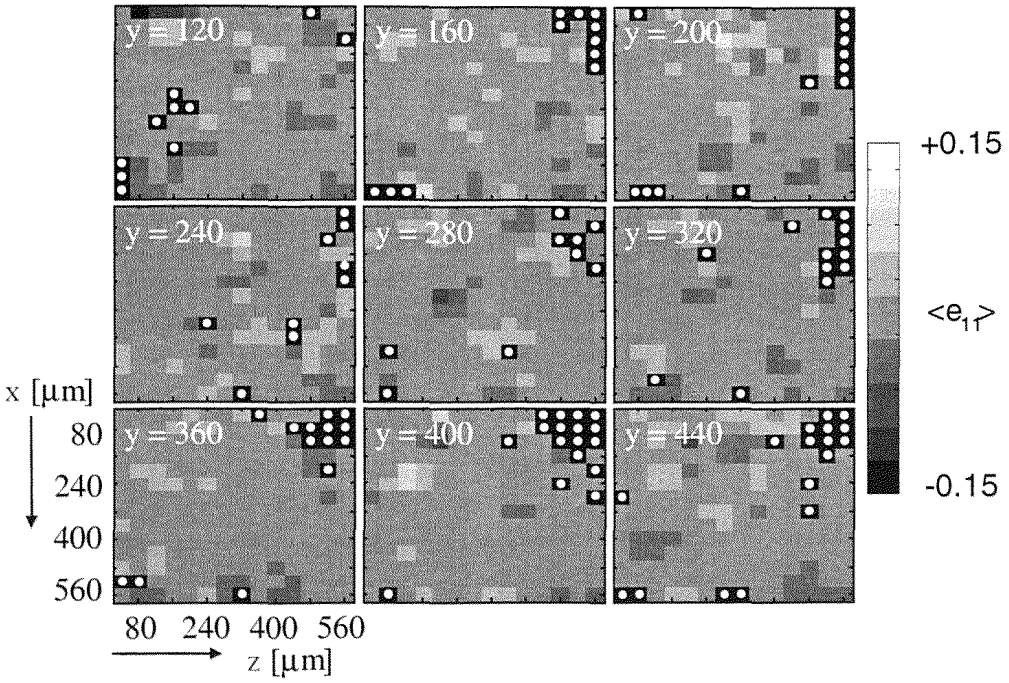

Fig. 5. Strain contours in three-dimensions for the displacement gradient tensor component e_{11}. The black voxels with the white dots are created during the interpolation on the regular grid where no particles were found within 15 μm from the grid point. For further details see Ref. [10].

After having established the technique with marker particles a sample with another geometry was investigated. The sample was again made by compacting Al and W powder as for the test sample described above. A cube with dimensions 0.8*0.8*1.5mm was machined from a larger specimen which afterwards served as a base for the sample itself. Through the centre of this sample a circular hole was made by spark erosion and the sample was afterwards subjected to a tomography-deformation-tomography investigation.

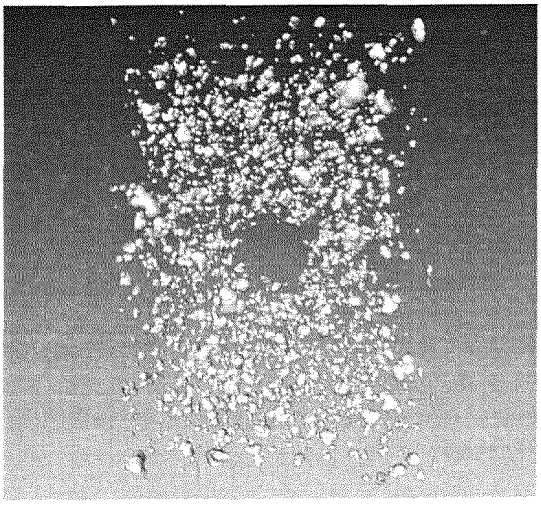

Fig. 6. A three-dimensional representation of isosurfaces in the reconstructed tomogram of the sample before deformation. The centre hole is clearly visible and the particles appear to be evenly distributed throughout the volume under consideration (app. 1 mm^3).

As seen in Fig. 6, the marker particles appear to be evenly distributed throughout the sample and the hole through the centre of the sample is clearly visible. The sample was deformed 3.3%, 13.6% and finally until fracture. The fracture mode was observed to be along approximately 45 degrees, from the centre hole to the corners.
Preliminary analysis of the tomograms and marker particle displacements for this sample has been started. Comparing Fig. 7 with Fig. 2, it is evident that deviations from the homogenous case is introduced by the altered geometry. The change in magnitude of the displacements above and below the hole are the most clearly seen.

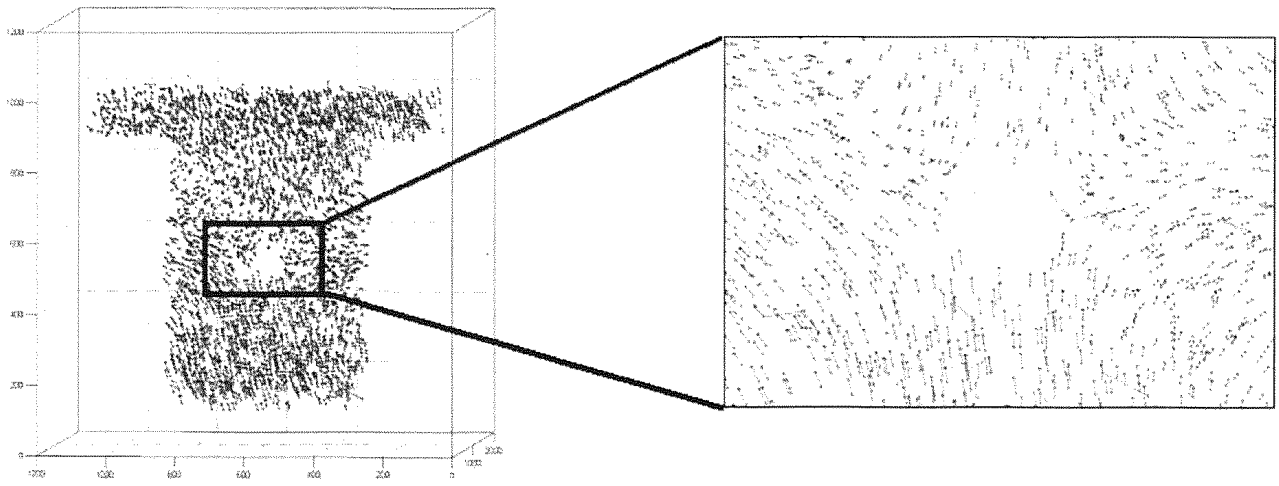

Fig. 7. Particle displacements for a subset of the identified particle-pairs in the undeformed sample and after 3.6% deformation. Comparing with Fig. 2, variations in the particle displacements are evident as well as some deviant particle displacements, which are caused by misidentified pairs – these have to be removed before quantitative data analysis. The numbers on the axes are in units of pixels of 1.5 μm.

Further data analysis is currently under way to quantify the expected variations in displacement gradients as a function of position in the sample, most notably around the hole region.

DISCRETE TOMOGRAPHY

The standard reconstruction technique is the filtered back projection (FBP). An entirely different approach for tomographic reconstruction consists of assuming that the cross section consists of an array of unknowns, and then setting up algebraic equations for the unknowns in terms of the measured projection data. This so-called Algebraic Reconstruction Technique (ART) was first published in the biomedical imaging literature in 1970 [11].
The set of linear equations can be written as **WV=P** or in expanded form as

$$\begin{aligned} w_{11}v_1 + w_{12}v_2 + w_{13}v_3 + \ldots + w_{1N}v_N &= p_1 \\ w_{21}v_1 + w_{22}v_2 + w_{23}v_3 + \ldots + w_{2N}v_N &= p_2 \\ \ldots & \\ w_{M1}v_1 + w_{M2}v_2 + w_{M3}v_3 + \ldots + w_{MN}v_N &= p_M \end{aligned} \qquad (2)$$

where **V** is the unknown column vector storing the values of all the voxels in the reconstructed n × n × n grid. **P** is composed of the values of the pixels in the combined set of all M projection images recorded at different angles and **W** is the weight matrix in which an element w_{ij} represent a measure of the influence that particular voxel has on the ray that ends up in a particular pixel on the detector.

From the mathematical point of view, the ART technique is a variation of the iterative method for solving a system of the simultaneous equations introduced by Kaczmarz in 1937 [12].
The ART reconstruction technique is well suited for situations where it is not possible to obtain a continuous set of projections [13]. Alternatively ART can be used to lower the number of projections in order to reduce the acquisition time.
The same slice through a cylindrical Al sample that contains W marker particles is reconstructed in Fig. 8 by both the ART and the FBP technique. The reconstruction time was app. 5 min on a standard PC for both techniques but only 90 projections was used in the ART reconstruction compared to 720 projections in FBP. The quality of the reconstructions is very similar. The marker particles can be identified with the same accuracy in the ART reconstruction as in the FBP but the acquisition time is in this case 8 times less.

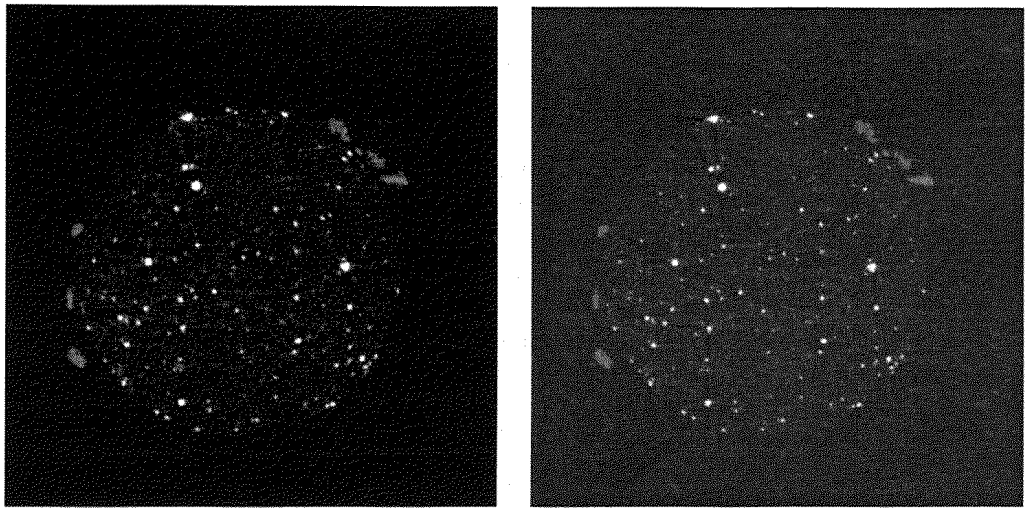

Fig. 8. Two reconstructions of the same slice through a cylindrical Al sample that contain W marker particles. Left: Reconstruction by the ART technique using 90 projections. Right: Reconstruction by the FBP technique using 720 projections.

It has been shown by Guan and Gordon [14] that in general only half the number of projections is needed in the ART compared to the FBP technique.
Assume that the ART reconstruction is done on a square grid with a side length of n voxels and that the region to be reconstructed is circular. The number of unknown voxel values will then be (1/4) πn^2 and n pixels per 1D image. To determine the linear set of equations (2) then the number of projection images M_{ART} has to be:

$$M_{ART} = \frac{(1/4)\pi n^2}{n} = \frac{\pi n}{4} \tag{3}$$

In Fourier space the sampling interval is at least $\Delta\omega = 1/nT_g$ where the maximum frequency is given by $\omega_{max} = 1/2T_g$. In a polar grid the density decreases as we go outwards. To ensure a sampling rate of at least $\Delta\omega$ everywhere in the polar grid then the angular spacing between the projections in frequency space needs to be:

$$\Delta\varphi_P = \frac{\Delta\omega}{\omega_{\max}} = \frac{T_g}{nT_g} = \frac{2}{n} \tag{4}$$

The interior frequency regions have to be oversampled in order to get sufficient sampling in the periphery. The number of projections then has to be

$$M_{FBP} = \frac{\pi}{\Delta\varphi_P} = \frac{\pi n}{2} \tag{5}$$

By changing the reconstruction technique to ART it is possible to lower the acquisition time by a factor of two ($M_{ART} = M_{FBP}/2$).

An alternative way of reduce the acquisition time is to optimize the experimental setup. Recently an ultra-fast tomography setup has been demonstrated using a white beam of x-rays with energies in the 100 keV range [15]. The

setup allows a continuously data collection while the sample is rotated. Tomograms can with this setup be obtained with a spatial resolution of 2.8 μm and a time resolution of down to 2 seconds. It is evident that this advance in instrumentation opens up for a wealth of dynamic studies in multiphase systems.

4. DISCUSSION

The described method for the non-destructive determination of the local plastic deformation in three dimensions in bulk material can be applied to study most cases of conventional deformation processes like rolling, tension, torsion and compression. The method can be applied to study heavy deformation as long as the marker particles do not fragment and as long as the deformation is performed step-wise, in such a way that the particles can be re-identified after each strain increment.

During deformation of a metal that contains particles which are harder than the matrix material, local compatibility stresses induce a plastic strain gradient in the matrix near each particle. This local deformation zone extends typically to a distance of about one particle diameter into the matrix material from the surface of the particle [16]. The described method uses the displacement of the particles to determine the local strain. Since the spacing of the particles is much larger than the deformation zone dimension, the deformation zone local to each particle is displaced with the particle and does not influence displacement of neighbouring particles. Thus, to a first approximation the measurements are not perturbed by the marker particles. The lower limit for the size of the marker particles is determined by the spatial resolution of the applied X-ray detector. At present, the best X-ray detectors for tomography experiments can detect particles of a diameter exceeding 0.3 μm. It is therefore possible for many commercial materials to use already existing impurities as marker particles, hence eliminating the risk of influencing the original system by adding marker particles.

REFERENCES

1. M.F. Bartholomeusz, J.A. Wert, Mater Charact. **33** (1994) 377.
2. P.A. Thorsen, J.B. Bilde-Sørensen, Mater. Sci. Eng. **A265** (1999) 140.
3. Y.L. Liu, G. Fischer, Scripta Mater., **36** (1997) 1187.
4. L. Berka, M. Sova, G. Fischer, Experimental Techniques, **22** (1998) 22.
5. E. Soppa, S. Schmauder, G. Fischer, J. Thesing, R. Ritter, Computational Materials Science, **16** (1999) 323.
6. H.A. Crostack, G. Fischer, E. Soppa, S. Schmauder, Y.L. Liu, J. Microscopy – Oxford, **201** (2001) 171.
7. I.Ya.Tarnovskii, A.A. Pozdeyev, V.B. Lyashkov, Deformation of Metals during rolling, Pergamon Press, Oxford, 1965.
8. Wert J.A. Acta mater. **50** (2002) 3125.
9. F. Beckmann, U. Bonse, T. Biermann, in Developments in X-ray Tomography II, Editor Ulrich Bonse, Proceedings of SPIE Vol. **3772** (1999) 179.
10. S.F. Nielsen, H.F. Poulsen, F. Beckmann, C. Thorning, J.A. Wert. Acta. Mater. **51** (2003) 2407.
11. R. Gordon, R. Bender and G.T. Herman. J. Theoret. Biol. Vol. **29** (1970) 471.
12. S. Kaczmarz. Bull. Int. Acad. Pol. Sci. Lett., A, Vol. **35** (1937) 355.
13. Fu, X.; Poulsen, H.F.; Schmidt, S.; Nielsen, S.F.; Lauridsen, E.M.; Juul Jensen, D., Scr. Mater. 49 (2003) 1093.
14. H. Guan and R. Gordon, Phys. Med. Biol., no. **41** (1996) 1727.
15. O. Lame, D. Bellet, M. Di Michiel, D. Bouvard. Acta Mat. **52** (2004) 977.
16. F.J. Humphreys, in *Dislocations and Properties of Real Materials*, ed. M.H. Loretto, Institute of Metals, London, 1985, 175-204.

J Bulk investigations of grain boundary migration during recrystallization utilizing the 3DXRD microscope

S. Schmidt, R. B. Godiksen and D. Juul Jensen, *Proceedings of Solid-Solid Phase Transformations in Inorganic Materials '05*, edited by J. M. Howe, D. E. Laughlin, J. K. Lee, D. J. Srolovitz and U. Dahmen, 583, (2005).

Solid-to-Solid Phase Transformations in Inorganic Materials 2005
Volume 1: Diffusional Transformations
Edited by James M. Howe, David E. Laughlin, Jong K. Lee, Ulrich Dahmen and William A. Soffa
TMS (The Minerals, Metals & Materials Society), 2005

Bulk investigations of grain boundary migration during recrystallization utilizing the 3DXRD microscope

S. Schmidt[1], R. B. Godiksen[1] and D. Juul Jensen[1]

[1]Center for Fundamental Research: Metal Structures in Four Dimensions
Risoe National Laboratory, Frederiksborgvej 399, P.O. 49,
DK-4000 Roskilde, Denmark

Keywords: Recrystallization, Nucleation, 3DXRD

Abstract

The Three Dimensional X-ray Diffraction (3DXRD) microscope located at the European Synchrotron Radiation Facility (ESRF) in Grenoble, utilizes high energy x-rays to reveal microstructure governing in the bulk of materials. In the present paper various 3DXRD experimental methods previously applied in recrystallization investigations are reviewed with emphasis on boundary migration during recrystallization, and limitations for studies of solid state phase transformations are discussed.

Introduction

When studying the kinetics of nucleation and growth during solid state phase transformations, qualitative microscopy and stereology remain very important tools. A problem however, is that the kinetics can not be followed *in-situ* in the bulk. E.g. when the new phase has nucleated at a specific site it is not possible to know what the microstructure was like at exactly that site before the nucleus developed. Only at the sample surface *in-situ* measurements of this type can be done. This lack of i*n-situ* bulk data can be a limitation for the understanding of both the nucleation and growth state of the phase transformation [1]. Furthermore, microscopy is most often done in 2D. In some cases serial sections is carried out to get full 3D information [2] which adds valuable information to the limited experimental basis available for the understanding.

In this paper a method for non-destructive characterization of microstructures in 3D is reviewed. The method on based in high energy x-rays carrying high penetration power. In addition, the measurements are fast allowing nucleation and growth to be followed *in-situ* [3]. The method will be illustrated by data from recrystallization of aluminum and nucleation in cobber. Recrystallization in many ways phenomenologically resembles phase transformations and is also described by the nucleation and growth kinetics. The mechanisms leading to nucleation are obviously different for phase transformation and recrystallization but this is not important for the method presented here.

The paper has the following outline. First an overview of the 3DXRD microscope is given. Afterwards, three experimental methods are reviewed: (i) growth curves of individual recrystallizing grains, (ii) full spatial measurements of boundary migration of recrystallizing grains as well as monitoring the deformed microstructure, and finally, (iii) nucleation of recrystallization. All 3DXRD measurements are obtained non-destructively in the bulk of the samples.

The 3DXRD microscope

The Three Dimensional X-ray Diffraction microscope (3DXRD) [4], is a new technique for fast and non-destructive characterization of the local microstructure in the bulk of materials. The microscope is situated at beamline ID-11 at the ESRF in Grenoble, France.

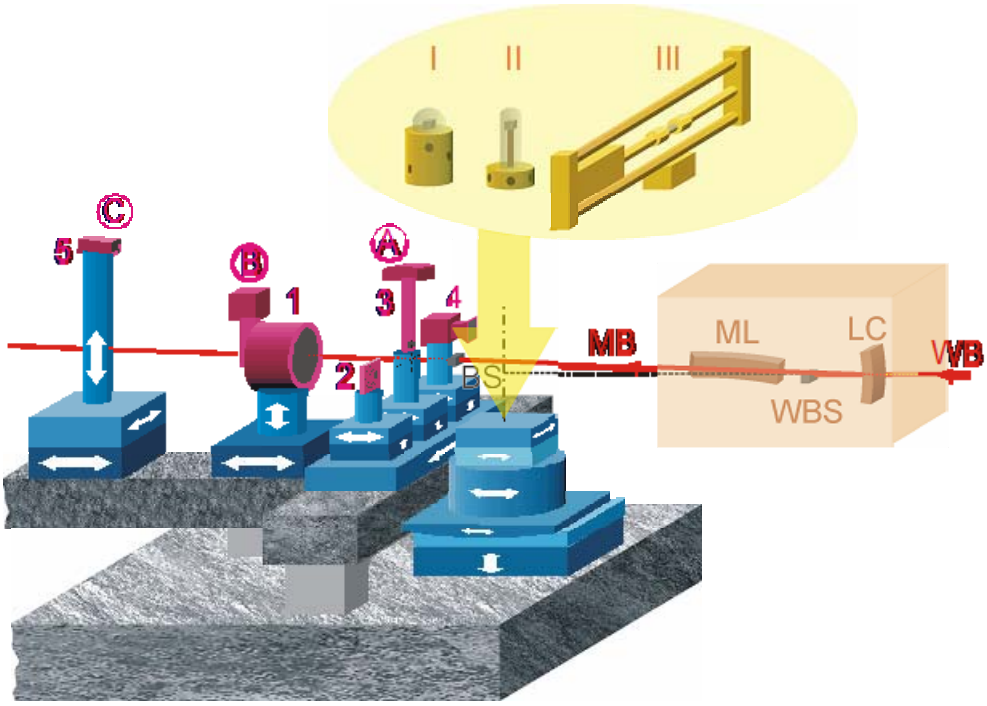

Figure 1. Schematic view of the current 3DXRD microscope**.** WB: White beam, LC: Bent Laue crystal, ML: Bent multi layer, WBS: White beam stop, MB: 2 dimensionally micro focussed monochromatic beam, BS: Monochromatic beam stop. Sample environment I: Cryostat, II: Furnace, III: 24kN Stress rig. 1: Large area detector, 2: Conical slit system, 3: High resolution area detector, 4: Optional detector system, 5: Small area detector.

A schematic view of the microscope is shown in Figure 1. The white beam (WB) from the synchrotron ring is mono-chromized and focused vertically using a bend Laue silicon single crystal (LC) yielding energies in the range 50-100 keV, enough to penetrate 4 cm aluminium or 1 mm of steel, with a cross section between 1-200 μm vertically, and 1000 μm horizontally. An optional multi layer (ML) focuses the monochromatic beam (MB) horizontally down to 5 μm with enough flux to resolve microstructures below 1 μm.

For annealing studies a furnace (II), see Figure 1, is mounted on the rotation stage located downstream from the focusing optics. The direction of the rotation axis is perpendicular to a vertically focused beam and the amount of rotation is given by ω, see Figure 2. In order to cover the whole reciprocal space, a set of images are recorded by successively moving Δω and oscillation +-Δω/2 around that point. Diffraction images are collected using two-dimensional CCD detectors. High-resolution detectors (A), see Figure 1, with pixel size of roughly 2 μm, are positioned closely to the sample giving information about the grain shapes, whereas low-resolution detectors (B), with pixel size of roughly 100 μm and much faster readout electronics, are used at larger distances for integrated grain volume and angular information, the latter for determining the crystallographic orientations of the grains.

Recrystallization, growth curves of individual grains

The first example which is reported in detail in [5], enables growth kinetics of the individual recrystallizing grains to be monitored *in-situ* in the bulk of the sample. The experimental setup is shown in Figure 2.

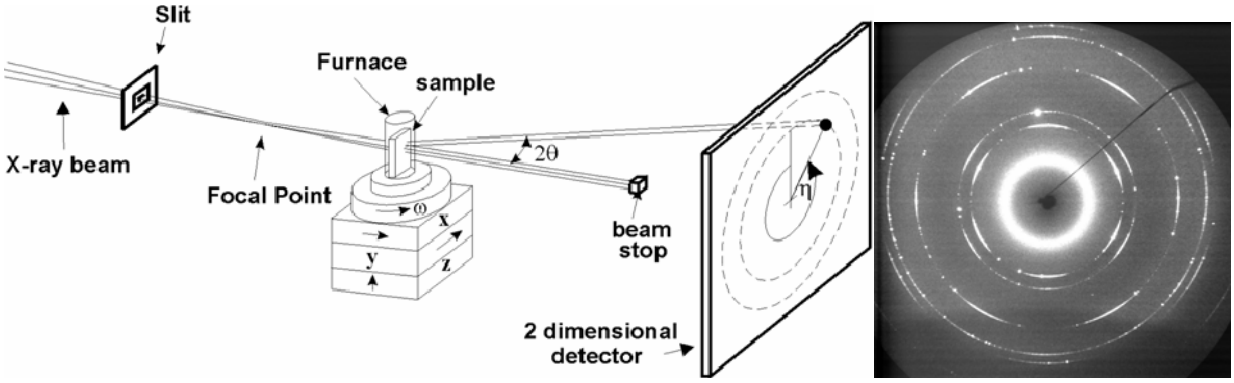

Figure 2. Left: Experimental setup with 50 keV beam, cross section of 100 µm x 100 µm, illuminating the sample mounted in the furnace. A low resolution, high sensitive detector (type B in Figure 1) is positioned downstream from the sample**.** Right: Example of recorded CCD data of a partly recrystallized sample. The signatures of the individual grains are given as diffraction peaks (spots) on the CCD detector.

For an Aluminum AA1050 sample deformed 90% by cold rolling and annealied *in-situ* at 270 °C, a total of 244 grains were measured by observing the total integrated intensity (grain volume) of the individual spots as function of annealing time, see Figure 3. The study revealed that it was not possible to find two identical growth curves, even within the same class of crystallographic orientations. Each grain had its own nucleation and growth kinetics.

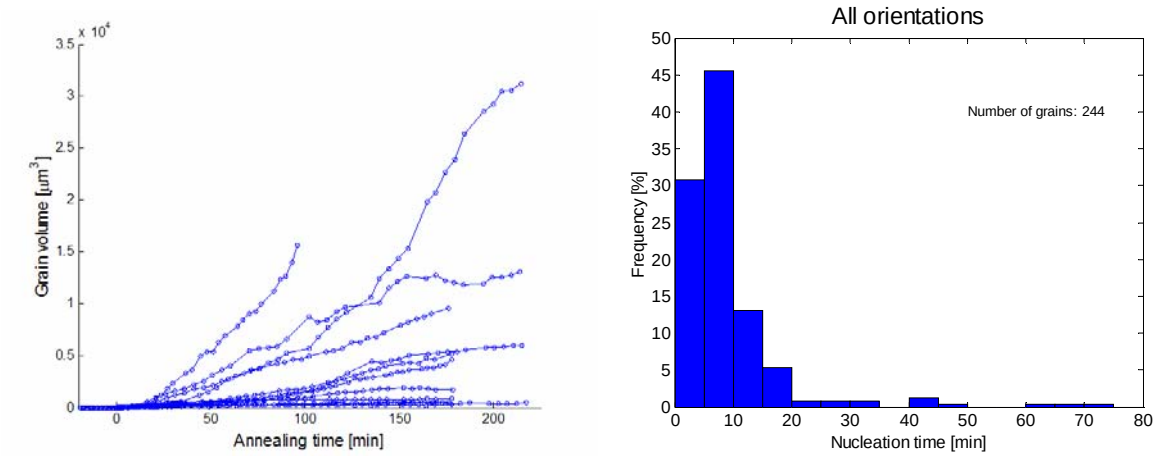

Figure 3. Left: The growth curves of the 14 cube grains observed (Cube: the position of the diffraction peak in the pole figure do not deviate with more that 10° from the Cube texture component {1 0 0}<0 0 1>). Right: Nucleation times of all 244 grains.

Due to the amount of statistics available it was possible to obtain histograms of nucleation times, grain sizes and growth rates of grains within various texture components. The data has been used as basis for modeling recrystallization kinetics [6]. It was shown that a variability of growth kinetics as observed here can completely change the interpretation of the overall kinetics curve.

Another aim was to make a direct measurement of the individual grain boundaries of a grain during recrystallization, i.e. a full four dimensional measurement (three spatial dimensions and time). To illustrate this an example from [3] is chosen. Here an aluminum single crystals of with initial crystallographic orientation {110}<001>, i.e. Goss, was deformed 42% by cold rolling to ensure enough driving force to facilitate enough driving force for recrystallization boundary migration keeping the resulting deformed microstructure relatively simple, see Figure 2 Left. As seen in Figure 2 Right, the mean orientation is still close to ideal Goss, with a spread of roughly 8 degrees. Controlled nucleation was stimulated by diamond shaped hardness indentations on the surface of the sample. The size of the sample was 1 mm along ND, 6 mm along RD and 5mm along TD.

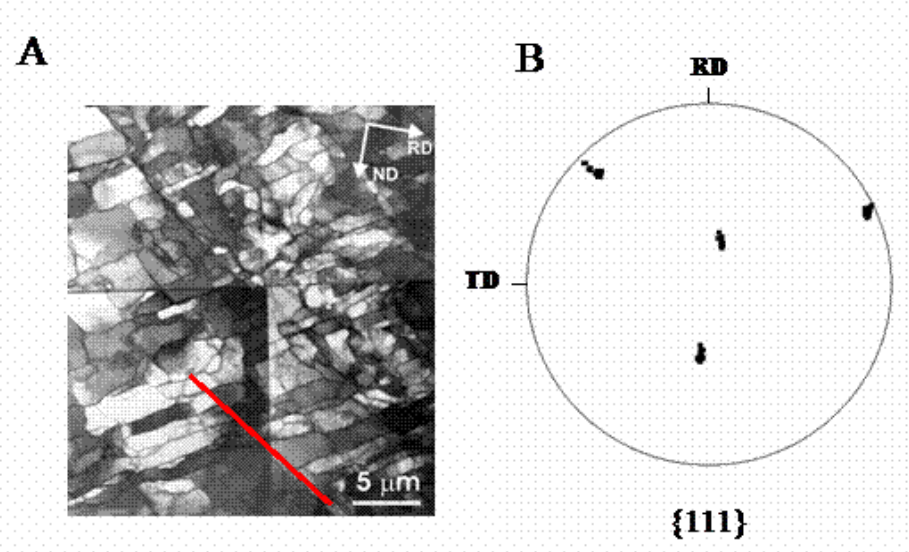

Figure 4. Left: Montage of TEM micrographs of 42% cold rolled Al single crystal with initial orientation {110}<001>. Right: {111} Pole figure of crystallographic orientations measured along a straight line shown in Figure 4 Left An orientation spread of roughly 8 degrees around the initial Goss orientation is seen.

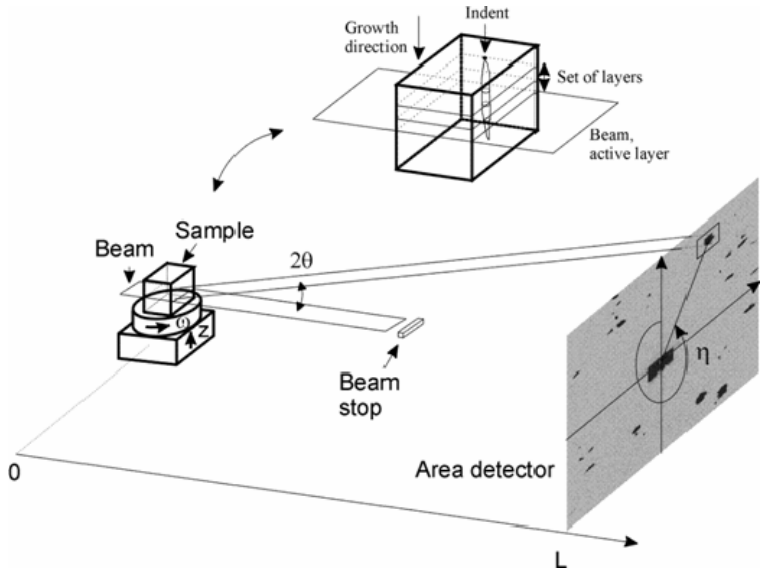

Figure 5. Schematic view of the experimental setup. The coordinate system (x,y,z) and angles (ω,2θ,η) are defined. L denotes the distance between the sample and the CCD detector.

Full 3D spatial information of a growing nucleus/grain was obtained non-destructively by utilizing the 3DXRD microscope. A schematic view of the experimental setup is shown in Figure 5.

The beam was constructed such that the height was 6 μm and the width was 600 μm, i.e. a planar shaped configuration. Initially, the sample was mounted such that Normal Direction (ND) was along the incident beam direction, Transverse Direction (TD) was transverse to it and Rolling Direction (RD) was normal to the beam direction. For a given nucleus/grain fulfilling the Bragg criterion the illuminated region constitutes a cross section of the grain and results in a diffraction spot on the detector of a shape given by the real cross section of the nucleus/grain except for an affine transformation related to the direction of the diffracted beam. By repeatedly recording an oscillation image followed by a 6 μm vertical translation of the sample, a "snapshot" of the grain was recorded, see the insert in Figure 5. In this way 3D grain shapes were obtained non-destructively. The annealing temperatures were in the range 280 ºC to 310 ºC. Each "snapshot" was recorded in typically 10 minutes. While annealing the sample, this procedure was repeated over time resulting in 4D (space and time) grain maps, which were obtained nondestructively. An example is shown in Figure 6.

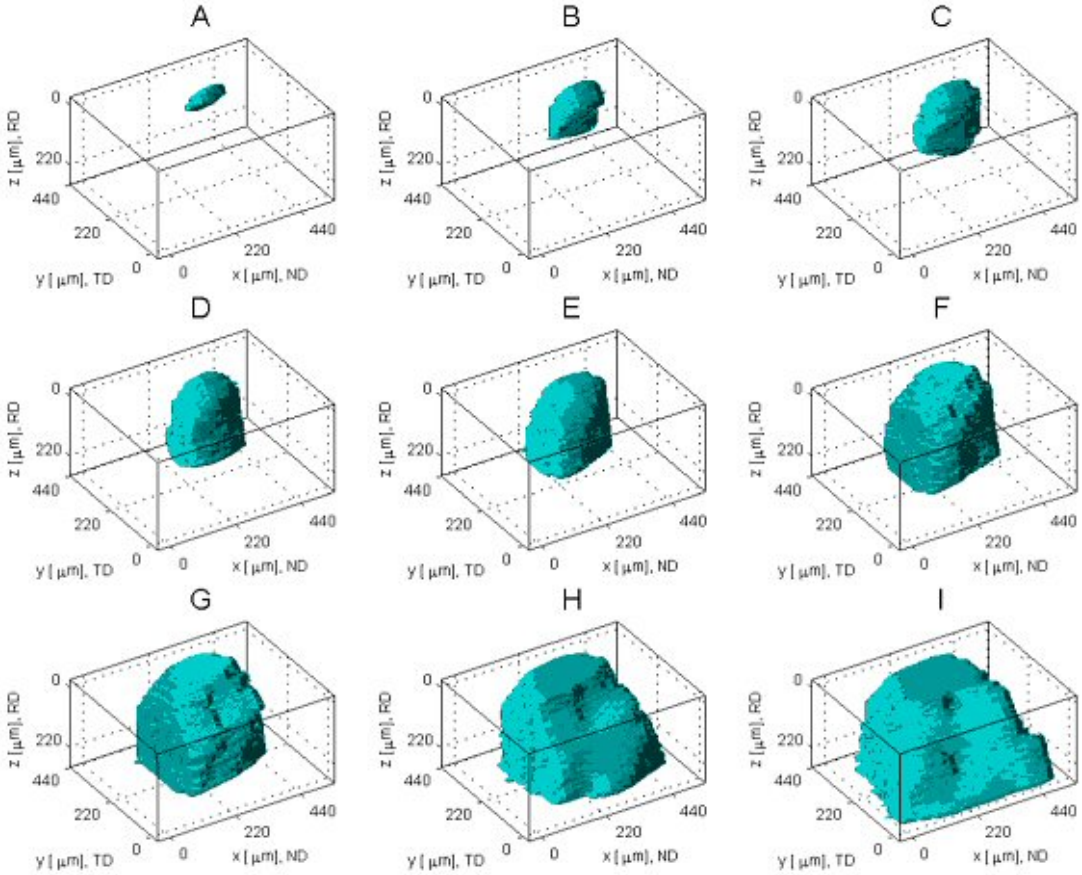

Figure 6. Storyboard of the evolution of a grain represented by 9 "snapshots" [3].

Initially, the grain appeared as a small flattened object. At later stages the grain shape appeared more complicated, resulting from a series of abrupt growth intervals. This is in contrast to the assumption of smooth steady-state growth in the classical models of recrystallization. All the grains measured so far exhibited irregular movements contradicting the assumption of smooth growth in the classical models of recrystallization. The information content provided in this new type of measurements makes it possible to probe the mechanisms of recrystallization *locally* since the position of individual grain boundary segments are known along with the

crystallographic orientation of the recrystallzing grain as well as the average orientation of the surrounding deformed microstructure.

Deformed microstructure

It turns out that the deformed microstructure in the sample can also, to some extent, be monitored through the experimental method described previously. From TEM measurements, see Figure 4, typical cell sizes in the deformed microstructure has been measured to 2-5 μm. Signals on the CCD detector arising from the deformed microstructure comprise of cells present in the illuminate region, given by 1000 μm (along x direction) by 700 μm (along y direction) by 6 μm (along z direction), which fulfill the Bragg criterion. With $\Delta\omega$=0.5º and an orientation spread in the deformed microstructure of roughly 8º, not all cells deposit intensity in one oscillation image. Despite of this it is not possible to disentangle the diffraction signal from the individual cells due to geometrical limitations in the experimental setup, i.e. the low inclination of the diffracted beam and the pixel size on the CCD detector. Instead, a superposition of cells distributed throughout the illuminated region is recorded.

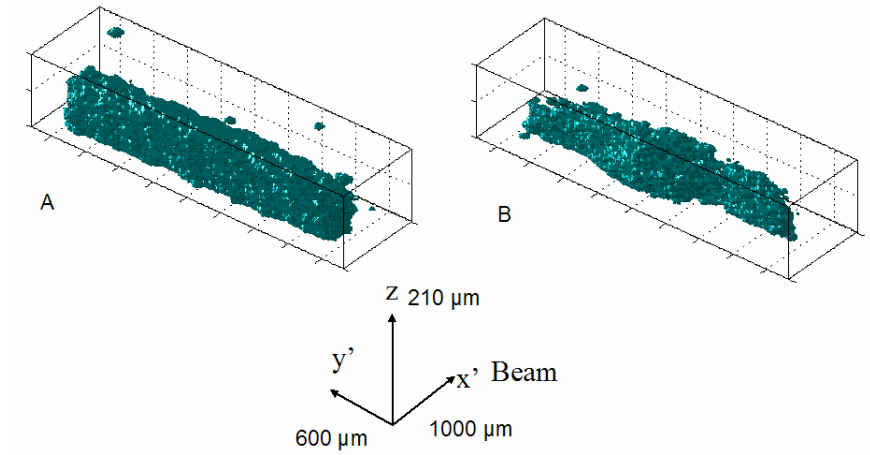

Figure 7. Two "snapshots" of the deformed microstructure. In the ω-rotated reference system x' is along, y' is transverse and z is normal to the beam direction, respectively. As noted in the figure, the size of the gauge volume is 1000 μm along x', 600 μm along y' and 210 μm along z. Left: Before annealing. Right: After 20 hours of annealing. These "snapshots" constitute a "photographic negative" of the recrystallized volume.

Figure 7 Left shows a "snapshot" of the deformed structure at an early annealing stage. The shape in Figure 7 Left resembles a box which effectively is the total gauge volume consisting of 30 layers. Figure 7 Right shows the same gauge volume after 20 hours of annealing. The volume of the deformed microstructure has been reduced at the expense of the increasing recrystallized volume. In fact, the reduced volume is a "photographic negative" of the recrystallized volume where the shapes of all the rerystallizing grains in the gauge volume are present.

Nucleation

Also the nucleation can be followed *in*-situ in the bulk. Particle-free 99.995% pure oxygen-free high conductivity copper, which was cold rolling to 20% reduction in thickness and annealed afterwards for 8 hours at 700° C to yield a microstructure with relatively coarse grains with an average size of 500 μm[7]. Prior to the 3DXRD measurements the samples were cut down to 300 μm thickness and regions with triple junctions were located on the surface using an Electron Back Scatter Pattern (EBSP) microscope.

The experimental setup was the same as shown in Figure 2 Left. In total three nuclei were identified and monitored during annealing. The annealing temperature was 290°C. All the nuclei were situated at least 65 μm from the surface with final sizes less than 10 μm. An example of an emerging nucleus is shown in Figure 8. The orientations of two of the nuclei were identical to first-order twins of the parental grains. The third nucleus, however, exhibited a new orientation that was not detected in the deformed parent grains.

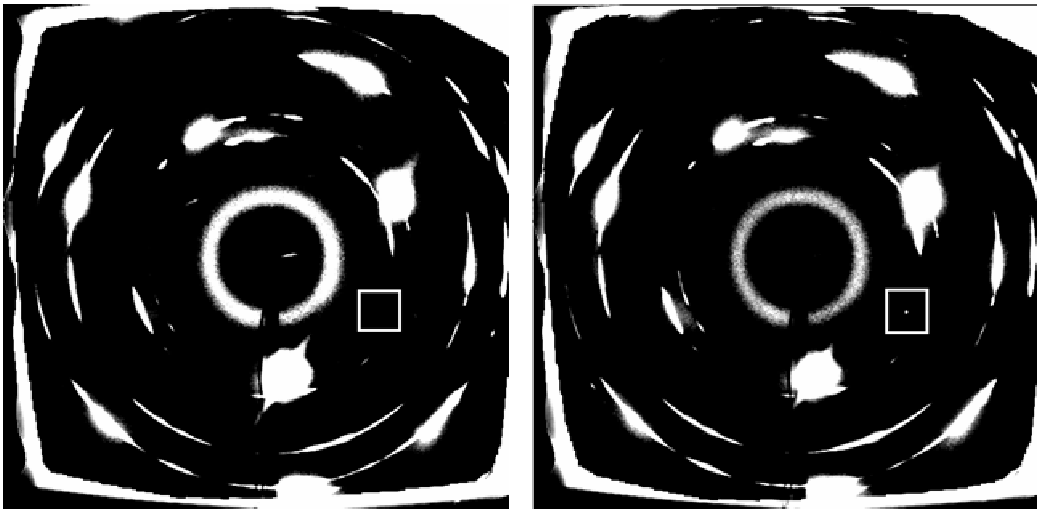

Figure 8. CCD images recorded during annealing. The two images is from the same position within the sample. Left: the as-deformed microstructure, and, Right: the microstructure in the sample annealed for 3 hours at 290°C. The white box indicates the position of a diffraction spot, showing an emerging nucleus.

Summary and limitations for phase transformation studies

The 3DXRD microscope facilitates *in-situ* observations of structural changes in the bulk of materials non-destructively. In this paper we have reviewed three experimental 3DXRD methods which may also serve as suitable tools in the investigation of phase transformations. One important limitation, though, is that in recrystallization experiments, the migration rates can be slowed down by lowering the annealing temperature enabling a sufficient time resolution. Taken together with the spatial resolution this puts a constraint on the types of phase transformation experiments suitable for investigation using these methods. It should be mentioned that the 3DXRD microscope is available to outside users too. Access is based on pier review of proposals. See www.esrf.fr for guidance in submitting a proposal.

References

1. S. E. Offerman, N. H. van Dijk, J. Sietsma, S. Grigull, E. M. Lauridsen, L. Margulies, H. F. Poulsen, M. Th. Rekveldt, S. van der Zwaag, "Grain Nucleation and Growth During Phase Transformations", *Science*, 298 (2002), 1003-1005.
2. M.V. Kral, G. Spanos, "Three Dimensional Analysis of Proeutectoid Cementite Precipitates", *Acta. Mat.,* 47 (1999) , 711-724.
3. S. Schmidt, S.F. Nielsen, C. Gundlach, L. Margulies, X. Huang and D. Juul Jensen, "Watching the Growth of Bulk Grains During Recrystallization of Deformed Metals", *Science*, 305 (2004), 229-232.
4. H.F. Poulsen, S. Garbe, T. Frello, R. Feidenhans'l, H. Graafsma, *J. Synchrotron Rad.*, 4 (1997), 147-154.
5. E. M. Lauridsen, H.F. Poulsen, S.F. Nielsen, D. Juul Jensen, "Recrystallization kinetics of individual bulk grains in 90% cold-rolled aluminium", *Acta Mat.*, 51 (2003), 4423-4435.
6. D. Juul Jensen, E.M. Lauridsen, R.A. Vandermeer, "In-situ determination of grain boundary migration during recrystallization ", 2002 TMS annual meeting, international symposium in honor of Dr. Bhakta Rath, Seattle , WA (US) 17-21 Feb 2002. S. Ankem, C.S. Pande, I. Ovid'ko, S. Ranganathan (Eds) (TMS, Warrendale, PA, 2002), 361-374.
7. A. W. Larsen, H.F. Poulsen, L. Margulies, C. Gundlach, Q. Xing, X. Huang, D. Juul Jensen, "Nucleation of recrystallization observed in situ in the bulk of a deformed metal", *Scripta Mat.,* 53 (2005), 553-557.

K Data From MD Simulations

LJ

Type (Two Bnd.)	M [10^-3 r0^4/τ ε]	v [10^-3 r0/τ]	P [10^-1 ε/r0^3]	T [ε/kB]	θb deg.	θd deg.	N #	lx Å	ly Å	lz Å	Reps. #
A	3.75	1.15	3.07	0.333	40	10	92763	60.67	147.3	7.35	3
A	5.88	1.75	2.98	0.400	40	10	92763	60.67	147.3	7.35	3
A	9.41	2.74	2.91	0.467	40	10	92763	60.67	147.3	7.35	3
A	8.38	2.42	2.88	0.533	40	10	92763	60.67	147.3	7.35	3
A	13.06	3.73	2.85	0.600	40	10	92763	60.67	147.3	7.35	3

Type (Four Bnd.)	M [10^3 r0^4/τ ε]	v [10^3 r0/τ]	P [10 ε/r0^3]	T [ε/kB]	θb deg.	θd deg.	N #	lx Å	ly Å	lz Å	Reps. #
A	5.03	3.27	6.51	0.333	40	10	92676	60.67	147.3	7.35	3
A	4.2	2.68	6.39	0.400	40	10	92676	60.67	147.3	7.35	3
A	3.45	2.19	6.34	0.467	40	10	92676	60.67	147.3	7.35	3
A	6.14	3.81	6.21	0.533	40	10	92676	60.67	147.3	7.35	3
A	9.14	5.56	6.09	0.600	40	10	92676	60.67	147.3	7.35	3

Type (annihilation)	M [10^3 r0^4/τ ε]	v [10^3 r0/τ]	P [10 ε/r0^3]	T [ε/kB]	θb deg.	θd deg.	N #	lx Å	ly Å	lz Å	Reps. #
A	-	-	-	0.333	40	10	21996	47.6	44.5	7.35	2
A	-	-	-	0.333	40	10	95038	47.6	44.5	31.8	1

Conversion factors: Al: r0 = 2.9 Å, τ =0.289 ps, ε = 0.28 eV Cu: r0 = 2.5 Å, τ =0.384 ps, ε = 0.30 eV

EAM-Al

Type	M [Å^4/ps eV]	v [10^-2 Å/ps]	P [10^-4 eV/Å^3]	T [K]	θb deg.	θd deg.	N #	lx Å	ly Å	lz Å	Reps. #
A	-	-	8.59	100	40	10	110292	172.9	499.2	20.94	1
A	-	-	8.33	200	40	10	110292	172.9	499.2	20.94	1
A	-	-	7.97	300	40	10	110292	172.9	499.2	20.94	1
A	3.9	0.3	7.75	400	40	10	110292	172.9	499.2	20.94	1
A	5.58	0.41	7.27	500	40	10	110292	172.9	499.2	20.94	1
A	45.27	3.22	7.12	600	40	10	110292	172.9	499.2	20.94	1
A	100.24	7.16	7.15	700	40	10	110292	172.9	499.2	20.94	1
A	142.4	9.92	6.97	800	40	10	110292	172.9	499.2	20.94	1
A	189.56	11.08	5.85	900	40	10	110292	172.9	499.2	20.94	1

EMT-Cu

Type	M [Å^4/ps eV]	v [10^-2 Å/ps]	P [10^-4 eV/Å^3]	T [K]	θb deg.	θd deg.	N #	lx Å	ly Å	lz Å	Reps. #
A	30.26	1.4	4.62	1200	24.79	6.01	106240	170.5	295.2	25.0	26
B	46.08	1.87	4.06	1200	24.79	6.01	106160	170.5	295.2	25.0	4
C	39.65	1.38	3.46	1200	24.79	6.01/3.00	106136	170.5	295.2	25.0	4
D	117.55	2.17	1.85	1200	24.79	6.01	106594	24.4	295.2	175.1	4
E	108.01	2.54	2.36	1200	24.79	6.01	106388	24.4	295.2	175.1	4

Type θd	M [Å^4/ps eV]	v [10^-2 Å/ps]	P [10^-4 eV/Å^3]	T [K]	θb deg.	θd deg.	N #	lx Å	ly Å	lz Å	Reps. #
A	0,00	0,00	0,00	1200	41.27	0	108216	162.9	313.7	25.0	1
A	23.18	0.63	2.73	1200	39.98	2.56	107627	162.9	313.7	25.0	1
A	17.42	0.88	5.04	1200	41.06	4.7	107708	162.9	313.7	25.0	1
A	42.98	2.49	5.78	1200	40.24	7.01	107716	162.9	313.7	25.0	1
A	53.15	3.62	6.8	1200	41.31	9.85	107732	162.9	313.7	25.0	1
A	60.1	4.61	7.68	1200	40.04	11.76	107740	162.9	313.7	25.0	1
A	64.55	5.54	8.58	1200	41.25	14.17	107720	162.9	313.7	25.0	1
A	74.41	7.05	9.47	1200	39.93	16.8	107728	162.9	313.7	25.0	1
A	83.68	8.47	10.12	1200	41.04	19.11	107728	162.9	313.7	25.0	1

Type θd	M [Å^4/ps eV]	v [10^-2 Å/ps]	P [10^-4 eV/Å^3]	T [K]	θb deg.	θd deg.	N #	lx Å	ly Å	lz Å	Reps. #
D	126.89	3.18	2.51	1200	36.1	4.22	212086	60,0	415.9	100	1
D	134.01	3.88	2.89	1200	40.89	5.36	159698	47.3	397.7	100	1
D	116.34	3.62	3.11	1200	35.21	6.01	139522	42.2	389.6	100	1
D	140,00	5.07	3.62	1200	42.52	8.61	102036	29.44	407.9	100	1
D	136.46	5.26	3.85	1200	33.00	10.42	156996	48.7	379.6	100	1
D	145.95	6.3	4.32	1200	44.39	12.36	149040	41.1	426.9	100	1
D	157.54	7.07	4.49	1200	45.44	14.45	163732	52.7	365.4	100	1
D	139.51	6.41	4.6	1200	37.31	19.03	142064	40.1	416.9	100	1

Type (density)	M [Å^4/ps eV]	v [10^-2 Å/ps]	P [10^-4 eV/Å^3]	T [K]	θb deg.	θd deg.	N #	lx Å	ly Å	lz Å	Reps. #
A	57.2	5.62	9.82	1200	37.15	9.9	77144	102.5	355,0	25.0	1
A	62.29	4.37	7.02	1200	37.15	9.9	115860	153.7	355,0	25.0	1
A	58.23	3.04	5.23	1200	37.15	9.9	154576	205,0	355,0	25.0	1
A	50.23	2.17	4.33	1200	37.15	9.9	193292	256.2	355,0	25.0	1
A	50.37	1.7	3.38	1200	37.15	9.9	232008	307.5	355,0	25.0	1
A	63.17	1.69	2.68	1200	37.15	9.9	270724	358.7	355,0	25.0	1
A	57.06	1.46	2.56	1200	37.15	9.9	309440	410,0	355,0	25.0	1

Type θb	M [Å^4/ps eV]	v [10^-2 Å/ps]	P [10^-4 eV/Å^3]	T [K]	θb deg.	θd deg.	N #	lx Å	ly Å	lz Å	Reps. #
A	90.64	9.02	9.95	1200	14.9	9.9	90680	103.03	416.4	25.0	1
A	88.72	8.54	9.62	1200	20	9.9	78024	103.2	357.7	25.0	1
A	66.03	5.69	8.61	1200	25.69	9.9	89116	102.5	412.1	25.0	1
A	53.66	4.25	7.92	1200	30	9.9	86692	102.49	400.8	25.0	1
A	48.81	4.34	8.89	1200	34.31	9.9	89144	102.49	412.1	25.0	1
A	47.73	4.76	9.97	1200	39.97	9.9	78020	103.2	357.7	25.0	1
A	68.26	5.38	7.88	1200	45.30	9.9	83984	100.56	391,9	25.0	1
A	54.93	6.14	11.17	1200	50.17	9.9	88320	103.63	403.8	25.0	1
A	67.46	6.56	9.73	1200	55.05	9.9	96056	102.49	443.8	25.0	1
A	53.08	4.74	8.92	1200	60	9.9	83904	99.55	397.9	25.0	1

Type Ea - 40/6	M [Å^4/ps eV]	v [10^-2 Å/ps]	P [10^-4 eV/Å^3]	T [K]	θb deg.	θd deg.	N #	lx Å	ly Å	lz Å	Reps. #
A	-	-	2.77	500	40.34	6.01	107420	147.9	341.6	25.0	1
A	-	-	3.77	600	40.34	6.01	107420	147.9	341.6	25.0	1
A	1.01	0.04	3.53	700	40.34	6.01	107420	147.9	341.6	25.0	1
A	1.55	0.06	3.75	800	40.34	6.01	107420	147.9	341.6	25.0	1
A	6.01	0.23	3.80	900	40.34	6.01	107420	147.9	341.6	25.0	1
A	21.61	0.85	3.93	1000	40.34	6.01	107420	147.9	341.6	25.0	1
A	42.11	1.72	4.08	1100	40.34	6.01	107420	147.9	341.6	25.0	1
A	58.01	2.50	4.31	1200	40.34	6.01	107420	147.9	341.6	25.0	1

Type Ea - 40/10	M [Å^4/ps eV]	v [10^-2 Å/ps]	P [10^-4 eV/Å^3]	T [K]	θb deg.	θd deg.	N #	lx Å	ly Å	lz Å	Reps. #
A	-	-	5.1	100	39.92	10.24	161336	148.6	513.1	25.0	1
A	-	-	7.59	200	39.92	10.24	161336	148.6	513.1	25.0	1
A	-	-	6.17	300	39.92	10.24	161336	148.6	513.1	25.0	1
A	-	-	5.06	400	39.92	10.24	161336	148.6	513.1	25.0	1
A	-	-	4.62	500	39.92	10.24	161336	148.6	513.1	25.0	1
A	1.09	0.05	4.49	600	39.92	10.24	161336	148.6	513.1	25.0	1
A	1.75	0.09	4.89	700	39.92	10.24	161336	148.6	513.1	25.0	1
A	2.35	0.12	5.24	800	39.92	10.24	161336	148.6	513.1	25.0	1
A	7.84	0.4	5.06	900	39.92	10.24	161336	148.6	513.1	25.0	1
A	19.87	1.07	5.38	1000	39.92	10.24	161336	148.6	513.1	25.0	1
A	38.61	2.27	5.87	1100	39.92	10.24	161336	148.6	513.1	25.0	1
A	54.76	3.36	6.14	1200	39.92	10.24	161336	148.6	513.1	25.0	1
A	-	-	-	1300	39.92	10.24	161336	148.6	513.1	25.0	1

Type Ea - 25/6	M [Å^4/ps eV]	v [10^-2 Å/ps]	P [10^-4 eV/Å^3]	T [K]	θb deg.	θd deg.	N #	lx Å	ly Å	lz Å	Reps. #
A	-	-	1.97	100	24.79	6.01	106240	170.5	295.2	25.0	1
A	-	-	6.11	200	24.79	6.01	106240	170.5	295.2	25.0	1
A	-	-	6.24	300	24.79	6.01	106240	170.5	295.2	25.0	1
A	-	-	5.07	400	24.79	6.01	106240	170.5	295.2	25.0	1
A	1.16	0.04	3.62	500	24.79	6.01	106240	170.5	295.2	25.0	1
A	4.4	0.15	3.32	600	24.79	6.01	106240	170.5	295.2	25.0	1
A	10.57	0.38	3.6	700	24.79	6.01	106240	170.5	295.2	25.0	1
A	13.09	0.52	3.98	800	24.79	6.01	106240	170.5	295.2	25.0	1
A	23.83	1.02	4.27	900	24.79	6.01	106240	170.5	295.2	25.0	1
A	32.52	1.48	4.54	1000	24.79	6.01	106240	170.5	295.2	25.0	1
A	31.6	1.37	4.32	1100	24.79	6.01	106240	170.5	295.2	25.0	1
A	38.21	1.55	4.07	1200	24.79	6.01	106240	170.5	295.2	25.0	1
A	-	-	-	1300	24.79	6.01	106240	170.5	295.2	25.0	1

Type Ea - 25/6	M [Å^4/ps eV]	v [10^-2 Å/ps]	P [10^-4 eV/Å^3]	T [K]	θb deg.	θd deg.	N #	lx Å	ly Å	lz Å	Reps. #
D	-	-	1.77	100	24.79	6.01	106594	24.4	295.2	175.1	1
D	-	-	2.29	200	24.79	6.01	106594	24.4	295.2	175.1	1
D	-	-	2.4	300	24.79	6.01	106594	24.4	295.2	175.1	1
D	5.62	0.05	0.9	400	24.79	6.01	106594	24.4	295.2	175.1	1
D	7.75	0.11	1.47	500	24.79	6.01	106594	24.4	295.2	175.1	1
D	16.16	0.26	1.64	600	24.79	6.01	106594	24.4	295.2	175.1	1
D	25.29	0.45	1.76	700	24.79	6.01	106594	24.4	295.2	175.1	1
D	68.73	1.09	1.59	800	24.79	6.01	106594	24.4	295.2	175.1	1
D	108.46	1.87	1.73	900	24.79	6.01	106594	24.4	295.2	175.1	1
D	96.49	1.43	1.49	1000	24.79	6.01	106594	24.4	295.2	175.1	1
D	158.65	3,00	1.89	1100	24.79	6.01	106594	24.4	295.2	175.1	1
D	106.3	2.1	1.97	1200	24.79	6.01	106594	24.4	295.2	175.1	1
D	-	-	-	1300	24.79	6.01	106594	24.4	295.2	175.1	1

Risø's research is aimed at solving concrete problems in the society.

Research targets are set through continuous dialogue with business, the political system and researchers.

The effects of our research are sustainable energy supply and new technology for the health sector.